LA-11491-T
Thesis

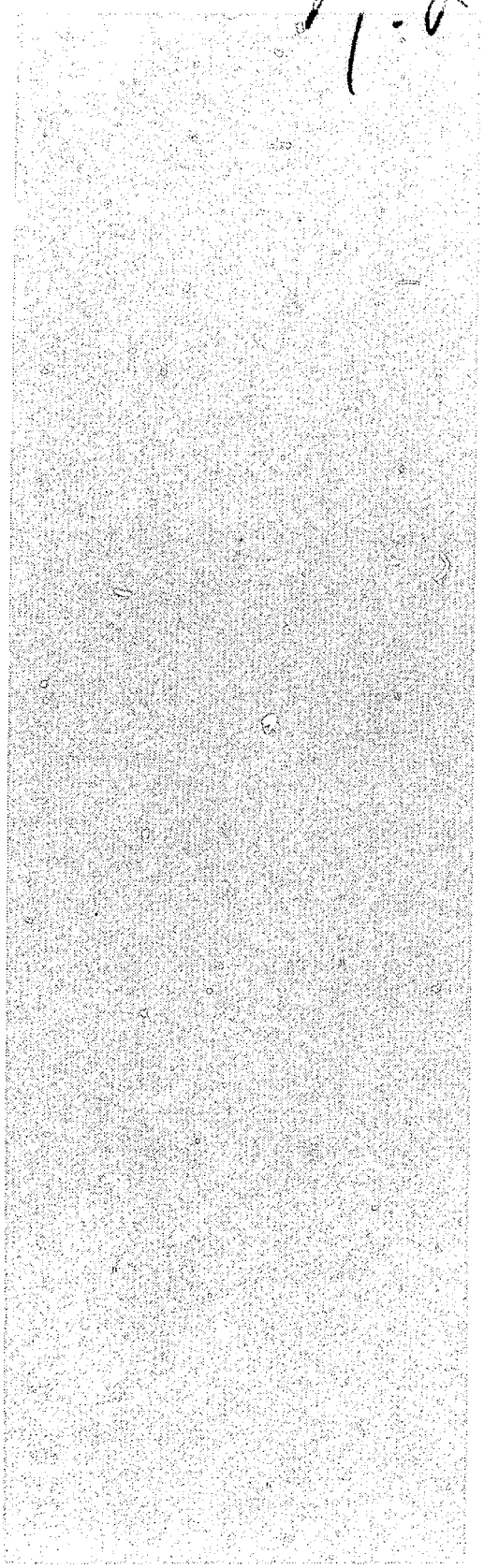

Measurement of np Elastic Scattering Spin-Spin Correlation Parameters at 484, 634, and 788 MeV

Los Alamos

Los Alamos National Laboratory is operated by the University of California for the United States Department of Energy under contract W-7405-ENG-36.

This thesis was accepted by the Department of Physics, New Mexico State University, Las Cruces, New Mexico, in partial fulfillment of the requirements for the degree of Doctor of Philosophy. It is the independent work of the author and has not been edited by the IS-11 Writing and Editing Staff.

This work was supported by the US Department of Energy and Argonne National Laboratory, Division of Educational Programs.

An Affirmative Action/Equal Opportunity Employer

LA-11491-T
Thesis

UC-413
Issued: March 1989

LA--11491-T

DE89 008409

Measurement of np Elastic Scattering Spin-Spin Correlation Parameters at 484, 634, and 788 MeV

Robert William Garnett

Los Alamos National Laboratory
Los Alamos, New Mexico 87545

ACKNOWLEDGEMENTS

I wish to thank my advisor Dr. George Burleson, without who's advice, patience and guidance this dissertation would not have been possible. In addition, I wish to thank Dr. Harold Spinka of Argonne National Laboratory who also acted as my advisor while at Los Alamos. His guidance and insight was always of great help. Working with him helped me grow a great deal as a physicist. I also wish to thank the entire experimental collaboration, in particular, Prof. Gerald Tripard, who helped with some aspects of the Monte-Carlo model. Finally, I wish to thank the LAMPF staff for their assistance and the Argonne Division of Educational Programs for financial support, during my stay at Los Alamos.

MEASUREMENT OF *np* ELASTIC SCATTERING SPIN-SPIN CORRELATION PARAMETERS AT 484, 634, AND 788 MeV

BY

ROBERT WILLIAM GARNETT

ABSTRACT

The spin-spin correlation parameters C_{LL} and C_{SL} were measured for *np* elastic scattering at the incident neutron kinetic energy of $634 MeV$. Good agreement was obtained with previously measured data. Additionally, the first measurement of the correlation parameter C_{SS} was made at the three energies, 484, 634, and $788 MeV$. It was found that the new values, in general, do not agree well with phase shift predictions. A study was carried out to determine which of the isospin-0 partial waves will be affected by

this new data. It was found that the ${}^1P_1$ partial wave will be affected significantly at all three measurement energies. At 634 and $788MeV$, the ${}^3S_1$ phase shifts will also change.

Contents

List of Tables

List of Figures

CHAPTER 1 INTRODUCTION AND MOTIVATION

It has been known for some time that the strong nucleon-nucleon ($N-N$) interaction depends upon the relative orientation of the spins of the interacting nucleons. This characteristic was originally discovered through the analysis of scattering experiments and from the study of nuclear energy levels. With the development of highly polarized proton beams and targets in the last 15 years or so, it has become evermore possible to do detailed studies of the $N-N$ interaction for spin states which are experimentally well-determined.

The $N-N$ interaction is poorly understood in the intermediate energy region from about 200 to $1000 MeV$. However, an understanding of this interaction is fundamental, of course, to a basic understanding of nucleon-nucleus interactions and of nuclear matter in general. At present, there is no coherent and tractable theory of the $N-N$ interaction at intermediate energies. It is hoped that the QCD descriptions, for example Bag Models of the nucleon [De-75,Mu-83,Fa-87], will eventually lead to such a theory. However, to date, the predictive power of these models has been weak. Other, more phenomenological, types of analyses such as dispersion relations [Gr-82], potential mod-

els [El-88], and phase shift analyses (PSA) have been the most sucessful approaches to date. In order to study the spin dependence, polarization phenomena in the $N - N$ interaction have been studied in great detail over the past several decades, and measured polarization (spin) parameters have been used to remove ambiguities among various otherwise acceptable sets of $N - N$ phase shifts. It is hoped that in the near future a unique set of phase shifts will be determined in the intermediate energy region.

A complete determination of the five isospin-one ($I = 1$) and five isospin-zero ($I = 0$) elastic scattering amplitudes requires a large number of measurements of different spin parameters at each energy and scattering angle. In general, a minimum of nine observables in both the proton-proton (pp) and neutron-proton (np) systems are required to determine an unambiguous set of amplitudes above the pion production threshold. These ideas will be discussed further in the next chapter. The $I = 1$ elastic scattering amplitudes are fairly well known up to about $1GeV$ from pp elastic scattering experiments [Ar-83]. The $I = 0$ amplitudes are poorly known. The np elastic and inelastic interaction data base is particularly sparse above $500MeV$. There are a significant number of np differential cross section and polarization measurements, but only a few measurements of other spin parameters. Figure 1.1 shows a plot of the present np and pp scattering data as a function of laboratory incident beam energy and c.m. scattering angle [Ar-83]. Only spin parameters other than differential cross sections and polarizations are shown. The location of the measured data is indicated by a "box" for data

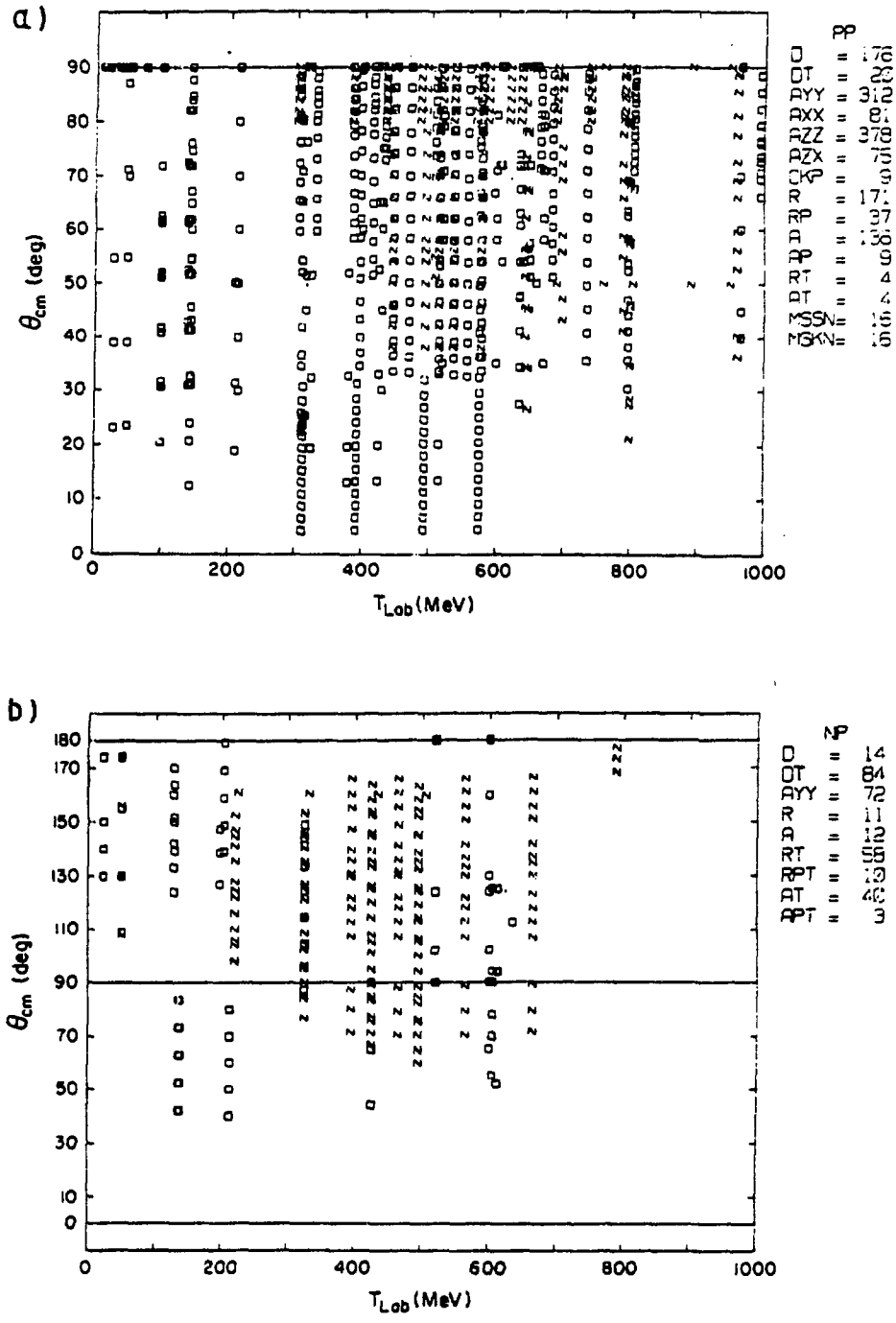

Figure 1.1: The present status of the *np* scattering data base. This figure was taken from SAID database. a)$pp \rightarrow pp$. b)$np \rightarrow np$.

taken before 1978 and by an "N" for data taken later.

Phase-shift predictions of unmeasured spin observables have generally not fit the *pp* data very well until a model independent amplitude (MIA) analysis of the existing data was performed. It is likely that this will also be true for the *np* data. An MIA analysis is able to determine the amplitudes and, consequently, the observables without the bias of particular theoretical assumptions. This will also be discussed in greater detail in the following chapter.

It should be noted that various theoretical approaches have shown qualitative agreement with the observed behavior of the $I = 1$ phase-shifts. However, they generally fail to reproduce the measured spin-averaged total cross sections to better than within $5 - 10mb$. In addition, the partial waves corresponding to the short range part of the $N - N$ interaction are generally not well understood.

Various phase-shift predictions for measured spin parameters have indicated the possibility of resonance-like behavior in certain partial waves. This behavior has been attributed to the possible existence of dibaryon resonances. Evidence for these resonances has been seen in *pp* ($I = 1$) scattering experiments [Au-77]. The interpretation of the observed behavior of the ${}^1D_2$, ${}^3F_3$, and possibly the ${}^3P_0$ partial waves in *pp* elastic scattering seen variously in the phase-shift analyses of VPI [Ar-87], Japan [Ho-78], Saclay-Geneva [By-87], and Queen Mary College [Du-82] are clouded by the presence of the $pp \rightarrow N\Delta$ and $pp \rightarrow \pi D$ inelastic channels. It has been proposed that the opening

of inelastic channels such as these may be responsible for the observed energy-dependent structures [Sh-88]. For this reason, a comparison between the $I = 1$ and $I = 0$ amplitudes should prove instructive because these inelastic channels are not allowed in the $I = 0$ amplitudes. However, the inelastic channels $NN \rightarrow NN^*$ and $NN \rightarrow \Delta\Delta$ can occur at higher energies and can take place through both $I = 1$ and $I = 0$ states. Because of the fundamental nature of the $N - N$ interaction, it is important to know whether such resonances exist. This question is crucial to the further development of six-quark Bag Models. Some of these models predict rich resonance structures in the $N - N$ channel above $2180 MeV$ [He-83]. Therefore, these investigations suggest that large spin effects are related to the composite, or quark, nature of the nucleon.

The experiment discussed in this dissertatic · was motivated by both the possible existence of dibaryon resonances and the goal of determining the $I = 0$, $N-N$ amplitudes. This experiment was but one in a group of experiments performed at the Los Alamos Meson Physics Facility and other laboratories to measure spin-dependent parameters in np elastic-scattering . The aim of this work was to contribute to the rather sparse existing data base of measured np spin-dependent parameters in the $500 - 800 MeV$ energy range.

The nucleon-nucleon scattering formalism, amplitude reconstruction, and phase-shift analysis are discussed in the next chapter. Chapter 3 gives a brief discussion of dibaryon resonances and their possible relationship to measured spin observables.

Chapter 4 describes the experimental set-up used to measure the spin-spin correlation parameters and Chapter 5 describes a Monte-Carlo model developed to check the magnetic field parameterization for our spectrometer. Chapter 6 discusses the data and error analysis techniques. Chapter 7 gives a summary of the results and, finally, Chapter 8 gives the conclusions. A comparison of the measured results to various theoretical predictions is also made in this final chapter. Appendix A discusses a study done to determine the contribution of the background nucleon polarization to the total target polarization. Appendix B describes the algorithm used to do a 3-dimensional fit of the magnetic field of the spectrometer magnet. Appendix C is a listing of the Monte-Carlo program used to check the spectrometer magnetic field parameterization. Appendix D gives a brief description of spin precession in the presence of magnetic fields and Appendix E gives a description of corrections made to the data for this effect.

CHAPTER 2 NUCLEON-NUCLEON SCATTERING FORMALISM

2.1 Introduction

The discussion in this chapter is meant to be a brief overview showing the connection between various aspects of the nucleon-nucleon scattering formalism when one considers spin degrees of freedom. For a rigorous discussion and development of the ideas presented here, the reader is encouraged to examine the articles written by Hoshizaki [Ho-68] and Bourrely et al. [Bo-80].

2.2 The Spin-Spin Correlation Parameters

Experimentally, spin observables are characterized by the particles for which the spin is observed and by their spin direction. The initial-state spin-spin correlation parameters measured in this dissertation are defined by the expression below:

$$C_{ij} = \frac{1}{p_b p_t} \frac{(I^{++} + I^{--}) - (I^{+-} + I^{-+})}{(I^{++} + I^{--}) + (I^{+-} + I^{-+})} \tag{2.1}$$

where the subscripts i and j denote the initial beam and target spin directions, respectively. The numerator is the difference between the number of particles scattered with

beam and target spins parallel, and the number scattered with spins antiparallel. This measured asymmetry is then normalized with respect to the inverse of the beam and target polarizations, p_b and p_t. The spin directions, in the laboratory reference frame, are defined as shown in Fig. 2.1. It should be noted that for these parameters, only the initial beam and target spin directions need to be known.

2.3 Isospin Decomposition

The total isospin, I, of a nucleon (neutron or proton) is defined to be $I = \frac{1}{2}$. The third component of $\vec{I}$ is used to distinguish neutrons and protons; $I_3 = +\frac{1}{2}$ for the proton and $I_3 = -\frac{1}{2}$ for the neutron. This component, in isotopic spin space, is analogous to the z-component of spin in ordinary spin space. The charge of the nucleon is related to I_3 by the expression

$$q = I_3 + \frac{1}{2} \ . \tag{2.2}$$

The $N - N$ interaction depends only on the total isospin of the state and not on the isospins (charges) of the individual nucleons in this state. Therefore, conservation of I_3 in any reaction is simply a manifestation of charge conservation, whereas conservation of $\vec{I}$ is a representation of the charge independence of the strong interaction. Because the strong interaction obeys this symmetry principle (charge independence) it is possible to simplify the $N - N$ elastic scattering matrix. This will be discussed in the next section.

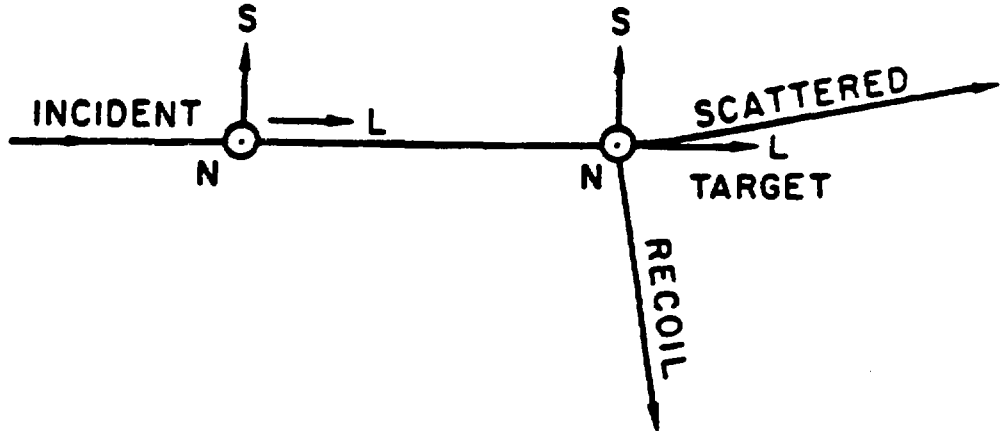

N: NORMAL TO THE SCATTERING PLANE
L: LONGITUDINAL DIRECTION
S = N x L IN THE SCATTERING PLANE

Figure 2.1: Spin directions as defined in the laboratory for a typical two-body scattering process.

The proton and neutron isospin wavefunctions can be defined as follows:

$$U_p = \begin{pmatrix} 1 \\ 0 \end{pmatrix} \equiv \textit{proton}$$

and

$$U_n = \begin{pmatrix} 0 \\ 1 \end{pmatrix} \equiv \textit{neutron}$$

where $U_p^* U_p$ ($U_n^* U_n$) is the probability that the particle is a proton (neutron). For two nucleons labeled (1) and (2), there are four possible isospin wavefunctions ξ_i, which can be written:

$$\xi_1(pp) = U_p(1)U_p(2) \tag{2.3}$$

$$\xi_2(nn) = U_n(1)U_n(2) \tag{2.4}$$

$$\xi_3(np) = \frac{1}{\sqrt{2}}[U_p(1)U_n(2) + U_p(2)U_n(1)] \tag{2.5}$$

$$\xi_4(np) = \frac{1}{\sqrt{2}}[U_p(1)U_n(2) - U_p(2)U_n(1)] \ . \tag{2.6}$$

The wavefunctions ξ_1, ξ_2, and ξ_3 are symmetric under the interchange of particles whereas ξ_4 is antisymmetric. It should be mentioned that these wavefunctions are derived in a manner exactly analogous to that used to derive spin wavefunctions for two spin-$\frac{1}{2}$ particles (see for example, Eder [Ed-68]).

For two nucleons, the total value of the isospin I is either 0 or 1. The three symmetric isospin wavefunctions correspond to $I = 1$ where $I_3 = +1(pp)$, $0(np)$, or $-1(nn)$. The

antisymmetric wavefunction, ξ_4, corresponds to the $I = 0$, $I_3 = 0$ state of a neutron-proton system. Therefore, it can be seen that for the case of neutron-proton elastic scattering the state is a mixture of both isospin-0 and isospin-1. In order to be able to extract pure $I = 0$ elastic scattering amplitudes from *np* scattering the $I = 1$ amplitudes must be known from *pp* elastic scattering.

2.4 The Nucleon-Nucleon Scattering Matrix

For each energy and angle, elastic nucleon-nucleon scattering can be described by a scattering matrix in which the amplitudes depend upon the spin orientation of the nucleons. It is convenient to describe the scattering amplitude, $f^{(u)}$, as a matrix in spin space [Wo-52]. Let $\chi^{(u)}$ be a spinor with four components representing one of the initial spin states u. The scattered wavefunction can then be written as a vector

$$\psi^{(u)} = e^{i(\vec{k_i}\bullet\vec{r})}\chi^{(u)} + f^{(u)}\frac{e^{ikr}}{r} \tag{2.7}$$

with $f^{(u)} = M\chi^{(u)}$. M is a 4×4 matrix operating on the initial spin state. It is called the spin scattering matrix for the two-nucleon system. Here $f^{(u)}$ is the total scattered wave amplitude. The operator M depends on the initial and final momenta in the c.m. system and on the Pauli spin operators for the two particles. If one assumes parity and

time-reversal invariance in addition to isospin invariance for the $N-N$ interaction, the spin scattering matrix can be written in the form [Oe-54, Pu-57, Le-67]

$$\begin{aligned} M(\hat{k_f},\hat{k_i}) &= \frac{1}{2}[(a+b)+(a-b)(\vec{\sigma_1}\cdot\hat{n})(\vec{\sigma_2}\cdot\hat{n})+(c+d)(\vec{\sigma_1}\cdot\hat{m})(\vec{\sigma_2}\cdot\hat{m}) \\ &+ (c-d)(\vec{\sigma_1}\cdot\hat{l})(\vec{\sigma_2}\cdot\hat{l})+e(\vec{\sigma_1}+\vec{\sigma_2})\cdot\hat{n}] \,. \end{aligned} \tag{2.8}$$

The five independent amplitudes a, b, c, d, and e are complex functions of the c.m. system energy k and the scattering angle θ. These amplitudes are called the invariant c.m. amplitudes and are just one possible set of amplitudes to use to describe the system. The basis vectors for this representation are given by

$$\hat{l}=\frac{\hat{k_f}+\hat{k_i}}{|\hat{k_f}+\hat{k_i}|},\ \hat{m}=\frac{\hat{k_f}-\hat{k_i}}{|\hat{k_f}-\hat{k_i}|},\ \hat{n}=\frac{\hat{k_f}\times\hat{k_i}}{|\hat{k_f}\times\hat{k_i}|} \tag{2.9}$$

where $\hat{k_i}$ and $\hat{k_f}$ are unit vectors in the direction of the incident and scattered particle momenta, respectively.

Isospin invariance requires that the most general form of M be

$$M = M_0 P_0 + M_1 P_1 \tag{2.10}$$

where P_I is the projection operator for states with total isospin I. These operators are given by

$$P_0 = \left[\frac{1-(\vec{I_1}\cdot\vec{I_2})}{4}\right] \tag{2.11}$$

$$P_1 = \left[\frac{3+(\vec{I_1}\cdot\vec{I_2})}{4}\right] \tag{2.12}$$

where $\vec{I_1}$ and $\vec{I_2}$ are the nucleon isospin matrices, and M_0 and M_1 are isosinglet and isotriplet scattering matrices, respectively. The matrices, M_0 and M_1, are represented by the same form as M given in Eqn. 2.8. The real scattering processes are therefore described by

$$M(pp \rightarrow pp) = M(nn \rightarrow nn) = M_1 \tag{2.13}$$

$$M(np \rightarrow np) = \frac{1}{2}(M_0 + M_1) \tag{2.14}$$

$$M(pn \rightarrow np) = \frac{1}{2}(M_1 - M_0)\ . \tag{2.15}$$

The spin scattering matrix, M, is related to the usual scattering matrix S by [Ho-68]

$$M = \frac{2\pi}{ik}\langle\theta_f\phi_f|S - 1|\theta_i\phi_i\rangle\ . \tag{2.16}$$

The observables are determined by taking the trace of various combinations of M and the Pauli spin matrices, σ_i. For example, the spin-spin correlation parameter C_{NN}, as defined in the laboratory coordinate system, is given by

$$\frac{d\sigma}{d\Omega}C_{NN} = \frac{1}{4}Tr(MM^{\dagger}\sigma_N^{(1)}\sigma_N^{(2)}) \tag{2.17}$$

where $\frac{d\sigma}{d\Omega}$ is the spin-averaged differential cross section and $\sigma_N^{(1)}$ and $\sigma_N^{(2)}$ are the initial spin matrices for the incident and target particles, respectively. A complete list of observables expressed as traces of M can be found in either Hoshizaki's paper [Ho-68] or the paper of Bystricky et al. [By-78].

2.5 Helicity Amplitudes

As discussed earlier, the invariant c.m. amplitudes are not the only amplitudes which can be used in a description of $N - N$ scattering when one does not want to ignore spin effects. There are many sets of amplitudes which can be used; however, the most widely used are the so-called c.m. s-channel helicity amplitudes of Jacob and Wick [Ja-59]. These amplitudes are defined with respect to two-body reactions and are labelled by the individual particle 3-momenta and helicities. By choosing this representaion, the relativistic corrections to the scattering matrix are also simplified.

The helicity, λ, is defined as the component of spin along the direction of motion of the particle. The helicity operator commutes with the momentum operator and is defined by

$$\lambda \equiv \vec{J} \cdot \vec{p} \,. \tag{2.18}$$

However, since $\vec{L} \cdot \vec{p} = \vec{p} \cdot \vec{L} = 0$, the helicity operator depends only on the spin angular momentum. Therefore, the expression above simplifies to

$$\lambda = \vec{\sigma} \cdot \vec{p} \,. \tag{2.19}$$

It should be noted that λ is a pseudo-scalar quantity. The s-channel helicity amplitudes are defined in the rest frame where $\vec{p_1} + \vec{p_2} = 0$ for the reaction $1 + 2 \rightarrow 3 + 4$. The helicity of a nucleon is then chosen to be $+\frac{1}{2}$ if the spin is parallel to the momentum and $-\frac{1}{2}$ if it is antiparallel.

The total number of helicity amplitudes in the process $1 + 2 \rightarrow 3 + 4$ is given by $n = (2s_1 + 1)(2s_2 + 1)(2s_3 + 1)(2s_4 + 1)$, where s_i is the spin of the ith particle [Ka-84]. For $NN \rightarrow NN$ this gives 16 amplitudes. However, assuming the symmetries discussed in Sec. 2.3 (time-reversal, etc.), then for $N - N$ elastic scattering these reduce to five independent amplitudes. These can be expressed in the form:

$$M_{fi} = \langle \lambda_3 \lambda_4 | M | \lambda_1 \lambda_2 \rangle \tag{2.20}$$

where λ_j is the helicity of the jth particle. The five independent amplitudes are then given by

$$\begin{aligned} \phi_1 &= \langle ++|M|++\rangle \\ \phi_2 &= \langle ++|M|--\rangle \\ \phi_3 &= \langle +-|M|+-\rangle \\ \phi_4 &= \langle +-|M|-+\rangle \\ \phi_5 &= \langle ++|M|+-\rangle \,. \end{aligned} \tag{2.21}$$

It should be noted that ϕ_1 and ϕ_3 are non-spin-flip amplitudes, ϕ_5 is a single spin-flip amplitude, and ϕ_2 and ϕ_4 are double spin-flip amplitudes.

By substituting Eqn. 2.8 for M and calculating the appropriate matrix elements, it is possible to obtain expressions for these five amplitudes in terms of the invariant c.m.

amplitudes a, b, c, d, and e:

$$\begin{aligned}
\phi_1 &= \frac{1}{2}(a\cos\theta + b - c + d + ie\sin\theta) \\
\phi_2 &= \frac{1}{2}(a\cos\theta - b + c + d + ie\sin\theta) \\
\phi_3 &= \frac{1}{2}(a\cos\theta + b + c - d + ie\sin\theta) \\
\phi_4 &= \frac{1}{2}(-a\cos\theta + b + c + d - ie\sin\theta) \\
\phi_5 &= \frac{1}{2}(-a\cos\theta + ie\sin\theta)
\end{aligned} \tag{2.22}$$

where θ is the c.m. scattering angle [By-78]. It should be noted that for forward scattering ($\theta = 0$), angular momentum conservation requires that $\phi_4 = \phi_5 = 0$.

When discussing meson exchange, it is useful to use the t-channel exchange amplitudes. Here t is the four-momentum transfer given by $t = (p_1 - p_3)^2 = (p_2 - p_4)^2 = m_1^2 + m_3^2 - 2E_1E_3 + 2\vec{p_1}\cdot\vec{p_3}$. These amplitudes are defined as various linear combinations of the s-channel helicity amplitudes and are given by [Ha-74]

$$\begin{aligned}
N_0 &= K(\phi_1 + \phi_3) \\
N_1 &= \phi_5 \\
N_2 &= K(\phi_4 - \phi_2) \\
U_0 &= K(\phi_1 - \phi_3) \\
U_2 &= K(\phi_4 + \phi_2)
\end{aligned} \tag{2.23}$$

where K is a constant.

2.6 Observables and Amplitude Reconstruction

For $N - N$ elastic scattering there are a total of $4^4(= 256)$ possible spin observables which one can measure at a single scattering angle. Most of these are either redundant or zero. For example, 128 of the observables are pseudo-scalars which vanish since parity is conserved. Table 2.1 lists many of the pertinent spin observables in terms of the s-channel helicity amplitudes. It should be noted that in this table, the differential cross section, $\frac{d\sigma}{d\Omega}$ is denoted by σ and the total cross section by σ^{tot}. In addition to the notation introduced in Sec. 2.1, a somewhat more informative notation is also shown for each observable. The notation $(i, j; k, l)$ is shown where i and j are the initial beam and target spins, respectively. The final state scattered and recoil spins are given by k and l. A value of zero for i, j, k, or l implies that the spin orientation is not known or measured. As can be seen, there are a wide variety of spin observables, including those where both initial and final state spin orientations are measured. Table 2.2 shows the same observables expressed in terms of the t-channel exchange amplitudes.

The normalization of the s-channel c.m. helicity amplitudes is chosen such that [Go-60]

$$\sigma_{tot} = \frac{2\pi}{k} Im\left[\phi_1(0) + \phi_3(0)\right] \quad at \quad t = 0 \tag{2.24}$$

and

$$\frac{d\sigma}{dt} = \frac{\pi}{2k^2}\left[|\phi_1|^2 + |\phi_2|^2 + |\phi_3|^2 + |\phi_4|^2 + 4|\phi_5|^2\right] . \tag{2.25}$$

Table 2.1: Spin observables expressed in terms of the s-channel helicity amplitudes.

Observables (B,T;S,R)		Helicity Amplitudes
(Single Scattering)		
σ^{Tot}		$(2\pi/k)\ \mathrm{Im}\{\phi_1 + \phi_3(0)\}$
$\Delta\sigma_L^{Tot}$		$(4\pi/k)\ \mathrm{Im}\{\phi_1(0) - \phi_3(0)\}$
$\Delta\sigma_T^{Tot}$		$-(4\pi/k)\ \mathrm{Im}\ \phi_2(0)$
σ	$= (0,0;0,0)$	$\frac{1}{2}\{\lvert\phi_1\rvert^2 + \lvert\phi_2\rvert^2 + \lvert\phi_3\rvert^2 + \lvert\phi_4\rvert^2 + 4\lvert\phi_5\rvert^2\}$
P	$= (0,N;0,0)$	$\mathrm{Im}\{(\phi_1 + \phi_2 + \phi_3 - \phi_4)^* \phi_5\}/\sigma$
C_{NN}	$= (N,N;0,0)$	$\mathrm{Re}\{\phi_1 * \phi_2 - \phi_3 * \phi_4) + 2\lvert\phi_5\rvert^2\}/\sigma$
C_{SS}	$= (S,S;0,0)$	$\mathrm{Re}\{\phi_1 * \phi_2 + \phi_3 * \phi_4)/\sigma$
C_{SL}	$= (S,L;0,0)$	$\mathrm{Re}\{(\phi_1 + \phi_2 - \phi_3 + \phi_4)^* \phi_5\}/\sigma$
C_{LL}	$= (L,L;0,0)$	$\frac{1}{2}\{-\lvert\phi_1\rvert^2 - \lvert\phi_2\rvert^2 + \lvert\phi_3\rvert^2 + \lvert\phi_4\rvert^2\}/\sigma$
Note: $d\sigma/dt = \sigma \cdot \pi/k^2$.		
(Double Scattering		
(1) K_{jk} measurement		
K_{NN}	$= (N,0;0,N)$	$\{-\mathrm{Re}(\phi_1 * \phi_4 - \phi_2 * \phi_3) + 2\lvert\phi_5\rvert^2\}/\sigma$
K_{SS}	$= (S,0;0,S)$	$[\sin\theta_R\ \mathrm{Re}\{(\phi_1 - \phi_2 - \phi_3 - \phi_4)^*\phi_5\} - \cos\theta_R\ \mathrm{Re}(\phi_1^*\phi_4 + \phi_2^*\phi_3)]/\sigma$
K_{LS}	$= (L,0;0,S)$	$[-\frac{1}{2}\sin\theta_R\{\lvert\phi_1\rvert^2 - \lvert\phi_2\rvert^2 - \lvert\phi_3\rvert^2 + \lvert\phi_4\rvert^2) + \cos\theta_R\ \mathrm{Re}\{(\phi_1 - \phi_2 - \phi_3 - \phi_4)^*\phi_5\}]/\sigma$
(2) D_{jk} measurement		
D_{NN}	$= (0,N;0,N)$	$\{\mathrm{Re}(\phi_1 * \phi_3 - \phi_2 * \phi_4) + 2\lvert\phi_5\rvert^2\}/\sigma$
D_{SS}	$= (0,S;0,S)$	$[-\sin\theta_R\mathrm{Re}\{(\phi_1 - \phi_2 + \phi_3 + \phi_4)^*\phi_5\} - \cos\theta_R\mathrm{Re}\{\phi_1^*\phi_3 + \phi_2^*\phi_4)\}]/\sigma$
D_{LS}	$= (0,L;0,S)$	$[\frac{1}{2}\sin\theta_R\{\lvert\phi_1\rvert^2 - \lvert\phi_2\rvert^2 + \lvert\phi_3\rvert^2 - \lvert\phi_4\rvert^2 - \cos\theta_R\mathrm{Re}\{(\phi_1 - \phi_2 + \phi_3 + \phi_4)^*\phi_5\}]/\sigma$
(3) Three Spin Measurement		
H_{SNS}	$= (S,N;0,S)$	$[-\sin\theta_R\ \mathrm{Im}(\phi_1^*\phi_2 + \phi_3^*\phi_4) + \cos\theta_R\mathrm{Im}\{(\phi_1 - \phi_2 - \phi_3 - \phi_4)^*\phi_5\}]/\sigma$
H_{NSS}	$= (N,S;0,S)$	$[\sin\theta_R\ \mathrm{Im}(\phi_1^*\phi_2 - \phi_3^*\phi_4) - \cos\theta_R\mathrm{Im}\{(\phi_1 - \phi_2 + \phi_3 + \phi_4)^*\phi_5\}]/\sigma$
H_{SSN}	$= (S,S;0,N)$	$\mathrm{Im}\{(\phi_1 + \phi_2 - \phi_3 + \phi_4)^*\phi_5\}/\sigma$
H_{LSN}	$= (L,S;0,N)$	$-\mathrm{Im}(\phi_1 * \phi_2 - \phi_2 * \phi_4)/\sigma$
H_{NLS}	$= (N,L;0,S)$	$[\sin\theta_R\mathrm{Im}\{(\phi_1 - \phi_2 + \phi_3 + \phi_4)^*\phi_5\} - \cos\theta_R\ \mathrm{Im}(\phi_1^*\phi_4 + \phi_2^*\phi_3)]/\sigma$
H_{SLN}	$= (S,L;0,S)$	$\mathrm{Im}(\phi_1 * \phi_4 - \phi_2 * \phi_3)/\sigma$
H_{LNS}	$= (L,N;0,S)$	$[-\sin\theta_R\mathrm{Im}\{(\phi_1 - \phi_2 - \phi_3 - \phi_4)^*\phi_5\} - \cos\theta_R\ \mathrm{Im}(\phi_1^*\phi_3 + \phi_2^*\phi_4)]/\sigma$

Note: θ_R is the laboratory recoil angle.

Table 2.2: Spin observables expressed in terms of the t-channel exchange amplitudes.

Observables (B, T; S, R)		Exchange Amplitudes
(Single Scattering)		
σ^{Tot}		$4\pi/k\ \mathrm{Im}N_0$
$\Delta\sigma_L^{Tot}$		$8\pi/k\ \mathrm{Im}U_0$
$\Delta\sigma_T^{Tot}$		$-8\pi/k\ \mathrm{Im}U_2$
σ	= (0,0;0,0)	$\lvert N_0\rvert^2 + 2\lvert N_1\rvert^2 + \lvert N_2\rvert^2 + \lvert U_0\rvert^2 + \lvert U_2\rvert^2$
P	= (0,N;0,0) = (N,0;0,0)	$-2\mathrm{Im}\{(N_0 - N_2)N_1^*\}/\sigma$
C_{NN}	= (N,N;0,0)	$2\mathrm{Re}(U_0U_2^* - N_0N_2^* + \lvert N_1\rvert^2)/\sigma$
C_{SS}	= (S,S;0,0)	$2\mathrm{Re}(N_0U_2^* - N_2U_0^*)/\sigma$
C_{SL}	= (S,L;0,0)	$2\mathrm{Re}\{(U_0 + U_2)N_1^*\}/\sigma$
C_{LL}	= (L,L;0,0)	$-2\mathrm{Re}(N_0U_0^* - N_2U_2^*)/\sigma$
Note:	$(d\sigma/dt = \sigma\cdot\pi/k^2)$	
(Double Scattering)		
1. K_{jk} Measurement		
K_{NN}	= (N,0;0,N)	$-2\mathrm{Re}(U_0U_2^* + N_0N_2^* - \lvert N_1\rvert^2)/\sigma$
K_{SS}	= (S,0;0,S)	$[-2\mathrm{Re}\{(U_2-U_0)N_1^*\}\sin\theta_R - 2\mathrm{Re}(N_0U_2^* + N_2U_0^*)\cos\theta_R]/\sigma$
K_{LS}	= (L,0;0,S)	$\{-2\mathrm{Re}(N_0U_0^* + N_2U_2^*)\sin\theta_R - 2\mathrm{Re}(N_1^*(U_2-U_0))\cos\theta_R\}/\sigma$
2. D_{jk} Measurement		
D_{NN}	= (0,N;0,N)	$\{\lvert N_0\rvert^2 + 2\lvert N_1\rvert^2 + \lvert N_2\rvert^2 - \lvert U_0\rvert^2 - \lvert U_2\rvert^2\}/\sigma$
D_{SS}	= (0,S;0,S)	$[-2\mathrm{Re}\{(N_0 + N_2)N_1^*\}\sin\theta_R - (\lvert N_0\rvert^2 - \lvert N_2\rvert^2 + \lvert U_2\rvert^2 - \lvert U_0\rvert^2)\cos\theta_R]/\sigma$
D_{LS}	= (0,L;0,S)	$[(\lvert N_0\rvert^2 - \lvert N_2\rvert^2 - \lvert U_2\rvert^2 + \lvert U_0\rvert^2)\sin\theta_R - 2\mathrm{Re}\{(N_0 + N_2)N_1^*\}\cos\theta_R]/\sigma$
3. Three-Spin Measurement		
H_{SNS}	= (S,N;0,S)	$[2\mathrm{Im}(N_0U_2^* + N_2U_0^*)\sin\theta_R + 2\mathrm{Im}\{(U_2 - U_0)N_1^*\}\cos\theta_R]/\sigma$
H_{NSS}	= (N,S;0,S)	$[-2\mathrm{Im}(U_0U_2^* - N_0N_2^*)\sin\theta_R + 2\mathrm{Im}\{(N_0 + N_2)N_1^*\}\cos\theta_R]/\sigma$
H_{SSN}	= (S,S;0,N)	$-2\mathrm{Im}\{(U_2 + U_0)N_1^*\}/\sigma$
H_{LSN}	= (L,S;0,N)	$2\mathrm{Im}(U_0N_0^* - U_2N_2^*)/\sigma$
H_{NLS}	= (N,L;0,S)	$[-2\mathrm{Im}\{(N_0 + N_2)N_1^*\}\sin\theta_R + 2\mathrm{Im}(U_0U_2^* + N_0N_2^*)\cos\theta_R]/\sigma$
H_{SLN}	= (S,L;0,N)	$-2\mathrm{Im}(N_0U_2^* - N_2U_0^*)/\sigma$
H_{LNS}	= (L,N;0,S)	$[-2\mathrm{Im}\{(U_2 - U_0)N_1^*\}\sin\theta_R + 2\mathrm{Im}\{U_0N_0^* + U_2N_2^*\}\cos\theta_R]/\sigma$

Because of isospin conservation, if the pp scattering matrix is completely known at a specified energy and angle, then it is possible to reconstruct the $I = 0$ scattering matrix from fewer np measurements. This can be understood by the following argument. An np elastic scattering observable, $\vartheta_{np}(\theta)$, is expressed in the form of a trace such as

$$\begin{aligned} \vartheta_{np}(\theta) &= \frac{1}{4} Tr(M_{np}\sigma^{(\nu)} M_{np}^{\dagger}\sigma^{(\mu)}) \quad \mu,\nu = 1,2 \\ &= \vartheta_1(\theta) + \vartheta_0(\theta) + \vartheta_{int}(\theta) \end{aligned} \tag{2.26}$$

where $\vartheta_{int}(\theta)$ is an interference term. The isospin-0 and isospin-1 pieces have the form

$$\vartheta_I = \frac{1}{16} Tr(M_I\sigma^{(\nu)} M_I^{\dagger}\sigma^{(\mu)}) \tag{2.27}$$

and the interference term has the form

$$\vartheta_{int} = \frac{1}{16}\left[Tr(M_1\sigma^{(\nu)} M_0^{\dagger}\sigma^{(\mu)}) + Tr(M_0\sigma^{(\nu)} M_1^{\dagger}\sigma^{(\mu)})\right] . \tag{2.28}$$

Because of the interference term, measurements of ϑ_{np} at a pair of scattering angles θ and $\pi - \theta$ are still independent. This is not the case for pp elastic scattering since the particles are identical. The relations between the amplitudes at θ and $\pi - \theta$ are given simply by

$$\begin{aligned} \phi_1(\pi - \theta) &= (-1)^{I+1}\phi_1(\theta) \\ \phi_2(\pi - \theta) &= (-1)^{I+1}\phi_2(\theta) \\ \phi_3(\pi - \theta) &= (-1)^{I}\phi_4(\theta) \\ \phi_5(\pi - \theta) &= (-1)^{I}\phi_5(\theta) . \end{aligned} \tag{2.29}$$

These expressions were taken from Goldberger et al. [Go-60]. From Eqn. 2.14 it is clear that the *np* amplitudes in terms of the $I = 0$ and $I = 1$ amplitudes are given by

$$\phi_{i,np} = \frac{1}{2}(\phi_{i,0} + \phi_{i,1}) \tag{2.30}$$

where $i = 1, 2, 3, 4$, or 5. It can therefore be seen that by taking appropriate combinations of the observables for *np* elastic scattering, and if the $I = 1$ amplitudes are known from *pp* elastic scattering, the $I = 0$ amplitudes can be determined in a model-independent fashion up to an arbitrary phase. The phase can be determined relative to the coulomb phase.

It has been shown by H. Spinka [Sp-84] that measurements of the six non-zero *np* elastic scattering spin observables $\frac{d\sigma}{d\Omega}$, P, C_{LS}, C_{NN}, C_{SS}, and C_{LL} at one energy and both angles θ and $\pi - \theta$ allows the determination of the $I = 0$ amplitudes up to a four-fold ambiguity. Because the observables are bilinear in the amplitudes, it would be necessary to measure spin observables where the initial and final spins of one of the particles (beam or target) were measured in order to remove the ambiguity, such as the spin-transfer (K_{ij}) or depolarization (D_{ij}) parameters.

Following the analysis of Spinka, it is useful to form the following linear combinations of the s-channel helicity amplitudes:

$$\begin{aligned} \phi_s &= \frac{1}{2}(\phi_1 - \phi_2) \\ \phi_t &= \frac{1}{2}(\phi_1 + \phi_2) \end{aligned}$$

$$\begin{aligned} \phi_T &= \frac{1}{2}(\phi_3 - \phi_4) \\ \phi_\tau &= \frac{1}{2}(\phi_3 + \phi_4) \\ \phi_5 &= \phi_5 \end{aligned} \tag{2.31}$$

where ϕ_s contains only spin singlet contributions, ϕ_T and ϕ_τ contain only spin triplet partial waves, and ϕ_t and ϕ_5 contain coupled spin triplet terms [Sc-65]. The relations between these amplitudes at θ and $\pi - \theta$ are given by

$$\begin{aligned} \phi_{s,I}(\pi - \theta) &= (-1)^{I+1}\phi_{s,I}(\theta) \\ \phi_{t,I}(\pi - \theta) &= (-1)^{I+1}\phi_{t,I}(\theta) \\ \phi_{T,I}(\pi - \theta) &= (-1)^{I+1}\phi_{T,I}(\theta) \\ \phi_{\tau,I}(\pi - \theta) &= (-1)^{I}\phi_{\tau,I}(\theta) \\ \phi_{5,I}(\pi - \theta) &= (-1)^{I}\phi_{5,I}(\theta) \end{aligned} \tag{2.32}$$

for both $I = 0$ and $I = 1$.

In terms of these linear combinations of the helicity amplitudes, the elastic scattering spin observables are given by:

$$\frac{d\sigma}{d\Omega} = |\phi_s|^2 + |\phi_t|^2 + |\phi_T|^2 + |\phi_\tau|^2 + 2|\phi_5|^2 \tag{2.33}$$

$$P\frac{d\sigma}{d\Omega} = 2\,Im(\phi_t^*\phi_5 - \phi_T\phi_5^*) \tag{2.34}$$

$$C_{LS}\frac{d\sigma}{d\Omega} = 2\,Re(\phi_t^*\phi_5 - \phi_T\phi_5^*) \tag{2.35}$$

$$C_{NN}\frac{d\sigma}{d\Omega} = -|\phi_s|^2 + |\phi_t|^2 + |\phi_T|^2 - |\phi_\tau|^2 + 2|\phi_5|^2 \tag{2.36}$$

$$C_{SS}\frac{d\sigma}{d\Omega} = -|\phi_s|^2 + |\phi_t|^2 - |\phi_T|^2 + |\phi_\tau|^2 \quad (2.37)$$

$$C_{LL}\frac{d\sigma}{d\Omega} = -|\phi_s|^2 - |\phi_t|^2 + |\phi_T|^2 + |\phi_\tau|^2 \ . \quad (2.38)$$

The spin directions $\hat{L}$, $\hat{N}$, and $\hat{S}$ are as defined earlier. By taking the appropriate combinations of the five equations above, it is possible to express the amplitudes given in Eqn. 2.31 in terms of the observables. These relations hold for either the $I = 0$ or $I = 1$ amplitudes, where

$$|\phi_{s,I}|^2 = \frac{1}{4}(1 - C_{NN} - C_{SS} - C_{LL})\frac{d\sigma}{d\Omega} \quad (2.39)$$

$$|\phi_{\tau,I}|^2 = \frac{1}{4}(1 - C_{NN} + C_{SS} + C_{LL})\frac{d\sigma}{d\Omega} \quad (2.40)$$

$$|\phi_{t,I}|^2 + |\phi_{5,I}|^2 = \frac{1}{4}(1 + C_{NN} + C_{SS} - C_{LL})\frac{d\sigma}{d\Omega} \quad (2.41)$$

$$|\phi_{T,I}|^2 + |\phi_{5,I}|^2 = \frac{1}{4}(1 + C_{NN} - C_{SS} + C_{LL})\frac{d\sigma}{d\Omega} \ . \quad (2.42)$$

At $\theta = 90^o$, the conditions in Eqn. 2.32 require that two $I = 1$ and three $I = 0$ amplitudes vanish, namely $\phi_{\tau,1}$, $\phi_{s,1}$, $\phi_{s,0}$, $\phi_{t,0}$, and $\phi_{T,0}$. The following relations for the $I = 0$ observables can be derived from Eqns. 2.33-2.38 and the vanishing of the three $I = 0$ amplitudes:

$$C_{NN} + C_{SS} + C_{LL} = 1 \quad (2.43)$$

$$C_{SS} = C_{LL} = \frac{1}{2}(1 - C_{NN}) \ . \quad (2.44)$$

Equation 2.43 is analogous to the well-known $I = 1$ relation at $\theta_{cm} = 90^0$ when $\phi_{\tau,1} = 0$:

$$C_{NN,pp} - C_{SS,pp} - C_{LL,pp} = 1 \ . \quad (2.45)$$

The magnitudes of the two non-zero $I = 0$ amplitudes at $\theta_{cm} = 90^o$ are given by

$$|\phi_{\tau}|^2 = C_{LL}\frac{d\sigma}{d\Omega} \tag{2.46}$$

$$|\phi_5|^2 = \frac{1}{4}\frac{d\sigma}{d\Omega}(1 + C_{NN}) = \frac{1}{2}\frac{d\sigma}{d\Omega}(1 - C_{LL}) \; . \tag{2.47}$$

It is not possible to determine the phase of $\phi_{\tau,0}$ from these measurements. The amplitude $\phi_{5,0}$, however, can be determined uniquely from the relations

$$\left(P\frac{d\sigma}{d\Omega}\right)_{np} = \frac{1}{2}\,Im(\phi^*_{t,1}\phi_{5,0} - \phi_{T,1}\phi^*_{5,0}) \tag{2.48}$$

$$\left(C_{LS}\frac{d\sigma}{d\Omega}\right)_{np} = \frac{1}{2}\,Re(\phi^*_{t,1}\phi_{5,0} - \phi_{T,1}\phi^*_{5,0}) \tag{2.49}$$

assuming the $I = 1$ amplitudes are known. Therefore, the evaluation of $|\phi_5|$ provides a consistency check of the different experimental measurements and provides an estimate of the systematic errors on the amplitude determination.

There are other relations between np and pp spin observables which can be derived (see reference [By-78] for a more complete list.):

$$C_{SS,np} = C_{LL,np} + \frac{1}{4}[C_{NN,pp} - 1 - 2C_{LL,pp}]\frac{(d\sigma/d\Omega)_{pp}}{(d\sigma/d\Omega)_{np}} \tag{2.50}$$

$$2C_{SS,np} = 1 - C_{NN,np} + \frac{1}{4}[3C_{NN,pp} - 3 - 2C_{LL,pp}]\frac{(d\sigma/d\Omega)_{pp}}{(d\sigma/d\Omega)_{np}} \tag{2.51}$$

$$2C_{LL,np} = 1 - C_{NN,np} + \frac{1}{4}[C_{NN,pp} - 1 - 2C_{LL,pp}]\frac{(d\sigma/d\Omega)_{pp}}{(d\sigma/d\Omega)_{np}} \; . \tag{2.52}$$

Equation 2.50 above will be a particulary useful cross-check for the data discussed in this dissertation. It will provide a check of the overall normalization of the measured values of C_{SS}.

2.7 The Partial Wave Analysis

In the intermediate energy region, the $N-N$ amplitudes are usually determined using a partial wave analysis. The amplitudes are decomposed into a linear combination of spin singlet and triplet partial waves. Since each spin observable is some combination of the amplitudes, it can be expressed in terms of a partial wave expansion; in general, these are rather complicated expressions. The final step is then to fit the experimental data to obtain the partial wave amplitudes.

There are two ways to treat the data. One is to do an energy-dependent analysis. Possible forms of the energy dependence of the partial waves must be assumed in order to fit the data. The other method is to do a single-energy search where the phase shifts are determined for that energy alone. However, the two methods are interdependent; the energy-dependent analyses use single-energy searches as anchor points for the fitting and the single-energy searches frequently use the known energy dependence to make data measured at slightly different energies compatible. The energy-dependent analysis is used to connect and choose single-energy solutions.

In order to make the partial wave analysis tractable, the number of partial waves must be limited. This limits the number of free parmeters for the fitting. It is at this point, in general, that differences between the various partial wave analyses become apparent. Various theoretical inputs and constraints are used and these often differ

among the various partial wave analyses, reflecting to some extent the philosophies, styles, or judgements of the individual doing the analysis [Sp-84]. This point will be discussed in more detail at the end of this section.

The total scattered wave amplitude of Eqn. 2.7 can be written as follows [Wi-61]:

$$f = \frac{1}{k} \sum_l \sqrt{4\pi(2l+1)}\, \frac{\eta_l \exp(2i\delta_l) - 1}{2i}\, Y_l^m(\cos\theta) \tag{2.53}$$

where the quantities $\frac{1}{2i}[\eta_l \exp(2i\delta_l) - 1]$ are the partial wave amplitudes and the $Y_l^m(\cos\theta)$ the spherical harmonics. The δ_l are the phase shifts which contain the effect of the actual interaction which causes the scattering. The amount of inelasticity in each partial wave is contained in the η or "elasticity" parameter. Of course, for pure elastic scattering, η is identically equal to 1. Equation 2.53 can also be written in terms of the S-matrix. By combining Eqns. 2.7, 2.16, and 2.53, it can be seen that the S-matrix is given by

$$S = e^{2i\delta} \tag{2.54}$$

where δ is the phase shift operator. If one assumes charge-independence of the $N - N$ interaction, then in the collision of two nucleons, the total angular momentum J, total spin S, parity $P = (-1)^L$, and total isospin I are conserved. The orbital angular momentum, L, is no longer a good quantum number. The Pauli exclusion principle gives the condition of antisymmetry of states:

$$(-1)^{S+1}(-1)^{I+1}P = (-1)^{S+I+L} = -1 \ . \tag{2.55}$$

For the case of two protons in the spin singlet state, the orbital wave function can contain only partial waves with even-L. If the two protons are in the spin triplet state, only partial waves with odd-L are allowed. The same conditions hold for the case of two neutrons. Therefore, any two-proton (or two-neutron) state can only be a linear superposition of singlet and triplet spin states in the series

$$^1S,\ ^3P,\ ^1D,\ ^3F,\ ^1G,\ ^3H,\ ....,\ etc. \tag{2.56}$$

where the states are defined by the following notation: $^{2S+1}L_J$. Here $2s+1=1$ ($2s+1=3$) denotes the spin singlet (spin triplet) state. The total angular momentum value of the state, J, has been omitted.

For neutron-proton scattering, because the particles are different, there are no symmetry requirements; therefore, the *np* system can be a linear superposition of any of the spin singlet or triplet states:

$$^1S,\ ^3S,\ ^1P,\ ^3P,\ ^1D,\ ^3D,\ ^1F,\ ^3F,\ ^1G,\ ^3G,....,\ etc. \tag{2.57}$$

The presence of both spin singlet and triplet states corresponds to the presence of both isospin-singlet and isospin-triplet states.

Since parity is conserved, there can be no transitions between singlet and triplet states since these always have opposite parity. Transitions can occur, however, between states of different orbital angular momentum but the same J and parity. It is easily possible to define phase shifts for all initial states which cannot change their L values.

The triplet spin states having $L_{even} \geq 2$, however, can undergo L-mixing transitions. It is necessary to define quantities which give the degree to which the mixing occurs and to define the phase shifts for these states. This is accomplished through the S-matrix formalism.

Because the orbital angular momentum, L, is no longer a good quantum number, the S-matrix is not diagonal with respect to L. It is necessary therefore, to express the partial waves in terms of the total angular momentum J. For a given J, there are in addition to the $L = J$ states, two triplet states with $L = J \pm 1$ which couple to each other. These correspond to two outgoing elastic scattering channels having the same properties. These channels are connected by a 2×2 submatrix, S_J, of the full scattering matrix. This submatrix is defined by

$$S_J - 1 = \begin{pmatrix} R_{J-1,J} & -R^J \\ -R^J & R_{J+1,J} \end{pmatrix}$$

where the R^J and $R_{J\pm1,J}$ are the partial wave amplitudes. If there are no inelastic channels, S_J is a symmetric unitary 2×2 matrix which can be diagonalized using the parameterization of Stapp et al. [St-57]

$$S_J = \begin{pmatrix} e^{i\delta_{J-1,J}} & 0 \\ 0 & e^{i\delta_{J+1,J}} \end{pmatrix} \begin{pmatrix} \cos(2\epsilon_J) & i\sin(2\epsilon_J) \\ i\sin(2\epsilon_J) & \cos(2\epsilon_J) \end{pmatrix} \begin{pmatrix} e^{i\delta_{J-1,J}} & 0 \\ 0 & e^{i\delta_{J+1,J}} \end{pmatrix}$$

where the $\delta_{J-1,J}$ and $\delta_{J+1,J}$ are the "nuclear-bar phase shifts" and the ϵ_J are the "mixing parameters". The case where inelastic channels are open is even more complicated.

As described earlier, it is possible to express the helicity amplitudes in terms of singlet and triplet partial waves. Let the partial wave amplitudes be defined as by Scotti and Wong [Sc-65]:

$$R_J = \frac{1}{2i}(\eta_J e^{2i\delta_J} - 1) \tag{2.58}$$

$$R_{J,J} = \frac{1}{2i}(\eta_{JJ} e^{2i\delta_{J,J}} - 1) \tag{2.59}$$

$$R_{J-1,J} = \frac{1}{2i}\left[\eta_{J-1,J}(\cos(2\epsilon_J)\exp(2i\delta_{J-1,J}) - 1)\right] \tag{2.60}$$

$$R_{J+1,J} = \frac{1}{2i}\left[\eta_{J+1,J}(\cos(2\epsilon_J)\exp(2i\delta_{J+1,J}) - 1)\right] \tag{2.61}$$

$$R^J = \frac{1}{2k}\sin(2\epsilon_J)\exp\left[i(\delta_{J-1,J} + \delta_{J+1,J} + \eta^J)\right] \tag{2.62}$$

The first equation above is the singlet amplitude, the second is the uncoupled- triplet amplitude, and the last three are the coupled-triplet amplitudes. The last equation is sometimes also called the "mixing term". The partial wave expansion of the s-channel helicity amplitudes is given by [Go-60]:

$$\phi_1 = \tfrac{1}{k}\textstyle\sum_J\{(2J+1)R_J + JR_{J-1,J} + (J+1)R_{J+1,J} + 2[J(J+1)]^{1/2}R^J\}P_J \tag{2.63}$$

$$\phi_2 = \tfrac{1}{k}\textstyle\sum_J\{-(2J+1)R_J + JR_{J-1,J} + (J+1)R_{J+1,J} + 2[J(J+1)]^{1/2}R^J\}P_J \tag{2.64}$$

$$\phi_3 = \tfrac{1}{k}\textstyle\sum_J\{(J+1)R_{J-1,J} + JR_{J+1,J} - 2[J(J+1)]^{1/2}R^J + (2J+1)R_{J,J}\}d^J_{11} \tag{2.65}$$

$$\phi_4 = \tfrac{1}{k}\textstyle\sum_J\{(J+1)R_{J-1,J} + JR_{J+1,J} - 2[J(J+1)]^{1/2}R^J - (2J+1)R_{J,J}\}d^J_{-11} \tag{2.66}$$

$$\phi_5 = \tfrac{1}{k}\textstyle\sum_J\{[J(J+1)]^{1/2}(R_{J-1,J} - R_{J+1,J}) + R^J\}d^J_{10}\ . \tag{2.67}$$

Here k is the c.m. momentum, P_J is the usual Legendre polynomial, and

$$d^J_{11} = \frac{1}{1+z}\left[P_J + \left(\frac{J+1}{2J+1}\right)P_{J-1} + \left(\frac{J}{2J+1}\right)P_{J+1}\right] \quad (2.68)$$

$$d^J_{-11} = \frac{1}{1-z}\left[-P_J + \left(\frac{J+1}{2J+1}\right)P_{J-1} + \left(\frac{J}{2J+1}\right)P_{J+1}\right] \quad (2.69)$$

$$d^J_{10} = \frac{[J(J+1)]^{1/2}}{2J+1}\left[\frac{P_{J+1} - P_{J-1}}{(1-z^2)^{1/2}}\right] \quad (2.70)$$

where $z = \cos\theta$ and θ is the c.m. scattering angle. By using Eqns. 2.63–2.70, it is possible to express the observables (Eqns. 2.33–2.38) in terms of a partial wave expansion. As can easily be seen, the expressions for the observables will be rather complicated and will not be given here. For the case of an inelastic scattering observable, the situation is even worse since, in general, there are more than five amplitudes involved.

In the beginning of this section it was mentioned that various theoretical inputs and constraints are generally used in each partial wave analysis to limit the number of partial waves used in the expansion. Meson exchange calculations are generally used to determine the cutoff of the partial wave expansion. Of course, this cutoff varies from one analysis to the other. These are also used to determine the long-range part of the $N-N$ interaction. At energies below the pion production threshold ($T \sim 300 MeV$), the amplitudes must be purely elastic. Continuity constraints are also applied to the phase shift parameters in order to require a smooth energy dependence.

It was pointed out by H. Spinka [Sp-84] that in order to fully determine a partial wave amplitude with total angular momentum J, at least J angles must be measured.

This is because, for a given angular momentum J, the order of the Legendre polynomial in the partial wave expansion (see Eqns. 2.68–2.70) is of order J or $J \pm 1$. This point further complicates the situation from both an experimental and partial wave analysis point of view.

The main purpose of this section was to give the reader a sense of the complexity of the partial wave analysis and the extent to which additional inputs are required in order to actually perform the analysis. For the explicit theoretical inputs and constraints used by the various partial wave analyses, the reader is referred to the works of Arndt et al. [Ar-87], Bystricky et al. [By-87], and Hoshizaki [Ho-68], for example. Each author gives a description of both the theoretical assumptions and the global fitting procedures they use. It was recently pointed out by Sprung and Klarsfeld [Sp-88a] that perhaps one of the largest sources of discrepancy between the various partial wave analyses is due to their being based on different parameterizations of the coupled states.

CHAPTER 3 DIBARYONS

3.1 Introduction

As discussed in Chapter one, one of the motivations for doing the experiment discussed in this dissertation is the possible existence of non-strange dibaryons in the $N-N$ sector. The following sections will describe some of the criteria used to define a resonance, some of the experimental evidence for dibaryons in $N-N$ scattering, and the connection between dibaryons and spin-spin correlation parameters.

3.2 Kinematics of a Resonance

The partial wave amplitudes defined in Eqns. 2.58-2.62 can be displayed in an Argand plot as is shown in Fig. 3.1. Any partial wave of angular momentum J which shows a rapid increase of its phase δ by an increment $\Delta\delta \approx \pi$ (counterclockwise in the Argand plot) on top of a smooth background is considered to show resonance-like behavior. A rapid increase in phase means rapid relative to a typical energy scale; in this case the hadron masses. And of course, the resonance may be elastic or inelastic with the

requirement that the sum of the partial widths be equal to the total resonance width [Lo-85].

The Breit-Wigner form for a resonant elastic partial wave with a resonance at c.m. energy E_R, elastic width Γ_{el}, and total width Γ is

$$R = \frac{\frac{1}{2}\Gamma_{el}}{E_R - E - \frac{i}{2}\Gamma} \tag{3.1}$$

where E is the c.m. energy [PDG-86]. This expression will give a circle in the Argand plot with center $\frac{i}{2}x_{el}$ and radius $\frac{1}{2}x_{el}$ where $x_{el} = \Gamma_{el}/\Gamma$. The amplitude will have a pole at $E = E_R - \frac{i}{2}\Gamma$.

Above the pion production threshold, the formalism must include the inelastic channels which contribute to the background. In order to determine whether resonance poles exist, various theoretical assumptions regarding the form of the inelastic contributions must be made. These, of course, reflect the tastes and philosophies of the individual doing the analysis. Additionally, there are various approaches; some use the S-matrix formalism, some the T-matrix, some the M-matrix, etc.

Using the formalism, for example, of Bhandari [Ba-82] and expressing the elastic S-matrix element as a product of a resonant part S_R and a background S_B, the elastic partial wave amplitude in terms of the T-matrix can be written as

$$T = \frac{1}{2i}(S_B S_R - 1) = S_B T_R + T_B \tag{3.2}$$

where $T_R = \frac{1}{2i}(S_R - 1)$ and $T_B = \frac{1}{2i}(S_B - 1)$. In terms of η and δ, $S = S_B S_R = \eta e^{2i\delta}$.

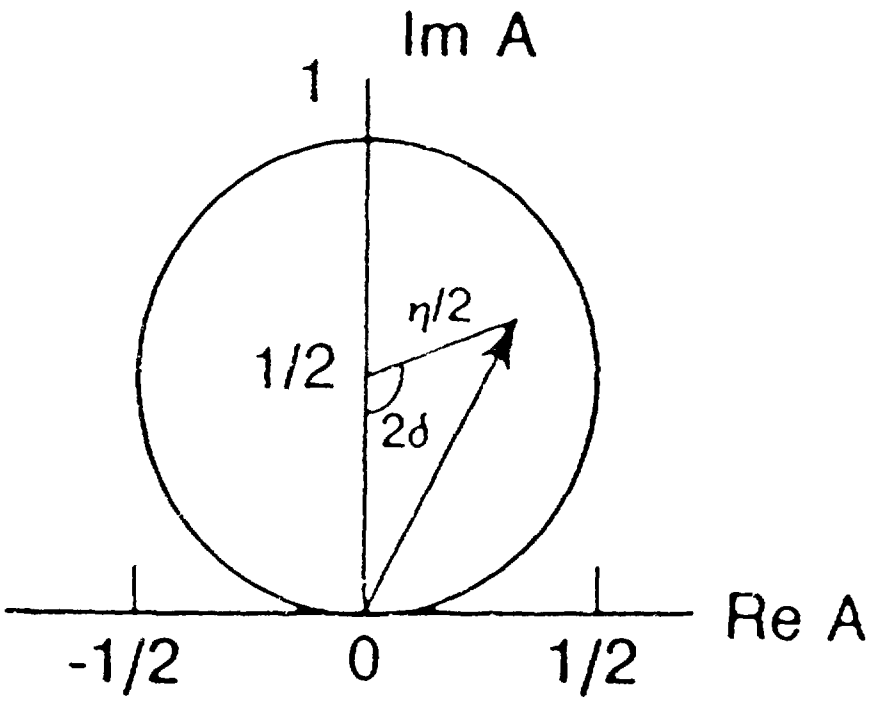

Figure 3.1: Argand plot of partial wave amplitude.

The Breit-Wigner form of the resonant partial wave is given by

$$T_R = \frac{\gamma_e^2 \Phi_e}{E_R - E - i\gamma_e^2 \Phi_e - i\sum_j \gamma_j^2 \Phi_j} \tag{3.3}$$

where the index j sums over all the inelastic channels. The elastic and inelastic phase-space factors, Φ_e and Φ_j, are real functions of the c.m. energy. Here γ_e and γ_j are real coupling parameters. Specific forms of the background S-matrix elements, S_B, and both the elastic and inelastic phase-space factors must be assumed.

The procedure to determine the resonance parameters typically consists of fitting the $N - N$ partial wave phases (δ), for a particular resonance candidate, as a function of energy with the Breit-Wigner form of Eqn. 3.3. More (less) inelastic channels are included (omitted) until the best fit is achieved. The mass of the resonance, m_R, corresponds to the real energy at which the real part of the denominator in Eqn. 3.3 vanishes. This energy corresponds to the position of the resonance pole and is generally found by some iterative numerical method. The full width of the resonance is given by

$$\Gamma_R = -2\, Im(E_R - E - i\gamma_e^2 \Phi_e - i\sum_j \gamma_j^2 \Phi_j) \ . \tag{3.4}$$

The ratios of the partial widths to the full width are

$$x_j = \frac{\Gamma_j}{\Gamma_R} = 2\gamma_j^2 \ . \tag{3.5}$$

It is clear that the success to which such procedures as this are able to fit the phases is determined by one's ability to calculate the phase-space factors for the various

inelastic channels. It has been shown by various analyses that in general all dibaryon candidates in the $N - N$ sector must be highly inelastic. It would be advantageous to be able to separate the elastic and inelastic contributions experimentally. This idea will be discussed more in Sec. 3.4.

3.3 Experimental Evidence

The first theoretical discussion of dibaryon resonances was probably given by Oakes in 1963 [Oa-63]. The first experimental hints were in a Λp invariant-mass distribution of Dahl et al. in 1961 [Da-61], and in the $^1D_2$ state in a partial wave analysis of pp elastic scattering by Arndt in 1968 [Ar-68].

In 1977, strong energy dependent structures were observed in polarized pp total cross section measurements at the Argonne Zero Gradient Synchrotron (ZGS) [Yo-85]. These observations rekindled interest in the possible existence of dibaryons; especially since no structure was observed in the spin-averaged cross section (Fig. 3.2). Additionally, at about the same time, Hoshizaki claimed to have found dibaryon resonances in his partial wave analysis of pp scattering [Ho-77,78] and Jaffe gave a detailed discussion of multiquark states [Ja-77]. Also in 1977, Kamae et al. suggested the possible observation of a dibaryon resonance in the reaction $\gamma d \rightarrow p^{\uparrow}n$ [Ka-77]. The observed energy dependence of the proton polarization could not be explained without the introduction of a diproton resonance. However, there does not yet seem to be ageement among

researchers in the field as to whether these resonances actually exist.

Figure 3.3 shows the Argonne ZGS data and additional measurements made later by other groups. Figure 3.3a shows the total cross section difference for beam and target spin orientations parallel and antiparallel, but transverse to the beam momentum, for *pp* scattering. This quantity is expressed as follows:

$$\Delta\sigma_T(pp) = \sigma(\downarrow\uparrow) - \sigma(\uparrow\uparrow) \ . \tag{3.6}$$

Figure 3.3b shows a similar cross section difference for longitudinal beam and target spin orientations. The sudden rise in $\Delta\sigma_T$ near $500MeV$ $(1.15\frac{GeV}{c})$ was found to be caused by the possible resonance-like behavior of the $^1D_2$ partial wave. Similarly, the dip near $800MeV$ $(1.5\frac{GeV}{c})$ in $\Delta\sigma_L$ is due to the $^3F_3$ partial wave. Figure 3.4 shows the counterclockwise looping of these partial waves in the Argand plane as determined by the partial wave analysis of Arndt [Ar-85].

It is clear now that there are distinct structures in the $N-N$ partial wave amplitudes. However, the question is whether these are caused by resonance poles in the complex plane or possibly by some other structure in the scattering amplitudes. The idea has been put forth [Kl-81,83] that the opening of inelastic channels such as $NN \rightarrow N\Delta$ or $NN \rightarrow \Delta\Delta$ create resonance-like loops in the Argand plane when no resonance actually exists.

In the past, several fits to the $^1D_2$ and $^3F_3$ partial wave amplitudes have been done.

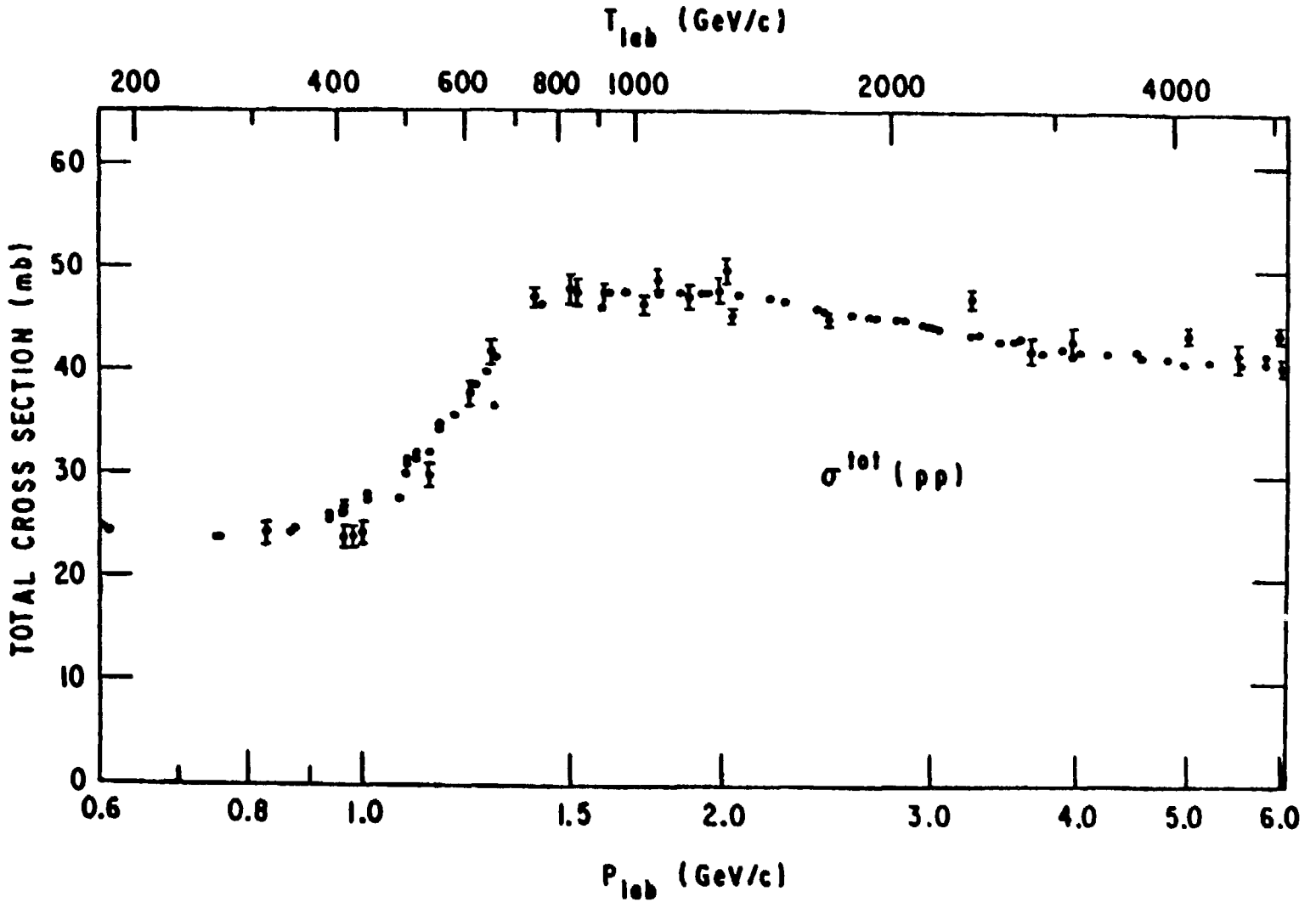

Figure 3.2: The $I = 1$ spin-averaged total cross section [Gi-71].

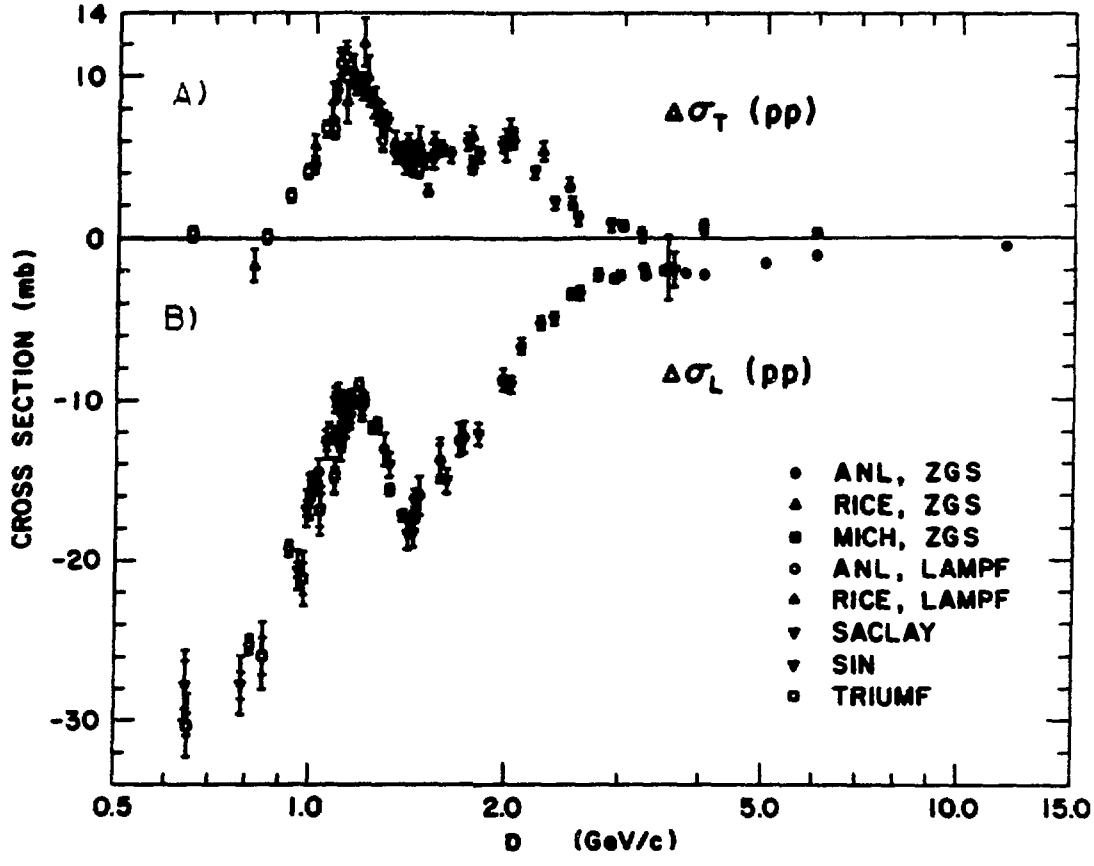

Figure 3.3: a) $\Delta\sigma_T$ for polarized pp scattering. b) $\Delta\sigma_L$ for pp scattering.

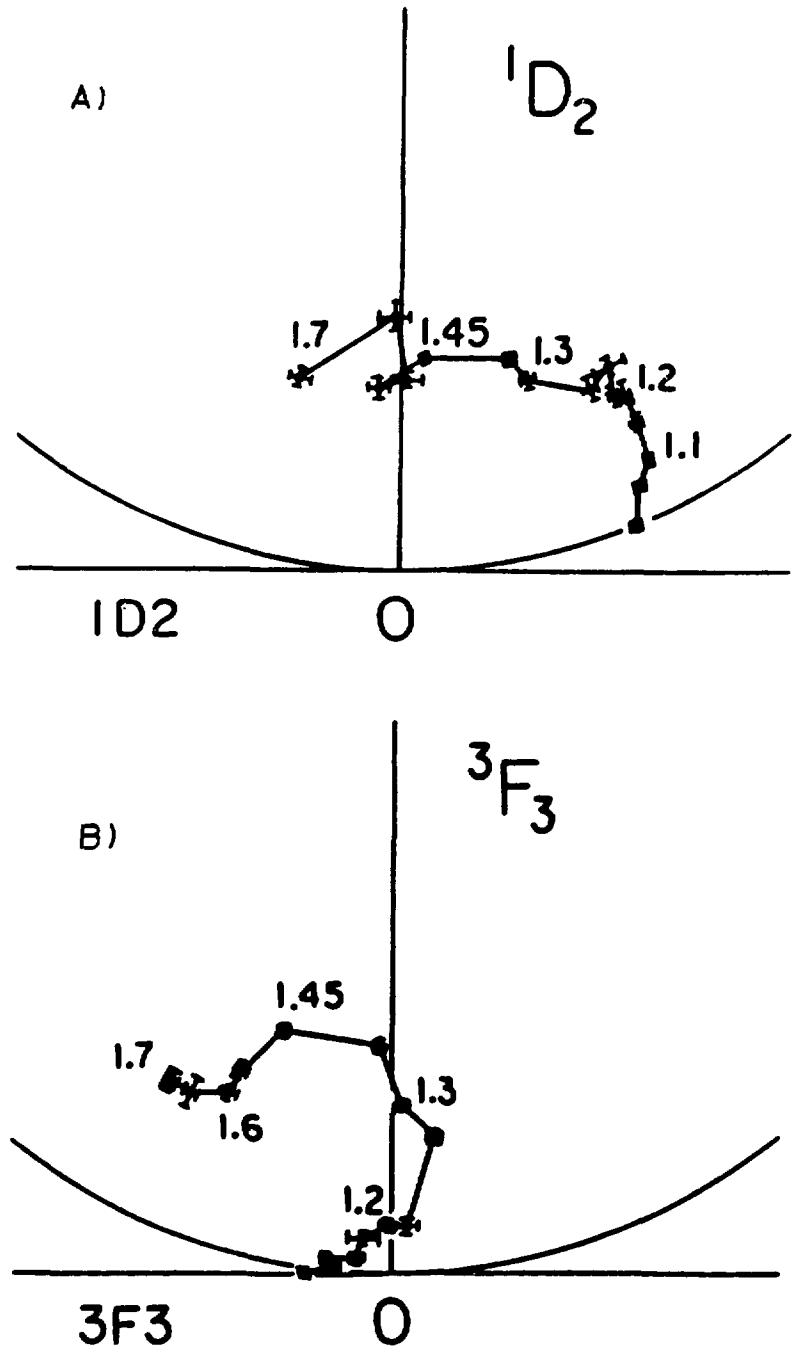

Figure 3.4: a) Resonance-like looping of the $^1D_2$ partial wave in the Argand plot. b) Resonance-like looping of the $^3F_3$ partial wave.

Some of these report the existence of resonance poles [Ue-82, Kl-83] and some do not [Ve-82]. It is, therefore, clear that the existence of dibaryons is still controversial.

3.4 Correlation Parameters and Dibaryons

In the intermediate energy region it is attractive to study the $I = 0$ observables when looking for energy-dependent structure. For the $I = 0$ case, there are no threshold effects to cloud the interpretation of the results in the $200 - 800 MeV$ energy region. The inelastic channels, $NN \rightarrow N\Delta$ and $NN \rightarrow \pi d$, with their thresholds near 600 and $300 MeV$ in the laboratory, respectively, can only occur through $I = 1$ states because of isospin conservation. The $NN \rightarrow \Delta\Delta$ threshold lies above $1 GeV$ and therefore also can not contribute. If structure were to be seen in $\Delta\sigma_L(I = 0)$ or $\Delta\sigma_T(I = 0)$, for example, the controversy over the extent to which the inelastic channels contribute may be settled. The spin-averaged $I = 0$ total cross section (Fig. 3.5) also shows little energy dependence as does the $I = 1$ case, discussed earlier. It would therefore be no surprise if some structure were seen in $\Delta\sigma_L(I = 0)$ or $\Delta\sigma_T(I = 0)$, as was the case for $I = 1$.

It is possible to express the elastic portion of $\Delta\sigma_T$ and $\Delta\sigma_L$ in terms of the spin-spin correlation parameters by

$$\Delta\sigma_T(elastic) = -\int (C_{NN} + C_{SS}) \frac{d\sigma}{d\Omega} d\Omega \qquad (3.7)$$

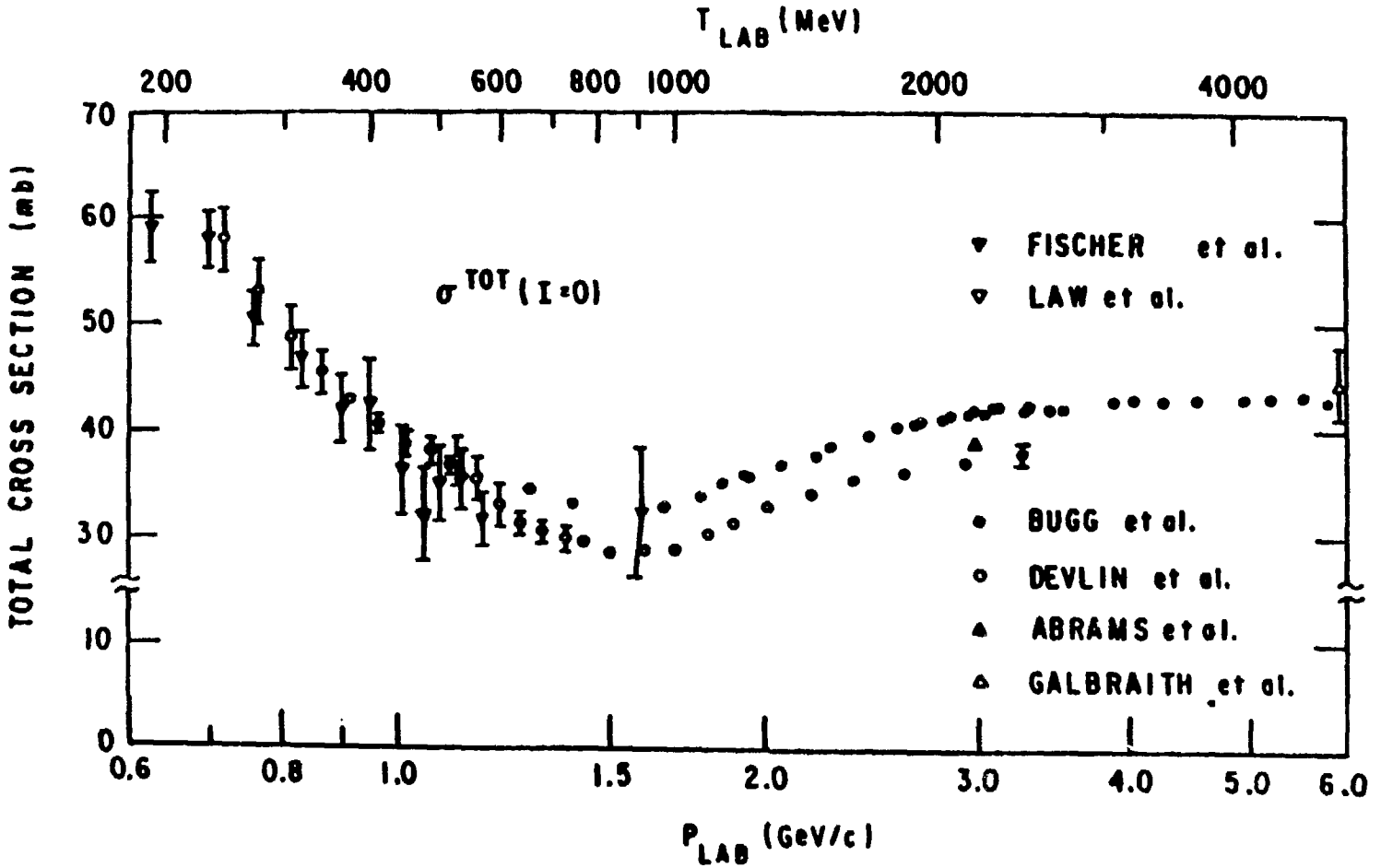

Figure 3.5: The spin-averaged $I = 0$ total cross section [Li-82].

$$\Delta\sigma_L(elastic) \;=\; -2\int C_{LL}\frac{d\sigma}{d\Omega}d\Omega \;. \tag{3.8}$$

These expressions apply to any isospin configuration. By using Eqns. 3.7-3.8 it is possible to separate the elastic and inelastic contributions to $\Delta\sigma_L$ or $\Delta\sigma_T$. These expressions are both important and useful because the $I = 0$ inelastic cross section is poorly known [By-87].

If data over the entire angular range ($0^o \leq \theta_{cm} \leq 180^o$) existed for C_{NN}, C_{SS}, and C_{LL}, the above integrals could be evaluated numerically. One possible procedure to do so might be as follows:

1. Determine the functional form of $C_{LL}\frac{d\sigma}{d\Omega}$ in terms of Legendre polynomials.
2. Subtract off One-Pion-Exchange contributions at high partial waves.
3. Fit the data to the functional form over the angular range of the measurements.
4. Numerically integrate the fitted form.

At present, the smallest angle at which data exist is $\theta_{cm} \sim 75^o$. This would cause a substantial amount of the total elastic cross section to be missing from the integral; since σ^{tot}_{elas} peaks at $\theta_{cm} = 0^o$. This problem could be eliminated by additional measurements of the spin-spin correlation parameters at smaller c.m. angles.

If fits were made to the presently existing data, one particular constraint could be used. If multiple solutions, all with good χ^2, exist, then it may be possible to eliminate some candidates based on their behavior near $\theta_{cm} = 0^o$. Those fits which give

$|C_{LL}\frac{d\sigma}{d\Omega}| > \frac{d\sigma}{d\Omega}$, for example, would be rejected.

Finally, a few comments about what one might expect to see in the data can be made. If $\sigma_{inel} \simeq 0$, then $\Gamma_{el} = \Gamma$, and the resonance form is given by Eqn. 3.1. If the total width is not too large, this would result in a large peak in $\sigma_{tot}(I = 0)$, which is not observed. If $\sigma_{inel} > 0$, then Γ would be broad, and a large peak would not necessarily be seen in $\sigma_{tot}(np)$ or $\sigma_{tot}(I = 0)$. If the inelasticity were large and many resonances occurred close together, compared with the total width, then this would complicate the behavior of the partial waves.

CHAPTER 4 THE EXPERIMENT

4.1 Introduction

The experiment discussed in this dissertation was performed at the Clinton P. Anderson Meson Physics Facility (LAMPF) of Los Alamos National Laboratory. An overview of LAMPF is shown in Fig. 4.1. An enlarged overview of area BR is shown in Fig. 4.2. A polarized proton beam, in the energy range $500 - 800\ MeV$, from the LAMPF accelerator was transported through a liquid deuterium LD_2 target to produce a polarized neutron beam, which was scattered from a polarized proton target. The momentum, time of flight, and scattering angle of the recoil proton were measured with a spectrometer system consisting of the following components: a trigger scintillator (S1), two multiwire proportional chambers (P0,P2), three drift chambers (P1,P3,P4), a large aperture magnet (SCM105), and a scintillator hodoscope (S2). Figure 4.3 shows an overview of the experimental set-up.

Table 4.1 shows the various spectrometer angle and target polarization combinations which were used in this experiment. It also shows the spin-spin correlation parameters

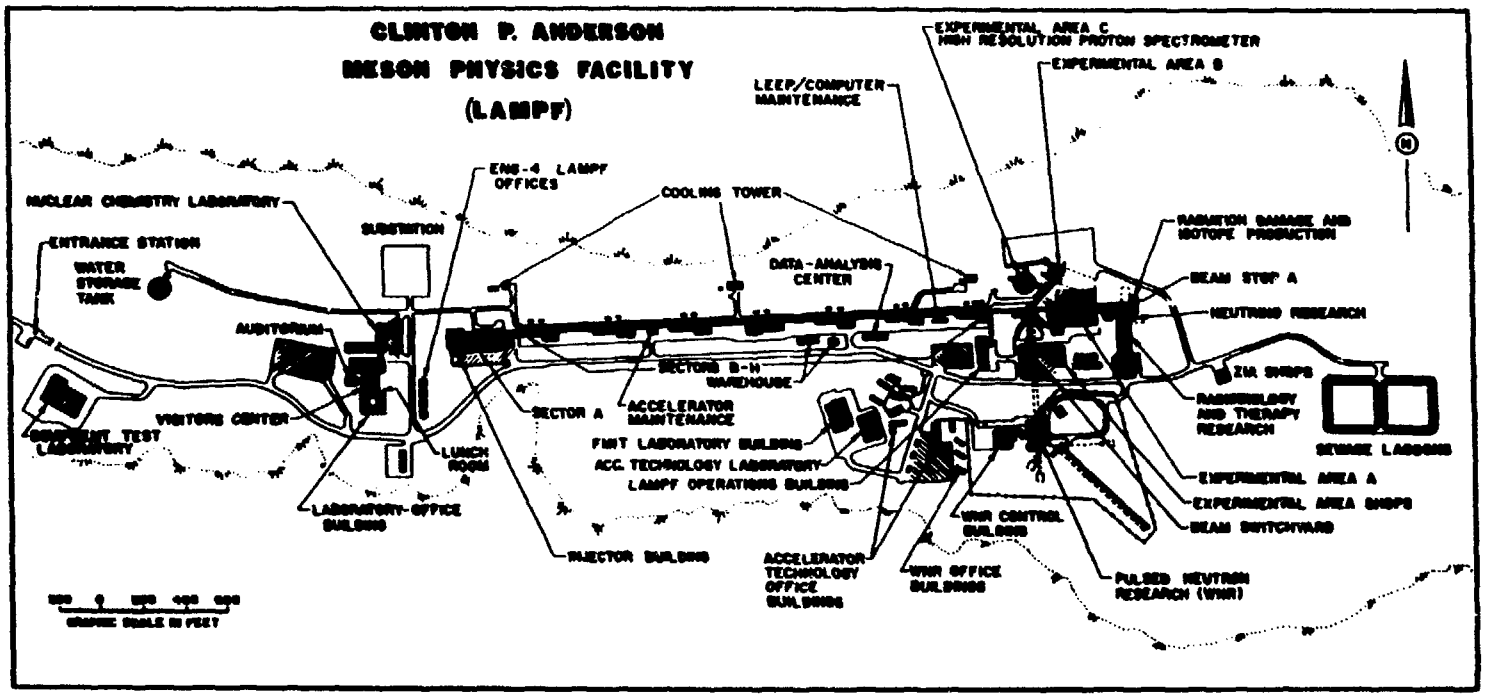

Figure 4.1: Overview of the Los Alamos Meson Physics Facility.

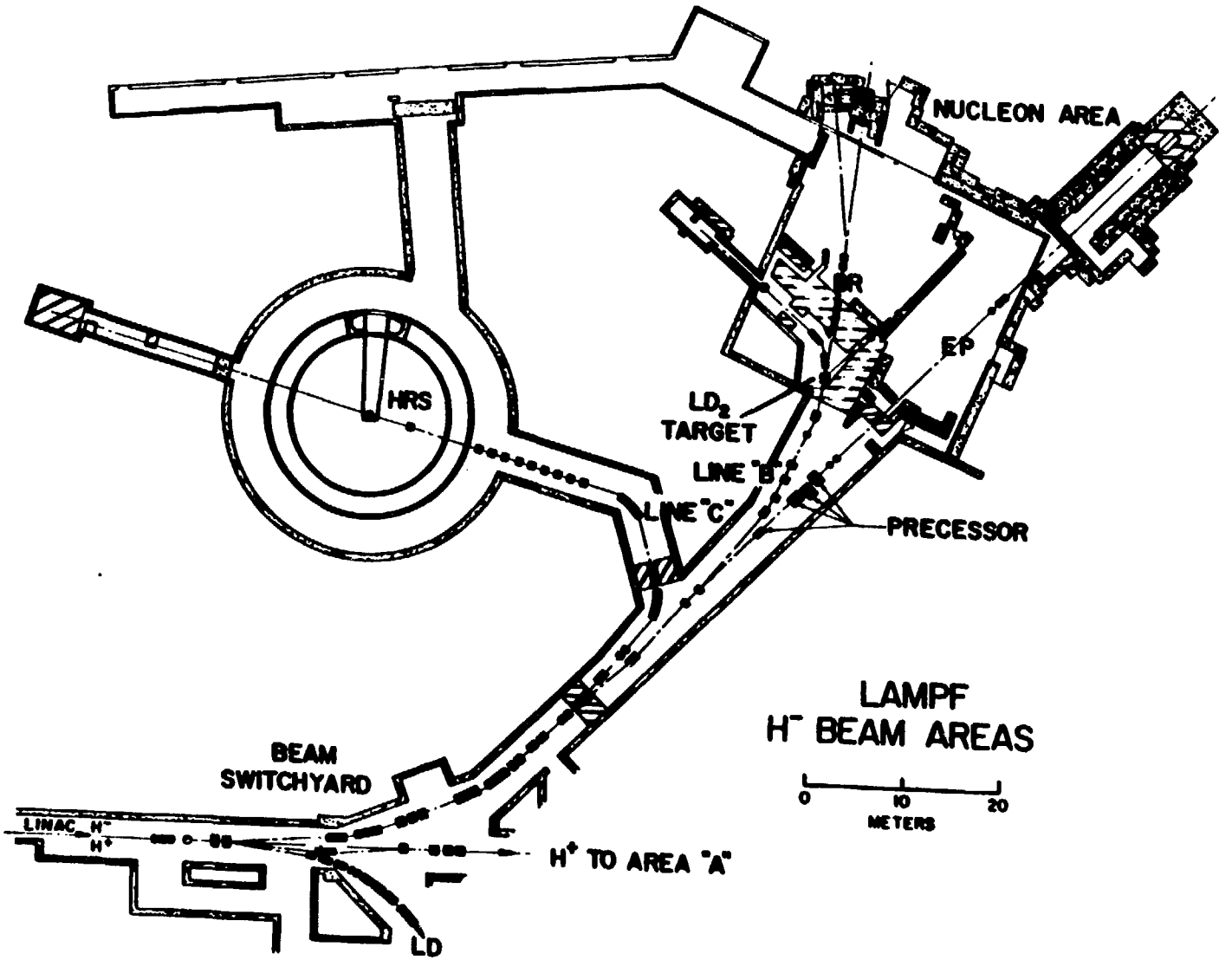

Figure 4.2: Overview of the nucleon-nucleon experimental area — BR.

Table 4.1: The experimental configurations used and the spin-spin correlation parameters measured with each.

Spectrometer Angle	Target Angle	Neutron Beam Energy	Parameter Measured
10°	37.5°	$484 MeV$	$C_{\sigma\sigma}$
		$634 MeV$	$C_{\sigma\sigma}$
		$788 MeV$	$C_{\sigma\sigma}$
35°	37.5°	$484 MeV$	$C_{\sigma\sigma}$
		$634 MeV$	$C_{\sigma\sigma}$
		$788 MeV$	$C_{\sigma\sigma}$
35°	0.0°	$634 MeV$	C_{LL}
35°	0.0°	$634 MeV$	C_{SL}

which were measured. The case $C_{\sigma\sigma}$ is essentially a linear combination of pure C_{SS} and C_{SL}.

4.2 The Polarized Beam

A polarized proton beam at LAMPF is produced by a $50 nA$ Lamb-shift ion source [Oh-70], shown schematically in Fig. 4.4. This source is located in the high-voltage dome of a $750 keV$ Cockroft-Walton accelerator which is used as the injector stage of the LAMPF linac.

In the source, a $500 eV$ proton beam is converted to a partially metastable $H(2S_{1/2})+H(1S_{1/2})$ atomic beam by means of electron capture while passing through a cesium-vapor cell. The remaining charged particles are swept out of the beam, and the atomic beam then enters the spin filter. The spin filter consists of a longitudinal $1608 MHz$

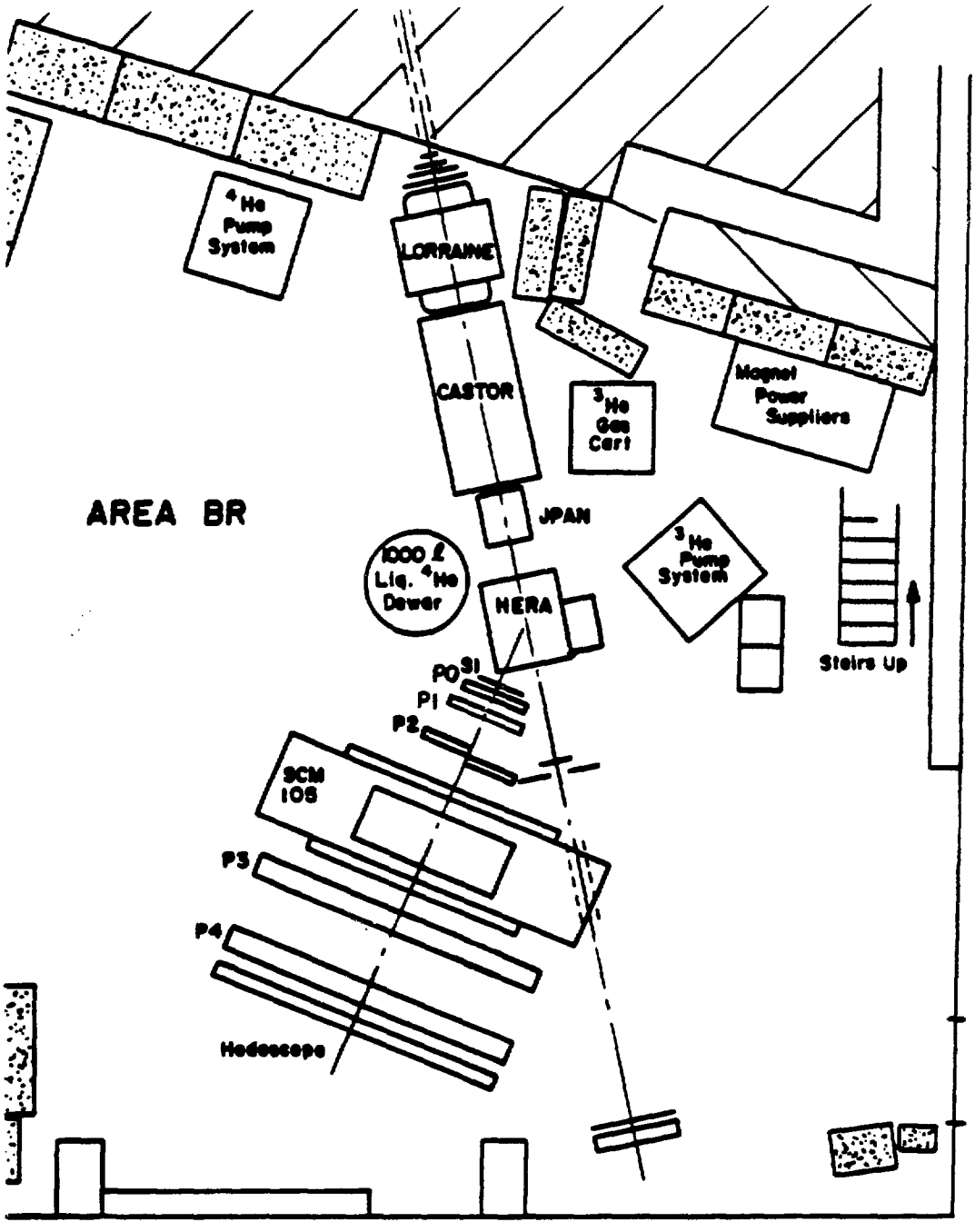

Figure 4.3: Overview of the experimental setup.

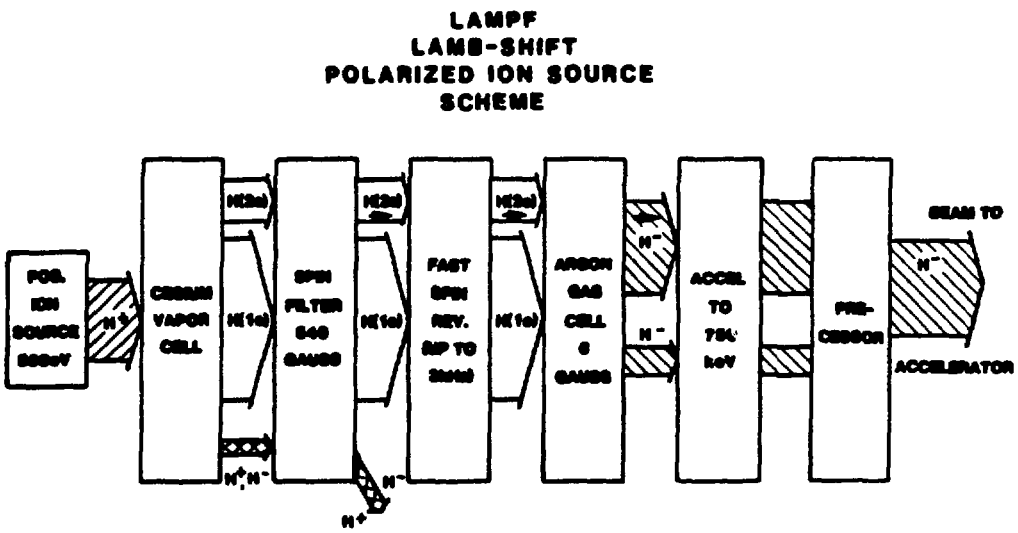

Figure 4.4: Schematic veiw of the Lamb-shift ion source.

r.f. field, a 535 gauss solenoidal magnetic field, and a transverse d.c. field [Oh-69]. The presence of the electromagnetic fields "quenches" all the metastable $2S_{1/2}$ atoms, except those in one particular longitudinal spin state, to the $1S_{1/2}$ ground state. This process makes use of the three-level interaction discovered by Lamb and Retherford [La-51]. The beam then passes into an argon cell where most of the metastable atoms are ionized. Only very few of the ground-state atoms are ionized (becomes H^-), but those that are ionized limit the attainable beam polarization to approximately 90 percent. The spin is then precessed 180 degrees by changing the solenoid field in the spin filter and argon cell. The ionized beam (H^-) is sent through another spin precessor to orient the proton spin before injection into the accelerator.

The polarized ion beam (P^-) is then accelerated to 750 keV in the injector (Cockcroft-Walton) stage of the accelerator. Next, the beam is bunched and injected into the Alvarez-type drift-tube stage. This stage is approximately 61 meters in length and accelerates the beam to 100 MeV. The final acceleration is accomplished by a 0.8 km long, 805 MHz side-coupled cavity accelerator section. The beam is accelerated to a maximum kinetic energy of 800 MeV in this final stage. Specifications for the accelerator can be found in Table 4.2 [Ro-85]. The P^- beam is sent from the beam switchyard by bending magnets to line B, which leads to area BR, as shown in Fig. 4.2. It is passed through a stripper foil to remove the electrons and then emerges in area BR, just upstream of the liquid deuterium neutron production target (LD_2), as the P^+

beam.

The P^+ beam polarization is measured by two different techniques, the first being the "quench" method. This technique uses a ratio of the quenched (I_q) and the unquenched (I) beam currents to determine the absolute polarization of the beam. At LAMPF, a polarized-quenched cycle operates continuously with a 60 *sec* period, asynchronously with the usual 130 *sec* spin reversal cycle [Dy-82]. The quenched current is measured by detuning the spin filter. The proton beam would be 100% polarized ($P_p = 1$) if it were not for the small fraction of unpolarized ionized ground-state atoms contributing to the total beam current. If this background (quenched) current, I_q, were not polarized, then the beam polarization would be given by the ratio of the polarized beam current ($I - I_q$) to the total beam current (I) [Oh-70] :

$$P = P_p \frac{I - I_q}{I} = P_p(1 - \frac{I_q}{I}). \tag{4.1}$$

However, the quenched beam typically has a small polarization ($P_q \sim -0.03$) in a direction opposite to that of the P^- beam. Therefore, it is necessary to take a weighted average of the two polarizations to obtain the true beam polarization:

$$P = P_p \frac{I - I_q}{I} + P_q \frac{I_q}{I}. \tag{4.2}$$

It should be noted that the beam is quenched for 10 *sec* after every spin-flip. Signals from the spin filter are available to the experimenter. The polarization determined by the "quench" method gives a redundant check of the polarization as determined by the

Table 4.2: LAMPF accelerator operating specifications.

Parameter	
•Energy	Variable up to 800 MeV
•Intensity	1.2 mA operational capability demonstrated; routine operation at 0.8 to 0.9 mA
•Extraction efficiency	>99.8%
•Energy spread at 1/2 max	0.1%
•Duty factor	>9%
•RF power sources	Computer-controlled reliable and stable rf power; >80% beam availability
•Accelerator structures	At 1 mA, 6% duty factor, ~30% of rf power is converted to beam power
•H^+ and H^- beams	Simultaneous dual-beam operation; energy variability; 20 nA average 90% polarized H^-
•Secondary beams	12 experimental ports plus 6 neutron lines at WNR
•Practical applications	WNR; isotope production;[a] pion therapy (successfully initiated, now in abeyance); and muon spin rotation applied to condensed-matter studies.

second method used, the beam line polarimeter.

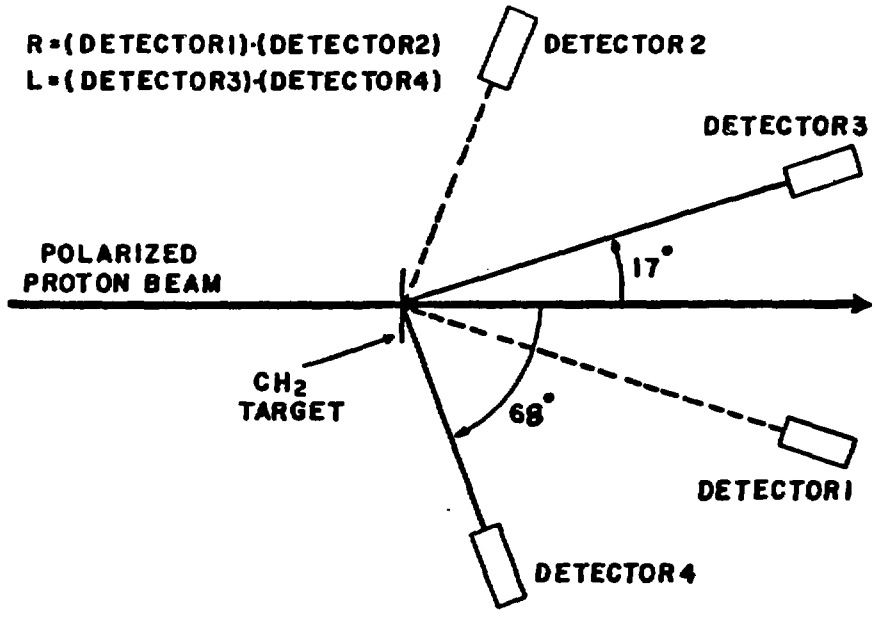

Figure 4.5: Line-B polarimeter just upstream of the LD_2 target.

The Line-B polarimeter (Fig. 4.5) is located just upstream of LB-BM-05, the final bending magnet upstream of the LD_2 target. It consists of a polyethelene (CH_2) target and scintillator counters arranged symmetrically in both the horizontal and vertical planes to measure the transverse polarization by detecting the scattered and recoil protons in elastic scattering. The angular acceptance is broad enough to be usable over the $300 - 800\,MeV$ energy range without angle changes. It should be noted that the acceptance is small enough, however, to reject most inelastic events. The polarization

is determined by the relation

$$P = \frac{\epsilon}{A} \tag{4.3}$$

where A is the hydrogen analyzing power and ϵ is the measured scattering asymmetry. Protons scattered from the CH_2 target to both left and right are detected simultaneously while flipping the beam spin every 130 *sec*. The left-right asymmetry, ϵ is defined as

$$\epsilon = \frac{(L - R)}{(L + R)} \tag{4.4}$$

L is the geometric mean of the events scattered left [Mc-81a] while the beam spin is up, $L\uparrow$, and right while the beam is down, $R\downarrow$; similarly

$$R = [(R\uparrow)(L\downarrow)]^{\frac{1}{2}}. \tag{4.5}$$

Use of this averaging technique is known to cancel instrumental uncertainties to a high order [Oh-73]. The left-right asymmetry is calculated for N-type beam. The up-down asymmetry is calculated for S-type beam polarization, where L is replaced by U (up) and R is replaced by D (down) in Equation 4.4. The analyzing power is well known for *pp* elastic-scattering in the $500 - 800\ MeV$ range [Mc-81b], with an average value of 0.5 ± 0.02 (see Fig. 4.6). The value of the beam polarization as determined by the two methods generally agreed to within $\pm 3\%$, however, the quench polarization was found to be more stable as a function of time.

The spin direction is defined as shown in Fig. 4.7 where L-type (or longitudinal) is along the direction of the beam momentum, N-type (normal) is up in the laboratory

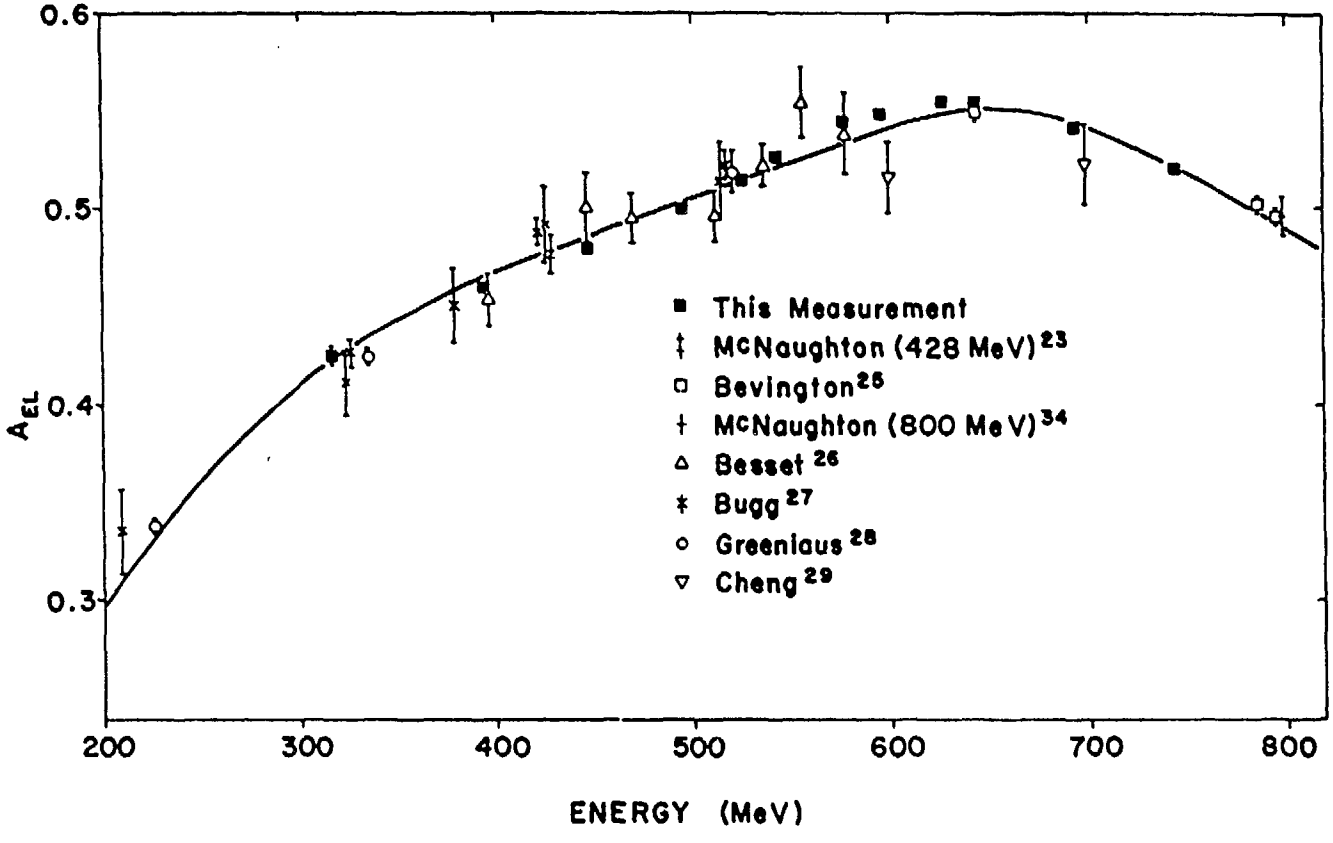

Figure 4.6: Maximum value of the analyzing power for *pp* elastic-scattering as a function of energy at a scattering angle of 17° in the laboratory.

frame, and S-type is sideways ($\hat{L} \times \hat{S} = \hat{N}$). For our measurements we used both N and S-type orientations of the beam spin, as measured upstream of the Line-B solenoid.

The polarized neutron beam is produced by the charge-exchange reaction $\vec{p} + d \rightarrow \vec{n} + X$ with the P^+ beam incident on the LD_2 target. This reaction produces a neutron spectrum at 0° with a sharp peak just below the incident proton momentum (see Fig. 4.8) and a well-separated inelastic background. Approximately 40% of the beam lies in the region of the peak.

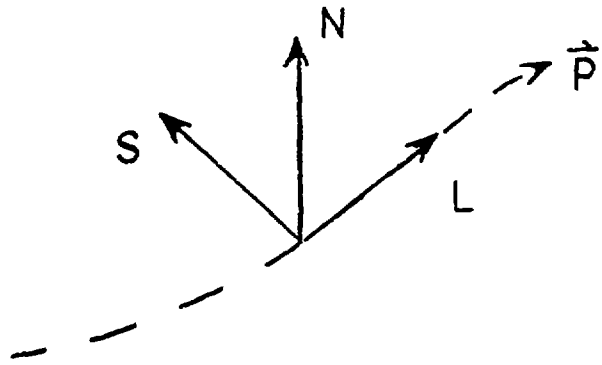

Figure 4.7: Orthogonal coordinate system used to define the proton beam spin direction.

A frontal view schematic of the LD_2 target (looking upstream) is shown in Fig. 4.9. A detailed description of the workings of the LD_2 target can be found in the thesis of

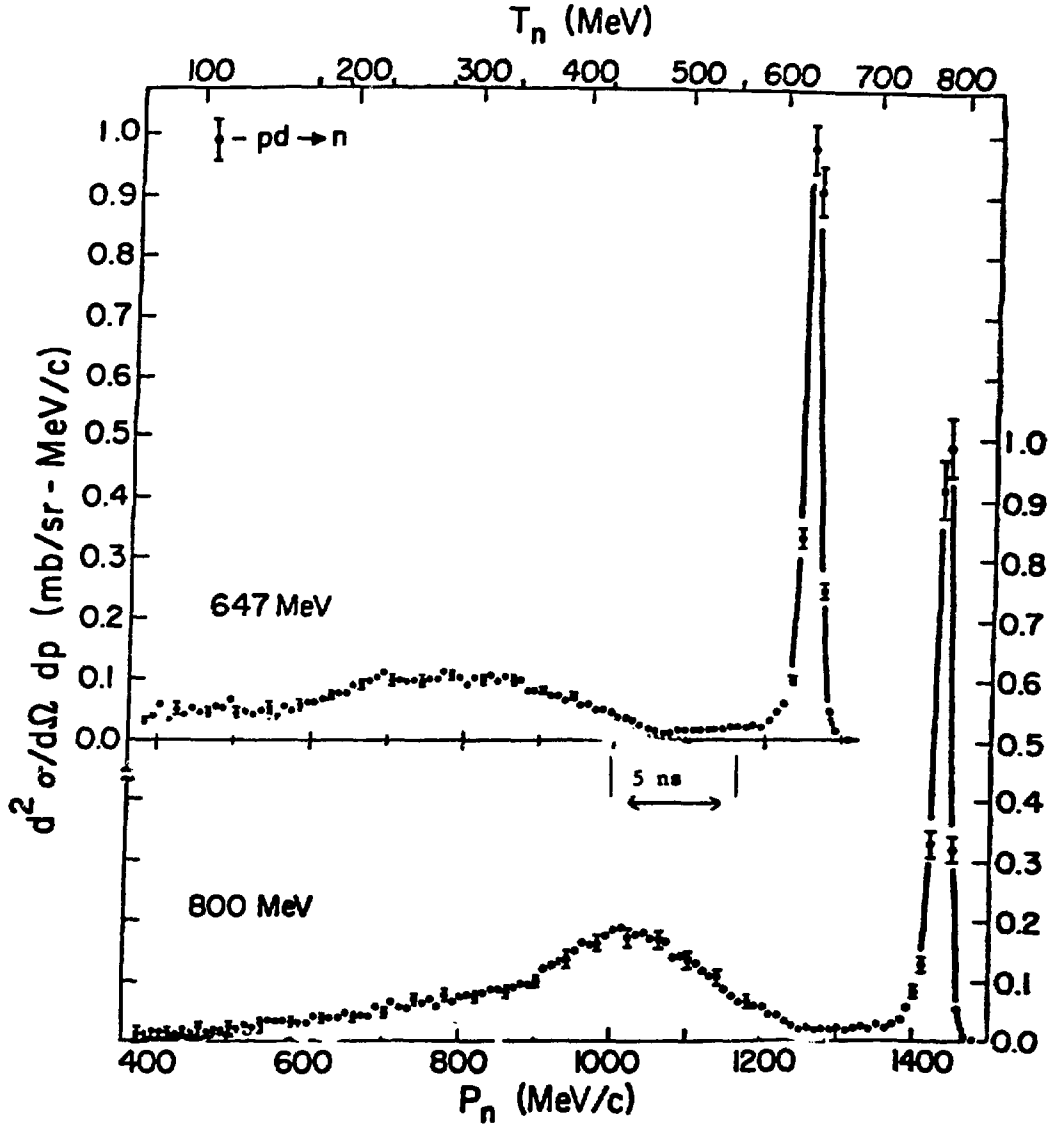

Figure 4.8: Momentum spectrum of the neutrons produced by the polarized proton beam at 0° incident angle.

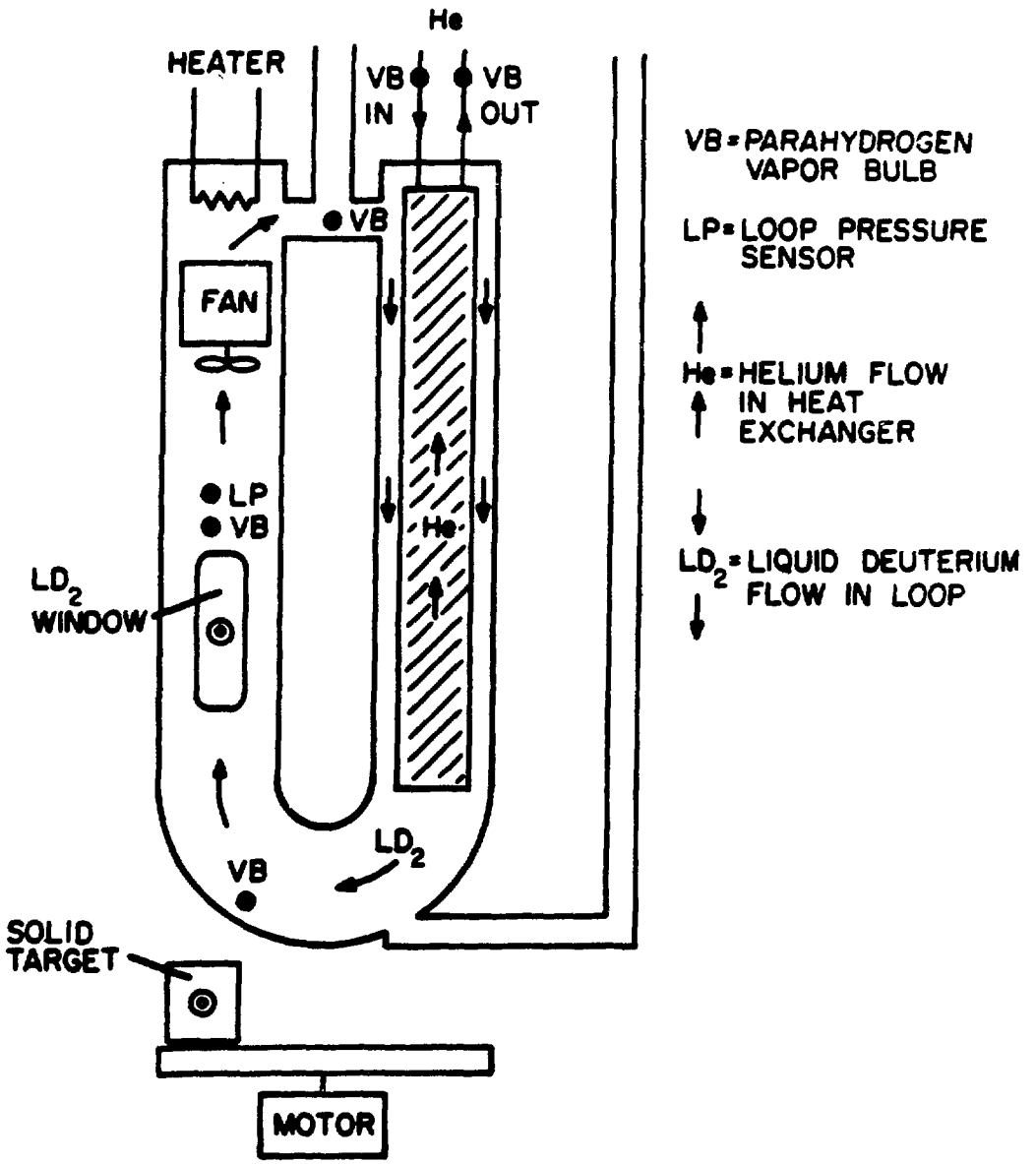

Figure 4.9: Schematic view of the liquid deuterium target.

C. Bjork [Bj-75]. Only a brief description is given here.

The target consists of a heat-exchange, forced convection loop with a helium refrigerator. The entire apparatus sits in a vacuum jacket which is part of the P^+ beam line vacuum system. It can be lowered (raised) by a stepping motor to provide the polarized neutron (proton) beam to area BR.

The loop is pre-cooled by passing liquid helium through it prior to filling with deuterium. Deuterium is brought in at a pressure of about 10 psig until enough has condensed to fill the loop. The fan forces the deuterium past the He heat exchanger (HEX) and circulates it through the loop. As heat is exchanged between the HEX and the liquid deuterium, it is necessary to circulate helium between the HEX and a Cryovac helium refrigerator to maintain cooling of the deuterium. A heater is also part of the loop. The heater is adjusted to compensate for the difference between the refrigerator power and the P^+ beam heating rate and thereby maintain a uniform temperature.

The P^+ beam enters the LD_2 target through a $25\mu m$ thick Havar foil window and exits through a stainless-steel window ($75\mu m$ thick). The window openings are $3.2\,cm$ wide and $15.24\,cm$ long. The entrance and exit windows are separated by approximately $25.4\,cm$. This distance includes the bulging of the windows due to the fact that the target is in a vacuum. This length of liquid deuterium at a density of $0.168\frac{gm}{cm^3}$ results in a $4.26\,MeV$ energy loss for $800\,MeV$ protons. There is also an approximate energy loss of $0.3 - 0.4\,MeV$ through the window material. Additionally, there is a kinematic

energy loss of 7.2 MeV between the beam proton and the outgoing neutron. Combining all these gives an approximate 12 MeV total energy loss for a P^+ beam energy of 800 MeV and an approximate 13 MeV loss for 497 and 647 MeV.

As mentioned earlier, both N- and S- type P^- beam spins were used. This spin is precessed in Line-B by the Line-B superconducting solenoid [Ho-79] and bending magnets such that by the time a proton reaches the LD_2 target, the largest component of its spin is in the $-L$ direction. This is a necessary condition to produce a longitudinally polarized neutron beam of the largest possible polarization. The longitudinal spin transfer, K_{LL}, to the elastically scattered 0 deg neutrons is large and negative in comparison to the transverse spin transfer, K_{NN}. The energy dependence of K_{LL} and K_{NN} can be seen in Fig. 4.10. These spin transfer parameters were measured at LAMPF by Chalmers et al. [Ch-85] at our three measurement energies, 497, 647, and 800 MeV and earlier by Riley et al.[Ri-81] at 800 MeV. The neutron polarization components are simply given by the expressions

$$P'_L = K_{LL} P_L \tag{4.6}$$

$$P'_N = K_{NN} P_N \tag{4.7}$$

where P_L and P_N are the proton polarization components. The magnitude of the polarization is therefore given by

$$P = (P_L^2 K_{LL}^2 \cos^2\theta + P_N^2 K_{NN}^2 \sin^2\theta)^{\frac{1}{2}} \quad . \tag{4.8}$$

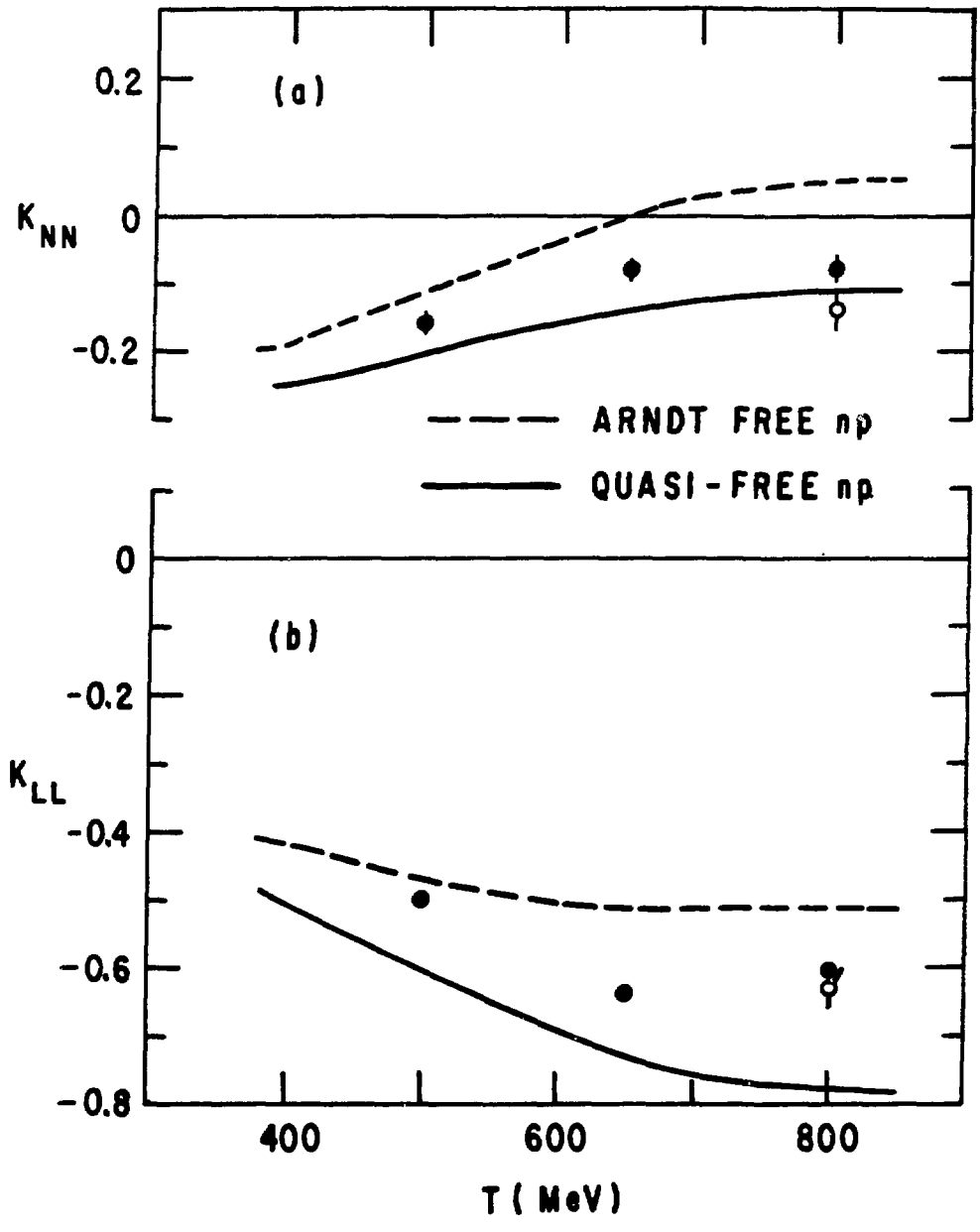

Figure 4.10: Energy dependence of the spin transfer coefficients, K_{LL} and K_{NN}, at 500, 650, and 800MeV.

Since the transverse spin transfer is small, a small transverse polarization in the protons tends to be washed out in the neutrons produced. When calculating the spin-spin correlation parameters, corrections must be made for the N-component of the beam spin. These corrections will be discussed later.

The charged particles produced and the noninteracting P^+ beam are swept out by a dipole magnet, and the neutron beam passes through a 4 meter long, 2.54 cm diameter, stainless steel and lead collimator before emerging in the experimental area. For a 20 nA primary proton beam, the neutron flux is $\sim 10^4 n/sec$ in a 3 cm spot at the polarized target. The beam spot size was roughly measured by placing a polaroid film on the downstream side of the target, in the beam. An image of the target was formed on the film by the secondary charged particles produced in the target.

4.3 The Spin Precession Magnets

Two spin precession magnets, LORRAINE and CASTOR, were used between the collimator and the polarized target to orient the neutron beam spin in a desired direction. LORRAINE was also used to sweep out charged particles produced in the CH_2 target of the front beam monitor, FMON, which is described below. LORRAINE and CASTOR had effective lengths of $\sim$ 110cm and $\sim$ 187cm, respectively. The setting of these magnets for particular polarizations was accomplished through the use of the polarimeter JPAN.

JPAN was very much like the Line-B polarimeter described earlier. Fig. 4.11 shows the detector configuration and logic diagram for JPAN. To determine the ideal magnet current settings for a desired beam polarization, a CH_2 target was installed in JPAN and a magnet sweep was performed for each energy-polarization combination prior to data taking. The sweep consisted of measuring the up-down (ϵ_{ud}) and the left-right (ϵ_{lr}) scattering asymmetries as a function of magnet current. For example, for a desired L-type beam polarization the ideal magnet current setting would be one which would give $\epsilon_{lr} \simeq \epsilon_{ud} \simeq 0$. Figure 4.12 shows ϵ_{ud} vs. magnet current for a typical sweep at $788 MeV$. To arrive at the best value for the magnet current, a least-squares fit to a cosine form of the plotted asymmetry values was performed and the current intercept point where ϵ was a maximum was determined.

For S-type beam polarization, the magnet current was chosen such that ϵ_{ud} was a maximum. Some uncertainty in the position of the maximum existed since often the measured peak was broad or not enough measurements were taken to accurately define the peak. The effect of this and its corrections for the C_{SL} measurements will be discussed later. A discussion of spin precession is given in Appendix D.

4.4 The Polarized Target

The polarized proton target (PPT) consisted of a complex set of components: a magnet (HERA) surrounding the target, the target cryostat and liquid helium systems

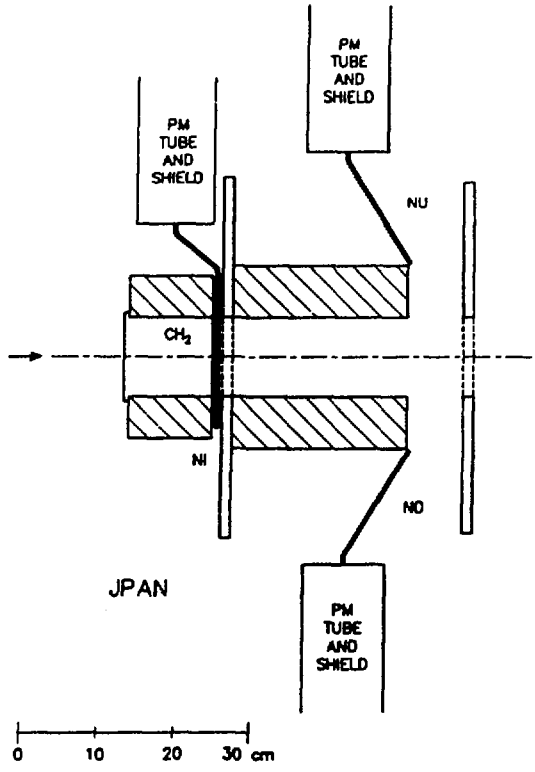

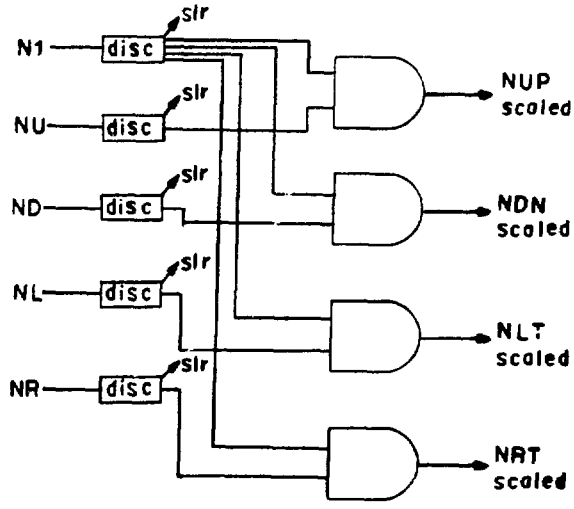

Figure 4.11: Detector configuration and logic for the neutron beam polarimeter — JPAN.

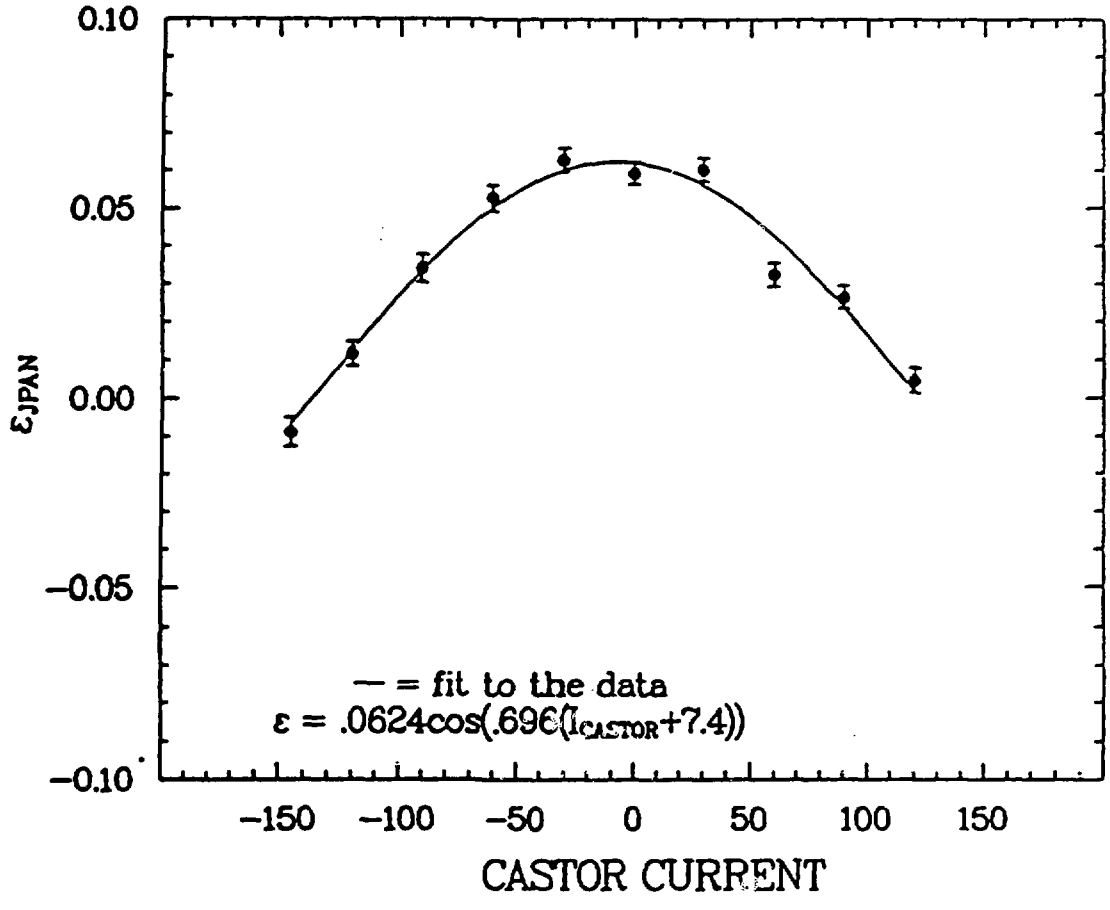

Figure 4.12: Measured asymmetry for a typical CASTOR magnet sweep at $788 MeV$.

to cool the target, microwave electronics to polarize the target, a nuclear magnetic resonance (NMR) system to measure the target polarization, and a target monitoring system to monitor target temperatures, pressures, and coolant flows. All critical target controls and monitors were located outside the experimental area, in a separate trailer, where they were easily accessible at all times.

4.4.1 Dynamic Nuclear Polarization (DNP)

The PPT was a continuously polarizing-type target, utilizing the technique of dynamic nuclear polarization as discussed by Abragam [Ab-78]. This process utilizes the dipole-dipole interaction between the spin of the proton and that of a free radical in the target material. A free radical is an atom or molecule having a large magnetic moment due to an unpaired orbital electron. A general discussion of the DNP process is given below.

Figure 4.13 shows an energy level diagram for the spin-spin interaction of the proton-free radical system in an external magnetic field. The energy splitting between states "a" and "b" ("c" and "d") is due to the proton spin orientation. Likewise, the splitting between states "a" and "c" ("b" and "d") is due to the spin orientation of the unpaired electron. This energy splitting due to electron spin is approximately 1000 times larger than that due to the proton spin. Transitions I, II, III, and IV are allowed transitions. Transitions V and VI are forbidden; that is, they occur with very low probability.

These transitions require a "spin flip" of both the proton and the unpaired electron. The relative population, P, of each state is determined by the Boltzmann distribution, $P \propto exp[-(\mu_e+\mu_p)B/kT]$ where μ_e and μ_p are the electron and proton magetic moments respectively, B is the magnetic field magnitude, k is the Boltzmann constant, and T is the temperature of the target material. To get a high degree of polarization one requires a high magnetic field and a low temperature.

When the target material is placed in the external magnetic field, the proton and electron spins align themselves either parallel or antiparallel to the field direction. At this time the populations of states "a" and "b" are approximately equal. For state "a" the proton spin is parallel to the field and for state "b", antiparallel. To obtain a high polarization, either parallel or antiparallel to the field, it is necessary to overpopulate state "a" or state "b". This overpopulation is achieved by stimulating one of the forbidden transitions (V or VI), which is then followed by a rapid decay through transition I or II to state "a" or "b". A microwave source is used to cause the electron spin to flip. Because angular momentum must be conserved, the proton spin also flips, causing the transition to a forbidden state. The microwaves therefore "pump" these transitions. Without this pumping, a net polarization of only about $\frac{1}{2}$% is achieved. To achieve polarizations of 70 – 80% this pumping method must be used. For example, to overpopulate state "a", transition V is stimulated by applying a microwave frequency $(\nu_e - \nu_p)$, where ν_e is the frequency required to flip the electron spin and ν_p is the fre-

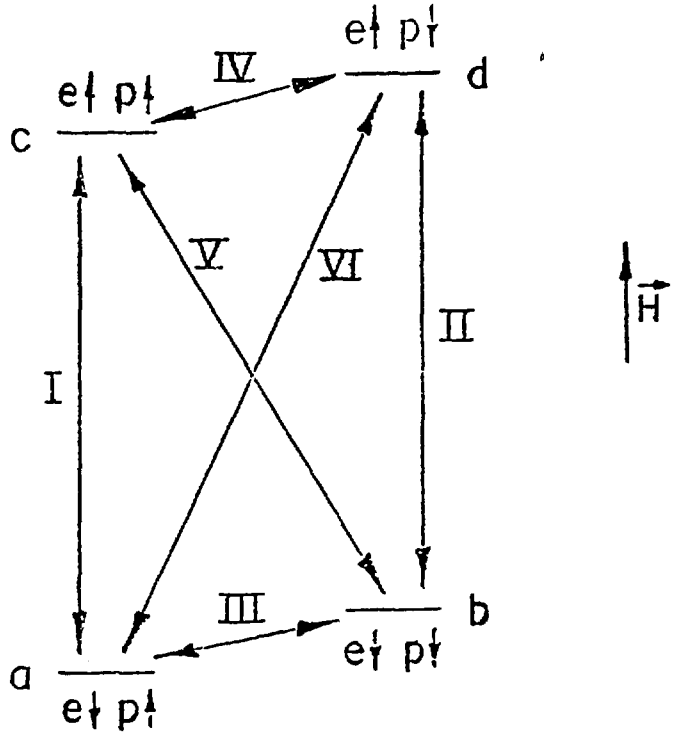

Figure 4.13: Energy level diagram for the spin-spin interaction. The allowed and forbidden transitions are shown.

quency required to flip the proton. To overpopulate state "b", a microwave frequency $(\nu_e + \nu_p)$ is applied to stimulate transition VI, which is followed by the rapid decay by transition II. Therefore, it can be seen that the direction of the proton polarization can be changed merely by changing the microwave frequency by $\pm 2\nu_p$ and that no change in the magnetic field is required. Typical values of ν_e and ν_p are $70\,GHz$ and $53.2\,MHz$, respectively (for $B \approx 2.5T$).

4.4.2 The Polarized Target Magnet (HERA)

The HERA magnet consisted of an iron-free Helmholtz coil configuration. This superconducting magnet and the ^3He refrigerator were constructed at the CEN laboratory at Saclay, France, and had been used in previous experiments there [Au-72]. Modifications made to the magnet at LAMPF are discussed by Auer et al. [Au-83]. It produces a 25 kilogauss (2.5 tesla) field, uniform to within 4.5 gauss in a sphere of $5\,cm$ in diameter [De-67]. In order to allow for the detection of scattered particles, the magnet provides a free, unobstructed cone of 90° opening angle with respect to the polarization direction. For pure C_{LL} measurements, the magnet was positioned with the field (polarization) direction along the beam. For pure C_{SL} measurements the field was also along the beam, causing a rotation of the beam spin. The magnet was also rotated at an angle of 37.5^o with respect to the beam to allow measurement to be made of a linear combination of C_{SS} and C_{SL}. Because of the limited opening angle, it was not possible to rotate the

target to a pure $\hat{S}$-type orientation and measure C_{SS} for laboratory angles smaller than $\theta = 45^{o}$.

The HERA field rotates the scattering plane by causing the outcoming recoil proton trajectory to bend. The total bend angle (radians) is given by the expression:

$$\Theta_{bend} = \frac{c \int B \perp dl}{p} \tag{4.9}$$

where c is the velocity of light (m/sec), p the particle momentum (MeV/c), and $\int B \perp dl$ the component of the field perpendicular to the momentum integrated along the trajectory ($kG-m$). For a trajectory entering the magnet between the coils and passing to the magnet center, the $\int B \perp dl = 4.935kG - m$. This value was determined by mapping the field of the magnet and summing the $B \perp \Delta l$ values along this path. An $800\,MeV$ proton would be bent approximately 6° in exiting the target. In addition, as is expected, the HERA field precesses the spin of the incoming neutron when the field is not along the neutron's incident spin direction. Corrections for both these effects will be discussed later in the chapter on data analysis and reduction.

4.4.3 Target Cryostat and Liquid Helium System

The target cryostat consists of two components, the ^{4}He cryostat and the target insert. A cutaway view of the target cryostat is shown in Fig. 4.14. The ^{4}He cryostat vacuum jacket is evacuated to a pressure of less than 10^{-6} torr to provide thermal insulation of the cryogenics. It also provides the cooling power to liquify the ^{3}He in

the target insert. The target insert consists of the ^3He cooling system, which cools the target to $\sim 0.5°K$, and the target cell.

The ^4He heat exchangers are located between the stainless steel inner and outer walls of the cryostat. The inner volume of the cryostat is further subdivided by an aluminum wall. The volume between this wall and the inner most cryostat wall is maintained at approximately $10°K$ by the ^4He system.

The target cell consists of a copper cylinder containing an inner Teflon cell which holds the target material. The NMR coils support this cell inside the copper cavity. The microwaves which are used to polarize the target are fed into the copper cavity by a waveguide. A delivery tube allows liquid ^3He to flow freely through the target cell.

The ^4He system provides a bath of liquid ^4He at a temperature of about $2°K$ to liquify the ^3He. This is accomplished by pumping on the system. The latent heat of ^4He is about 5 joules/mole, and it takes an additional 400 joules/mole to warm the cold gas to room temperature. As a result, there is a large amount of additional cooling power needed to cool the ^3He gas prior to liquification and to cool the heat shield. Consumption of liquid ^4He is generally less than 2 liters/hr.

The gaseous ^3He is liquified and provides a bath to cool the target material to a temperature below $0.5°K$. The ^3He is costly, so it is flowed in a closed gas loop. In the loop, it is liquified by thermal contact with the ^4He, pumped out at low pressure, cleaned and then recycled. The ^3He pump system consists of several stages of Roots-

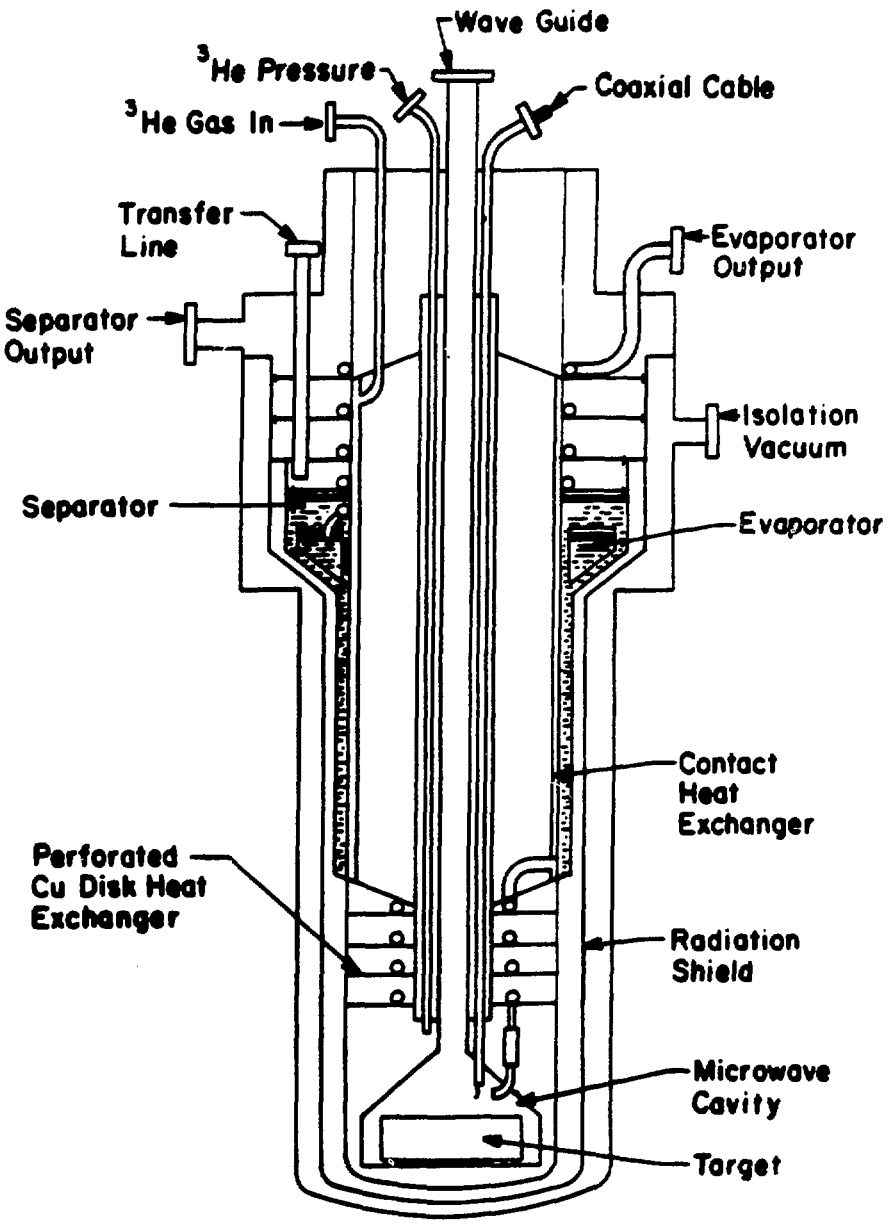

Figure 4.14: Cutaway view of the target cryostat.

type blowers (turbo pumps) coupled to a double-stage rotary vane backup pump. The ^3He vapor pressure is monitored with a remote-sensing capacitance manometer.

4.4.4 Target Material

The target had a 3.7 cm diameter and a 5.5 cm length. Two types of target materials were used during the experiment. During the C_{LL} and C_{SL} data taking, "magic beads" were used and for the C_{SS} measurements, "super beads". The target material, "magic beads", consisted of 85% ethylamine (C_2NH_7) and 15% borane ammonia (BH_3NH_3) by weight. The atomic composition by weight, was as follows: 45.3% carbon, 5.3% boron, 33.2% nitrogen, and 16.1% hydrogen. The "super beads" had a larger percentage by weight of hydrogen (16.8%) and contained the following percentages of impurity atoms: 23.8% carbon, 4.3% boron, and 54.6% nitrogen. Both target materials were doped with a chromate radical for polarization transfer. The materials were prepared in $\sim$ 1mm diameter beads in order to improve thermal contact with the ^3He bath and also to dissipate the heat load of the absorbed microwave radiation.

A study of the effective bound-nucleon polarization arising from the polarized background nuclei (^{12}C,^{14}N,^{9}B,^{10}B) of this target material was studied by Dan Hill and Hal Spinka of Argonne National Laboratory. The details of their study can be found in Appendix A. It was found that this effect contributes to less than 1% of the total target polarization.

4.4.5 The Microwave System

Microwaves with a frequency of 70 GHz are used to transfer the spin of the electrons to the protons in the target material. The target spin is reversed or "flipped" by changing the microwave frequency by 106.4 MHz.

The microwaves are supplied by a $400mW$ carcinotron. The frequency may be changed by adjusting the carcinotron. It is measured by either one of two adjustable resonant cavities (wavemeters) coupled to a crystal detector. The wavemeters may also be used to lock the oscillator frequency. To do this, one wavemeter is tuned to the optimum frequency for positive polarization and the other for negative polarization. Control is remotely switched from one wavemeter to the other to reverse the polarization.

An attenuator is used to adjust the level of microwave power at the target. It is adjusted to optimize the target polarization. Enough power is required to saturate transitions to the metastable state (section 4.4.1), but excess RF power causes unnecessary heating of the target beads which reduces the electron polarization. The absorbed power may be measured by turning off the microwave source and adjusting the joule heating of a resistor on the target (placed there for this purpose) to achieve the same ^3He vapor pressure without adjusting the pumping conditions.

4.4.6 The NMR System

The NMR system (Fig. 4.15) was used to measure the relative target polarization. The detector used was similar to that of Court [Co-80]. This detector allows for making very high precision measurements of the target polarization, using the Q-meter method to measure the nuclear magnetic resonance of the polarized nuclei. This method involves having all of the polarized material within the inductive part of an LC circuit. The resonance frequency of this circuit is adjusted to be the same as the NMR frequency for the particular value of the external magnetic field being used.

The polarized nuclei have a complex magnetic susceptibility $\chi(\chi = \chi' - i\chi'')$ and therefore modify the inductance L of the circuit such that

$$L' = L(1 + 4\pi\eta\chi) \tag{4.10}$$

where L' is the new inductance of the circuit-target system, and η is the packing fraction of the system.

The polarized nuclei therefore produce a change in the Q-value of the system, and, therefore, a change in the impedence of the tuned circuit at the NMR resonance frequency. Recall that the Q-value is a figure of merit of an energy storing system equal to

$$Q = 2\pi(ave.\ energy\ stored/energy\ dissipated\ per\ half\ cycle) \tag{4.11}$$

which is equal to $\omega L/R$ for an inductor, where R is the equivalent series resistance.

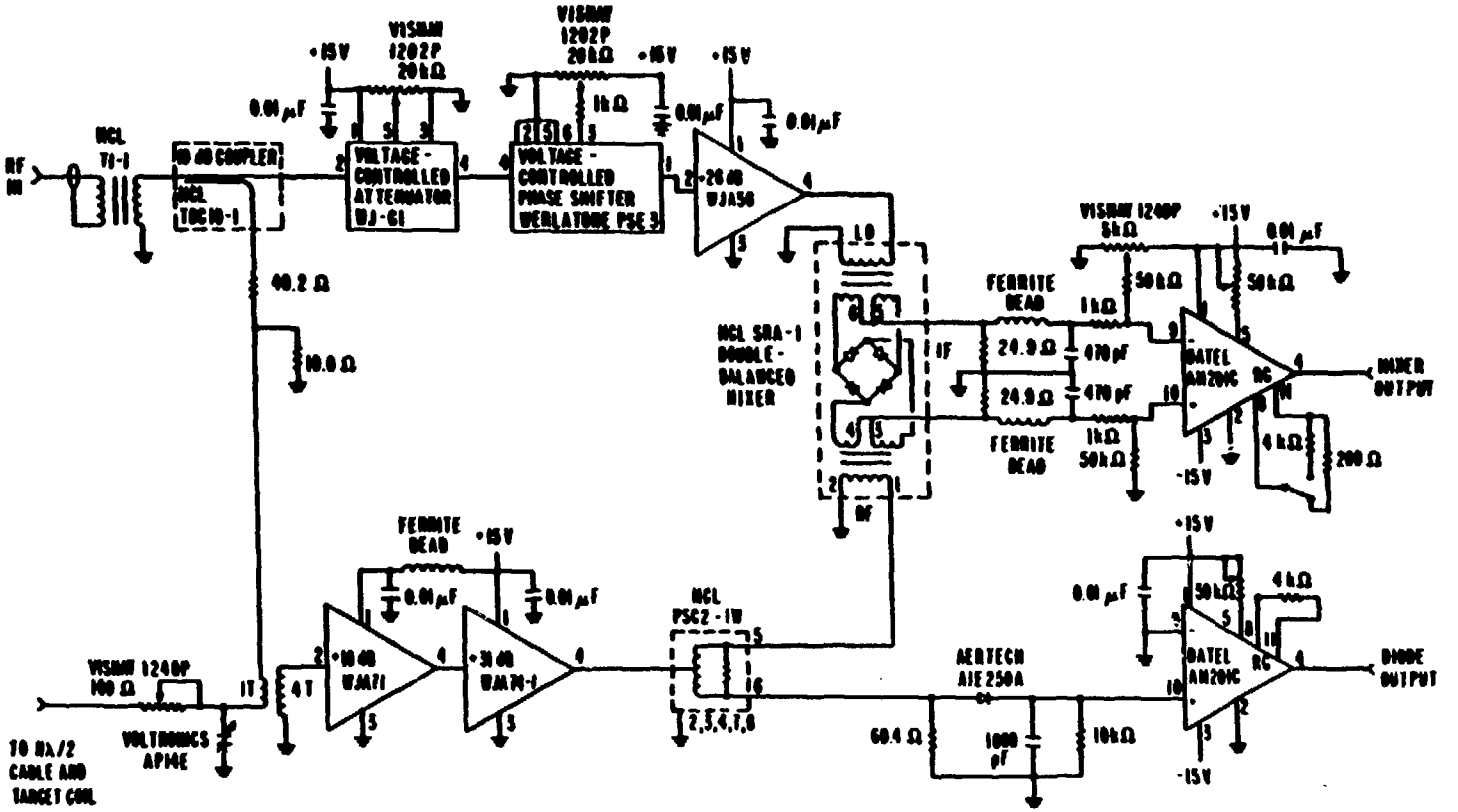

Figure 4.15: Schematic diagram of the polarized target NMR system.

The energy difference between protons in the "normal" and "reverse" polarization states is given by $h\nu = 2\mu_p B$. Transitions between the two are induced by pumping the target material with an RF frequency $\nu = 2\mu_p B/h = 106.4 MHz$. If the populations of the two states are unequal, then the transitions will occur from the most populated state to the other in an attempt to bring the two populations to equilibrium, and hence depolarize the target. As this occurs, energy is either released or absorbed from the RF field, causing the amplitude of the signal to be modulated in proportion to the target polarization.

The value of η in general can not be determined, therefore the system is calibrated by measuring the NMR signal of a target of known polarization. With the microwave source off, the target is allowed to come to thermal equilibrium. The nucleon polarization is then determined from Boltzmann statistics by knowing the magnetic field magnitude and the target temperature. The magnetic field magnitude was known to better than $\pm 0.01\%$ and the target temperature was measured indirectly to within $\pm 0.1\%$ using a capacitance manometer to measure the ^3He gas pressure at the target and converting the pressure to a temperature.

The NMR system consists of the RF oscillator which drives two identical circuits. One circuit drives the NMR coils, and the second acts as a dummy system for background subtraction. Two NMR coils are present in the target holder; however, only one was used to measure the target polarization. A difference is taken between the coil

signal and the dummy, which produces random noise. This difference is then amplified by a differential amplifier and processed with a signal averager. The detected signals are then transferred to an on-line PDP 11/23 computer. The NMR software consists of an integration routine, which integrates over a frequency range of $640kHz$. Additional routines are used to store the target polarization and to monitor the target microwave frequencies. Typical uncertainties in the target polarizations determined by this method are on the order of $2 - 3\%$.

4.5 The Spectrometer

This was a single-arm experiment, in which only the recoil proton was momentum analyzed. Kinematical constraints, which included the recoil angle of the proton, were used to determine the missing mass of the scattered neutron. The measurements were carried out using a large solid angle spectrometer. We were able to measure a 25° angular region in the laboratory in a single spectrometer setting. Our momentum resolution was on the order of 1-2 %.

The various detectors were rigidly mounted on frames attached to the spectrometer magnet (SCM105). This made it possible to move the spectrometer as a single unit. The spectrometer magnet rode on air pads and was moved to three positions, with respect to the beam direction, for data taking, which were 10.0°, 35.0°, and 57.5°. The SCM105 position was surveyed after each time it was moved. It was found each

time that the spectromter was not perfectly aligned with the scattering angle marks on the experimental area floor. Corrections for this were made to the kinematics in the data analysis and Monte-Carlo modelling. The various spectrometer components are discussed in detail below.

Three helium gas bags were used between the chambers to minimize multiple scattering. Small gas bags were used between P1 and P2, and between P3 and P4 and a large bag was inserted into, and through the SCM105 magnet aperture between P2 and P3. All three bags were made of polypropylene plastic with 0.05 *mm* mylar entrance and exit windows supported by external wood frames. The small bags were fed continously by a regulated He gas cylinder, while the large bag used the waste helium boiled off by the polarized target cryostat.

As an aside, for future discussions, let us define the following coordinate system with origin at the SCM105 magnet center: $+z$ is downstream through the spectrometer, $+x$ is left, and $+y$ is up. This defines a right-handed coordinate system.

4.5.1 Scintillators

Two scintillation detectors, S1, and the hodoscope, S2, were used as part of the spectrometer. The signal from S1 was used as a start pulse for the TOF measurements between S1 and S2. A fast coincidence between S1 and S2 was used for charged particle identification and as the fast trigger for the spectrometer.

S1 consisted of two 25.5 cm wide by 28 cm high plastic scintillators placed one next to the other to produce a 51 cm wide by 28 cm high scintillator plane. A photomultiplier (PM) tube was mounted at each end of each scintillator in the vertical plane. The two signals from each scintillator were discriminated and time-averaged.

S2 was a 25-element scintillator hodoscope. Each element had a height of 112 cm, a width of 13.3 cm, and a 1.27 cm thickness. Adjacent elements overlapped by approximately 0.64 cm. The time difference between signals from the top and bottom PM tubes were used to determine a crude y-position in the hodoscope. For the TOF measurement, the top and bottom signals were time-averaged. It was also possible to obtain a crude x-position by knowing which element was hit. The x-resolution was then simply the width of the element.

Additionally, S2 was displaced in the $+x$-direction by 56 cm to compensate for the bend of the particle trajectories by the spectrometer magnet. Corrections of the TOF were made based on which hodoscope element was hit.

4.5.2 Multiwire Proportional Chambers (MWPC)

Three MWPC's were used to obtain position information of a particle before it entered the spectrometer magnet. P0 was located between the trigger scintillator (S1) and the small drift chamber (P1), as can be seen in Fig. 4.3. P2 consisted of two MWPC's (left and right, P2L and P2R, respectively), both located just upstream of the SCM105

magnet. P2L and P2R were displaced by approximately 10 cm in the z-direction, with P2R upstream of P2L. There was a dead spot in the center of P2 due to the overlap of the frames of P2L and P2R. Because P2 was used in the trigger, this "hole" could be seen in the chamber position and momentum histograms. Typical chamber efficiencies for P0 and P2 were 84% and 92%, respectively.

All three chambers were identical, in that each had three sense-wire planes; an x, an x' and a y-plane. Both P2L and P2R were square chambers with 256 wires with 2 mm spacing per plane. P0 was a rectangular chamber having 256 wires in x and 128 wires in y. This gave an active area of $530 \times 530 mm^2$ for P2L and P2R, and $530 \times 265 mm^2$for P0. The sense wires were 20μm diameter gold-plated-tungsten [Ha-86]. Three additional wires of increasing diameter were located parallel to the sense wires, near each edge of the chambers, to prevent electrical breakdown at the G10 frame.

The spacing between a cathode plane and a sense-wire plane was 6.4 mm. Each plane was supported in a separate G10 frame. The individual frames were bolted together with threaded nylon rods and nuts. The entire assembly was sealed with silicon-rubber glue (RTV) to make the gas seal.

The outer gas windows were 50μm mylar covered with opaque mylar tape. The cathode planes were 50μm aluminized mylar. The chambers were operated at local atmospheric pressure, about 20% less than at sea level. The gas mixture used consisted of a 65%–35% $Ar - CO_2$ mix with 0.4–0.5% Freon - 13 Bl ($CBrF_3$) added to reduce

chamber sparking.

The threshold on the electronics for these chambers was equivalent to $1\,mV$ across a 100Ω input resistor [Ni-77]. The number of collected electrons per beam particle was estimated to be $10^6 - 10^7$. The operating voltage was approximately $4200\,V$, this being $100 - 200\,V$ above the knee of the plateau curve.

Preampifiers for each sense wire were mounted on each MWPC. The preamp signals traveled approximately 200 feet to the electronics trailer by way of a twisted-pair cable. The signals were then fed to the amplifier cards.

The amplifiers were mounted on "sister" boards and were sensitive to signals over $5\,mV$. Eight chamber wires were connected to each amplifier card. The amplifier cards contained eight amplifiers each, producing a fast OR output for each wire hit and a latch that was continuously set by the fast-logic "STORE-DATA" pulse [Au-81]. Each sister board contained two blocks of eight amplifier cards (128 wires), with the amplifier bus hardwired between them. A circuit that gave the fast OR of all 64 wires on half a sister board also existed. A set of these was used for the chamber read-out trigger.

When a trigger occurred, the "STORE-DATA" signal (NIM) was sent to all sister boards and an ordered readout of all the cards began. The signals were sent to a RCVR/XMTR, module where they were translated to TTL levels and then sent to the CAMAC readout modules. The readout system is discussed in great detail by Nield and Daly [Ni-77].

4.5.3 Drift Chambers

A small drift chamber with an active area of $60 \times 60cm^2$ was used upstream of the SCM105 magnet. It consisted of three detector planes; x, x', and y. The wires of the x' plane were offset by $\sim 2mm$ with respect to those in the x plane. There were 76 wires per plane, each spaced at $8mm$, with a field-shaping wire halfway between each pair of sense wires. The sense (field-shaping) wires were $20\mu m$ ($25.4\mu m$) gold-plated tungsten.

There was a cathode plane between each sense plane. The cathode planes were $76.2\mu m$ aluminized mylar. The sense wire - to - cathode plane spacing was $4.76mm$. The outer windows were made of $254\mu m$ mylar.

The gas mixture used, in parts per volume, was 7.5 parts Argon, 1.5 parts Isobutane, 1.5 parts Argon/4.5% Freon, and ethanol at $0°C$ vapor pressure. The chamber was operated at local atmospheric pressure.

The readout system was based on the delay-line technique which determines which wire was hit by measuring differences of propagation times [Mo-82]. The preamps used on the delay lines had a gain of $\sim$ 40. The signals went to Philips constant fraction discriminators and LeCroy Research Systems (LRS) 2228A time-to-digital converters (TDC's). The field-shaping was done using home-built differential amplifiers. It was found that typical resolutions for this chamber ranged from $150\mu m$ to $300\mu m$.

Two $3 \times 1m^2$ drift chambers (DC) were used for particle tracking behind the SCM105 magnet. The two chambers were identical in construction; however, P3 was constructed

at New Mexico State University and P4 at Argonne National Laboratory. Typical chamber efficiencies were 97% for P3 and 79% for P4. A much more detailed description of these chambers is given by Haberichter et al. [Ha-88].

The chambers consisted of eleven wire planes mounted inside a gas-tight aluminium box having two removable mylar, entrance and exit, windows. There were four sense-wire planes and five cathode (HV) planes per chamber. There was a cathode plane between each set of sense planes; however, the two outer wire planes were held at ground potential.

The four sense wire planes defined four coordinates — x, x', u, and v. The x and x'-planes were identical, but with x' displaced by half a wire spacing. The $u(v)$ plane was rotated by 17.63° counterclockwise (clockwise) relative to the vertical x wires. The x and x' sense planes had 160 wires with a 19.05 mm spacing. The u and v planes had 176 wires, spaced at 18.16 mm. Figure 4.16 shows a schematic diagram of the chamber assembly. The field-shaping wires and sense wires were gold-plated tungsten, 76μm and 25μm in diameter, respectively. The cathode planes consisted of 76μm diameter stainless-steel wire spaced at 2 mm intervals. For both P3 and P4, groups of 16 wires were brought to connectors at the top of the gas box via a 34-conductor flat cable. The entrance and exit windows were 76μm mylar bonded to 13μm aluminium. Thus, the sealed system acted as a Faraday cage, minimizing external electrical noise pickup.

The readout system for P3 consisted of the LRS 4290 Time Digitizing System op-

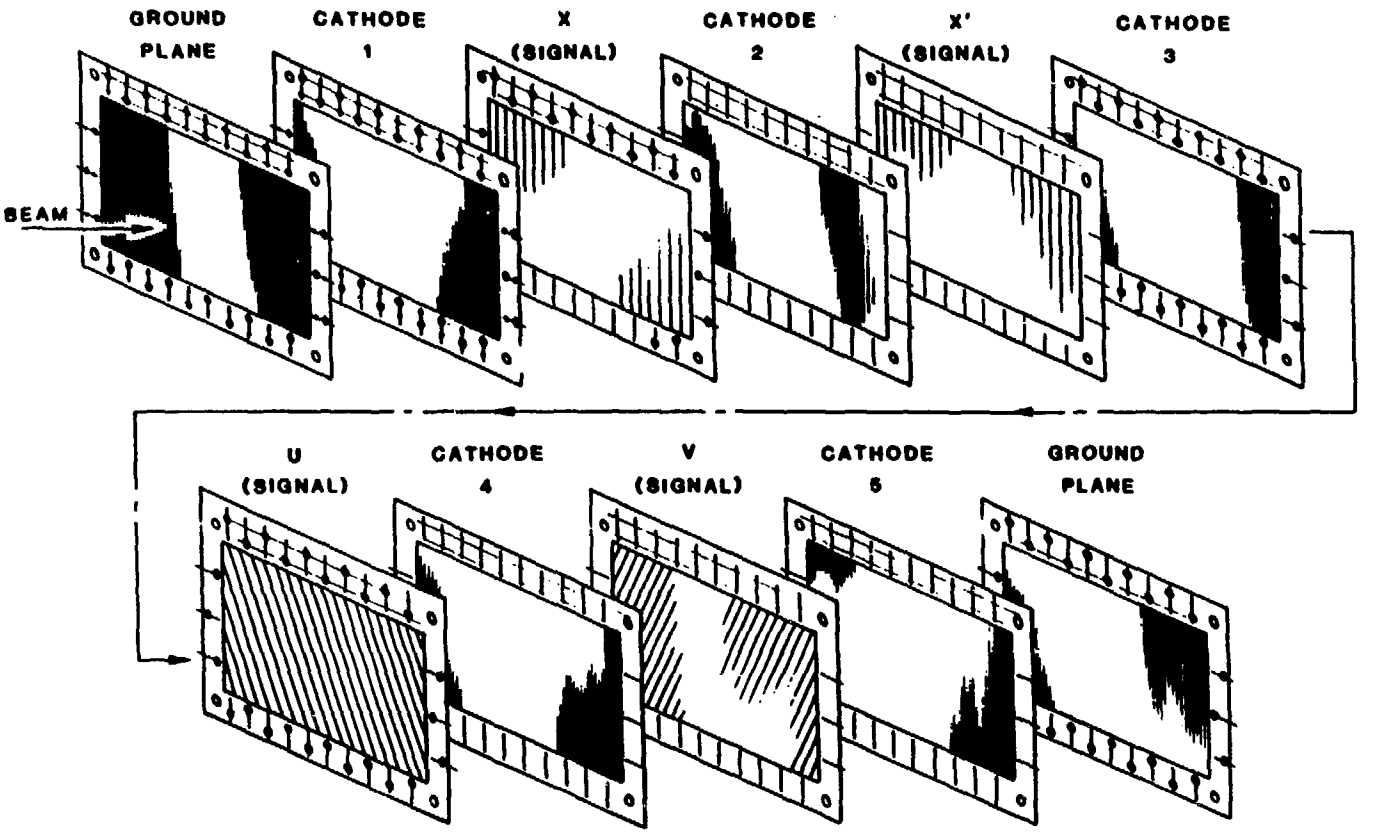

Figure 4.16: Schematic view of the large drift chamber construction and plane assembly.

erating in the Common Stop mode. Amplifier boards with 16 channels of amplification and discrimination (one TDC for each signal wire in a 16 wire group) were used. The Autotrim feature of the 4290 system was used to determine the pedestals for the TDC's.

Figure 4.17 shows a schematic diagram of the 16-channel amplifier. In the Common Stop mode, if a TDC was to get another start signal, after-pulsing could give rise to incorrect drift times. To eliminate this problem, the output of the AM685 discriminator was latched to $\sim 200\,nsec$ width to ensure no accidental TDC starts.

The readout system for P4 was based on the technique of determining which wires were hit by measuring differences of propagation times, as discussed earlier for P1. For P4, each group of 16 wires was connected to a delay-line board. This limited multiplicities to one hit per 16 wires.

Figure 4.18 shows a schematic diagram of the delay board. Chamber signals were passed through a ground base input stage before tapping into the delay line. This feature was found to be necessary, for such a large drift chamber, since the characteristics of a delay line change drastically as capacitance is added at various places. At both the left and right ends of the delay line, the signals were amplified and then sent to LRS 623B, 620AL, or 620CL discriminators via RG58 coaxial cables. Next, each output was fed into an LRS 2228A TDC with a $250psec$ resolution operating in the Common Start mode. Additionally, each left output was fed into a CAMAC coincidence register which was strobed by the trigger. The CAMAC electronics were read into the data acquisition

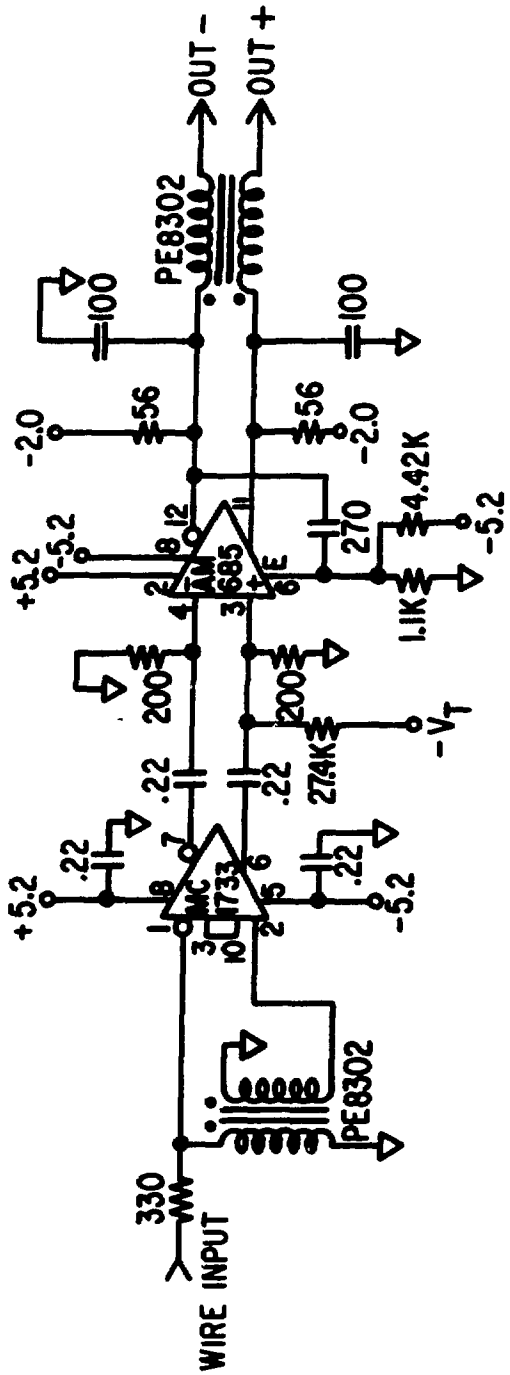

Figure 4.17: Schematic diagram of the 16-channel amplifier used on P3.

computer through a BiRa Systems Microprogrammable Branch Driver (MBD) [Sh-74] which was programmed to read only those left-right TDC pairs which were flagged by the coincidence register. This technique minimized the number of drift chamber data words transferred. A rather detailed study of the resolutions of both P3 and P4 was

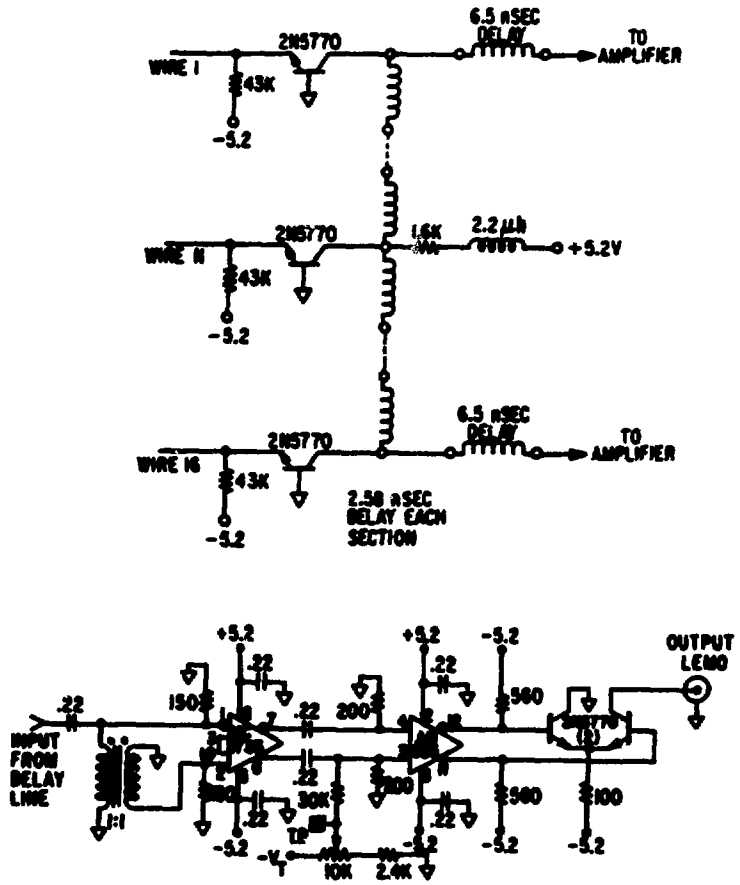

Figure 4.18: Schematic diagram of the delay-line boards used on P4.

conducted. Some of the 634 MeV, 35° C_{LL} data was used for this study. To measure the chamber resolution, a residual, R, was calculated:

$$R = x_{calc} - x = x' + (m \times s) - x \tag{4.12}$$

where x and x' are the measured cordinates at the X and X' planes, s is the distance between the planes, and m is the xz-slope. The slope, m, was calculated by an iterative least-squares fitting procedure which is discussed in more detail in the chapter on data analysis and reduction.

Figure 4.19 shows a typical distributions of R for P3 integrated over the whole chamber. The chamber resolution is obtained by converting the FWHM to a standard deviation, corrected for contributions from both the X and X' planes. This method gave calculated resolutions of $180 \pm 1\mu m$ and $285 \pm 1\mu m$ for P3 and P4, respectively.

4.5.4 The Spectrometer Magnet (SCM105)

A large $214 \times 84cm^2$ aperture magnet was used to momentum analyze the recoil proton. This magnet weighed approximately $110tons$ and was shipped from Argonne National Laboratory to LAMPF. The coil assemblies consisted of two-layer pancake wound coils combined in sets of six to make one upper or lower coil assembly. Each coil had 240 turns having a resistance of $0.0894Ohms$. The magnet was operated at $214volts$ $D.C.$ and a current of $2000Amps$.

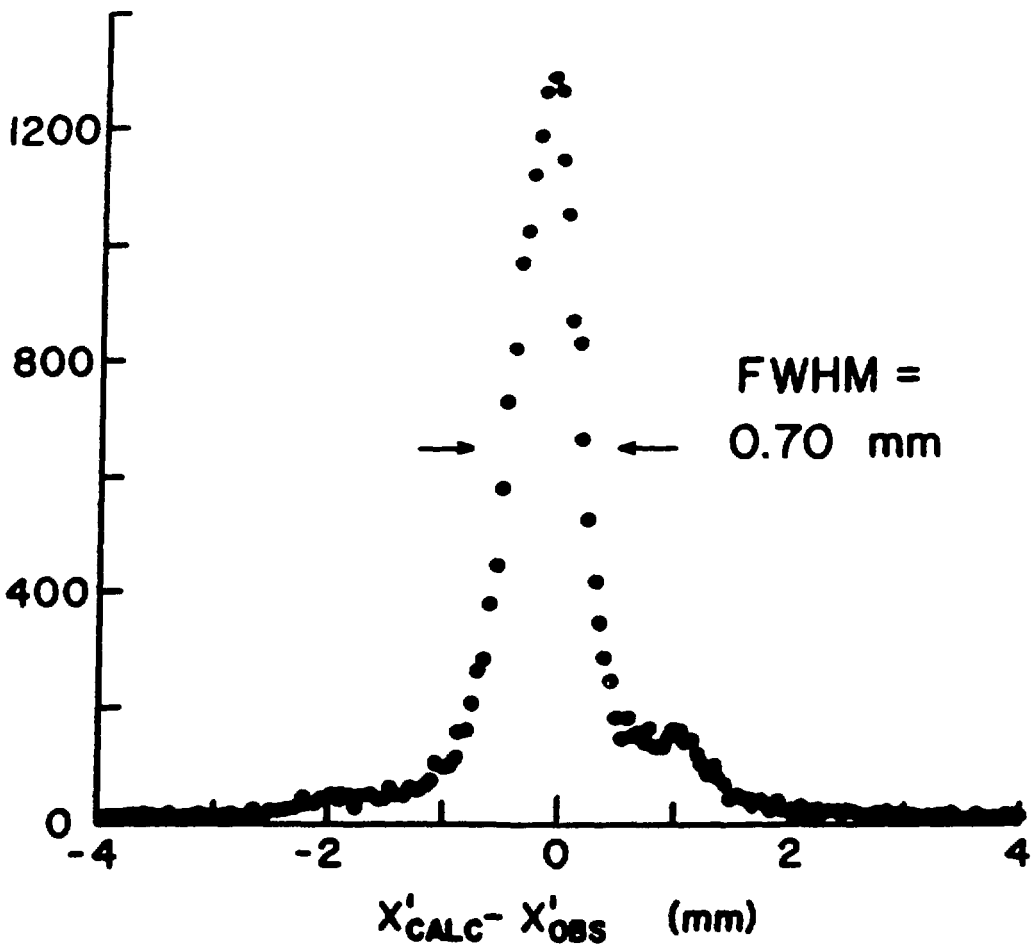

Figure 4.19: Typical residual distributions for both large drift chambers, P3 and P4.

The maximum field strength attainable was $16.0KG$; however, the magnet was operated at lower fields during the experiment. For all energies ($484, 634, 788MeV$) where the spectrometer angle was 10^o or 35^o, the SCM105 was operated at $2000Amps$ which gave a field of $\sim 15KG$.

4.6 Beam Monitoring

Three monitors were used to measure the relative beam intensity at various locations — FMON, TMON, and BMON. Each monitor will be discussed in detail below. The positions of these monitors with respect to the rest of the experimental setup can be seen in Fig. 4.3.

FMON was the front beam intensity monitor. It was located between the exit hole of the neutron beam collimator and the entrance aperture of LORRAINE. Figure 4.20 is a schematic diagram of its detector configuration. It consisted of a charged particle veto scintillator (A), a CH_2 block target which was used to produce charged secondary particles, and various scintillator coincidence planes (M1,M2,M3). The block target degraded the neutron beam intensity by $\sim 10\%$.

Figure 4.21 shows the logic diagram for FMON. A bar above an expression indicates the complement signal. The signals from all the individual detectors were discriminated and sent to scalers. Various combinations of an anticoincidence in A (neutral particle) and the other planes were also scaled. For instance, a quantity $MTOT = MLT + MRT$,

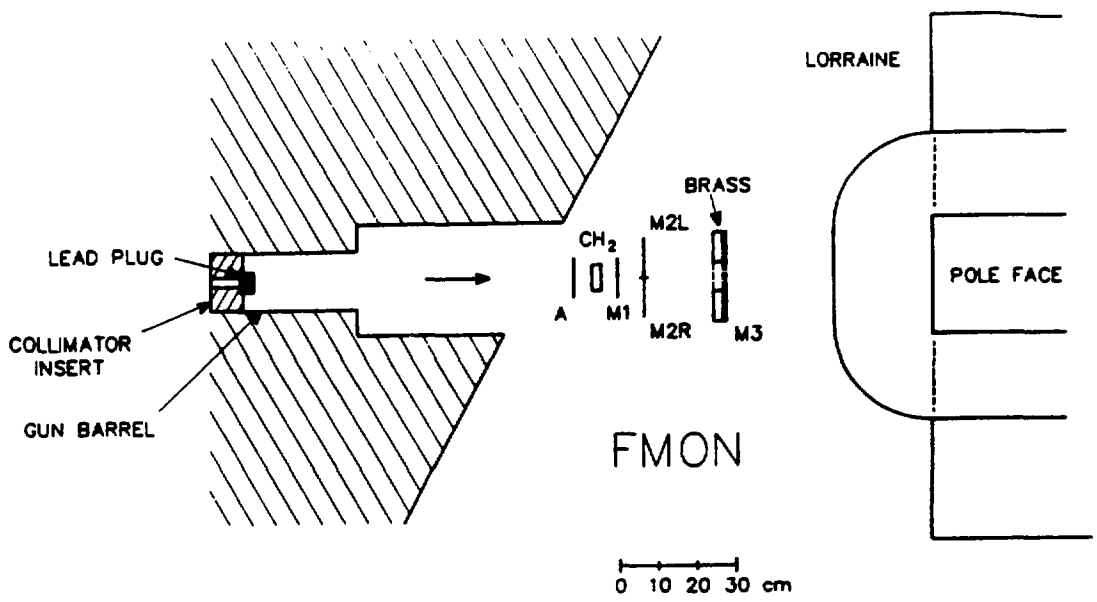

Figure 4.20: Schematic diagram of the detector configuration for the front beam monitor, FMON.

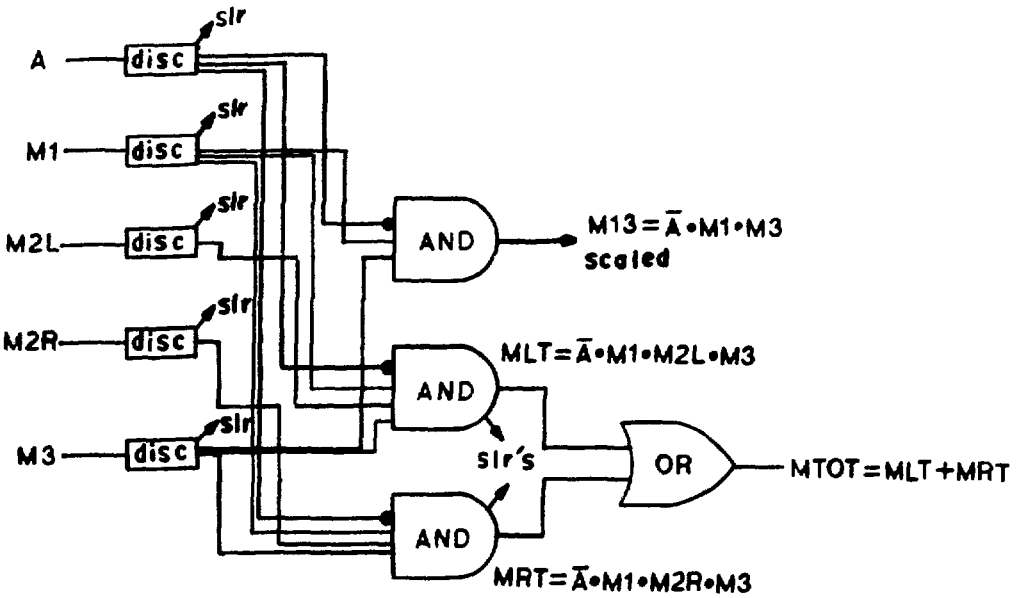

Figure 4.21: Logic diagram for FMON.

which is an OR of both the left and right coincidences in M1, M2, and M3, was scaled. MLT was defined to be $MLT = \bar{A} \cdot M1 \cdot M2L \cdot M3$ and MRT to be $MRT = \bar{A} \cdot M1 \cdot M2R \cdot M3$. Accidental rates were also scaled. These were produced by introducing a $60ns$ delay in the M1 output. The scintillator, A, had a resolving time of $30ns$, whereas M1–M3 had $10ns$ resolving times.

The target monitor, TMON consisted of five scintillators arranged as shown in Fig. 4.22 TMON was located directly behind the PPT, along the beam line. This monitor measured the flux of charged particles produced in the target and scattered in the forward direction, which should be proportional to the incident neutron flux on the polarized target. Again, as for FMON, the signals from T, TL, TR, TU, and TD were discriminated and scaled individually. Additionally, coincidences of TL, TR, TU, and TD with T were scaled. For TMON, accidental rates were produced by introducing a $64ns$ delay in the output signal from T. Coincidences between TU–TD and this delayed signal were also scaled. For an S-type beam there was a measurable UD-asymmetry in this monitor, as expected.

Unlike the other two beam intensity monitors, which measured a secondary charged particle flux using relatively thin ($\sim 1cm$) scintillator detectors, the back monitor (BMON) measured the relative neutron flux directly. The detector configuration and logic diagram for BMON is shown in Fig. 4.23. A thin scintillator veto counter (V) was used to reject events triggered by charged particles. The other two detectors (B1,B2)

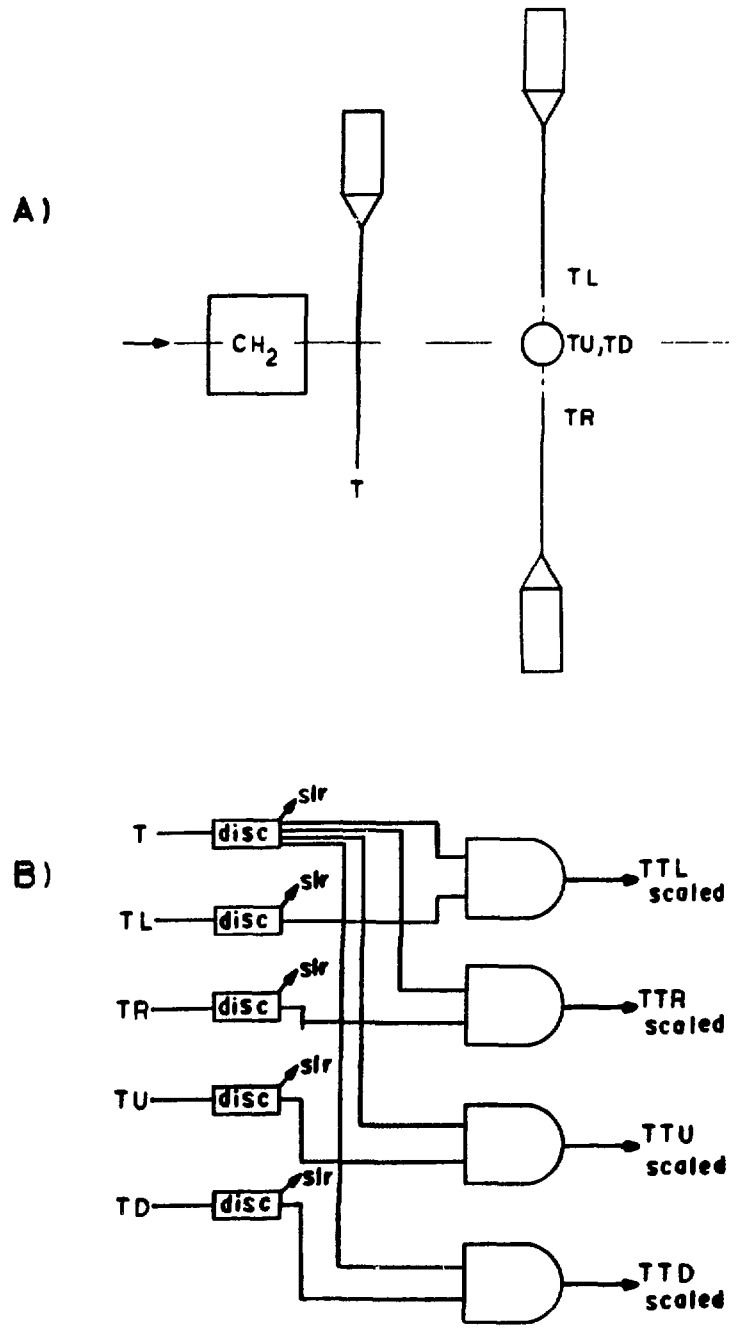

Figure 4.22: (a) Scintillator arrangment for TMON. (b) Logic diagram for TMON.

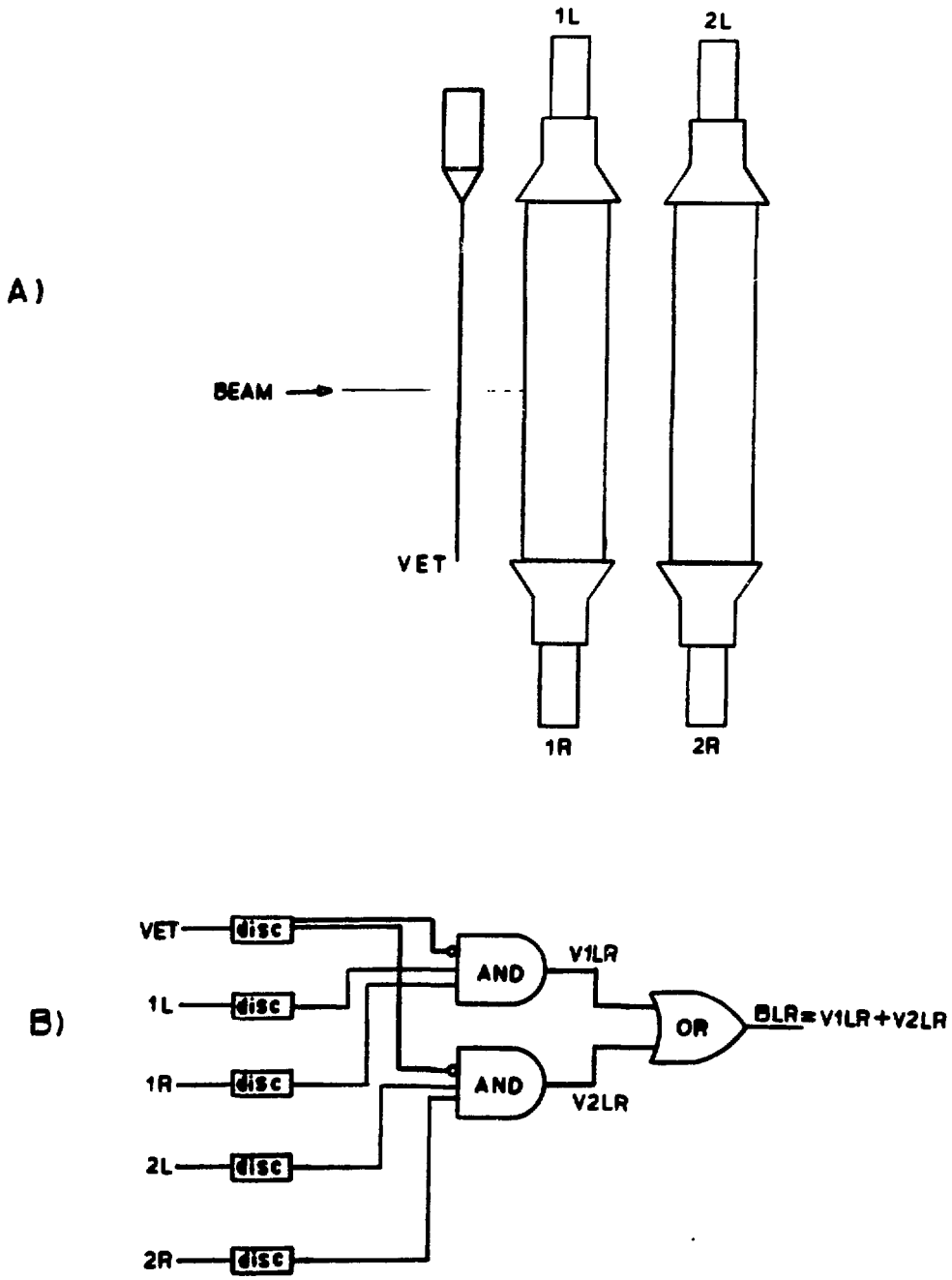

Figure 4.23: (a) Detector configuration for BMON. (b) Logic diagram for BMON.

were $60.96 \times 25.4 \times 11.43 cm^3$ polystyrene scintillators with the $25.4 cm$ thick edge facing the incoming beam. Photomultiplier tubes were mounted at both ends of each scintillator (B1,B2). The signals from the two ends were discriminated before being combined. An AND between $B1L$, $B1R$, and $\bar{V}$ was required to give a coincidence in B1. A similar AND was required for B2. The two outputs from these coincidences (V1LR,V2LR) were then OR'ed together to give the final BMON output, BLR. This output was then scaled. Accidental rates were produced by taking the OR of V1LR and V2LR delayed by $60 ns$. The neutron detection efficiency of BMON was calculated to be approximately 27% at $800 MeV$.

4.7 Data Acquisition

The data acquisition was accomplished by using a CAMAC system interfaced to a PDP 11/60 computer via a microprogrammable branch driver (MBD). The software to control the MBD and computer was written using the LAMPF "Q-System" [LA-85], a general data analysis and acquisition system. The particular version of the "Q" which was used was based on the DEC RSX11-M operating system. A special CAMAC unit called the LAMPF trigger module (LTM) was used to signal the MBD that a certain type of event had occurred. The MBD read in a specific set of CAMAC registers and transferred the data to the computer when a signal for a particular event type was received. The raw data were then written to tape. The computer was operated in the

"may process" mode during data taking. This meant that first priority was given to writing the raw data to tape, and during any computer idle time some data would be processed. For the off-line analysis, the analyzer program was run in the "must process" mode, requiring all events to be procesed. A description of the event trigger logic is given below.

4.7.1 Event Trigger Logic

The event trigger logic was used to define and trigger LTM events. It was separated into two parts, the spin gated run control logic (SGRC) and the EVENT 9 logic.

The SGRC logic was needed to trigger LTM EVENTS 7 and 9, as well as to monitor the status of the run and beam, and to define a number of CAMAC scaler inhibits. These signals were provided by a pair of LAMPF gate generators ($LGG1, LGG2$). EVENT 7 read in and cleared the CAMAC scalers at every beam spin change or at the end of a run. EVENT 8 read the target polarization every 10 minutes, as the signal was sent from the polarized target monitor/control computer. A schematic diagram of the SGRC logic is given in Fig. 4.24. The beam gate (BG) signal, sent from the central control room (CCR), was held true throughout the duration of each accelerator macropulse. The polarized beam gate (POL) was held "true"' for polarized beam and "false" when the proton beam was in the quench mode. This signal came from the ion source. The LGG1 run gate (RG) was set true by a signal sent from the data acquisition computer

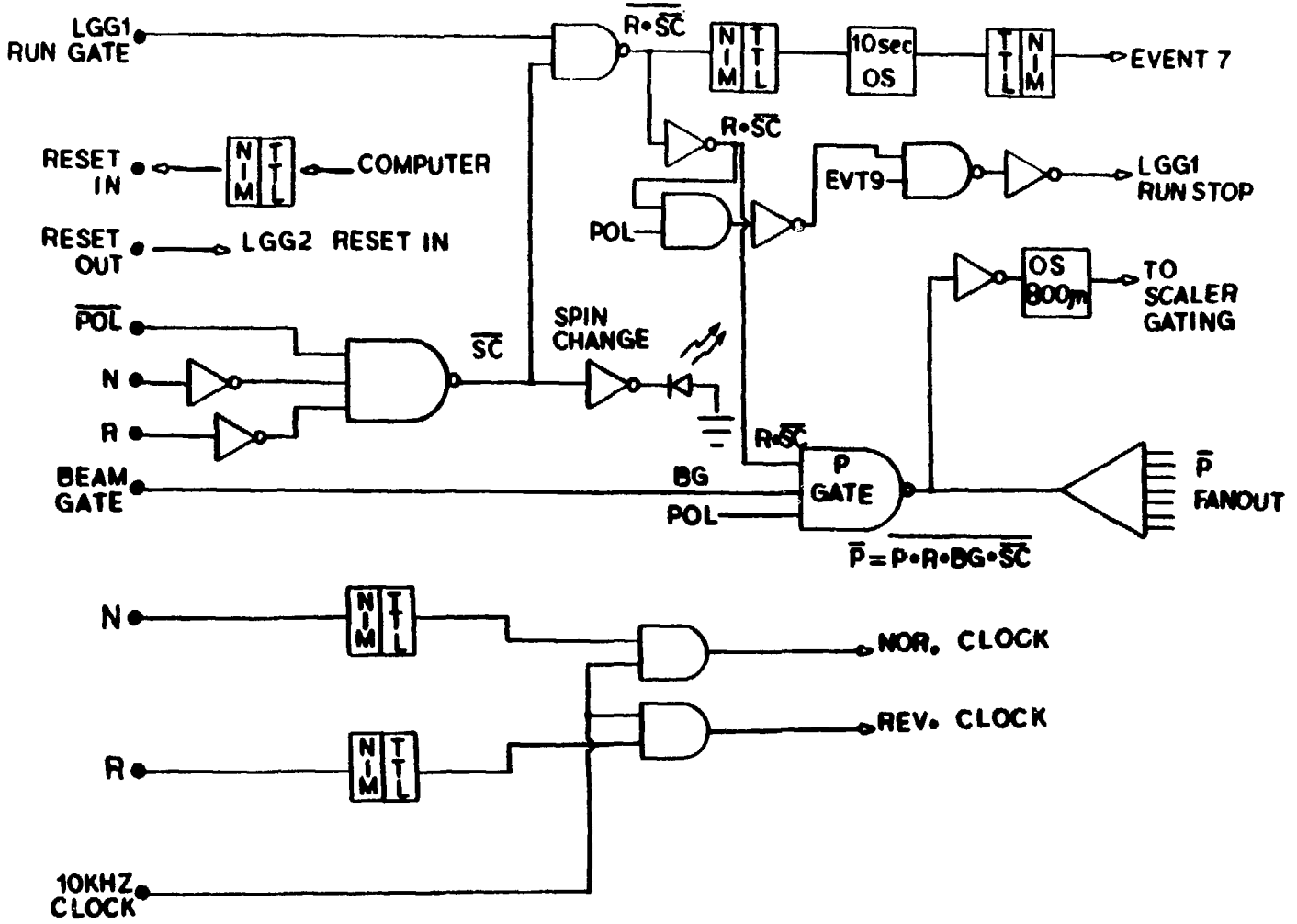

Figure 4.24: The Spin Gated Run Control Logic.

at the start of a run and set false at the end. LGG2 was also reset at this time. Two additional siganls, N and R, were also sent from the ion source to indicate whether the polarization was normal (N) or reverse (R) with respect to the direction of the beam momentum. Both N and R were false when a spin change was in progress. It should be noted that when the N and R signals changed, during a spin change, a noise signal was generated. A $10sec$ monostable (oneshot) pulse was added in order to prevent multiple EVENT 7 triggers by this noise. After being inverted several times, The N and R signals were routed to the LGG2 start and stop inputs, respectively. These states were read through a Kinetic Systems 3420 input gate and used to identify the spin state of an event. In addition, these signals were also used to determine which buffer to add the scaler values to. N and R were also AND'ed together with a $10KHz$ clock to generate normal and reverse clock signals.

Various scaler inhibit signals were generated by the SGRC logic. The $\bar{P}$ inhibit was used by the EVENT 9 trigger logic which will be discussed in the next section. The master inhibit, $\bar{I} = \bar{P} + EVTi\ busy$, was used to control data taking.

4.7.2 The EVENT 9 Logic

The EVENT 9 logic was used to trigger an LTM EVENT 9 whenever a fast coincidence between the trigger scintillator (S1) and the hodoscope (S2) occurred. A logic diagram for the EVENT 9 logic is shown in Fig. 4.25. An OR of elements 1-14 of S2 was taken

using an LRS 429A fan-in. This signal was combined with the left side of S1 as a logical AND. The S1LU (up) and S1LD (down) signals were discriminated and time-averaged before being combined in a logical AND with S2. A similar situation existed for elements 11-25 of S2 and the right side of S1. A fast trigger ($FSTRG$) signal was produced by the coincidence of S1L (S1R) and HL (HR). This trigger was inhibited when the beam was undergoing a spin change ($\bar{P} = P\bar{O}L \cdot \bar{B}G \cdot \bar{R}G \cdot SC$). The FSTRG signal was fanned out and used to trigger TDC starts for the drift chambers P1, P3 and P4, and the hodoscope. The FSTRG signal was also used in the fast trigger latch.

The fast trigger latch consisted of an LRS 364 4-fold coincidence logic gate with veto. This module was operated in the standard 2 of 2 voter coincidence mode. The veto was used to inhibit, or "latch", the reading out of the MWPC (P0,P2) information during a computer busy state or during a TDC/ADC fast clear. Additionally, if the MWPC, P2, did not fire and a FSTRG signal was received, the output would be latched. In this respect, P2 was part of the fast coincidence trigger discussed at the beginning of this section.

A master trigger, MTRG, was used to signal an EVENT 9 and to set the MWPC gate to read out the P0 and P2 information. MTRG consisted of an AND of the MWPC fast OR and the FSTRG. It should be noted that the FSTRG, FSTRG latch, and MTRG signals were also scaled for diagnostic purposes.

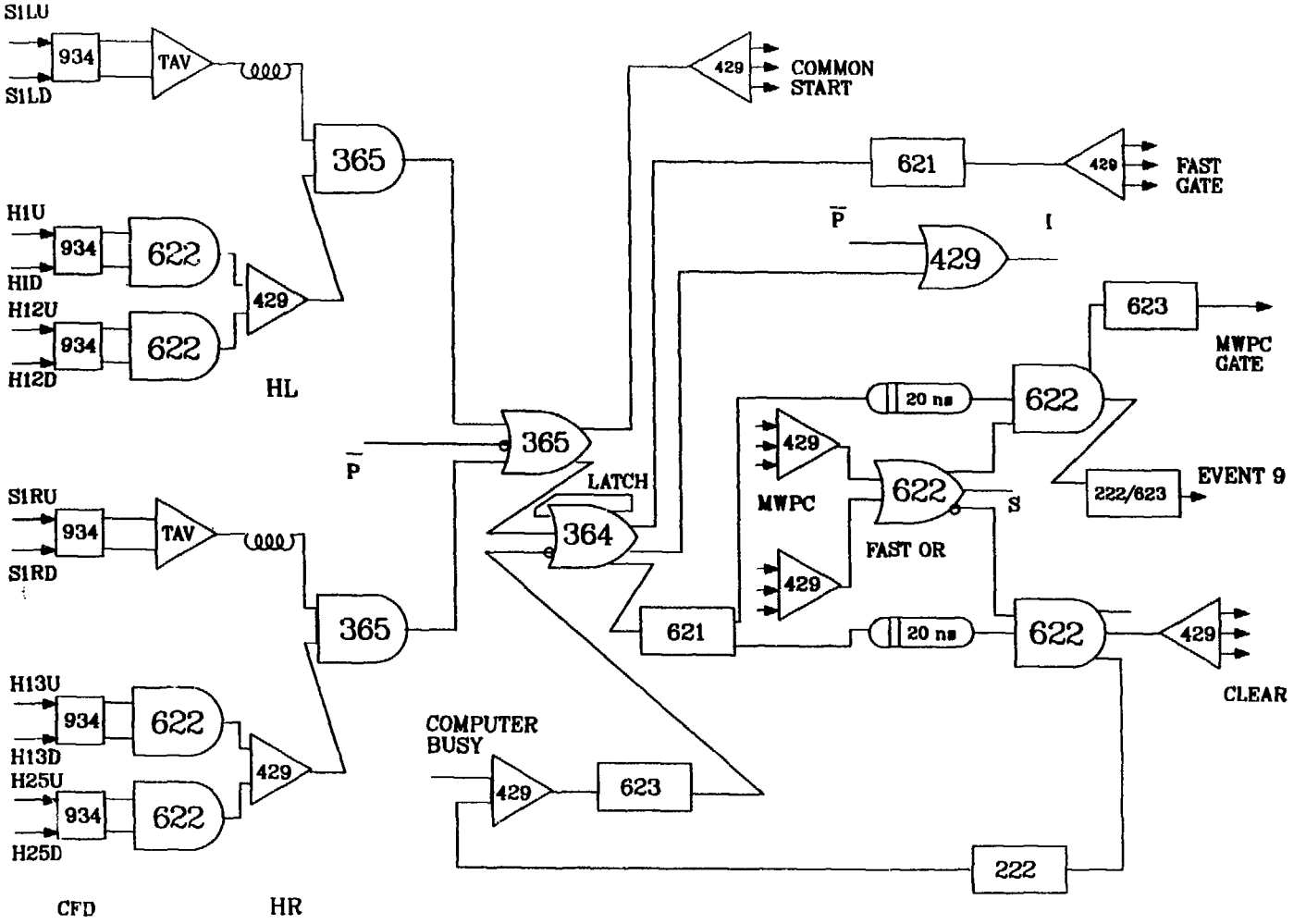

Figure 4.25: The EVENT 9 Logic.

CHAPTER 5 DATA ANALYSIS

5.1 Introduction

Both the data acquisition and analysis were carried out using the LAMPF standard data acquisition and analysis package, as discussed in the last chapter. It is a flexible system which allows the user to incorporate analysis subroutines which are uniquely required by a particular experiment. It also allows the user to set up multi-dimensional histograms and dot-plots, in addition to allowing logical tests on the data.

The analyzer software used for this experiment (E770) was a modified version of that used for experiment E665, which is discussed in the thesis of M.W. Rawool [Ra-88]. Only changes in the software for E770, including those required to accommodate the additional chambers – P0 and P3, will be discussed in this chapter. For detailed explanations of other software subroutines, see the aforementioned thesis.

This chapter will discuss the particular analyzer subroutines used to do particle tracking and data reduction, kinematical and other constraints required, and the background subtraction techniques used before an asymmetry was calculated. Corrections

of the data for systematic effects will be discussed along with a treatment of both statistical and systematic errors.

5.2 Particle Tracking

For this experiment, the E665 set-up was modified by adding two additional chambers to the spectrometer. An additional MWPC, P0, was added in the front close to P1, and P3, another large drift chamber, was added in the rear, as shown in Fig. 5.1. This combination produced a redundancy in the number of chambers required to determine a track both in front of and behind the SCM105 magnet. As a result, it was not necessary for all chambers to fire in order to produce an event that could be reconstructed.

Table 5.1 shows the possible chamber combinations used to determine the bend angle in the spectrometer. For the case where there was not enough P2 information to construct a coordinate, the two chambers in the rear were used to project to a point at the center-plane of the spectrometer magnet (see Fig. 5.1). This point and the coordinate in either P0 or P1 were then used to construct a track in the front.

Table 5.1: The allowed chamber combinations for reconstruction of a particle track.

Front Chambers	Rear Chambers
P0 or P1, P2	P3, P4
P0 or P1	P3, P4
P0 or P1, P2	P4

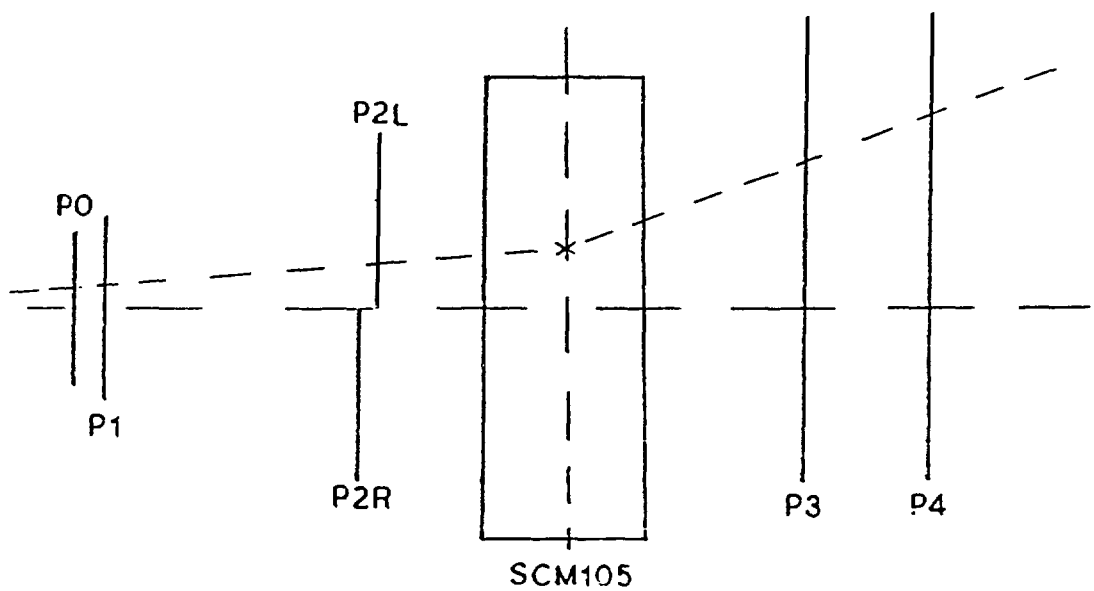

Figure 5.1: Typical reconstructed track using a point projected to the center-plane of the spectrometer magnet from the slope calculated in P3 and P4.

When there was not enough information in P3 to construct a coordinate, the tracking scheme incorporated in E665 was used: the front chambers P0 or P1, and P2 were used to construct a track in the front and to project to a point at the center-plane of the magnet. This point and the coordinate in P4 were then used to construct a track in the rear. If there was "good" chamber information in all three chambers in the front, then a least-squares fit to the three points was done to determine the slopes. What is meant here by a "good" chamber is that there was enough information to determine an x- and y-position in that chamber. A "good" chamber in the rear meant that at least three of the four planes in P3 or P4 fired.

The x and y tracking were done independently in the front. This meant that different chamber combinations were used to determine the xz- and yz-slopes. The tracking in the rear was a bit more complicated.

The tracking scheme in the rear used wire position and drift-time information from P3 and P4 to determine a track for a given event. This information was used to extract the position of the particle as it passed through each plane of a chamber. For the case where both P3 and P4 were "good", the information in these two chambers was sufficient to determine both the rear xz- and yz-slopes as well as the position at the midpoint of each chamber. Because of the construction of these drift chambers, it was necessary to have information in both the U- and V-planes in each chamber in order to be able to determine a y-position (see Chapt. 4, Sec. 4.5.3). However, if there was

a "good" event in both the X and X' planes as well as in one of the others (U or V), then a y-position could be reconstructed. It was for this reason that at least three of the four planes in a chamber were required in order to determine a track in the rear.

The algorithm used to determine the positions at each plane in P3 and P4 was as follows: First, several least-squares fits to determine the combination of wires which would give the best fit to a straight line were done. This was accomplished by looping over all possible combinations of wires which fired and choosing the fit with the smallest r.m.s. deviation. It was required that this r.m.s. deviation,χ, be less than or equal to $(2.0mm^2)^{1/2}$. The choice for this cut-off was determined by observing the χ distribution for a set of runs. The cut-off point was chosen so as to eliminate the fits in the tail of the distribution. Because it was possible for a plane to "misfire", occasionally it was not possible to get a $\chi \leq (2.0mm^2)^{1/2}$ by including all planes. In this event, a plane was discarded and the fitting procedure repeated until a good χ value was obtained. It should be mentioned that a maximum of four hits per plane was allowed. Finally, this interative least-squares fitting procedure, using the previously determined wire position information together with the drift-time information, was repeated to resolve the left-right ambiguity associated with a hit and to obtain the slope.

The procedure described above was also used in the event that there was no good information in P3. In this case however, a point at the center plane of the magnet (as described earlier) was used to constrain the fit in P4.

In the event that a chamber was not used in either the front or the rear due to lack of chamber information, the coordinates for that chamber were mocked-up either by interpolation or extrapolation. This was done primarily because certain chamber combinations were required to calculate the target and magnet-center projections. Additionally, these coordinates were required for the $\int B_y dl$ parameterization of the SCM105 magnet, as described below, and for diagnostic purposes.

These tracks in the front and rear were used to calculate the bend angle in the spectrometer and hence the particle momentum. The motion of a charged particle in a uniform magnetic field is given by

$$p \cos\lambda = \frac{0.3 \int B_y dl}{\theta_2 - \theta_1} \tag{5.1}$$

where λ is the pitch angle out of the xz-plane. Here θ_1 and θ_2 are the projections in the xz-plane in front of and behind the SCM105, respectively. And of course, $\theta_2 - \theta_1$ is the bend angle. The front slopes are given by the following expressions, for example:

$$\tan\theta_1 = \frac{x_{p_2} - x_{p_1}}{z_{p_2} - z_{p_1}} \tag{5.2}$$

$$\tan\alpha_1 = \frac{y_{p_2} - y_{p_1}}{z_{p_2} - z_{p_1}} \tag{5.3}$$

where $\tan\alpha_1$ is the yz-slope. The rear slopes are given similarly by the following:

$$\tan\theta_2 = \frac{x_{p_4} - x_{p_3}}{z_{p_4} - z_{p_3}} \tag{5.4}$$

$$\tan\alpha_2 = \frac{y_{p_4} - y_{p_3}}{z_{p_4} - z_{p_3}} \,. \tag{5.5}$$

The quantity $p\cos\lambda$ is the projection of p in the xz-plane, where $\cos\lambda$ is given by

$$\cos\lambda = \sqrt{\frac{1+\tan^2\theta_1}{1+\tan^2\theta_1\tan^2\alpha_1}}\ . \tag{5.6}$$

The $\int B_y dl$ for the SCM105 magnet was determined event-by-event using a polynomial parameterization of the SCM105 magnetic field. Details of this parameterization are discussed by M.W. Rawool [Ra-88].

With the allowed chamber redundancies it was possible to attain a typical reconstruction efficiency of about 75%, as compared to about 40% for E665. By allowing additional chamber combinations the overall resolution of the spectrometer was also improved.

5.3 The Data Summary Tape (DST)

Because of the extensive computer CPU time required to decode all the raw chamber information and do the particle tracking, the data analysis was carried out in two stages. The first stage consisted of making a data summary tape (DST) from a raw data tape.

In order to make a DST, the raw chamber information was decoded and the particle tracking done. The beam and target polarizations, TOF, chamber coordinates, and the front and rear slopes were then written to the DST event-by-event. Figure 5.2 shows a flow diagram for the analyzer program used to make a DST. No kinematic or other cuts were required to be passed in order for an event to be written to the DST, other

than the χ requirement discussed earlier, and the requirement that enough information exist such that the bend angle, scattering angle, etc. could be determined.

For each run which was replayed, an *output* file was produced which listed the beam and target polarizations, the scaler outputs, various scaler ratios, the number of particles which passed each analyzer software test, and a list of chamber and reconstruction efficiencies. Additionally, a histogram file was produced and stored on magnetic tape which contained histograms of raw chamber information such as wire positions, drift-time distributions, various residuals related to chamber resolutions, etc. These histograms were saved for diagnostic purposes in the event that it was necessary to determine whether or not a particular chamber was operating properly during that run. Histograms of calculated quantities such as TOF, particle mass, momentum, etc., were also saved.

The chamber efficiencies were calculated by taking the following ratio for each chamber:

$$\epsilon = \frac{N}{N_A} \tag{5.7}$$

where N_A is the number of events analyzed for that chamber and N is the number of events with enough information to allow reconstruction of a position in that chamber. A software test was applied which required both good front and rear tracking in addition to good TOF information. The reconstruction efficiency was calculated by taking the ratio of the number of events passing this test to the total number analyzed.

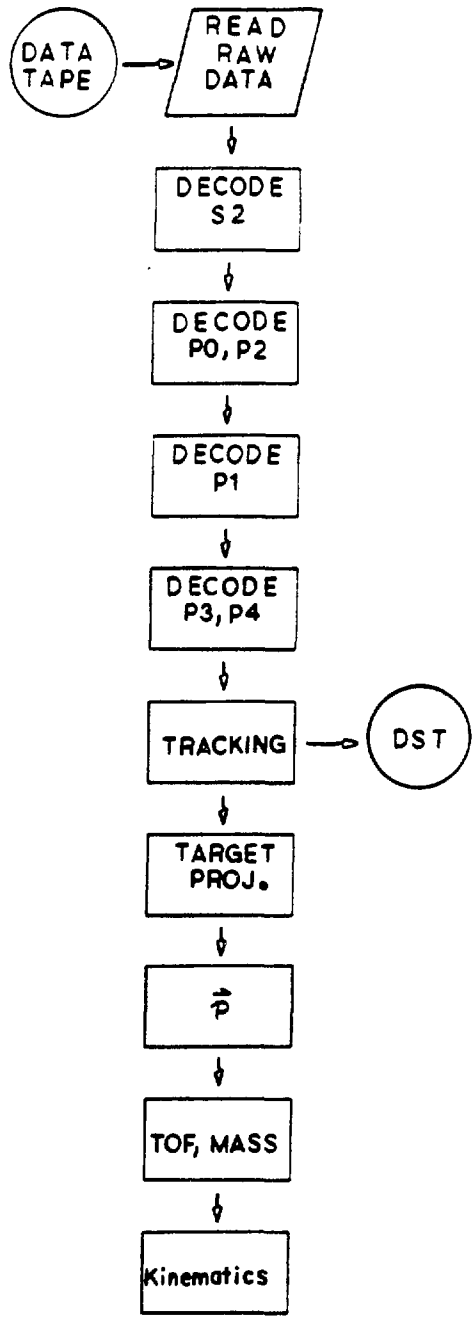

Figure 5.2: Flow diagram of the analyzer program used to produce a data summary tape.

By pre-analyzing the raw data and producing a DST, it was then possible to replay a run which normally would have taken about 30 CPU minutes in about 30 CPU seconds. This then made it reasonable to replay a run or set of runs several times under various conditions in a manageable amount of time. In the final data analysis stage, cuts were placed on various kinematic and other quantities for a replay of a run. These cuts were then varied and the replay of that run repeated. Without the DST, this would have been extremely time consuming and impractical, particularly since each raw data tape contained three or four runs and there were several hundred data tapes.

5.4 Kinematics and Time-of-Flight

After calculating the momentum of a particle, various other kinematic quantities were calculated by the analyzer program and histogrammed. Because only the recoil particle was detected, the missing-mass of the scattered neutron was calculated assuming *np* elastic-scattering kinematics. This quantity was used to determine the spin-spin correlation parameters.

If the incoming neutron kinetic energy, the scattering angle of the recoil proton, and the recoil proton momentum are known, then it is possible to calculate the neutron missing-mass. From conservation of energy, the total energy of the two-body system is given by

$$E_{tot} = E_p + E_{beam} \tag{5.8}$$

where

$$E_{beam} = T_b + m_n \tag{5.9}$$

and $E_p = m_p$ for a target proton at rest in the laboratory frame. T_b is the beam neutron kinetic energy and m_n is the neutron rest mass. Note that for this discussion, $c = 1$. The total energy of the recoil proton is given by

$$E' = (m_p^2 + p_r^2)^{1/2} \tag{5.10}$$

where p_r is the measured recoil momentum. Knowing E_{tot} and E', it is possible to determine the total energy of the scattered neutron by taking the difference:

$$E_{scatt} = E_{tot} - E' \tag{5.11}$$

From momentum conservation, the square of the momentum of the scattered neutron, p_{scatt}^2, is given by

$$p_{scatt}^2 = (\vec{p}_b - \vec{p}_r)^2 \tag{5.12}$$

$$= p_b^2 + p_r^2 - 2\,p_b\,p_r\,\cos\theta \tag{5.13}$$

where θ is the angle between the incident neutron momentum and the recoil proton momentum. Since θ and p_r were measured, p_{scatt} could be calculated. The peak beam momentum was used for p_b to calculate the missing-mass. Neutrons originating from the low-momentum tail of the neutron beam distribution had a shifted missing-mass value and were therefore a source of background for our measurements. Additionally,

charged particles other than an elastically scattered proton which were momentum-analyzed in the spectrometer would have a smeared missing-mass distribution. This will be discussed in greater detail in the next section. Once the scattered neutron momentum is known, the missing-mass is determined by

$$m^2 = E_{scatt}^2 - p_{scatt}^2 \cdot \tag{5.14}$$

Figure 5.3 shows the kinematics as defined in both the laboratory and center-of-momentum (c.m.) frames.

In order to be able to bin the missing-mass by c.m. angle, it was necessary to calculate the c.m. angle event-by-event for the recoil proton. This angle is given by

$$\theta_{cm} = \tan^{-1}(p_\perp / p_{\|-cm}) \tag{5.15}$$

where $p_{\|-cm} = \gamma(p_\| - \beta E')$ is the Lorentz transformed parallel component of the recoil proton momentum in the laboratory frame. Beta (β) is the c.m. velocity given by $\beta = p_b / E_{tot}$ and $\gamma = (1 - \beta^2)^{-1}$, as usual. The parallel and perpendicular components of the momentum are given by

$$p_\perp = p_r \sin\theta \tag{5.16}$$

$$p_\| = p_r \cos\theta \tag{5.17}$$

where θ is the scattering angle discussed earlier. In the final analysis, which will be discussed in detail later, the missing-mass was binned in 5^o c.m. angle bins to determine each C_{ij} data point. The neutron c.m. angle was given by $180^o - \theta_{cm}$.

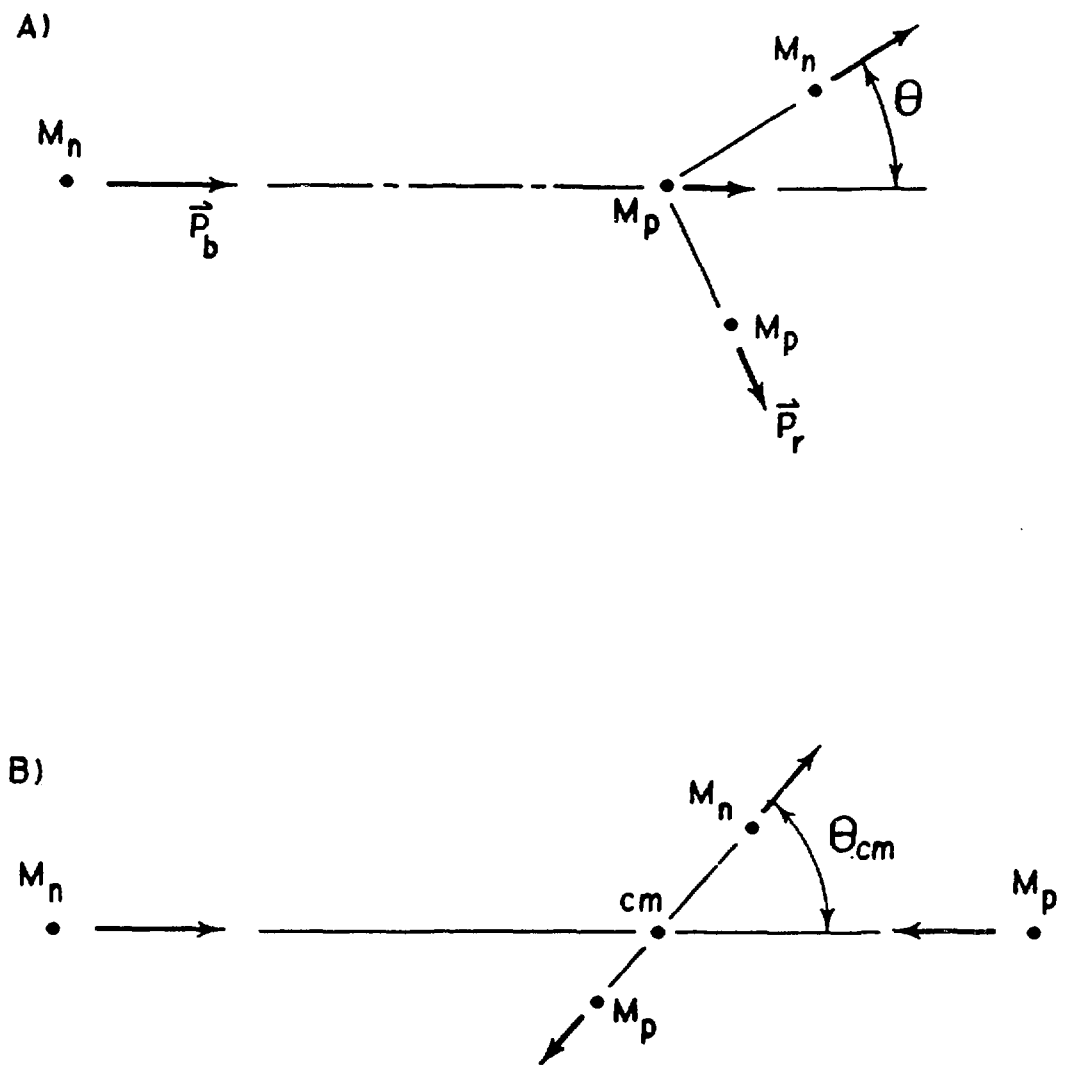

Figure 5.3: a) *np* kinematics in the laboratory frame. b) Kinematics in the center-of-momentum frame.

In addition to the missing-mass and the scattering angle, the x-, y-, and z-target projections were calculated. The x-target projection was calculated as follows:

$$x_{target} = x_{p2} + \frac{(x_{p1} - x_{p2})(z_t - z_{p2})}{z_{p1} - z_{p2}} \tag{5.18}$$

where z_t is the target z-position in a coordinate system whose origin is at the SCM105 magnet center and x_{p1} is the P1 x-position, etc. The y-target projection was calculated in the same way by replacing the x-coordinates by y. The z-target projection was calculated by

$$z_{target} = z_{p2} - \frac{x_{p2}(z_{p1} - z_{p2})}{x_{p1} - x_{p2}} \ . \tag{5.19}$$

Figure 5.4 shows typical target projections. Cuts were made on these projections in the final data analysis.

Because of the redundant chamber combinations, it was possible to calculate a difference (DXTT, DYTT) between the point projected from the front chambers to the magnet center-plane and the point projected from the rear. This difference was an indication of how good the matching of the two trajectories was at the center-plane of the magnet. Figure 5.5 shows typical DXTT and DYTT distributions. The distributions were Gaussian, as expected, with typical standard deviations of 2mm and 3mm for DXTT and DYTT, respectively. For an event having only one chamber in the front or the rear, and where the magnet center-plane point was used to calculate the slope, DXTT or DYTT was set identically to zero, which produced the spike at DXTT=0 in

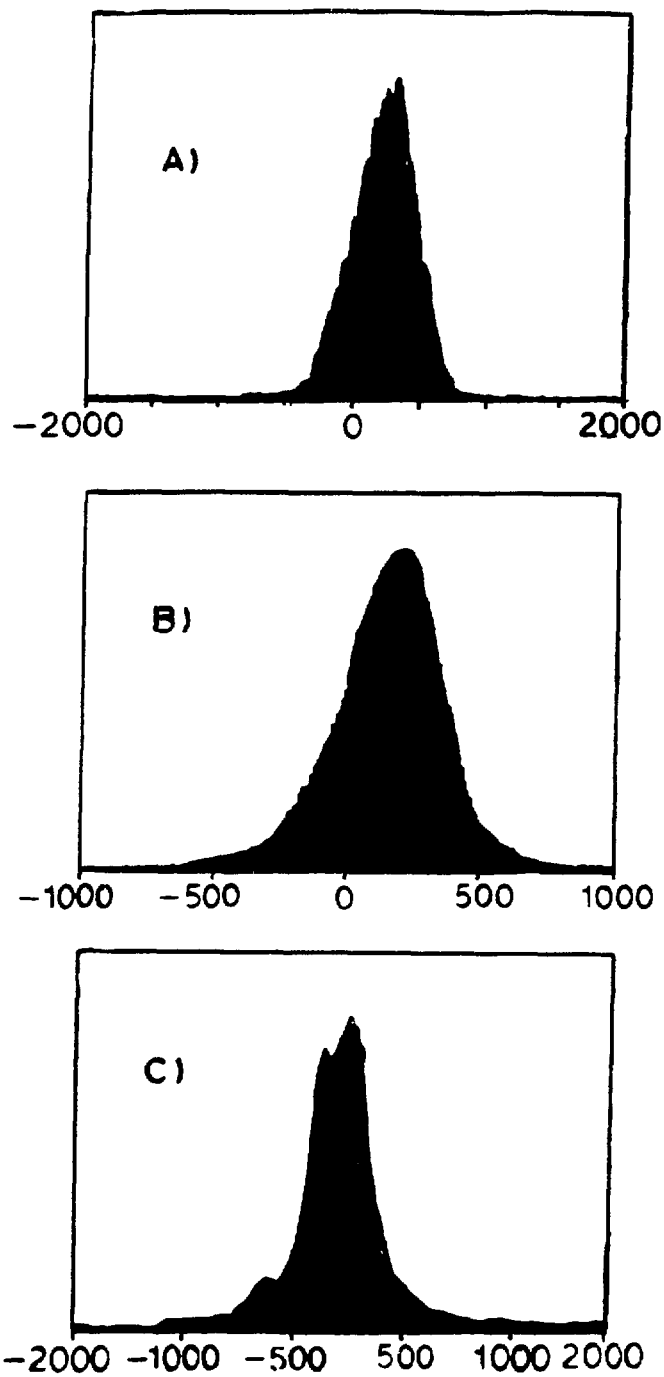

Figure 5.4: Typical target projections. Units are in tenths of a millimeter. a) x-target projection. b) y-target projection. c) z-target projection.

Fig. 5.5a.

The TOF method was used for particle identification. The β of a charged particle passing through the spectrometer could be determined if the TOF and the mean pathlength travelled were known, by the following expression:

$$\beta = \frac{1}{c}\frac{\Delta l}{TOF} . \tag{5.20}$$

As mentioned earlier, the TOF was measured between the trigger scintillator, S1, and the scintillator hodoscope, S2. The mean pathlength Δl was calculated by knowing the front trajectory and which hodoscope element was hit. The front pathlength, Δl_F, was determined by projecting a line from the target to the center-plane of the SCM105 using the known P2 coordinates. The front pathlength was then calculated as follows:

$$\Delta l_F = \sqrt{(\Delta x)^2 + (\Delta y)^2 + (\Delta z)^2} \tag{5.21}$$

where $\Delta x = x_{scm} - x_{target}$, etc. The rear pathlength, Δl_R, was calculated similarly using the SCM105 center-plane position and the position of the hit hodoscope element. The total mean pathlength Δl was given by the sum of Δl_F and Δl_R. The particle mass was calculated using the measured momentum from

$$\begin{aligned} m &= \frac{p}{\gamma\beta} \\ &= p\left(\frac{1}{\beta^2} - 1\right)^{1/2} \end{aligned} \tag{5.22}$$

Figure 5.6 shows a typical particle mass spectrum. As is obvious, only protons and deuterons are seen in the spectrum. Since pions have much higher values of β and

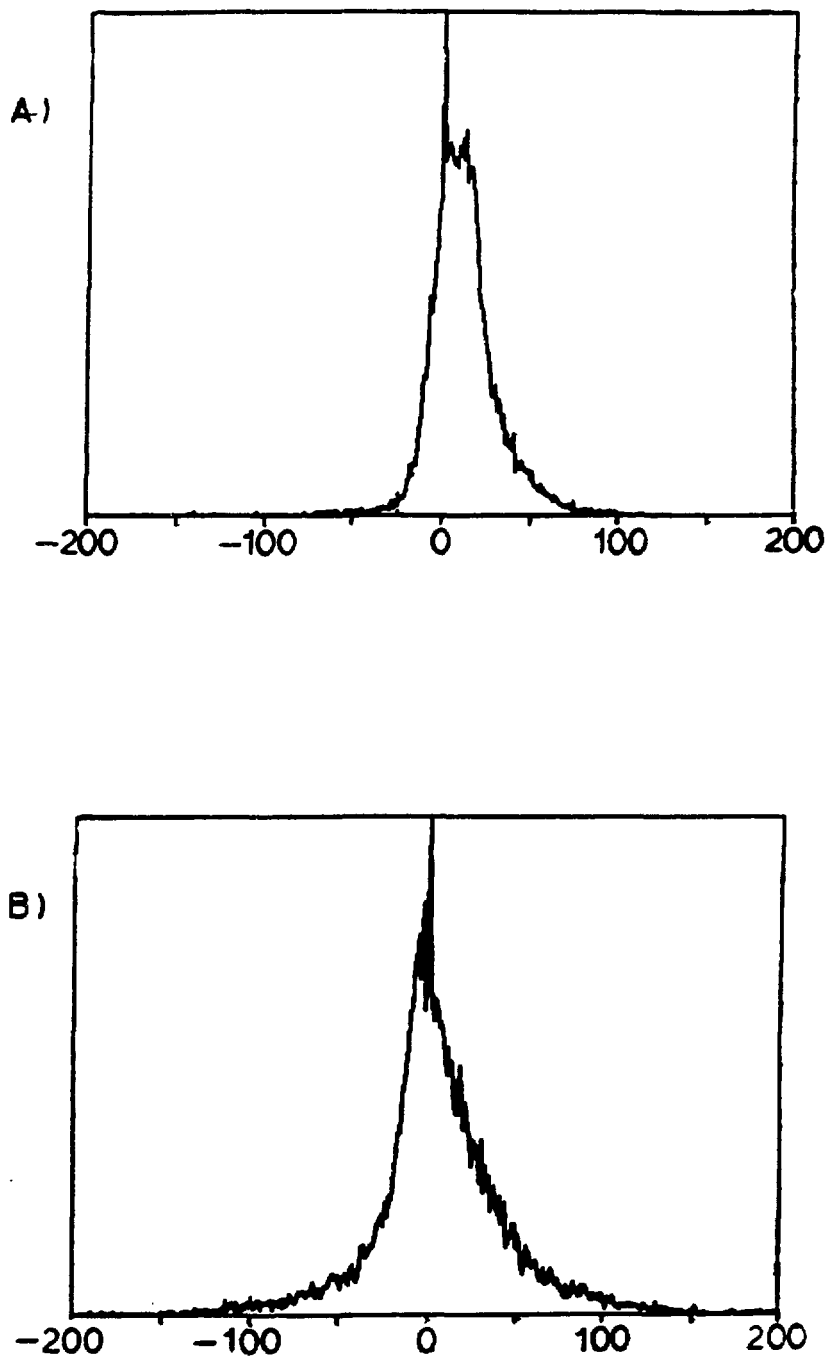

Figure 5.5: a) Magnet center-plane matching in x. Units are in tenths of a millimeter. b) Magnet center-plane matching in y.

therefore have a much smaller TOF, it was possible to cut out this source of background by an appropriate choice of hardware timing. The FWHM of the proton peak for that particular set of data typically ranged from 35 to 45$\frac{MeV}{c^2}$. The TOF resolution can be inferred from the mass resolution and was found to be better than $\pm 2nsec$.

The momentum resolution, $\frac{\delta p}{p}$, can be estimated from the missing-mass by the expression:

$$\delta m = \left(\frac{\delta p}{p}\right) \frac{p}{m_n} \left[\frac{p}{E_{scatt}}(m_p + E_{beam}) - p_b \cos\theta\right] \tag{5.23}$$

As an example, for a particlar $634MeV$, 5° c.m., angle bin with $\delta m = \pm 12\frac{MeV}{c^2}$, $E_{beam} = 1574MeV$, $P_b = 1262\frac{MeV}{c}$, and $p = 1100\frac{MeV}{c}$, the above expression gives $\frac{\delta p}{p} = \pm 1.25\%$. Using Eqn. 5.22 one finds $\frac{\delta p}{p} \sim \frac{\delta m}{m}$ which is consistent with the expression above.

5.5 Background Contributions

If one looks at Fig. 5.7a, which is a typical missing-mass distribution integated over the entire acceptance of the spectrometer, one clearly sees that the data were background-dominated. One sees a small peak near the neutron rest mass and a large continum background. Figure 5.7b shows the missing-mass distribution for a pure carbon target. It should be noted that there is no neutron peak.

There were several sources of background for our experiment. First, because the target material was not pure hydrogen, but consisted of other elements such as boron, nitrogen, and carbon, quasielastic scattering from bound nucleons in these effectively

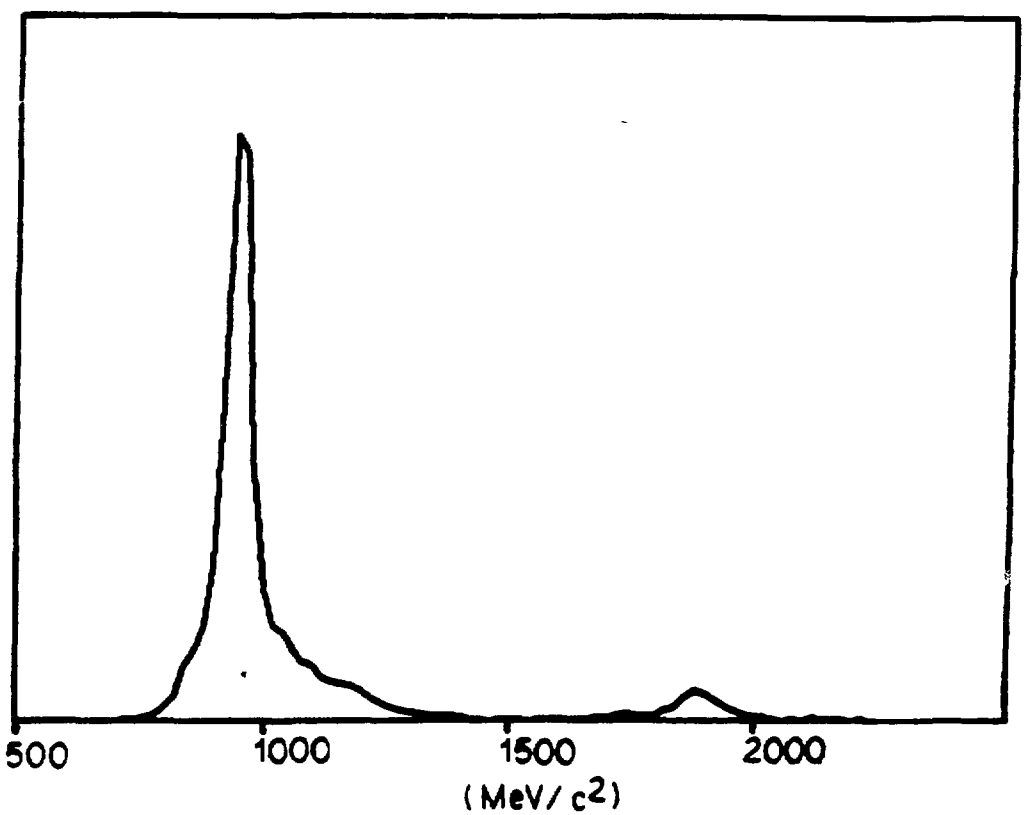

Figure 5.6: A typical particle mass spectrum determined from the measured particle momentum and TOF showing both a proton and deuteron peak.

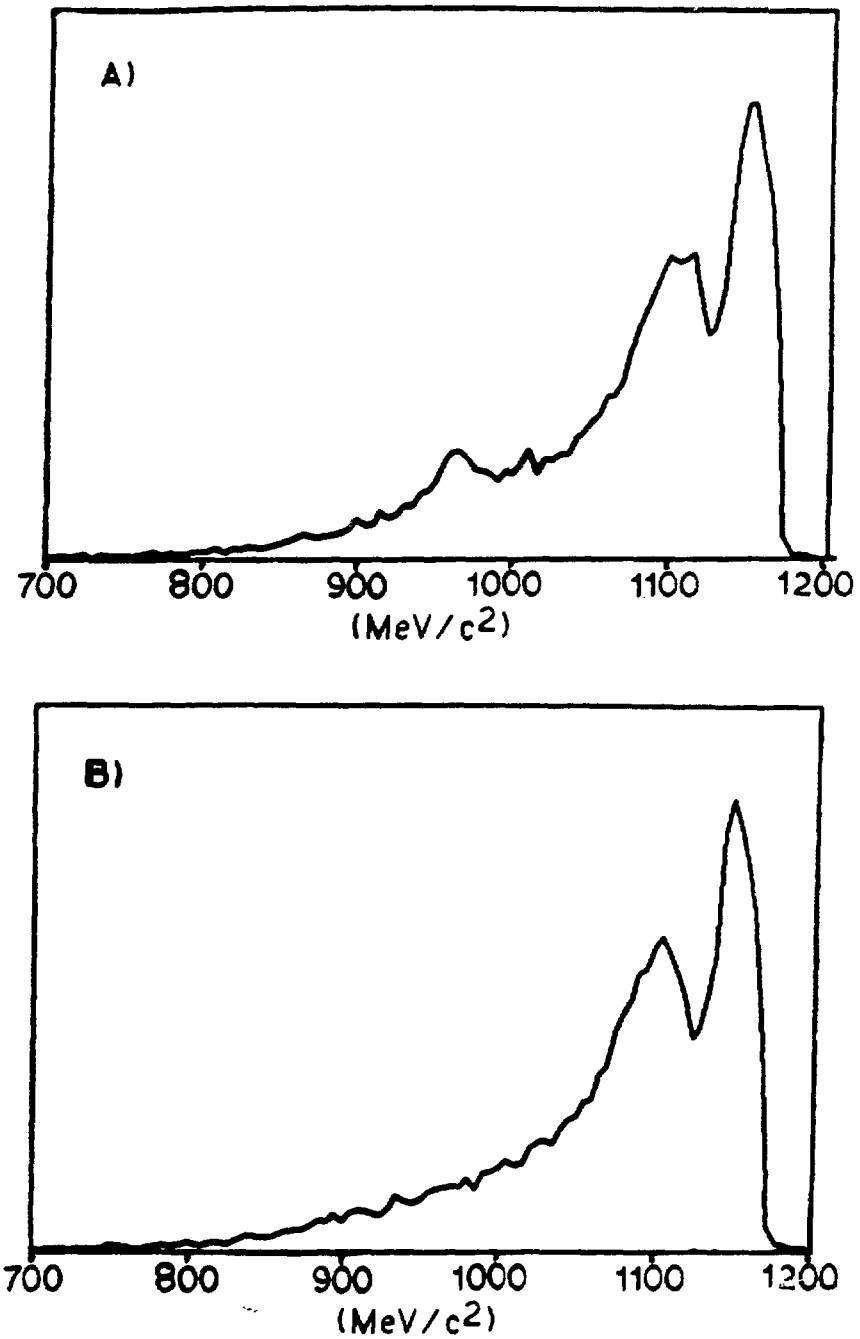

Figure 5.7: a) Neutron missing-mass for the polarized target integrated over the entire spectrometer acceptance. b) Missing-mass distribution for a carbon target.

unpolarized nuclei contributed to the background. These quasielastic events originated from both peak-energy and low-energy neutrons in the beam. Another contribution came from the elastically scattered low-energy neutrons. Additionally, protons originating from various inelastic processes such as $np \longrightarrow pp\pi^-$ also contributed.

A Monte-Carlo study was done to determine qualitatively where in the missing-mass distribution each of these contributions would lie. Figure 5.8 shows the results of this study for a fixed beam energy and scattering angle. As expected, the peak energy quasielastics lie centered at the neutron mass, but with the distribution smeared by the Fermi-motion of the bound nucleons. The low energy beam neutrons are shifted to high missing-mass. Protons produced via the opening of an inelastic channel would have the lowest scattered neutron energy and therefore would give the highest missing-mass.

The Monte-Carlo program assumed elastic-scattering kinematics. A quadratic form was assumed for the low energy neutron beam distribution and a peak for the full energy neutrons. The momentum of the outgoing recoil proton was smeared with the spectrometer resolution, but no multiple scattering effects in the spectrometer or target were modeled. To model the quasielastics, the target proton was given an arbitrary momentum. The maximum proton energy and momentum at a fixed θ_{lab} was calculated for the inelastic reaction $np \longrightarrow pp\pi^-$.

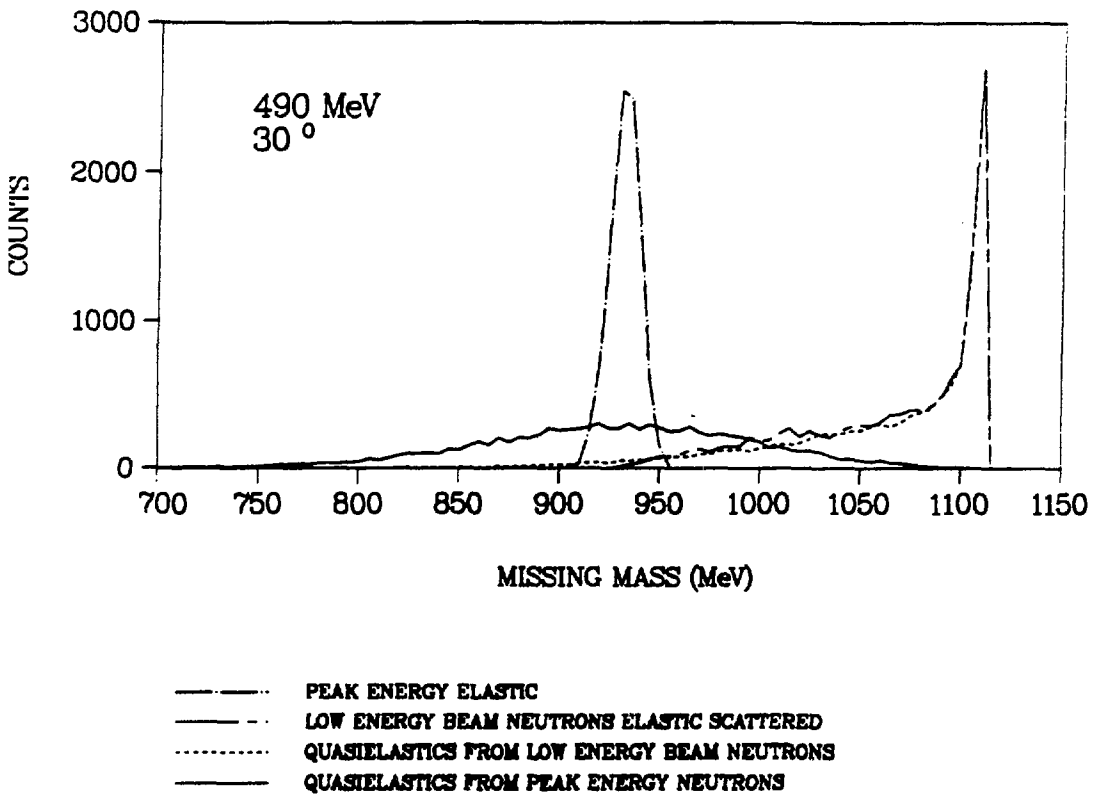

Figure 5.8: Results of the Monte-Carlo study showing the various modeled background contributions.

5.6 Final Pass Data Analysis

After having initially reduced the raw data to DST form, the final pass analysis was done to calculate the spin-spin correlation parameters. The procedure used will be discussed in its various stages in the next few sections. Figure 5.9 shows a flow diagram for the analyzer program used at this stage of the data analysis. The program was a modified version of that used for the first stage analysis, with calls to the chamber decoding subroutines removed.

Using the "Q" test package, software tests were set up to allow binning of the data by both c.m. scattering angle and spin orientation of the target and beam. Figure 5.10 shows a c.m. scattering angle distribution of the recoil protons for some $634 MeV$ data taken with the spectrometer set at 35^o in the laboratory. The data were binned in 5^o c.m. bins. The "hole" in the distribution is caused by the overlap region of the two halves of the detector P2. It should be noted that the calculated laboratory scattering angle was corrected for the target magnetic field effects, as is discussed in detail in Chapt.6, before the c.m. angle was calculated.

A software test which required beam and target spins to be either parallel ($\uparrow\uparrow$ or $\downarrow\downarrow$) or antiparallel ($\uparrow\downarrow$ or $\downarrow\uparrow$) was made on the data. Histograms for events parallel or antiparallel were made for each angle bin and these were added or subtracted appropriately to calculate C_{ij}.

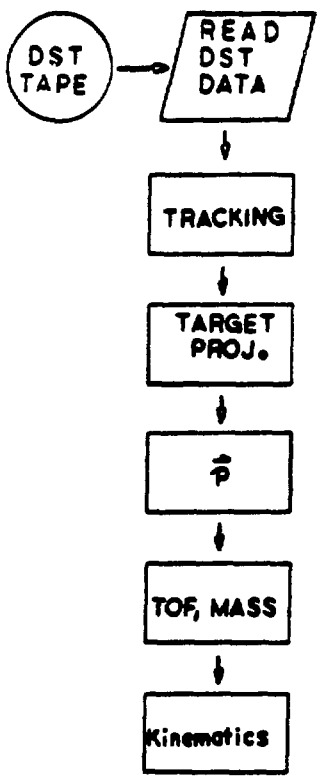

Figure 5.9: Flow diagram for the analyzer program used to replay the DST tapes.

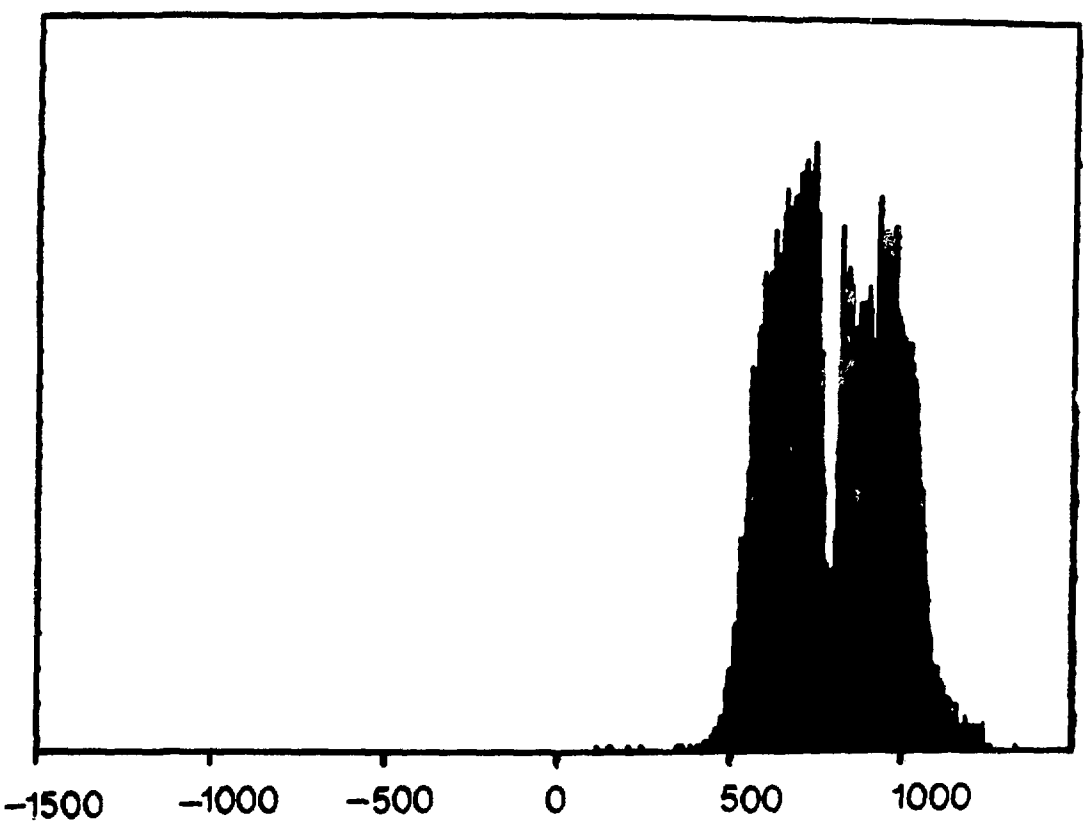

Figure 5.10: A typical center-of-momentum scattering angle distribution for a 35° spectrometer setting. Each channel corresponds to 0.1 degree.

5.7 Cuts on the Data

Cuts were placed on various calculated quantities for the final pass data analysis. These quantities included the x- and y-target projections, the magnet center-plane matching (DXTT, DYTT), and the particle mass. The cuts were varied within each data set and the final cuts were chosen such that the smallest statistical error bars were achieved.

The purpose of placing cuts on the target projections was to reject events which did not originate from the target. It was found that using a cut on the z-target projection had no effect and was therefore not used. Figure 5.11 shows the final cut placed on the x-target projection for $634MeV$, C_{LL} and C_{SL} data. Events outside the markers were rejected.

For the C_{SS} data where the target was rotated by 37.5° with respect to the incident beam, the target projections were even more important. Figure 5.12a shows the x-target projection for the $634MeV$, C_{SS} data, for a 35° spectrometer angle. Events originating from the magnet coils and cryostat can easily be picked out as the smaller peak on the right side of the large peak near $x = 0$. The final cuts which were used are also shown.

For the case of a rotated target and a 10° spectrometer angle (Fig.5.12b) the x-target projection looked somewhat different. Rather than having events which originated from the magnet coils (or cryostat) clearly separated from those originating in the target, the

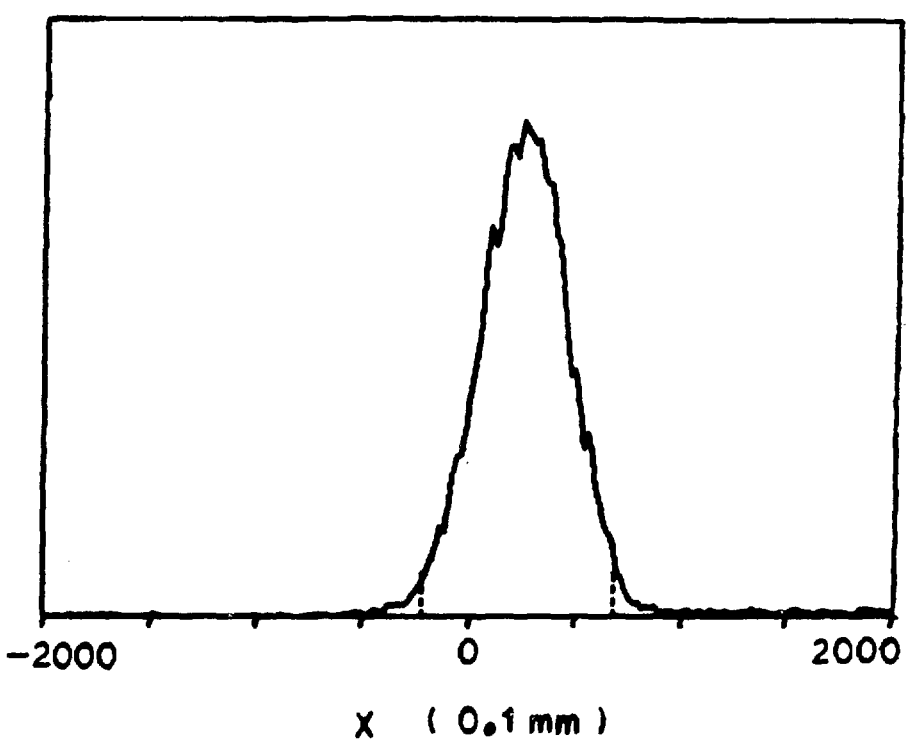

Figure 5.11: The x-target projection cuts used for the $634 MeV$ data.

distribution was continuous with a long tail on the large-x side of the peak. Additionally, at the 10^o spectrometer setting, because the angular acceptance of the spectrometer was so large, the unscattered portion of the beam went through the spectrometer. The beam therefore also contributed to the tail in the distribution.

In order to separate the two sets of events, a pair of two-dimensional histograms were set up. Figure 5.13a shows one of these two-dimensional histograms where the x-target projection is plotted against the x-position in P1. It can be seen that there is a large band of uncorrelated events (zero slope), which are assumed to originate from or near the target. There is also a band of events with large non-zero slope. These events were assumed to come primarily from the unscattered part of the beam. Shown in the figure are boxes which are two-dimensional cuts on the data. Events outside the boxes were rejected. A similar "box-cut" was made for the x-target projection and the P0 x-position. A logical OR between the two sets of box-cuts was required so as not to eliminate an event which missed the P0 acceptance but was reconstructed using only P1.

Figure 5.13b shows the x-target projection after the P0 and P1 box-cuts have been passed. An ordinary cut was then made on this distribution. These cuts are also shown in the figure.

Cuts on the magnet center-plane matching were made in a fashion identical to that discussed for the target projections. Figure 5.14 shows the cuts used for the $484MeV$,

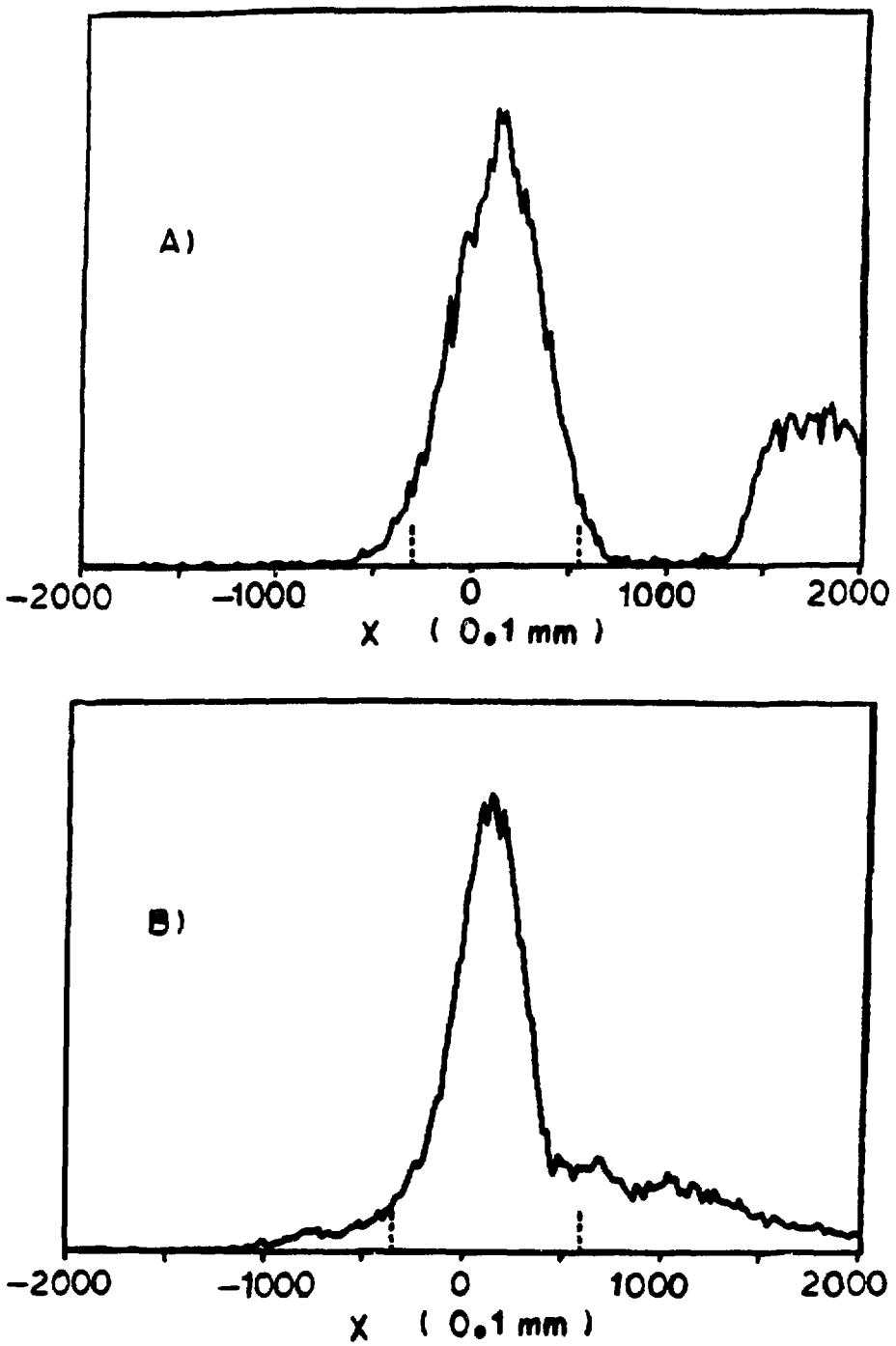

Figure 5.12: a) The x-target projection for a rotated target and 35° spectrometer angle. b) The x-target projection for a rotated target and a 10° spectrometer angle.

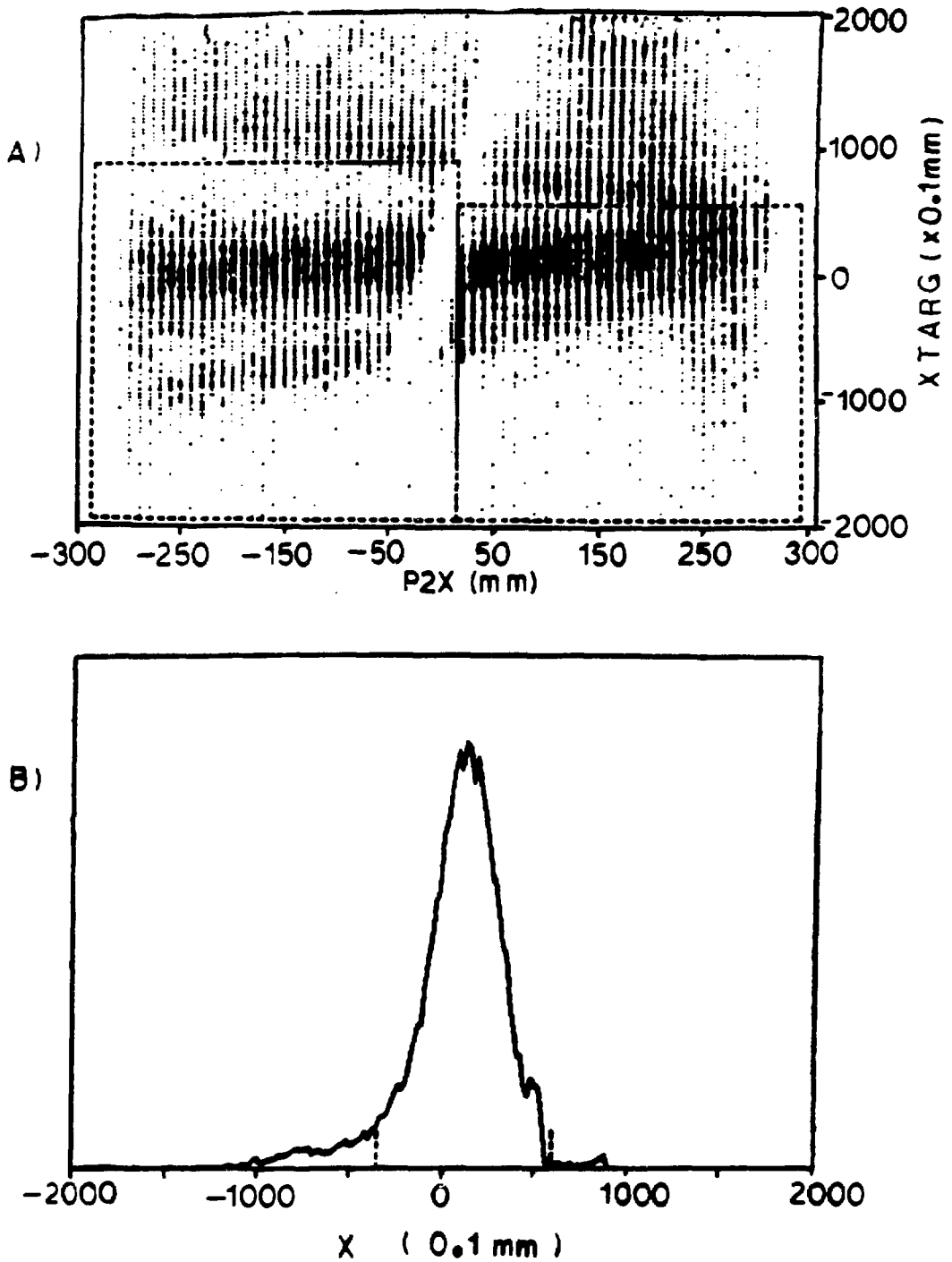

Figure 5.13: a) Two-dimensional histogram of the P1 x-position vs. the x-target projection b) The x-target projection for only the events passing the box-cuts.

C_{SS} data with a spectrometer angle of 10^o.

The cuts on the particle mass were very loose. The limits for these were placed with a minimum at $500 Mev/c^2$ and a maximum at $1500 Mev/c^2$ for all sets of data analyzed. These values were chosen so as to eliminate the deuteron background, but keep all protons (background included). Figure 5.15 shows the particle mass distribution with cuts.

5.8 Calculation of the Correlation Parameters

The spin-spin correlation parameters were calculated bin-by-bin as follows:

$$C_{ij} = \frac{1}{p_B p_T} \frac{P' - A'}{P' + A' - 2C'} \tag{5.24}$$

where P' is the total counts, elastic and background, in the missing-mass for parallel spins. A' is the total counts for antiparallel beam and target spins, normalized by the beam current so as to eliminate any artificial asymmetry. C' is the normalized carbon background described below. p_B and p_T are the beam and target polarizations, respectively. The statistical error for C_{ij} is given by

$$\begin{aligned}
(\delta C_{ij})^2 &= (\delta A')^2 \left[-\frac{1}{P' + A' - 2C'} - \frac{P' - A'}{(P' - A' - 2C')^2} \right]^2 \\
&+ (\delta P')^2 \left[\frac{1}{P' + A' - 2C'} - \frac{P' - A'}{(P' - A' - 2C')^2} \right]^2 \\
&+ (\delta C')^2 \left[\frac{2(P' - A')}{(P' - A' - 2C')^2} \right]^2
\end{aligned} \tag{5.25}$$

where $\delta A' = \sqrt{A'}$, $\delta P' = \sqrt{P'}$, and $\delta C' = \sqrt{\alpha C'}$, where α is discussed below.

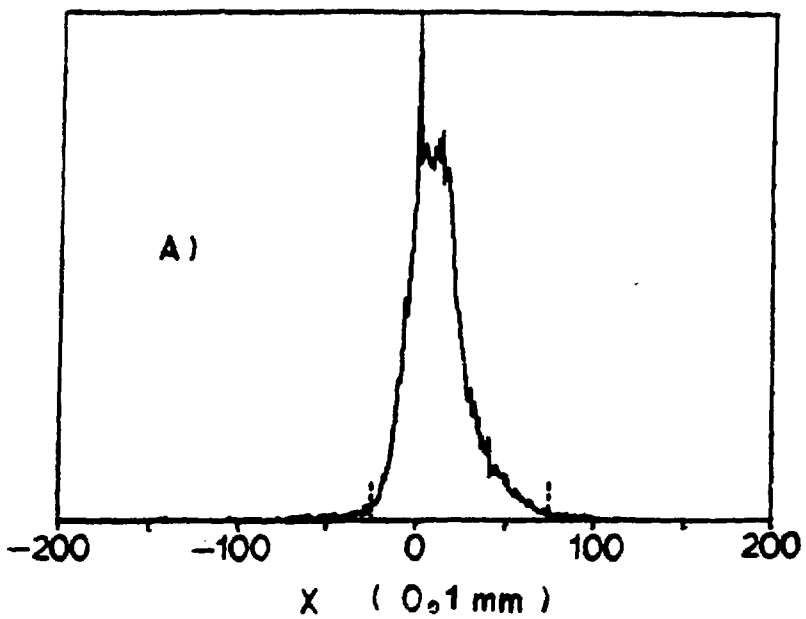

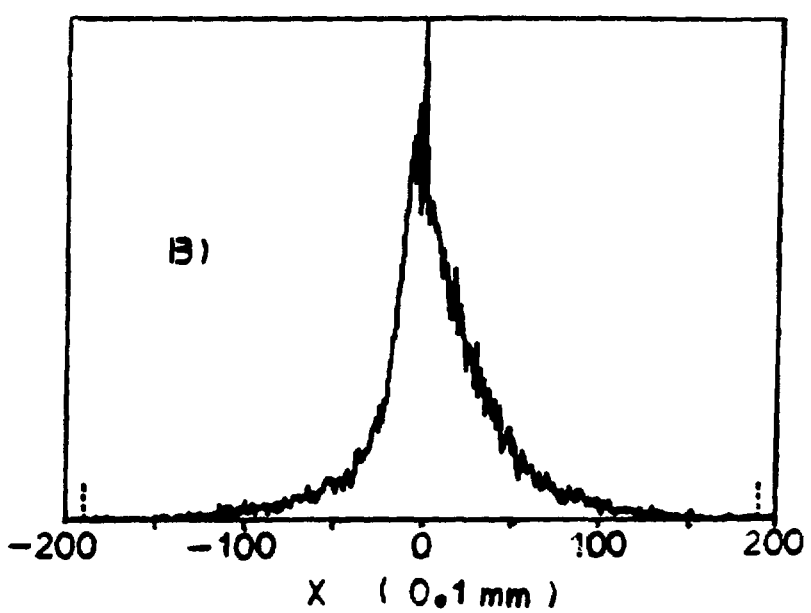

Figure 5.14: a) Typical x magnet center-plane matching with cuts. b) The y magnet center-plane matching with cuts.

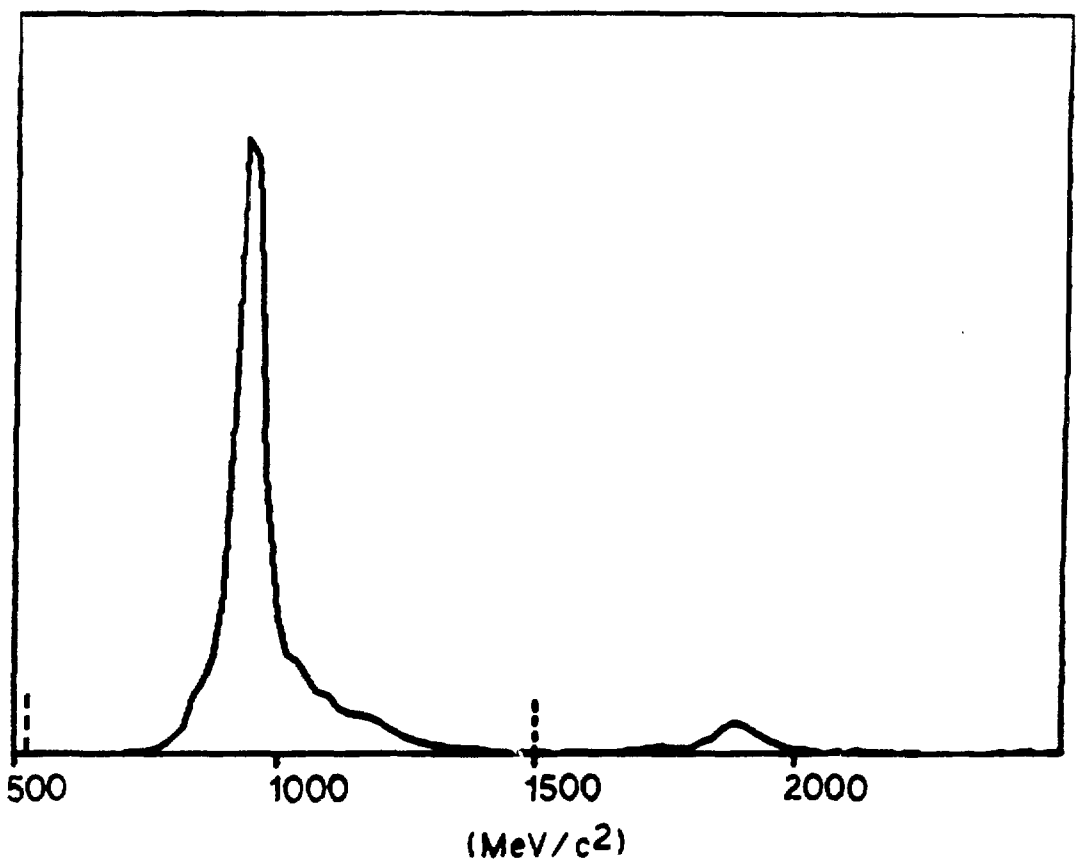

Figure 5.15: The particle mass distribution with loose cuts used to eliminate the deuteron background.

The background was subtracted in two steps. Figure 5.16a shows the missing-mass distribution for a particular 5^o c.m. angle bin. Figure 5.16b shows the missing-mass distribution for scattering off a carbon target for the same angle bin. If one overlays Fig. 5.16a and Fig. 5.16b, as is shown in Fig. 5.17, it can be seen that there is good matching of the background, however only on one side of the elastic peak. Because of this the carbon was normalized such that $P' - C' = 0$ (or $A' - C' = 0$) in the wings of the elastic peak. Therefore, $C' = \alpha C$ where C is the measured carbon and $\alpha = (P' + A')/2C$. Figure 5.18a shows the missing-mass distribution after the normalized carbon has been subtracted.

The final step of the background subtraction consisted of fitting either a linear or quadratic shape to the remaining residual background. Figure 5.18b shows a typical quadratic fit. The events between markers 1-2 and 3-4 were used to define the background shape for the fit. A study was done which compared the values of C_{ij} bin-by-bin and their statistical errors to determine the systematic error introduced by using a linear fit as compared to a quadratic fit. It was found that both the centroid of C_{ij} and the statistical error varied by no more than $1 - 2\%$ between the two orders of fitting. It should be mentioned also that a study of the 1-2-3-4 marker positions for the fit for each angle bin was done. The marker positions which gave the smallest statistical error bars were chosen.

The spin-spin correlation parameters were calculated by two methods. The first

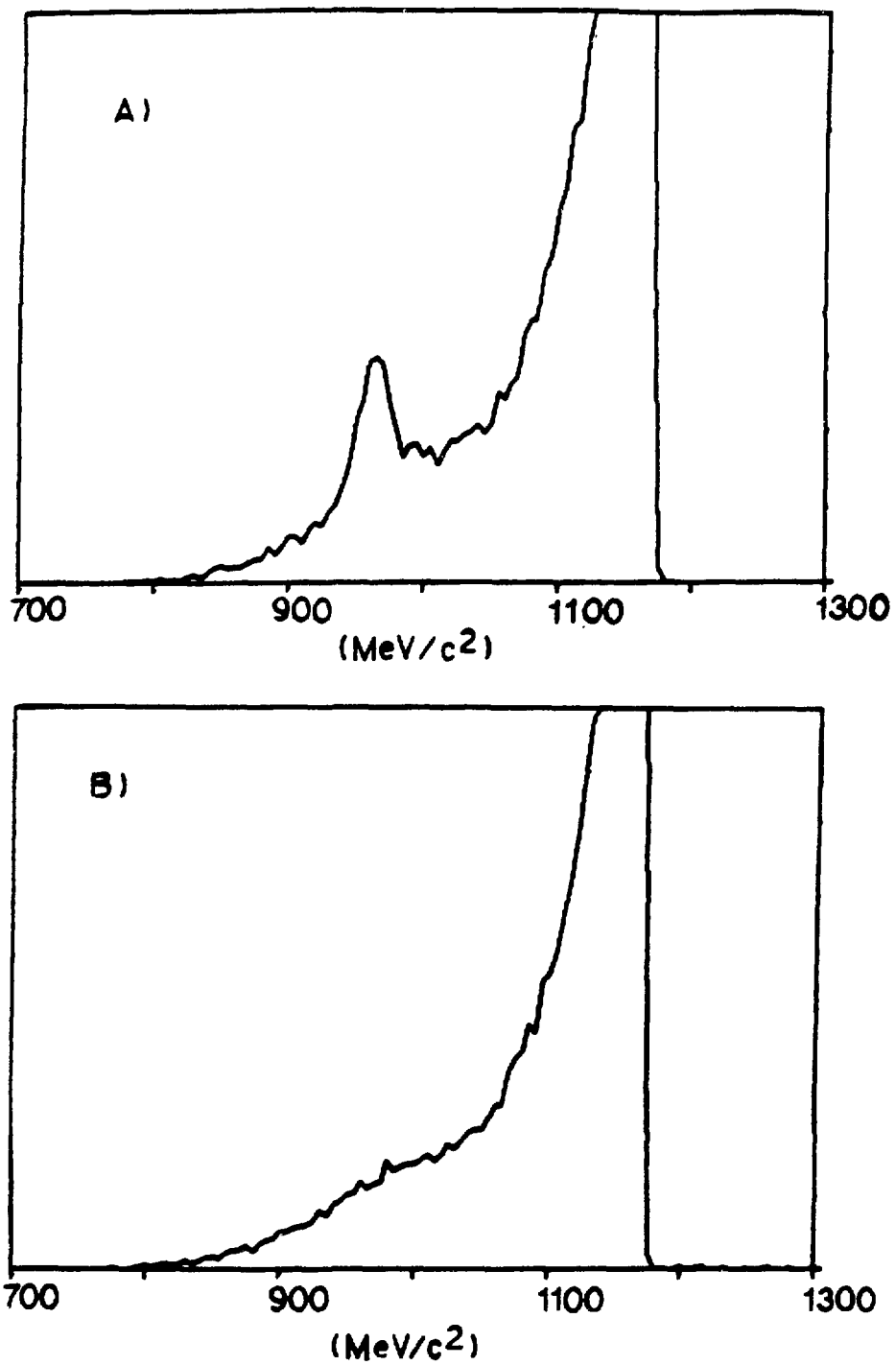

Figure 5.16: a) Missing-mass distribution for a 5° c.m. angle bin. b) Missing-mass for scattering of a carbon target for the same bin.

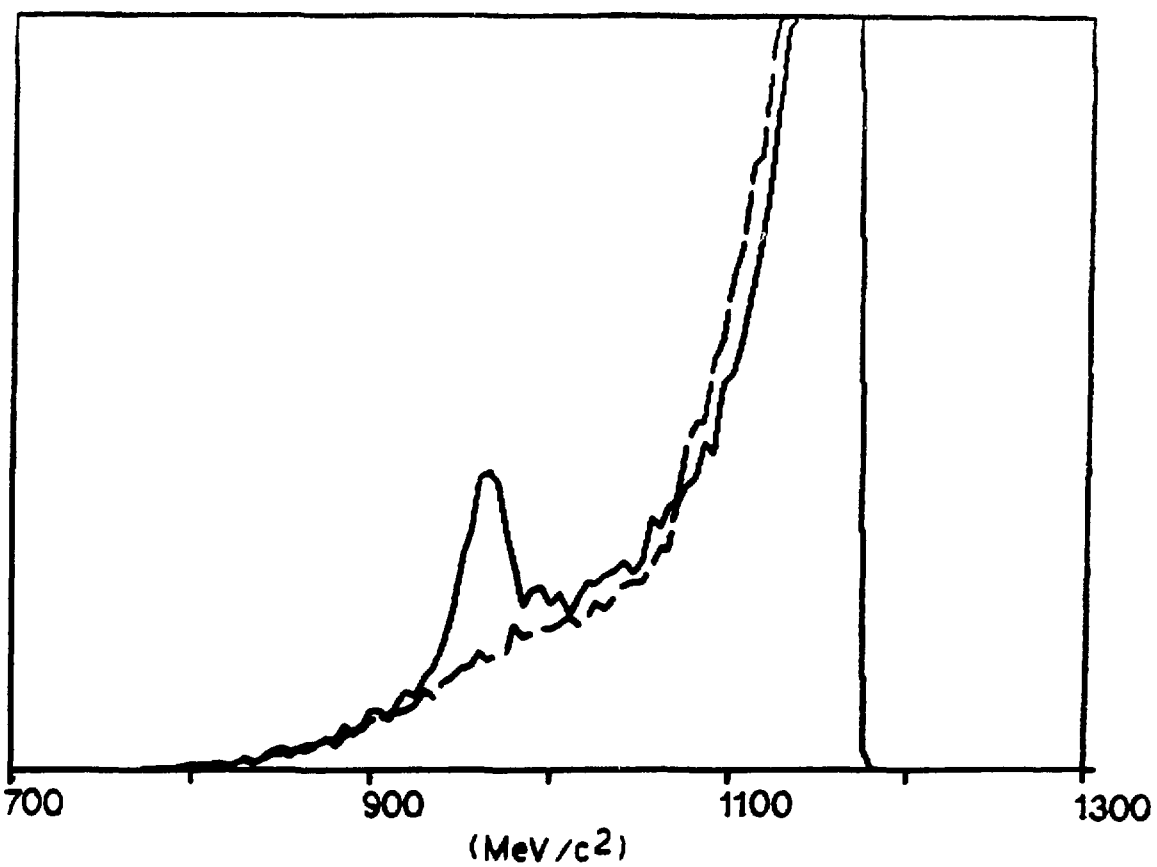

Figure 5.17: Overlayed polarized and carbon background data. The dashed line is the carbon data. There is good matching in the low missing-mass side of the peak.

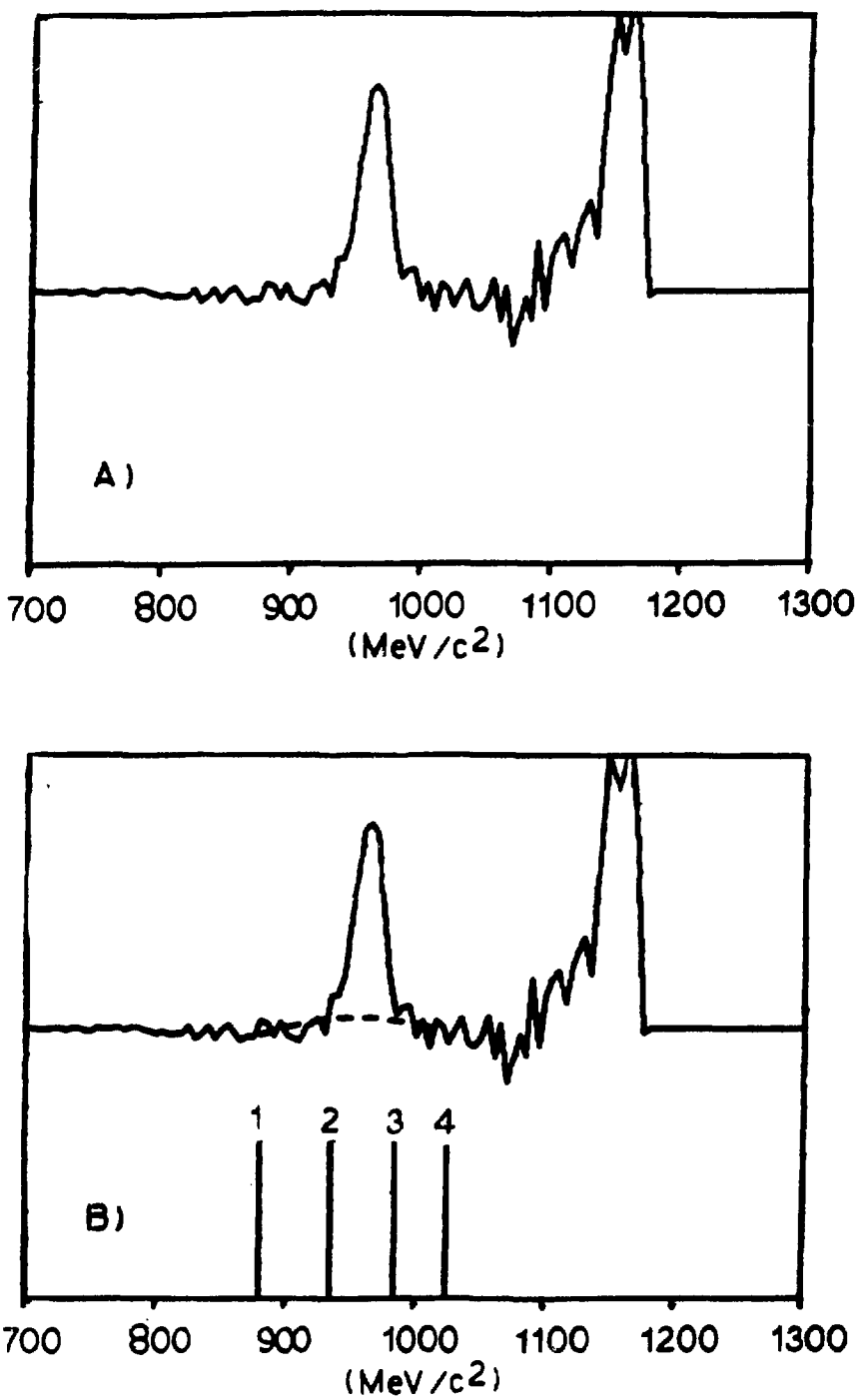

Figure 5.18: a) Missing-mass distribution after the normalized carbon background subtraction. b) Subtraction of the residual background by fitting of a polynomial shape determined by the background in the wings near the peak.

method consisted of calculating C_{ij} for each individual run and taking an average weighted by the statistical errors of all the runs. This method was used to find "bad" runs from a set of several runs where data were taken under identical experimental conditions. The individual χ^2 with respect to the weighted average for each run was calculated in addition to the χ^2/ degree of freedom (χ^2/df) for the entire set of runs. If a particular angle bin had a χ^2/df of low confidence level, then the individual runs in that set were examined for irregularities such as poor detector performance. If a run was suspect, usually indicated by an individual χ^2 of low confidence level, a χ^2 with respect to the average over all angle bins for that run was calculated. This χ^2 value was then compared to the χ^2 distribution for all other runs in that set. Less than 1% of the total runs were rejected on this basis.

The second method of determining C_{ij} consisted of summing all the events of the individual runs for each bin, with the "bad" runs removed, and then calculating the parameter. This method was used to calculated all the C_{ij} values quoted in this dissertation.

The two methods discussed above should in principle be statistically identical and yield identical results. It was found that the two methods agreed to within one standard deviation for all the angle bins.

5.9 Corrections for Systematic Effects

It was necessary to correct the data for various known sources of systematic error. Perhaps the most important of these was the presence of undesirable spin components in both the beam and the target.

A detailed study of the neutron beam spin as measured by the polarimeter JPAN was done by H. Spinka of Argonne National Laboratory [Sp-88b]. By making polynomial fits to the magnet sweeps used to set the spin precession magnets, it was possible to determine the beam spin components to within $\pm 1\%$. As a result of this study it was found that both the C_{LL} and C_{SL} measurements were actually a linear combination of the two. From this study it was also possible to determine the proton spin components just upstream of the LD_2 target. These components were used to determine the beam polarization from Eqn. 4.8, using the measured K_{LL} and K_{NN} values.

The actual measured quantities, $C_{\sigma L}$ and $C_{\lambda L}$, are then given as linear combinations of C_{LL} and C_{SL} by

$$C_{\sigma L} = aC_{LL} + bC_{SL} \tag{5.26}$$

$$C_{\lambda L} = dC_{LL} + eC_{SL} \tag{5.27}$$

where $a = \cos\theta_1$, $b = \sin\theta_1$, $d = \cos\theta_2$, and $e = \sin\theta_2$. Here θ_1 and θ_2 are the angles of the beam spin with respect to the $\hat{L}$-direction for the two cases, respectively. Table 5.2 shows the values of a, b, e, and d used. These equations can be inverted to give the

pure C_{SL} and C_{LL} in terms of the measured quantities where

$$C_{LL} = \frac{b}{bd - ea}\left(C_{\lambda L} - \frac{e}{b}C_{\sigma L}\right) \tag{5.28}$$

and

$$C_{SL} = \frac{1}{bd - ea}\left(dC_{\sigma L} - aC_{\lambda L}\right) . \tag{5.29}$$

Therefore, in order to determine the pure spin-spin correlation parameters these equations were solved simultaneously.

Table 5.2: Spin component admixture coefficients for the C_{LL} and C_{SL} data.

Energy	a	b	e	d
$634MeV$	0.1891	-0.9820	0.9983	0.0576

The error in C_{LL} is given in quadrature by

$$\begin{aligned}\sigma_{LL}^2 &= \left(\frac{\delta C_{LL}}{\delta C_{\sigma L}}\right)^2 \sigma_{\sigma L}^2 + \left(\frac{\delta C_{LL}}{\delta C_{\lambda L}}\right)^2 \sigma_{\lambda L}^2 \\ &+ \left(\frac{\delta C_{LL}}{\delta a}\right)^2 \sigma_a^2 + \left(\frac{\delta C_{LL}}{\delta b}\right)^2 \sigma_b^2 + \cdots\end{aligned} \tag{5.30}$$

where $\sigma_{\sigma L}$ and $\sigma_{\lambda L}$ are the statistical errors of $C_{\sigma L}$ and $C_{\lambda L}$, respectively. A similar expression holds for σ_{SL}^2. The errors in the coefficients (angles) a, b, d, and e are given by σ_a, σ_b, etc. and are of order $\pm 1\%$. Since $\sigma_{a,b,c,d}^2 \ll \sigma_{\lambda L}^2$ or $\sigma_{\sigma L}^2$, then to lowest order

$$\sigma_{LL}^2 = \frac{1}{(bd - ae)^2}(b^2\sigma_{\lambda L}^2 + e^2\sigma_{\sigma L}^2) \tag{5.31}$$

and

$$\sigma_{SL}^2 = \frac{1}{(bd - ae)^2}(a^2\sigma_{\lambda L}^2 + d^2\sigma_{\sigma L}^2) . \tag{5.32}$$

For the C_{SL} measurement, there was an additional correction which needed to be made due to the precession of the neutron beam spin by the HERA field (as discussed in Appendix D). The $\hat{S}$ component of the neutron beam spin was precessed in the $+\hat{N}$-direction. Additionally, the scattering plane was rotated because the outgoing proton trajectory was changed by the field.

A computer program was written which calculated the net rotation/precession angle, θ_{Net}, using a measured field map for the HERA magnet. This angle was calculated to be the difference between the precession angle, θ_p, and the scattering plane rotation angle, θ_R, where $\theta_{Net} = \theta_p - \theta_R$. Once θ_{Net} was known, the true value of C_{SL} could be determined from

$$(C_{SL})_{corrected} = C_{SL}\cos\theta_{Net} + C_{NL}\sin\theta_{Net} \tag{5.33}$$

where $(C_{SL})_{corrected}$ is the value corrected for an admixture of C_{LL}. However, from symmetry arguments C_{NL} is zero, giving

$$C_{SL} = \frac{(C_{SL})_{corrected}}{\cos\theta_{Net}} \, . \tag{5.34}$$

The angle θ_{Net} was typically on the order of $10 - 15^{o}$. The errors on C_{SL} were also scaled by $1/\cos\theta_{Net}$ to give the final quoted errors.

For the C_{SS} measurements, the situation was complicated further because the target was rotated by 37.5^{o} with respect to the $+\hat{L}$-direction. Appendix E gives a detailed derivation of the correction equation for the C_{SS} measurements. Only the final expres-

sion will be given here. The measured quantity, $C_{\sigma\sigma}$, was a linear combination of many other pure spin-spin correlation parameters due to the effects of the HERA magnetic field. An expression for $C_{\sigma\sigma}$ can be written in a fashion similar to that used earlier in Eqns. 5.26–5.27 where

$$C_{\sigma\sigma} = aC_{SS} + bC_{NN} + dC_{LL} + eC_{SL} \tag{5.35}$$

and

$$\begin{aligned}
a &= -\sin\theta_T\cos\theta_R[-\cos\theta_R\cos\theta_p\cos\theta_T\sin(\theta_B-\theta_T) \\
&- \cos\theta_R\sin\theta_T\cos(\theta_B-\theta_T)+\sin\theta_R\sin\theta_p\sin(\theta_B-\theta_T)] \\
b &= -\sin\theta_T\sin\theta_R[-\sin\theta_R\cos\theta_p\cos\theta_T\sin(\theta_B-\theta_T) \\
&- \sin\theta_R\sin\theta_T\cos(\theta_B-\theta_T)-\cos\theta_R\sin\theta_p\sin(\theta_B-\theta_T)] \\
d &= \cos\theta_T[-\cos\theta_p\sin\theta_T\sin(\theta_B-\theta_T)+\cos\theta_T\cos(\theta_B-\theta_T)] \\
e &= -\sin\theta_T\cos\theta_R[-\cos\theta_p\sin\theta_T\sin(\theta_B-\theta_T)+\cos\theta_T\cos(\theta_B-\theta_T)] \\
&+ \cos\theta_T[-\cos\theta_R\cos\theta_p\cos\theta_T\sin(\theta_B-\theta_T)-\cos\theta_R\sin\theta_T\cos(\theta_B-\theta_T) \\
&+ \sin\theta_R\sin\theta_p\sin(\theta_B-\theta_T)] \ .
\end{aligned}$$

The subscripts on the angles are as follows: T for target rotation angle, R for rotation angle of the scattering plane due to HERA, p for the neutron spin precesssion angle, and B for the initial angle of the beam spin with respect to the $\hat{L}$-direction. This equation was then solved for C_{SS}. Table 5.3, below, gives the average spin component admixture

coefficients used for the C_{SS} data at the three energies:

Table 5.3: Spin component admixture coefficients for the C_{SS} data.

Energy	a	b	d	e
$484MeV$	0.475	0.088	0.139	-0.744
$634MeV$	0.506	0.064	0.163	-0.809
$788MeV$	0.528	0.050	0.178	-0.824

To lowest order the error in C_{SS} was calculated as for Eqn.5.30 above by taking partial derivatives with respect to $C_{\sigma\sigma}$, C_{NN}, C_{LL}, and C_{LS}. The error is given by

$$\sigma_{SS}^2 = \frac{1}{a^2}(\sigma_{\sigma\sigma}^2 + b^2\sigma_{NN}^2 + d^2\sigma_{LL}^2 + e^2\sigma_{LS}^2) \; . \tag{5.36}$$

It should be noted, although it is obvious from Eqn. 5.35 above, that in order to have been able to extract a pure C_{SS} value, it was necessary to have the values of the other pure spin-spin parameters and their statistical errors at the same scattering angles. Therefore, to extract the pure C_{SS} values, C_{LL} and C_{LS} values from the thesis of M.W. Rawool were used. The values predicted from the single-energy phase-shift solutions (C500, C650, and C800) of the SAID program [Ar-87] were used for C_{NN}, since no C_{NN} data were yet available at the energies and angles where we measured C_{SS}.

CHAPTER 6 THE MONTE-CARLO SIMULATION

6.1 Program Description

A Monte-Carlo program was written in order to reduce the systematic errors caused by the analyzer program. Development of this program was started by C. Luchini of New Mexico State University.

The analyzer assumes, for example, that the interaction always occurs at the center of the target and makes no correction for the effects of the polarized target magnetic field. In addition, the quality of its parameterization of the magnetic field of the spectrometer was not known.

These systematic errors manifested themselves in many ways, one being reduced resolution of the neutron missing-mass peak. The Monte-Carlo program was used to determine quantities to use to correct the proton scattering angle and to check the parameterization of the magnetic field of the spectrometer. The determination of these correction factors will be discussed later.

The Monte-Carlo program, DICE, simulates the entire target-spectrometer system.

The target-spectrometer system, as discussed earlier, consisted of the polarized target and magnet (HERA), 19 detector planes, and the spectrometer magnet. Random elastic-scattering events are generated one by one, and the recoil proton is traced first through the HERA magnetic field and then through the spectrometer system. The initial momentum, target interaction point, detector-plane positions, and time of flight (TOF) for each event which makes it through the entire spectrometer system, is written to an output file. A listing of the program and subroutines can be found in Appendix C. The details of this program are as follows:

A Gaussian distribution for the scalar momentum of the neutron beam is generated in the subroutine INIT_P. The full-width-at-half-maximum (FWHM) of the actual beam is energy-dependent, and the experimentally measured values as determined by Bjork [Bj-75] are used as the limits for the generated distributions at the three measurement energies: 484, 634, and 788 MeV. The distributions are generated out to one standard deviation only. Figure 6.1 shows examples of the generated distributions.

In order to determine the x, y, and z components of the beam momentum, θ_b is generated as a Gaussian distribution and ϕ_b is generated uniformly (so, for example, p_x and p_y have the same distributions). The limits for θ_b and ϕ_b were determined by the known solid angle of the neutron beam collimator. These generated values of θ_b and ϕ_b are then used to calculate the beam particle momentum components in the laboratory

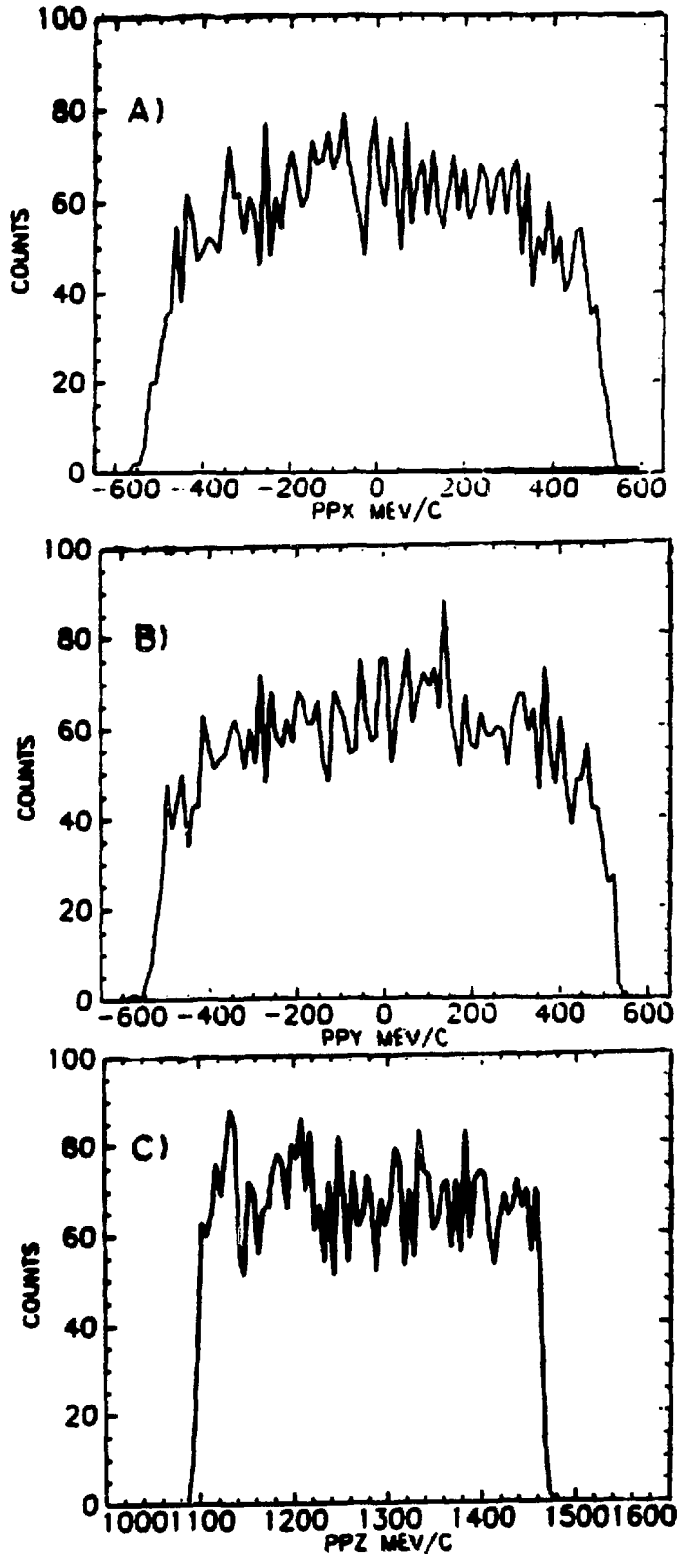

Figure 6.1: Generated Gaussian momentum distributions: a) p_x. b) p_y. c) p_z.

frame in the usual fashion:

$$\begin{aligned} p_x &= p \sin\theta_b \cos\phi_b \\ p_y &= p \sin\theta_b \sin\phi_b \\ p_z &= p \cos\theta_b \ . \end{aligned} \tag{6.1}$$

The components are then written to an internal record.

The interaction point in the target is also generated randomly in the subroutine INIT_P. Since the target is cylindrical, ρ_t, θ_t, and z_t are generated and then converted to Cartesian coordinates. The radius, ρ_t, is generated as a Gaussian distribution (with cutoff at $\rho = R$). This is done to model the reduced interaction probability near the edge of the target as compared to the target center, since the actual beam was approximately Gaussian. Theta is generated uniformly from 0 to 2π radians, and z_t is generated over the range $-L \leq z_t \leq L$, where L is half the target length.

Once the components of the neutron momentum are determined, the proton momentum is determined in the subroutine TARGET. If the scattering angles θ and ϕ are known, then the proton momentum is determined simply from kinematics. In order to maximize the efficiency of the overall Monte-Carlo program, only scattering angles in a predetermined range are generated. The angles generated are similar to "gunner's angles" (elevation and azimuth), where θ' is the angle with respect to the z-axis in the xz-plane (see Fig. 6.2) and ϕ' is the angle above or below that plane. The

transformation equations relating θ' and ϕ' to the usual spherical coordinates are as follows:

$$\cos\theta = \cos\theta' \cos\phi' \tag{6.2}$$

$$\sin\phi = \frac{\sin\phi'}{\sin\theta} . \tag{6.3}$$

These coordinates were chosen because of the ease with which they allow one to define the solid angle for scattering to a rectangular plane. However, because of the presence of the polarized target magnetic field and the fact that not all scattering occurs at the target center, not all events generated within the chosen θ' and ϕ' limits hit the first detector plane (S1).

The effect of the HERA magnet is to cause the particles to spiral out of the target. For a uniform distribution in θ' and ϕ', this produces a distorted distribution in x and y at S1 rather than the otherwise expected rectangular distribution for a zero field. Scattering from a point other than the target center also leads to a spread in x and y. When the Monte-Carlo program was run, a particular range of θ' and ϕ' was chosen for each energy-spectrometer angle combination and read from an input data file. Diagnostic dot-plots of the proton xy-position in S1 were then made to be sure that a uniform distribution was being generated over the entire plane (Fig. 6.3a). From the above transformation equations, one obtains θ and ϕ.

In order to reduce the computer processing time, it is also possible to choose the

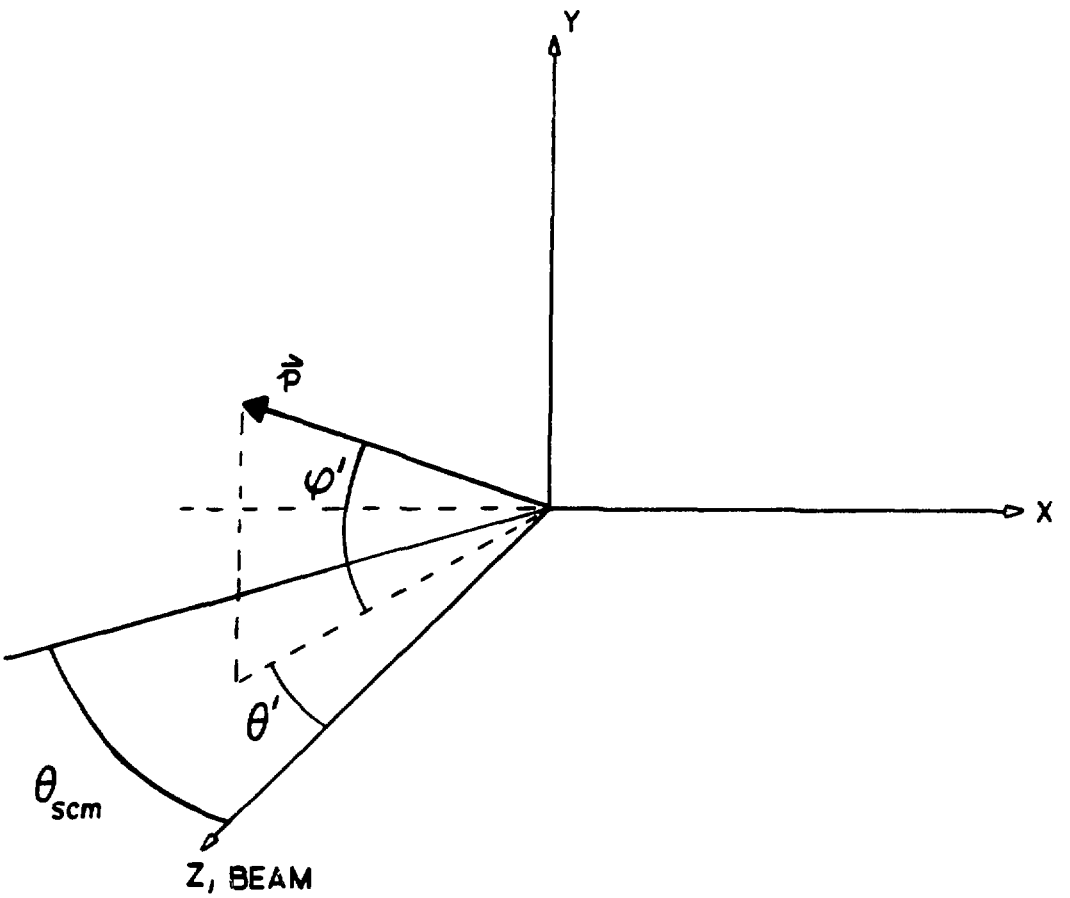

Figure 6.2: "Gunner's" angles coordinate system used to generate event distributions.

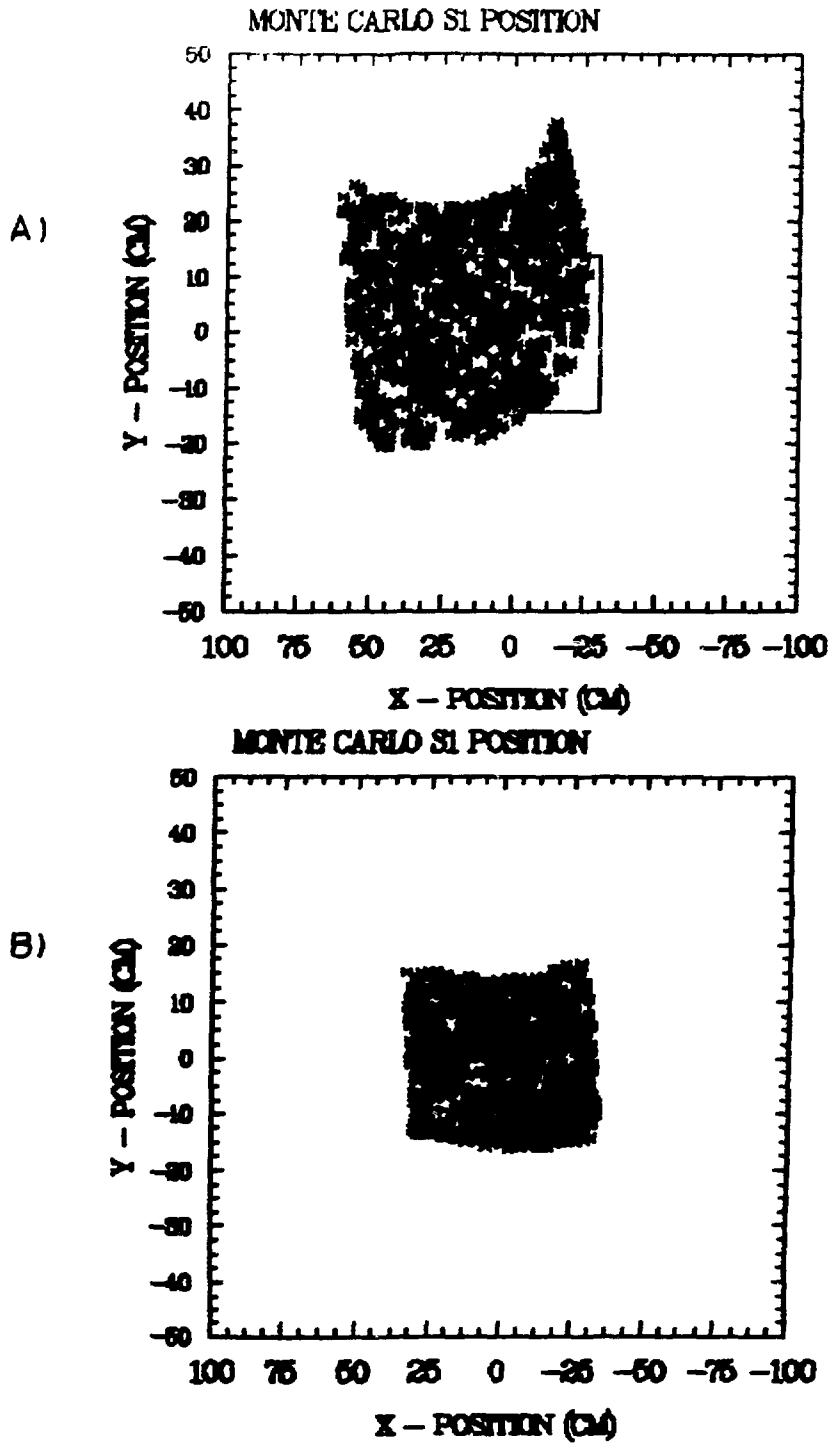

Figure 6.3: a) Generated event distribution of xy-positions in the S1 detector plane for unspecified angle slopes. b) Event distribution with correct choice of angle slopes.

upper and lower angle-slopes ($\frac{d\phi}{d\theta}$) for the scattering distribution. These slope limits are also read in from the input file. A test on the randomly generated ϕ' is performed for the upper boundary, where if

$$\phi' > \phi'_{max} + \frac{d\phi}{d\theta}(\theta - \theta_{min}), \tag{6.4}$$

the angle is rejected and a new angle is generated. A similar test is performed on the lower boundary. Figure 6.3b shows a generated distribution where the proper choice of upper and lower angle slopes has be made.

The proton momentum is next determined by the kinematics subroutine RECOIL_KIN. The proton mass, the beam momentum ($\vec{p} = 0$ for the target), and the proton scattering angle (θ) are passed to RECOIL_KIN and the final proton momentum is then passed back. The proton momentum is then passed to the subroutine P_TRACE, via a COMMON block, which then calls the ray-tracing subroutines, THERA2 and MANETR, and determines the position of the proton in each detector plane.

The subroutine which traces the proton through the HERA field was supplied with the magnet and is called, THERA2. It was modified specifically for our experiment. Changes were made to allow for an energy loss calculation using the Bethe-Bloch equation [Fr-74]

$$\frac{dE}{dx} = 4\pi \frac{N\rho}{A} Z^2 \left(\frac{e^2}{m_e c^2}\right)^2 \left(\frac{m_e c^2}{\beta^2}\right) \left\{ \ln\left[\frac{2m_e c^2 \beta^2}{I(1-\beta^2)}\right] - \beta^2 \right\} Z_{med} \tag{6.5}$$

where

$Z_{med} = 6$ for Carbon

$N = 6.0225 \times 10^{23}$ atoms/mole

$\rho = 2.265\ gm/cm^3$;density of Carbon

$A = 12.01$ gm/mole

$Z = 1$ for the proton

$(\frac{e^2}{m_e c^2}) = r_0 = 2.8178 \times 10^{-13}$ cm ,m_e is the electron rest mass.

$m_e c^2 = 0.511$ MeV

$\beta = \frac{v}{c}$ -ratio for the ionizing particle, $\beta = (1 + \frac{m_p^2}{p_p^2})^{-1/2}$

m_p is the proton rest mass and p_p is the proton scalar momentum.

$I = 9.1Z(1 + 1.9Z^{-0.67}) \times 10^{-6}$ MeV.

To correct for energy loss, the position where the proton leaves the target is calculated. Using this, and the position of the target interaction point, a distance Δx travelled in the target material is calculated (it is assumed the particle travels in a straight line in the target). Therefore, the energy loss in the target is simply given by

$$\Delta E = \frac{dE}{dx}\Delta x\ . \tag{6.6}$$

A new total energy E' for the proton is calculated by

$$E' = E - \Delta E \tag{6.7}$$

where $E = p_p^2 + m_p^2$ is in natural units ($\hbar = c = 1$). And a new scalar momentum p' by

$$p'^2 = E'^2 - m_p^2\ . \tag{6.8}$$

The direction (θ and ϕ) of the proton momentum at the point of leaving the target is determined from the momentum components at that point in the usual manner:

$$\theta = \arccos\left(\frac{p_z}{p}\right) \tag{6.9}$$

$$\phi = \arctan\left(\frac{p_y}{p_x}\right) . \tag{6.10}$$

New components of momentum are calculated using p', θ and ϕ. These are used in the ray tracing.

Additionally, the first two points along the trajectory are used to project back to the $z = 0$ plane to determine the x and y-target projections, and the $x = 0$ plane for the z-target projection. These projections are calculated by a call to the subroutine PROJECT_IT. These projected x,y,z values are also written to an internal record.

THERA2 was also modified to determine if the proton passes through a detector plane, since for small spectrometer angles some detectors are in the fringe field of the HERA magnet. THERA2 was written initially for ray-tracing in a polarized target where the polarization direction is always along the beam direction (z-axis). In our experiment, the HERA magnet was rotated to different orientations with respect to the beam. As a result, it is necessary, for each orientation, to first rotate the laboratory coordinate system so that the target polarization is along the z-axis before calling the subroutine THERA2 (the original coordinate system could be used and the HERA field map rotated for each particular orientation, but since the field map was measured

in cylindrical coordinates it seemed easier to do the ray tracing in this new reference frame and leave the field map unaltered). The origin of this coordinate system is at the target center with x pointing up and y pointing to the right. Both the position and the momentum of the proton are transformed. These coordinate transformations are accomplished by the subroutine HERA_ROT. After the proton is traced through the HERA field, the coordinates are rotated back.

THERA2 uses the initial proton momentum and a data file, HERA.DAT, containing the measured magnetic field map of the polarizing magnet, to find a new postion and momentum for a fixed interval of distance traveled: $dl = 2.0$ centimeters. THERA2 traces the proton out to a radius of 180 cm, the limit of the measured field map. In this subroutine, a check is made on the z-position of the proton with respect to the SCM105 magnet center. Before this check can be made, however, the coordinates must be rotated back to the laboratory system. Then the position must be transformed to the coordinate system used by the analyzer, whose origin lies at the center of the SCM105 magnet with the z-axis pointing downstream along the magnet axis, the x-axis pointing to the left, and the y-axis pointing up. This coordinate transformation is done in the subroutine HERASCM. The transformation consists of a clockwise rotation about the y-axis through the spectrometer angle, followed by a small translation along x' (see Fig. 6.4), and finally, by another small rotation about the y-axis. The translation and second rotation are small corrections for the fact that the spectrometer system was

never perpendicular to the proton recoil-angle, as marked on the floor by surveying in the experimental area. The amount of translation and second rotation are determined by the survey constants found for the particular setup used.

If the check shows that the z-position of the proton is greater than that of a detector plane, an interpolation subroutine, INTERP, is called. It interpolates back to the detector plane as follows: The proton position for z less than that of the plane is saved and used as one of the interpolation points. The other point used is at z greater than the plane. Then a subroutine CHKXY is called which checks to see if the xy-position lies within the limits for that particular detector. If the particle misses any plane, a flag, HIT, is set to "true" and the event is rejected. In this case, the program will start over again, generating a new beam momentum, etc. If the event is "good", the position in that plane is written to an internal record.

Should the particle make it through the the HERA field, control is then returned to the calling subroutine P_TRACE. A counter IPLANE keeps track of which detector planes have been encountered while in the HERA field. The counter also determines the next detector planes to be encountered outside of this field. After leaving the target, the proton position and momentum are transformed to the SCM105 coordinate system as described earlier. The rest of the ray-tracing calculations are done in this coordinate system.

The subroutine used to ray-trace outside of the target is called MANETR and was

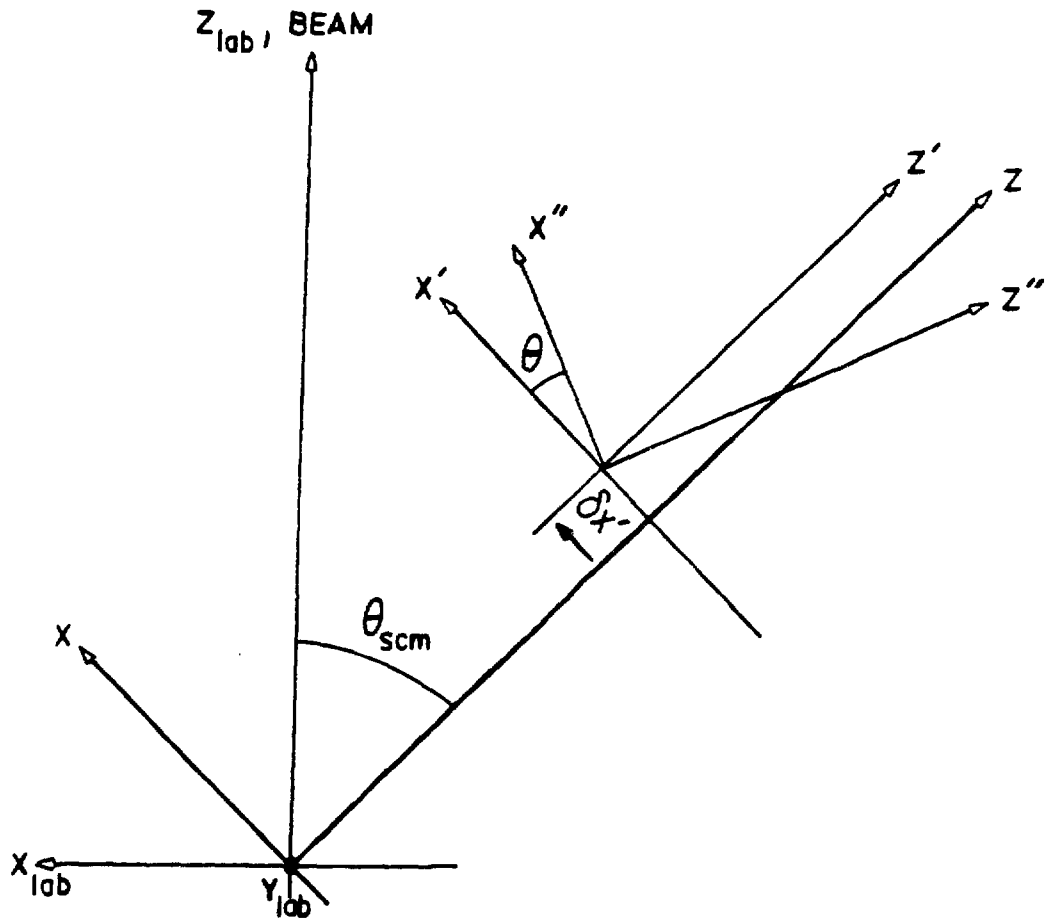

Figure 6.4: Diagram showing the relationship between the laboratory system and the rotated spectrometer system.

written by H. Spinka of Argonne National Laboratory [SP-85]. It uses a Runge-Kutta-Predictor-Corrector scheme to solve the problem of the motion of a charged particle through a magnetic field. MANETR uses magnetic field values for the SCM105 magnet, obtained by calling the subroutine SCM_HF3.

SCM_HF3 determines the magnetic field at an arbitrary point in space by doing a 3-dimensional least-squares fit and interpolation of the measured field map values. This fitting procedure will be discussed in the next section.

The proton time of flight (TOF) is also calculated. To do so, a short subroutine, TOF_INC, is called. It calculates a time increment, dt, using a calculated distance interval, dl, given by

$$dl = \sqrt{dx^2 + dy^2 + dz^2} \tag{6.11}$$

where

$$\begin{aligned} dx &= x_2 - x_1 \\ dy &= y_2 - y_1 \\ dz &= z_2 - z_1 \ . \end{aligned}$$

The initial position is (x_1, y_1, z_1) and (x_2, y_2, z_2) is the newly determined position. Therefore, $dt = dl/v$ where v is the proton velocity, determined by

$$v = c\left[1 + \left(\frac{m_p}{p}\right)^2\right]^{-1/2} \tag{6.12}$$

in units of cm/sec. Here p is the magnitude of the proton momentum determined after the energy-loss calculation and c is the velocity of light. The proton mass (m_p) is in units of MeV and the momentum is in units of MeV/c. The total TOF is determined by summing all the time intervals for the positions calculated between S1 and the hodoscope (S2).

As the proton trajectory is determined, checks on the z-position are made as discussed earlier. In similar fashion, the positions in all the remaining detector planes are determined by interpolation. As discussed earlier, the internal record containing the initial momentum, target interaction point, detector plane positions, and TOF is written to an output file only if an event makes it through the entire spectrometer system. Control is then returned to the main program and the next event is generated.

The final stage of the Monte-Carlo simulation incorporates the detector resolutions. The program, DICE, assumes the detectors have perfect resolution. The output file produced by DICE is read by another program called CHMBR_RES. CHMBR_RES adjusts the previously determined xy positions in each detector plane for the corresponding resolution of that detector. For the wire proportional chambers (P0,P2), the positions are made discrete; the position of the nearest wire is chosen. For the drift chambers (P1,P3,P4), a random error in the drift distance is introduced. A function, GAUSS, is called which uses a random number generator to calculate a drift distance. GAUSS generates a Gaussian distribution peaked at the x or y position (whichever is being

determined) in that plane and returns a distance within 2σ of that position. Sigma is the resolution of that detector. It should be noted that the program CHMBR_RES also calculates slopes and other quantities from the new detector positions, which would otherwise be determined in the analyzer subroutine HTRACK for real measured events. An output file is written in the Q-format by CHMBR_RES. This file is read into the analyzer to determine the correction factors first discussed at the beginning of this section.

6.2 Magnetic Field Fitting Procedure

The main subroutine called to determine the magnetic field components for an arbitrary point (x, y, z) within the SCM105 field map is SCM_HF3. When SCM_HF3 is first called, a check is made to determine where the particle is. There are four possibilities allowed:

1. The particle is in the field map. The field value will be determined in this case.

2. The particle is outside the field map region. The value $\vec{B} = 0$ will be passed back and the trajectory determined for that increment will be a straight line.

3. The particle is in the region of the poles or yoke material. This event is rejected.

4. The particle is in the magnet gap between the measured field map region and the pole or yoke. Here, the magnetic field is extrapolated.

The actual procedure followed for determining the field when the particle is in the field

map is discussed next.

The measured field map for the SCM105 magnet consists of a set of discrete points in space for which all three components of the magnetic field are known. As the particle is ray-traced through the SCM105 field, it is generally true that the endpoint for a given increment, dl, along the trajectory will not correspond to a measured point in the field map. Therefore, it is necessary to determine the value of the field at that point. A least-squares fit to the measured values with a one-point constraint, followed by a 3-dimensional interpolation, is used

It is assumed that each component of the field can be expressed as a truncated Taylor-series expansion of the form:

$$B_j(x,y,z) = B_{0j}(x_0,y_0,z_0) + \left.\frac{\partial B_j}{\partial x}\right|_{x_0}(x-x_0) + \left.\frac{\partial B_j}{\partial y}\right|_{y_0}(y-y_0) + \left.\frac{\partial B_j}{\partial z}\right|_{z_0}(z-z_0)$$

$$+ \left.\frac{1}{2}\frac{\partial^2 B_j}{\partial x^2}\right|_{x_0}(x-x_0)^2 + \left.\frac{1}{2}\frac{\partial^2 B_j}{\partial y^2}\right|_{y_0}(y-y_0)^2 + \left.\frac{1}{2}\frac{\partial^2 B_j}{\partial z^2}\right|_{z_0}(z-z_0)^2 . \qquad (6.13)$$

Above, $j = 1,2,3$ for the components B_x, B_y, B_z respectively. The point (x_0, y_0, z_0) is the field map point nearest the point in space where the field is to be determined. B_{0j} is the value of the field at this nearest point and is the zeroth-order term in the expansion above. It should be noted that second-order cross-terms involving, for example, $(x - x_0)(y - y_0)$ have been omitted. Least-squares fits are done separately along each of the three directions (x, y, z) to determine the higher order terms. To do so, it is assumed

that each component can be written as the following polynomial expression:

$$B_j(x) = \sum_{n=0}^{2}(a_n x^n) \quad j = 1,2,3\,. \tag{6.14}$$

Similar expressions are used for $B_j(y)$ and $B_j(z)$:

$$B_j(y) = \sum_{n=0}^{2}(b_n y^n) \tag{6.15}$$

$$B_j(z) = \sum_{n=0}^{2}(c_n z^n)\,. \tag{6.16}$$

Therefore, the derivatives of B_j are given by

$$\begin{aligned}
\left.\frac{\partial B_j}{\partial x}\right|_{x_0} &= a_1 + 2a_2x_0 \\
\left.\frac{\partial B_j}{\partial y}\right|_{y_0} &= b_1 + 2b_2y_0 \\
\left.\frac{\partial B_j}{\partial z}\right|_{z_0} &= c_1 + 2c_2z_0 \\
\left.\frac{\partial^2 B_j}{\partial x^2}\right|_{x_0} &= 2a_2 \\
\left.\frac{\partial^2 B_j}{\partial y^2}\right|_{y_0} &= 2b_2 \\
\left.\frac{\partial^2 B_j}{\partial z^2}\right|_{z_0} &= 2c_2\,.
\end{aligned} \tag{6.17}$$

To determine the a_n's, for example, the following expression for chi-square is minimized:

$$C = \sum_{i=1}^{M}\left[B_{ij} - \sum_{n=0}^{N} a_n x_i^n\right]^2 + \lambda F \tag{6.18}$$

where $F = \left[B_{kj} - \sum_{n=0}^{N} a_n x_k^n\right]$. The second term in Eqn. 6.18 is the constraint term, which causes the fitted curve to pass through the kth point, taken to be the middle of

the five fitted points. Two fits for x, y, and z are made for each point where $\vec{B}$ is to be found. Each fit is a fit to five points, the middle point in each case being the one lying to either side of the point where the field is to be determined. A weighted average of these fits is taken, as described below. In Eqn. 6.18, M is the number of points to fit, which was taken to be, five. N is the highest order of the polynomial ($N = 2$). And, the fit is constrained to go through the kth point. For a five-point fit, $k = 3$ (the middle point). Therefore, the coefficients are determined by solving a set of linear equations in $N + 2$ unknowns. The details of the solution can be found in Appendix C.

Once the two sets of coefficients for the fit are obtained, a weighted average of these is taken to determine the final coefficients. Should the error for any coefficient, a_i etc., in the two sets be zero, then the average would be weighted by the distance from the constrained points to the point of interest:

$$\langle a_i \rangle = a_{i1}(1 - d) + a_{i2}(d) \,. \tag{6.19}$$

Here, the distance between known field map points is taken to be one unit. Generally, the error is not zero and the average is weighted by both the distance to the nearest known field map points and the error in the coefficients. The expression used is

$$\langle a_i \rangle = \frac{\frac{a_{i1}}{(\Delta a_{i1})^2}(1 - d) + \frac{a_{i2}}{(\Delta a_{i2})^2}(d)}{\frac{1}{(\Delta a_{i1})^2}(1 - d) + \frac{1}{(\Delta a_{i2})^2}(d)} \,. \tag{6.20}$$

The same procedure, as outlined above, is used to determine the b_i's and c_i's.

Once all the coefficients have been calculated, Eqn. 6.17 is used to determine the

field component derivatives. These are then summed, along with the value for B_{0i}, in the Taylor-series expansion to give the fitted value of that component of the field (B_i).

6.3 Analyzer Corrections

The Monte-Carlo events, after having been written to a file in the Q-format, were read into the analyzer and processed as if they were real events. A modified version of the Data Summary (DST) analyzer was used. This analyzer processes data where the raw chamber information has already been decoded into xyz-positions in the coordinate system, as discussed before, with its origin at the SCM105 magnet center. It also requires the TOF information.

The DST analyzer uses the xyz-positions and only calls the subroutines which calculate the target projections, the momentum, the particle mass (using the momentum and TOF), and the scattering angles, in that order. Modifications were made to allow the Monte-Carlo data to be read. In particular, the data word was shortened since there was no spin information to be read for the Monte-Carlo data. Additionally, modifications were made to calculate various difference quantities. The following discussion describes the procedure which was used to correct the scattering angles (θ, ϕ), and the momentum (p). The basic correction procedure was as follows:

1. The difference (ΔX) between the known Monte-Carlo value and the value which the analyzer determines, using the chamber positions, was calculated for each event. A

histogram of this distribution was made along with histograms of each quantity to be corrected. Figure 6.5 shows histograms of the scattering angle ϕ. The upper histogram is a distribution of the Monte-Carlo generated angles, whereas the lower is the distribution calculated by the analyzer for the same events, using the generated chamber positions. The objective was to correct the analyzer events such that their distribution would be identical to the Monte-Carlo distribution.

2. The difference quantity, ΔX, is expressed as follows:

$$\Delta X = X_{mc} - X_{an} \tag{6.21}$$

where X_{mc} is the known Monte-Carlo or "true" value and X_{an}, the analyzer calculated value.

3. Dotplots were made of ΔX as a function of the chamber positions in order to determine whether any correlations with chamber position existed. Figures 6.6 and 6.7 show the dotplots of $\Delta\theta$, and $\Delta\phi$ as a function of the chamber positions.

4. If a correlation was found, the 3000 generated events were then fit by a least-squares method to a polynomial. This polynomial is an expression of ΔX as a function of the chamber position.

5. Using the polynomial determined above, it is then possible to obtain an expression for the "true" value in terms of the analyzer calculated value and the polynomial

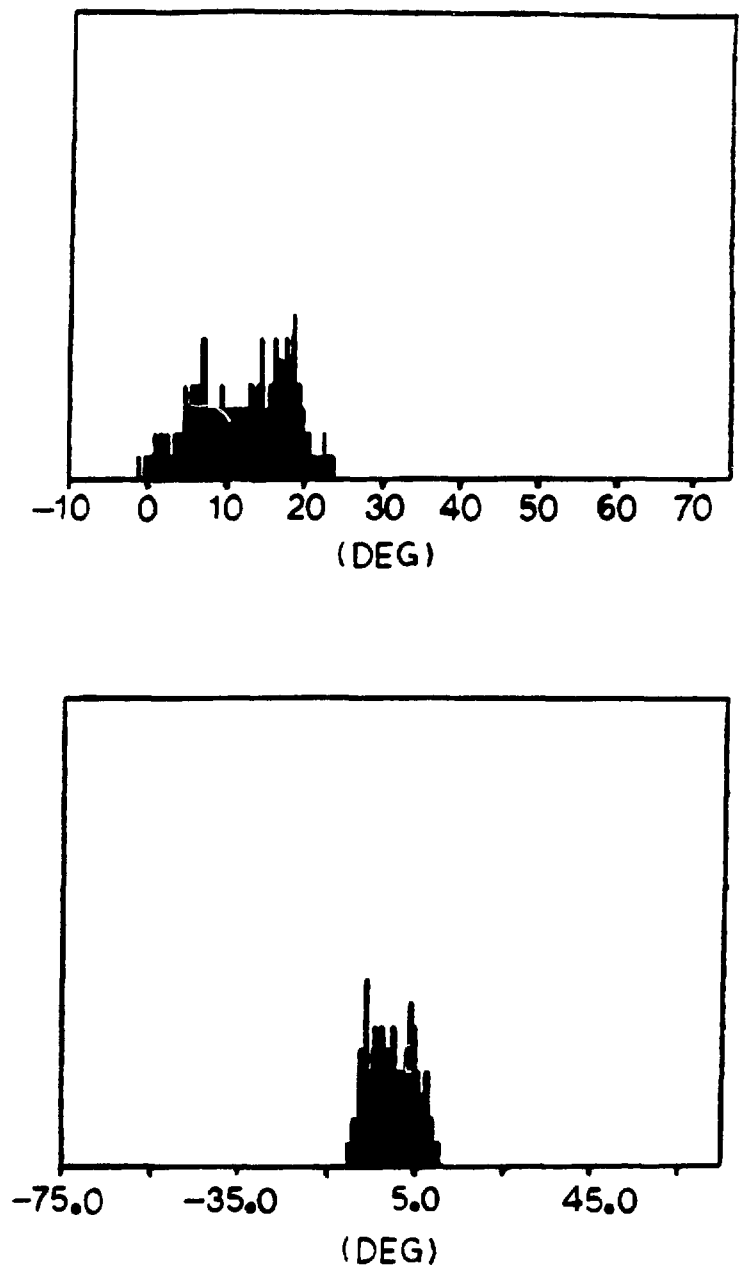

Figure 6.5: Monte-Carlo generated distributions of the scattering angle ϕ: The upper histogram shows the "true" distribution whereas the lower one shows the angles as calculated by the analyzer. The analyzer determined angles, of course, contain an error introduced by the HERA magnetic field.

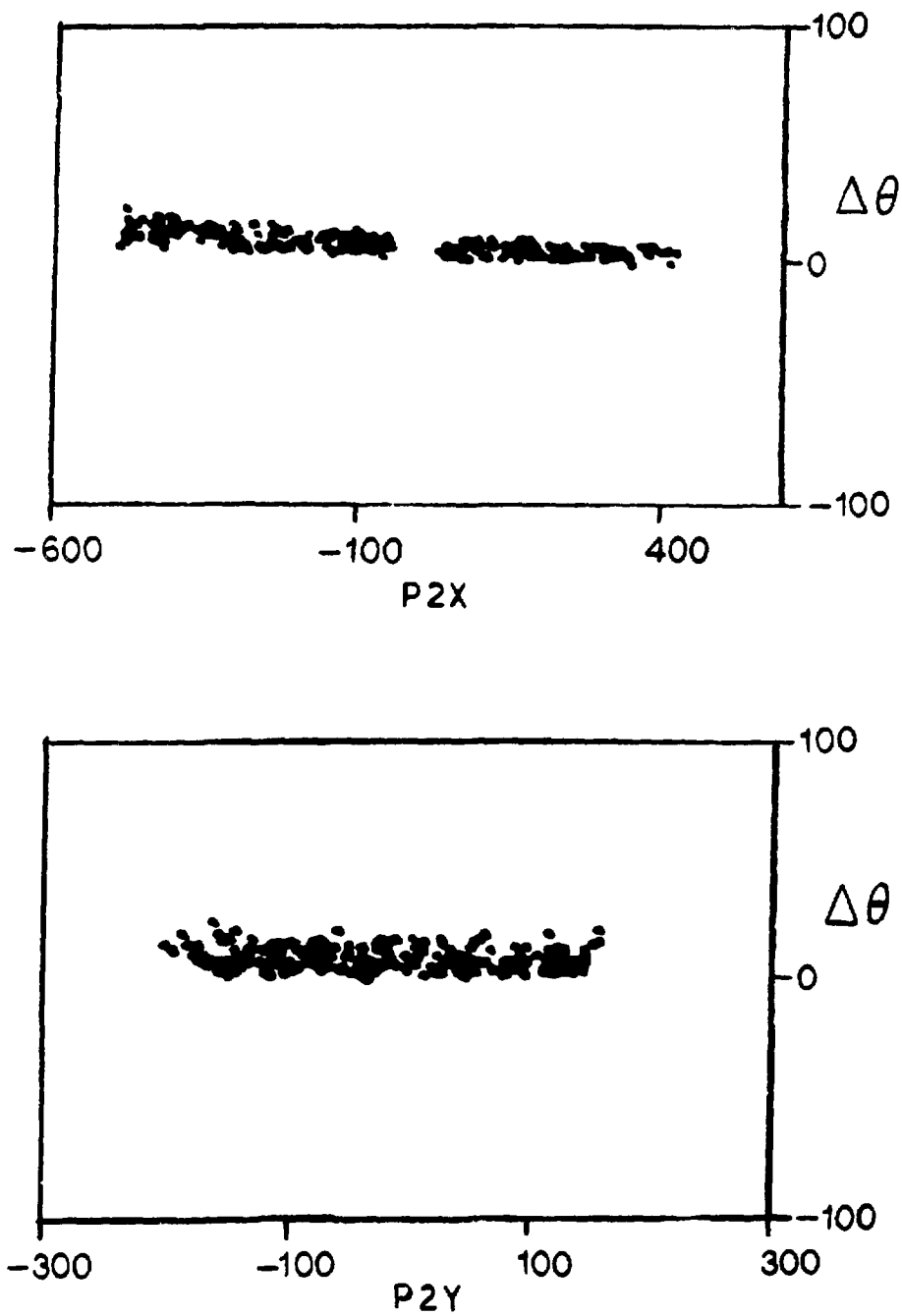

Figure 6.6: Dotplot of the difference between the Monte-Carlo values of θ and those given by the analyzer as a function of the P2 x- and y-positions.

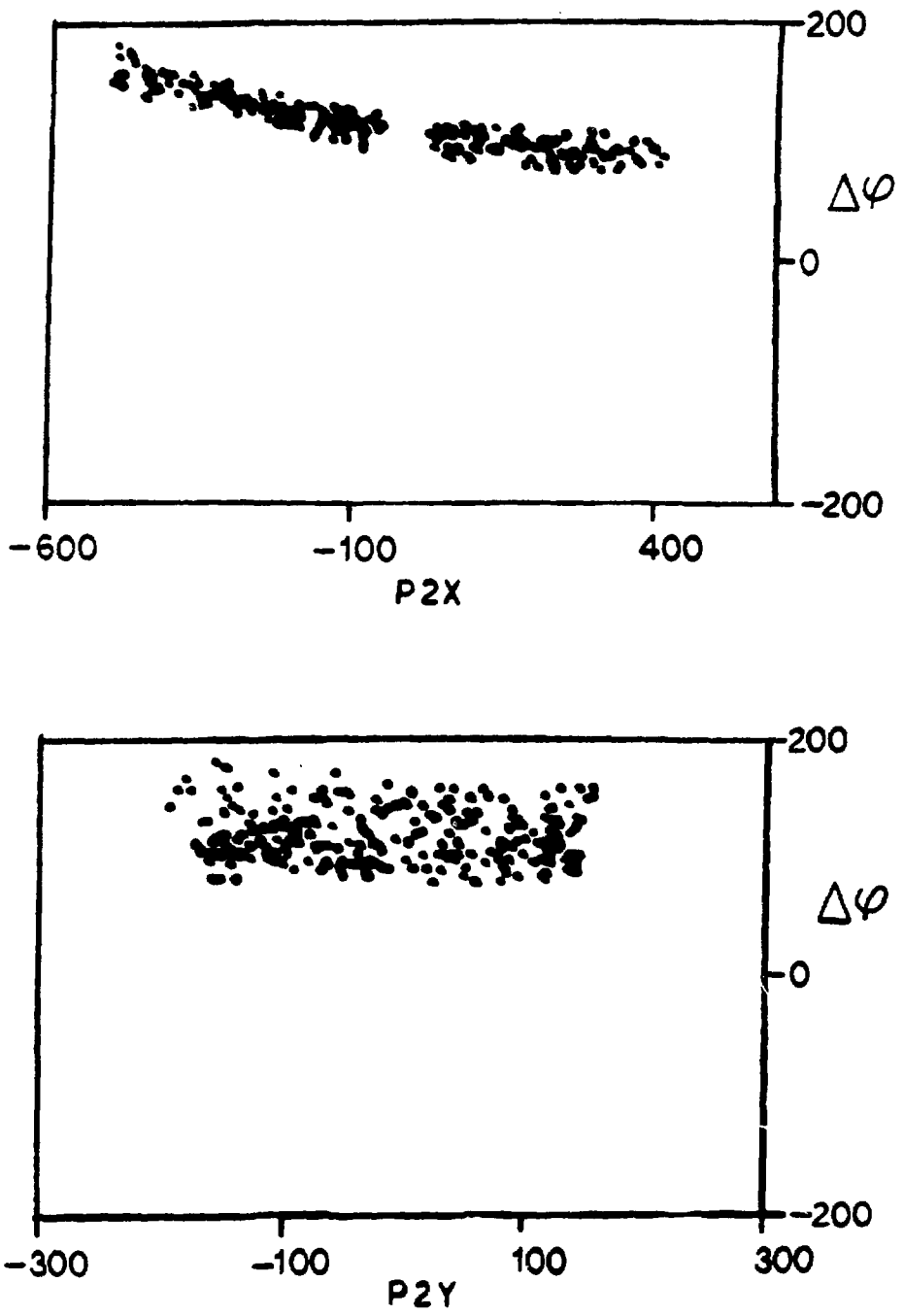

Figure 6.7: Dotplot of the difference between the Monte-Carlo values of ϕ and those given by the analyzer as a function of the P2 x- and y-positions.

function:

$$X_{true} = X_{an} + F(x_i, y_i) \,. \tag{6.22}$$

Here x_i and y_i are the particular chamber xy coordinates.

6. The correction coefficients were read into a COMMON block in the analyzer from an input file. The analyzer subroutines which calculate the momentum (PCALC), and the scattering angles (KINEM) were modified to include the corrections. Each subroutine was modified to correct that quantity event by event.

It can be seen from the dotplots that there was a strong correlation with chamber position. In all cases except for the momentum difference, a linear fit to the x-position in the front chamber P2, gave the best chi-square. Another indication of "goodness of fit" was the width of the peak in the difference histogram. In general, the narrower the difference peak was when centered about zero, the better the fit. Ideally, one would have wanted a delta function at zero difference. The fitting procedure to correct the momentum was not as straightforward and is discussed in greater detail next.

If one examines the momentum difference dotplot (Fig. 6.8) closely, it can be seen that there are events whose Δp does not follow the general trend of the correlation. These events generally had a Δp greater than $\pm 25 MeV/c$. It was guessed, and later confirmed, that these events passed near the pole faces or yoke of the spectrometer, where the $\int B \perp dl$ parameterization would be the worst. Figure 6.9 shows histograms of the P2 xy-positions for a typical run, the limits of which define the spectrometer

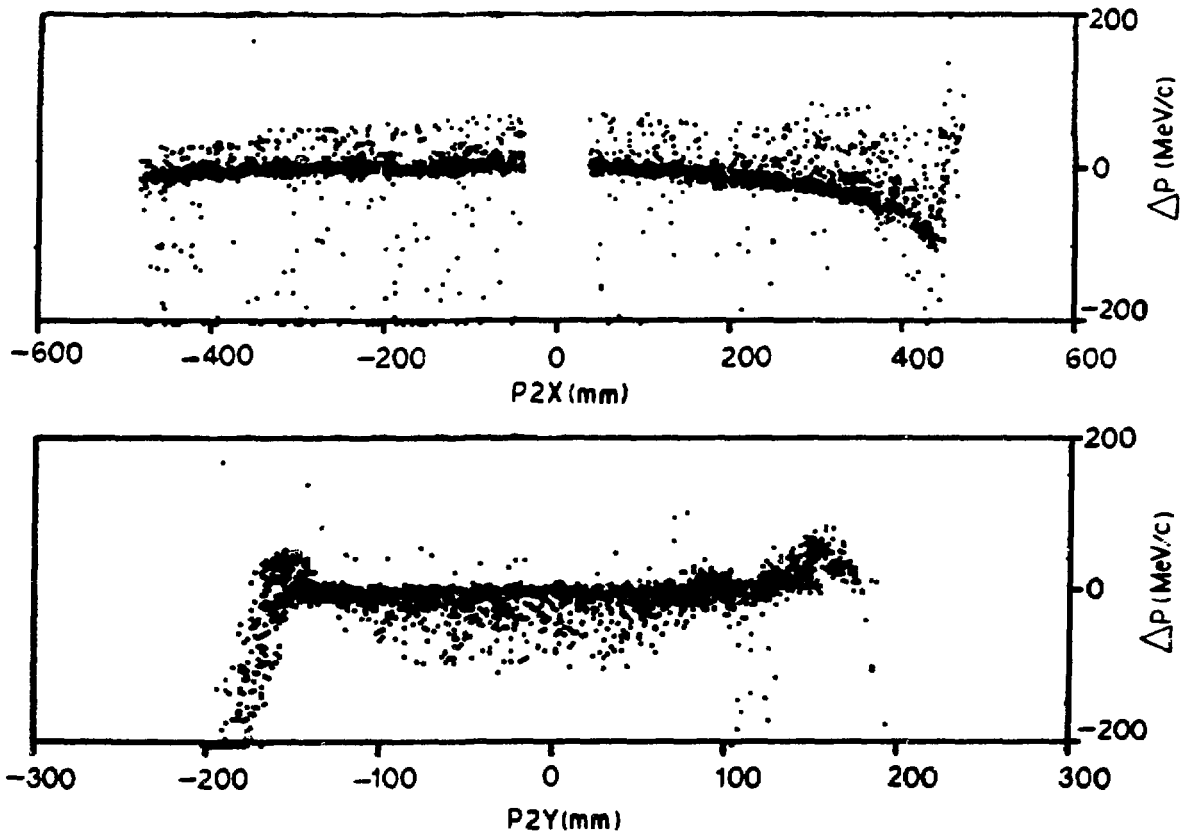

Figure 6.8: Dotplot of the difference between the Monte-Carlo values of the momentum and those given by the analyzer as a function of the P2 z- and y-positions.

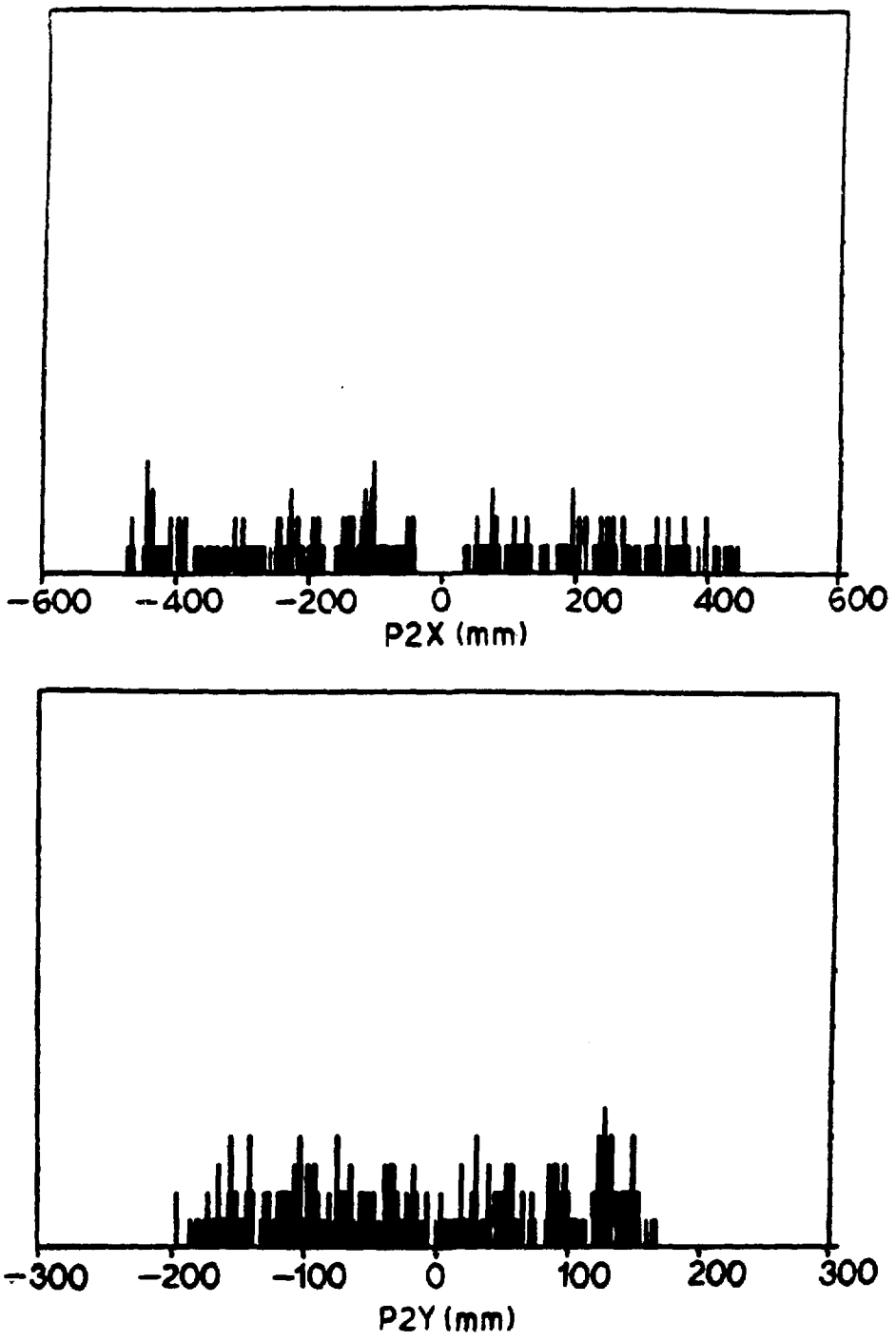

Figure 6.9: P2 xy-positions for a typical run.

acceptance. Figure 6.10 shows a doiplot of all events with $\Delta p > \pm 25 MeV/c$. It can be seen that these events roughly define a box whose xy dimensions correspond to the limits of the spectrometer acceptance. Figure 6.11 further shows where the events with $\Delta p > +25 MeV/c$ and where those with $\Delta p < -25 MeV/c$ originated from. It was never possible to achieve a good fit to all points using the procedure outlined earlier when trying to determine the correction coefficients for the momentum. It was discovered that by eliminating the events with $\Delta p > \pm 25 MeV/c$, a better fit to the majority of events could be achieved.

An attempt to improve the parameterization of the $\int B_\perp dl$ for the SCM105 field was made. A look-up table of $\int B_\perp dl$ values as a function of the xy-position at the center-plane of the magnet was created.

To create the look-up table, events were generated as described above. The position at the center-plane of the SCM105 and the bend-angle was calculated for each event. Since the momentum and bend angle were known, an $\int B_\perp dl$ value could be calculated by inverting Eqn. 5.1 for the momentum. Since the events were generated at random SCM105 center-plane positions, it was necessary to smooth the $\int B_\perp dl$ values to produce a uniformly distibuted look-up table. Figure 6.12 shows a comparison of the polynomial $\int B_\perp dl$ parameterization and the Monte-Carlo look-up table. It can be seen that qualitatively, the two are different.

Several sets of data were analyzed using both $\int B_\perp dl$ parameterizations. It was

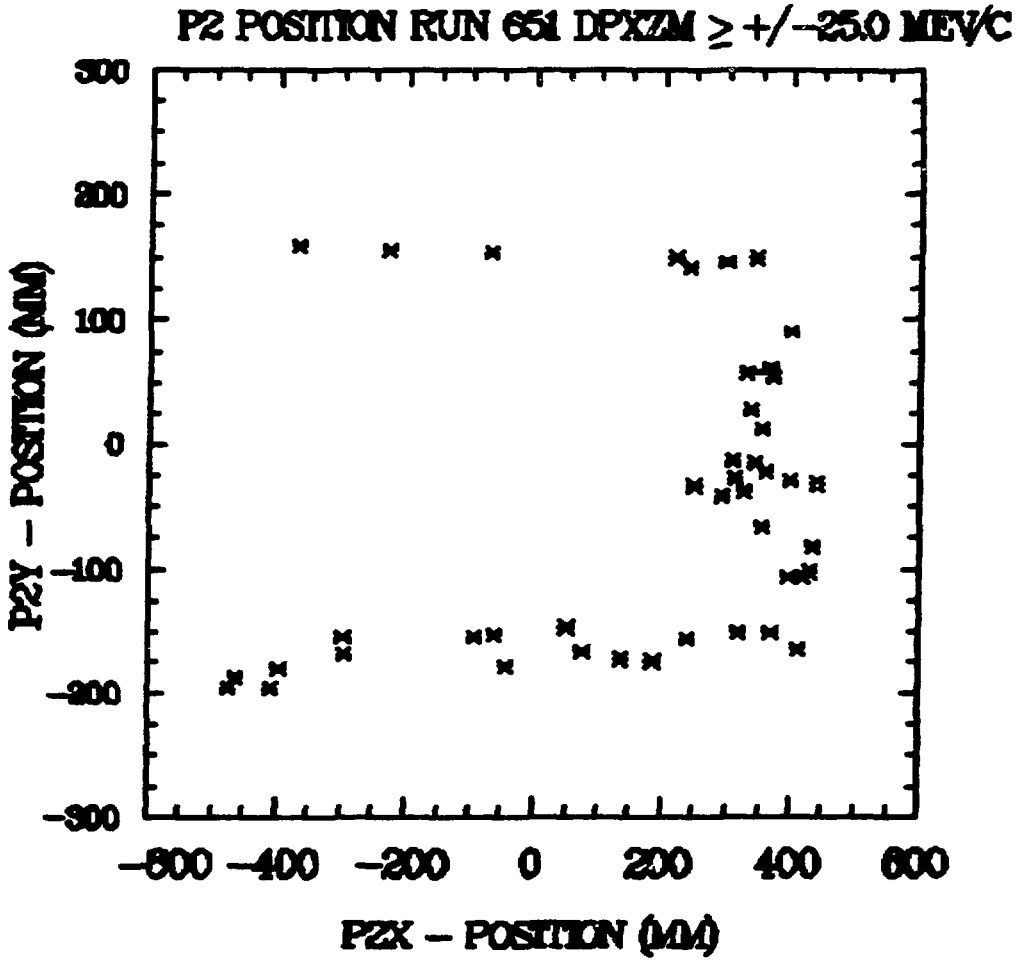

Figure 6.10: Dotplot of all events with $\Delta p > \pm 25 MeV/c$ as a function of the P2 x- and y-position.

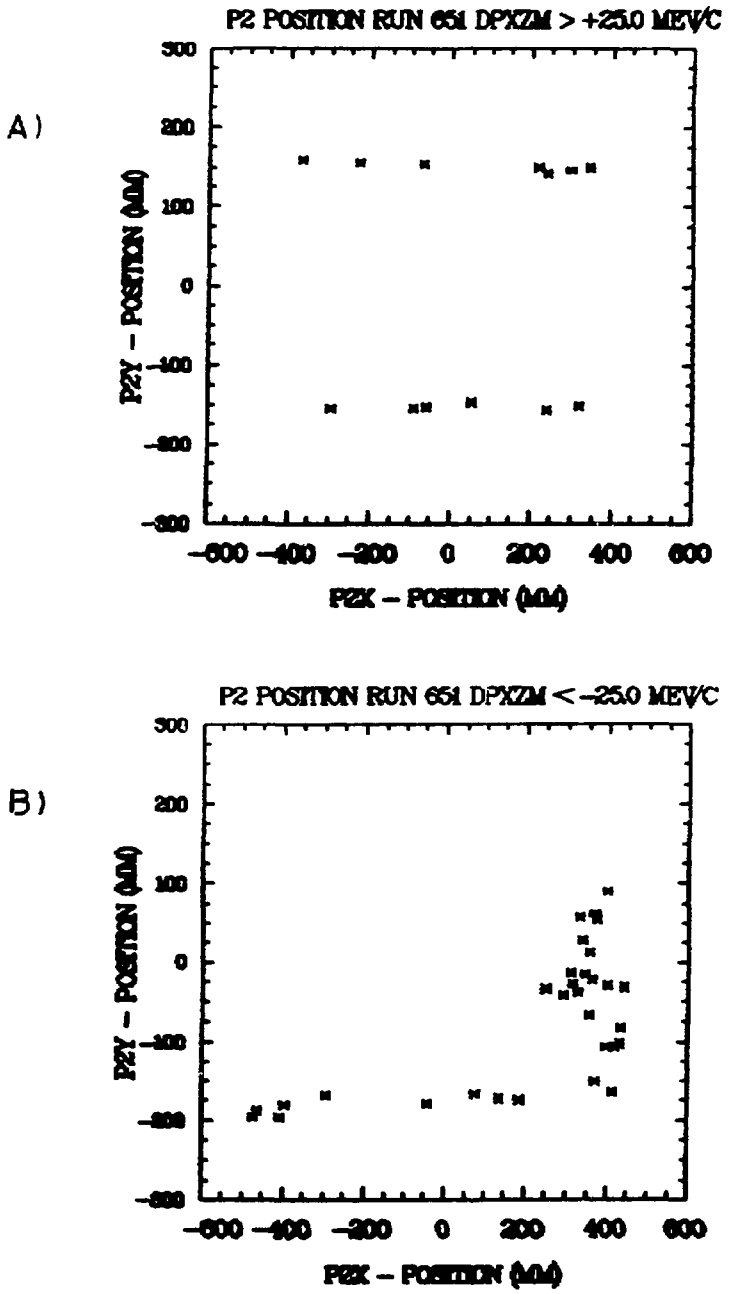

Figure 6.11: a) Dotplot of Monte-Carlo events with $\Delta p > +25 MeV/c$. b) Dotplot of Monte-Carlo events with $\Delta p < -25 MeV/c$.

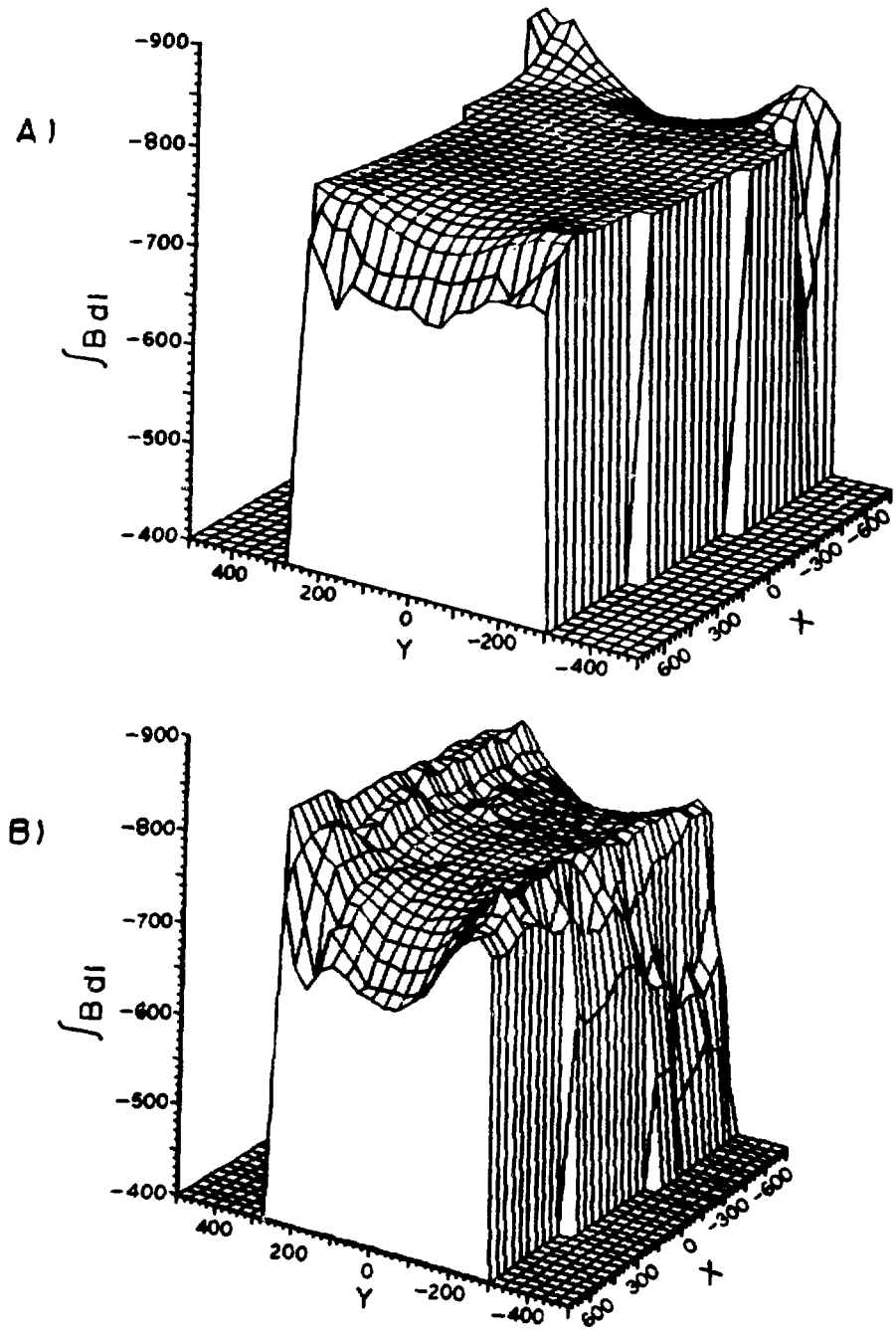

Figure 6.12: Three-dimesional plots of the $\int B_{\perp} dl$ parameterizations. The vertical axis is in units of $KG - cm$ and the other two axes are in units of cm at the SCM105 center-plane. a) The polynomial parameterization. b) The Monte-Carlo.

found that there was no marked improvement in the missing-mass resolution or signal-to-background ratio when the look-up table method was used. Therefore, in this respect, the look-up table method was a check of the quality of the polynomial parameterization.

CHAPTER 7 RESULTS

The results of the spin-spin correlation measurements are presented here. Further discussion is given in Chapter 8. The data are tabulated in Tables 7.1-7.5 as a function of the neutron c.m. scattering angle. The uncorrected values of C_{SS} ($C_{\sigma\sigma}$) are plotted in Figs. 7.1-7.3. Recall, that $C_{\sigma\sigma}$ is given by Eqn. 5.35, which can be written approximately as

$$\begin{aligned} C_{\sigma\sigma} &\approx C_{SS}\sin 37.5^{o} - C_{SL}\cos 37.5^{o} \\ &\approx (0.5)C_{SS} - (0.8)C_{SL} \ . \end{aligned} \tag{7.1}$$

Both the tabulated and plotted $C_{\sigma\sigma}$ values include only the statistical uncertainty in the measurement. In these five tables, a few points in the angular distribution are omitted due to low statistics in these bins, so that their errors are too large to be useful. These values are compared to the phase shift predictions of Arndt, the Basque group, and Hoshizaki as found in the SAID database [Ar-87].

The phase shift predictions were obtained by taking the phase shift predictions for pure C_{SS}, C_{NN}, C_{LL}, and C_{SL} at the desired scattering angles and energies. Equation

5.35 was used, along with the spin component admixture coefficients of Table 5.2, to calculate each phase shift prediction for the spin-mixed parameter. This was done so as to be able to use the small experimental error bars on the $C_{\sigma\sigma}$ values to distinguish between the quality of the various phase shift predictions.

Figures 7.4-7.6 show the values of C_{SS} corrected for other spin components. The errors associated with these data are dominated by the errors on the various other spin components in particular, C_{SL}, as can be seen by comparing the magnitudes of the coefficients in Table 5.2. The C_{SL} values were obtained from the thesis of M.R. Rawool as described on p.147. Here the error bar reflects the statistical uncertainty in the measurements. Figures 7.7-7.8 show a comparison between the values of C_{LL} and C_{SL} as measured in our experiment and the previous LAMPF experiment, E665. For the C_{LL} and C_{SL} values, both the statistical and systematic uncertainties have been included. The data are also plotted along with various phase-shift and Bonn meson-exchange model predictions [El-88] for comparison. The corrections were also performed as discussed in Chapt. 5, Sec. 9.

The C_{LL} and C_{SL} data were found to agree to within one standard deviation with the earlier data. An average, weighted by the errors, was calculated for C_{SL} over the c.m. angle range $80^{o} \leq \theta_{cm} \leq 125^{o}$. The weighted average for our data (E770) was found to be $< C_{SL} >= 0.027$ with a standard deviation of 0.182. For the earlier E665 data, the average value was $< C_{SL} >= 0.097$ with a standard deviation of 0.127. Both

sets of data are consistent with $< C_{SL} >= 0$ as predicted by the phase shifts of Arndt, Basque, and Hoshizaki, and the Bonn meson-exchange model.

Equation 2.50 was used to check the overall normalization of the experimentally determined C_{SS} values at $\theta_{c.m.} = 90^o$. Table 7.6 contains the $C_{LL,np}$, $C_{NN,pp}$, $C_{LL,pp}$, $\left(\frac{d\sigma}{d\Omega}\right)_{pp}$, and $\left(\frac{d\sigma}{d\Omega}\right)_{np}$ values used. These data were chosen from the SAID database because they corresponded most closely to our measurement energies, although other $(\frac{d\sigma}{d\Omega})_{pp}$ data exist. Table 7.7 shows the results of the calculation, along with the experimentally determined values for comparison. The errors for the calulated C_{SS} values were determined by summing the errors of the values in Table 7.6 in quadrature. As can be seen, there is agreement to within one standard deviation for both $634MeV$ and $788MeV$. The $484MeV$ results differ by about two combined standard deviations. It is unclear as to what the cause of this discrepancy may be or whether the difference is just a statistical fluctuation. The uncertainties in the beam and target polarizations are estimated to be $\sim 7\%$ [Ch-85] and $\sim 3.3\%$ [Hi-88], respectively. Combining these in quadrature gives a total systematic uncertainty of $\sim 8\%$ in the overall normalization of all the measured values. Perhaps, it is this normalization error which can account for the discrepancy in the $484MeV$ data.

Table 7.1: The 484 MeV C_{SS} data.

$\theta_{n,cm} \pm 0.45$ (deg)	$C_{\sigma\sigma}$ (uncorrected)	C_{SS} (corrected)
180.0	-0.498±0.076	-0.912±0.256
175.0	-0.405±0.040	-0.683±0.187
170.0	-0.401±0.041	-0.691±0.151
165.0	-0.322±0.042	-0.423±0.168
160.0	-0.195±0.055	-0.438±0.234
155.0	-0.001±0.106	-0.114±0.340
150.0	0.027±0.054	-0.146±0.184
145.0	-0.030±0.047	-0.453±0.211
140.0	-0.007±0.040	-0.529±0.206
135.0	-0.038±0.059	-0.417±0.256
130.0	0.026±0.131	-0.315±0.288
125.0	0.069±0.116	-0.068±0.284
120.0	0.062±0.059	-0.516±0.181
115.0	0.025±0.070	-0.244±0.213
110.0	-0.021±0.073	-0.337±0.231
100.0	-0.155±0.130	-0.604±0.413
95.0	-0.187±0.079	-0.662±0.232
90.0	-0.064±0.073	-0.606±0.260
85.0	-0.002±0.085	-0.180±0.330
80.0	0.059±0.068	0.131±0.144
75.0	-0.006±0.135	-0.027±0.285

Table 7.2: The 634 MeV C_{SS} data.

$\theta_{n.cm} \pm 0.45$ (deg)	$C_{\sigma\sigma}$ (uncorrected)	C_{SS} (corrected)
180.0	-0.738±0.119	-1.121±0.305
175.0	-0.504±0.063	-0.971±0.166
170.0	-0.502±0.058	-0.853±0.151
165.0	-0.392±0.059	-0.944±0.198
160.0	-0.167±0.076	0.034±0.295
155.0	-0.105±0.217	0.341±0.508
150.0	0.074±0.084	0.006±0.211
145.0	0.056±0.069	-0.227±0.239
140.0	0.076±0.088	-0.648±0.246
135.0	0.085±0.109	0.080±0.291
130.0	0.341±0.248	0.446±0.520
125.0	-0.106±0.105	-0.253±0.283
120.0	-0.174±0.076	-0.181±0.188
115.0	-0.297±0.079	-0.692±0.188
110.0	-0.152±0.078	-0.563±0.212
105.0	-0.165±0.105	-0.405±0.283
100.0	-0.217±0.143	-0.854±0.326
95.0	0.013±0.078	0.005±0.219
90.0	0.089±0.074	0.188±0.239
85.0	0.143±0.061	0.294±0.203
80.0	0.121±0.069	0.074±0.144
75.0	0.146±0.113	0.195±0.236

Table 7.3: The 788 MeV C_{SS} data.

$\theta_{n,cm} \pm 0.45$ (deg)	$C_{\sigma\sigma}$ (uncorrected)	C_{SS} (corrected)
180.0	-0.608±0.148	-0.689±0.343
175.0	-0.573±0.108	-0.506±0.245
170.0	-0.781±0.129	-1.284±0.269
165.0	-0.293±0.124	-0.380±0.275
160.0	-0.201±0.293	-0.034±0.643
150.0	0.231±0.146	-0.145±0.356
145.0	0.384±0.327	0.737±0.657
140.0	0.362±0.142	0.406±0.375
135.0	0.443±0.206	0.660±0.438
130.0	-0.268±0.258	-0.671±0.490
125.0	-0.155±0.153	-0.430±0.307
120.0	0.118±0.114	0.063±0.280
115.0	-0.042±0.114	0.036±0.266
110.0	0.178±0.124	0.285±0.296
105.0	0.161±0.142	0.151±0.320
95.0	0.276±0.148	0.298±0.358
90.0	0.085±0.125	0.030±0.298
85.0	0.109±0.164	-0.082±0.435
80.0	0.077±0.128	-0.080±0.313
75.0	0.217±0.133	0.457±0.266

Table 7.4: The uncorrected 634 MeV C_{LL} and C_{SL} data.

$\theta_{n,cm} \pm 0.45$ (deg)	C_{LL} (uncorrected)	C_{SL} (uncorrected)
125.0	0.345±0.123	-0.427±0.195
120.0	0.532±0.100	-0.245±0.132
115.0	0.434±0.108	-0.131±0.148
110.0	0.554±0.128	0.146±0.159
105.0	0.597±0.091	0.260±0.124
95.0	0.461±0.108	0.285±0.147
90.0	0.389±0.107	0.052±0.131
85.0	0.394±0.110	0.002±0.144
80.0	-0.031±0.164	-0.065±0.236

Table 7.5: The corrected 634 MeV C_{LL} and C_{SL} data.

$\theta_{n,cm} \pm 0.45$ (deg)	C_{LL} (corrected)	C_{SL} (corrected)
125.0	0.317±0.123	0.356±0.198
120.0	0.513±0.099	0.204±0.134
115.0	0.422±0.107	0.109±0.151
110.0	0.557±0.127	-0.122±0.162
105.0	0.606±0.090	-0.216±0.126
95.0	0.473±0.108	-0.237±0.150
90.0	0.388±0.106	-0.044±0.133
85.0	0.391±0.110	-0.002±0.147
80.0	-0.034±0.163	0.054±0.240

Table 7.6: Spin parameter data used to calculate C_{SS} from Eqn. 2.50.

Parameter	$484MeV$	$634MeV$	$788MeV$
$C_{LL,np}$	0.367±0.121 [Ra-88]	0.271±0.099 [Ra-88]	0.508±0.129 [Ra-88]
$C_{NN,pp}$	0.497±0.005 [Bh-82]	0.672±0.007 [Bh-82]	0.684±0.004 [Bh-82]
$C_{LL,pp}$	-0.011±0.059 [St-82]	0.181±0.046 [St-82]	0.198±0.040 [St-82]
$(\frac{d\sigma}{d\Omega})_{pp}$ (mb)	3.57±0.21 [Ry-71]	2.30±0.15 [Na-54]	0.65±0.13 [Ry-71]
$(\frac{d\sigma}{d\Omega})_{np}$ (mb)	1.21±0.03 [Bu-82]	0.86±0.04 [Ev-82]	0.43±0.03 [Ev-76]

Table 7.7: Comparison of measured values of C_{SS} at $\theta_{c.m.} = 90^o$ with those determined from Eqn. 2.50.

Parameter	$484MeV$	$634MeV$	$788MeV$
C_{SS} (measured)	-0.606±0.260	0.188±0.239	0.030±0.298
C_{SS} (calculated)	0.012±0.123	0.190±0.099	0.240±0.129

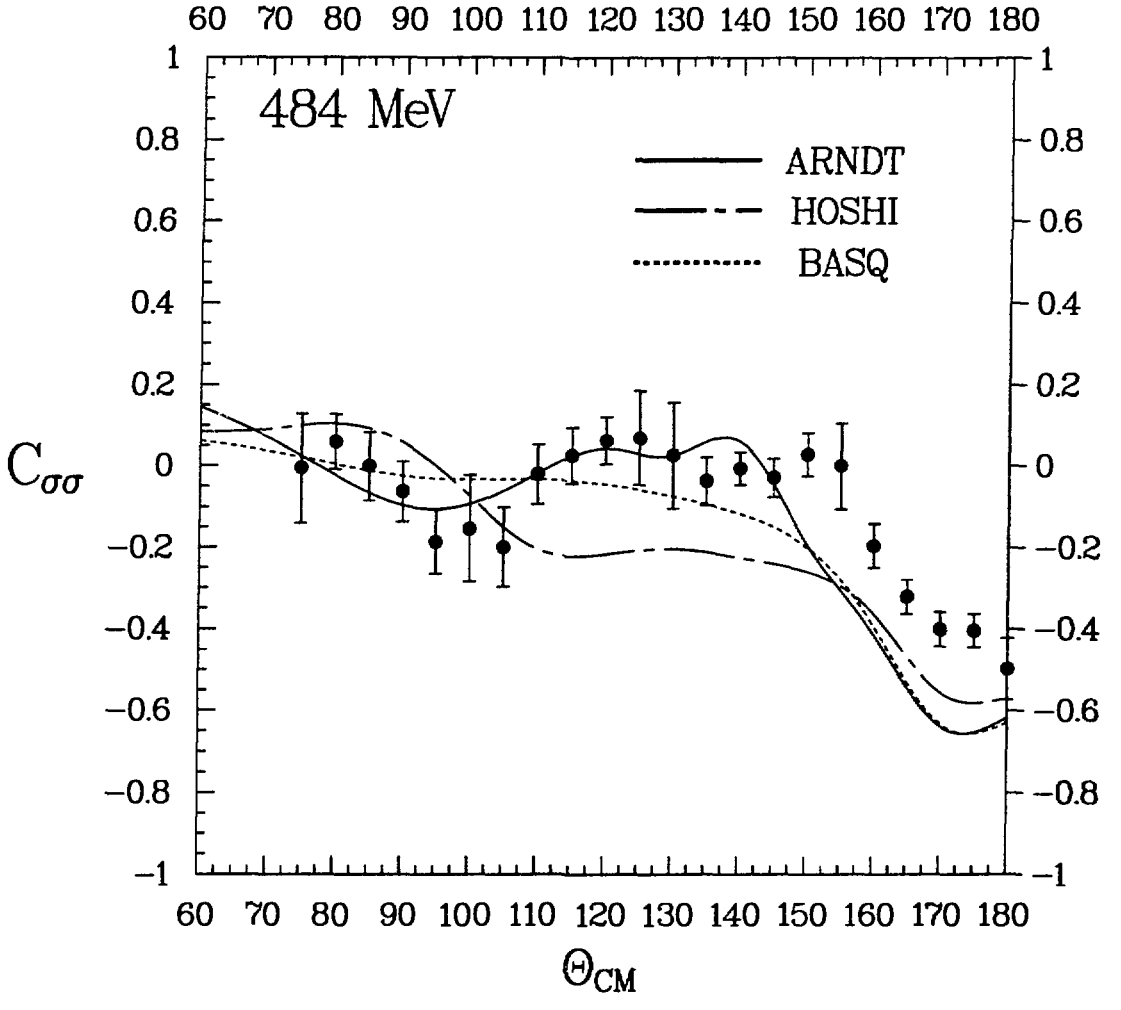

Figure 7.1: The uncorrected C_{SS} ($C_{\sigma\sigma}$) data for an incident neutron beam energy of $484 MeV$, compared with phase shift predictions.

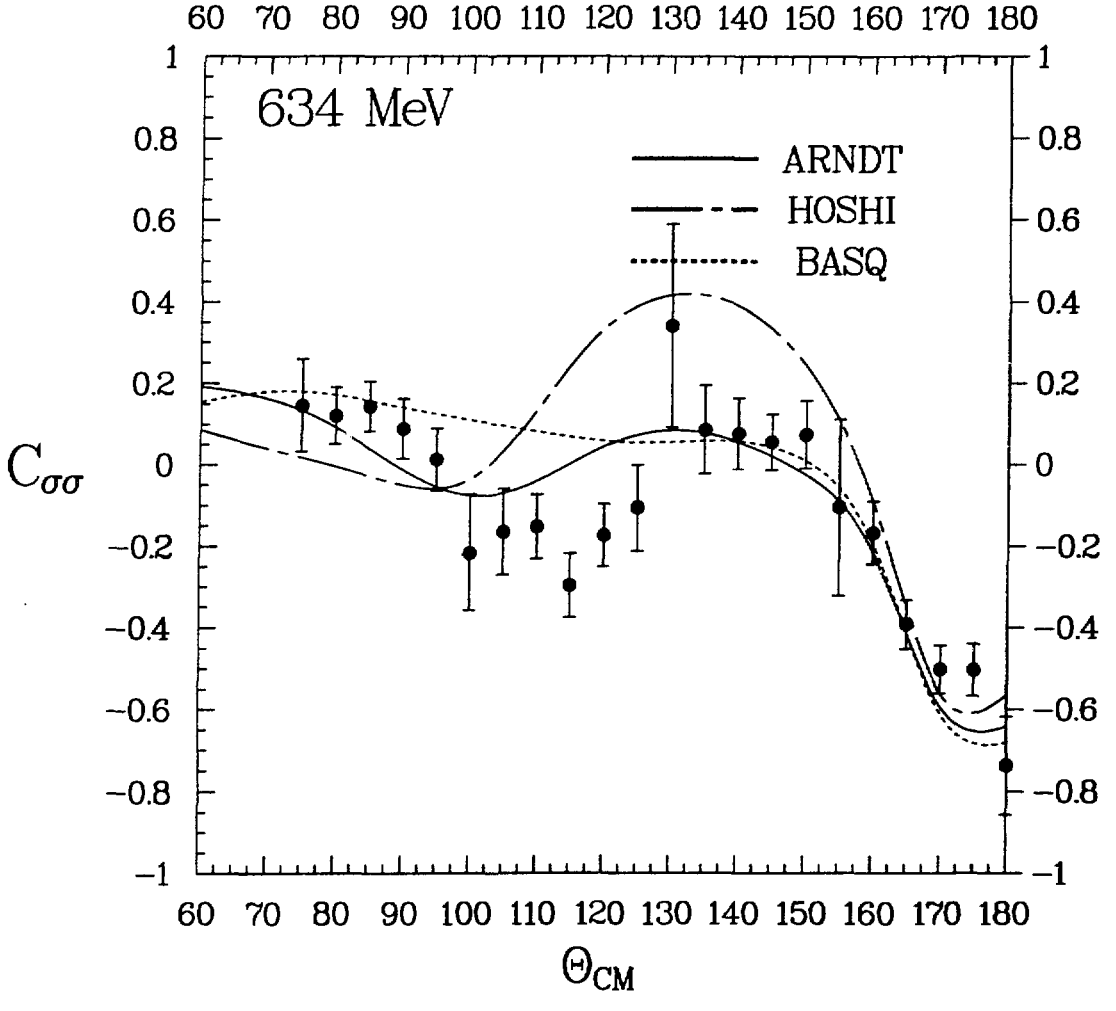

Figure 7.2: The uncorrected C_{SS} ($C_{\sigma\sigma}$) data for an incident neutron beam energy of $634 MeV$, compared with phase shift predictions.

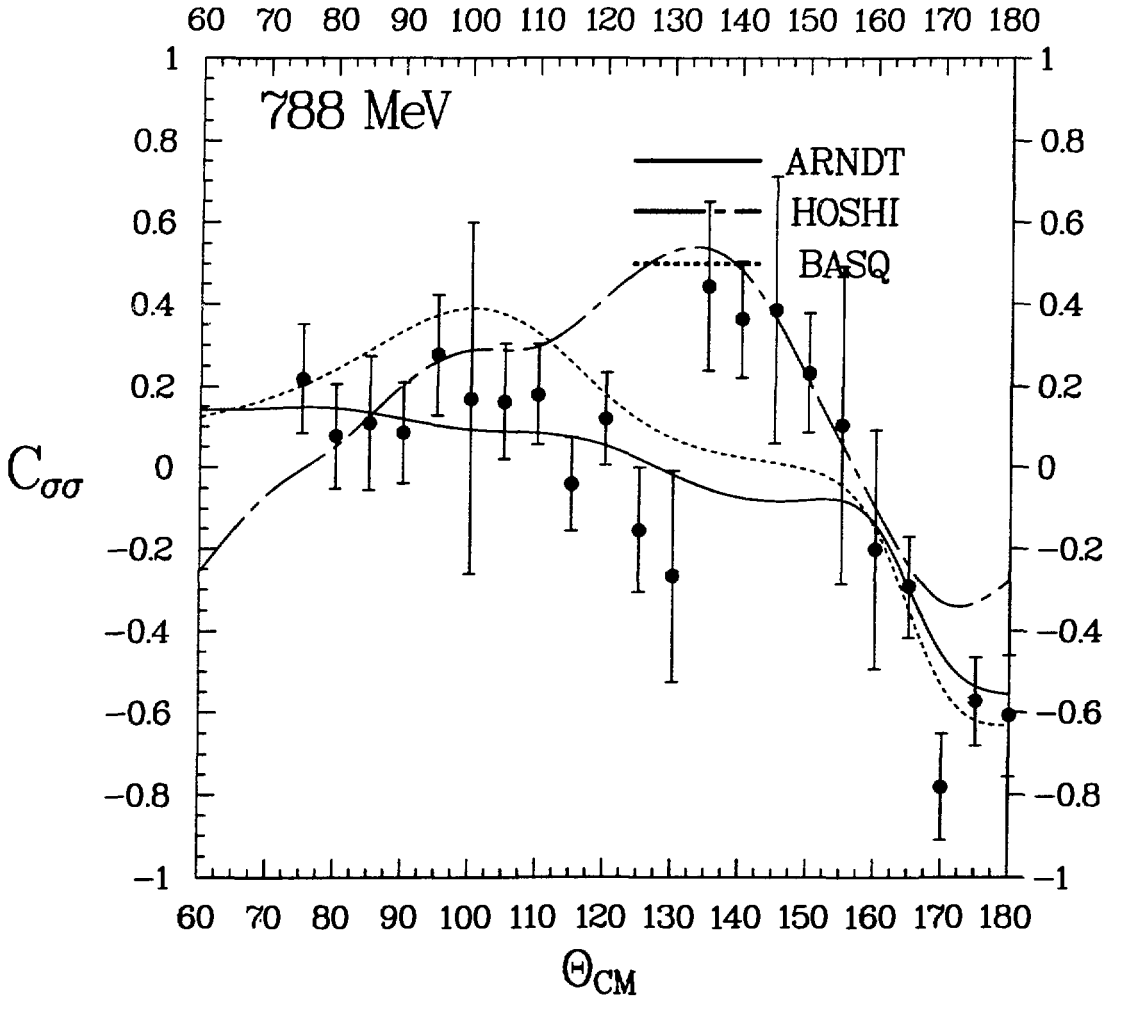

Figure 7.3: The uncorrected C_{SS} ($C_{\sigma\sigma}$) data for an incident neutron beam energy of $788 MeV$, compared with phase shift predictions.

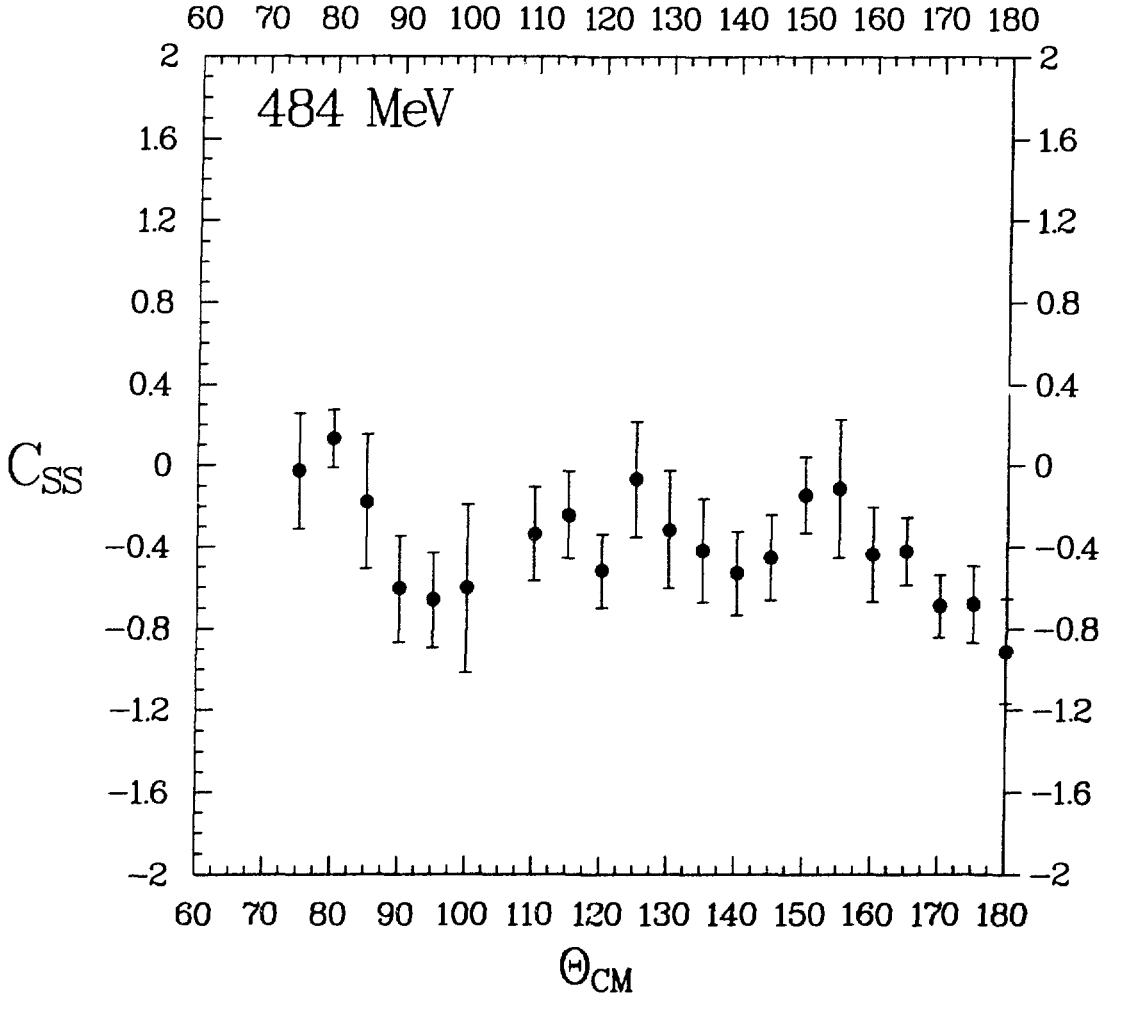

Figure 7.4: The C_{SS} data corrected for other spin components for an incident neutron beam energy of $484 MeV$.

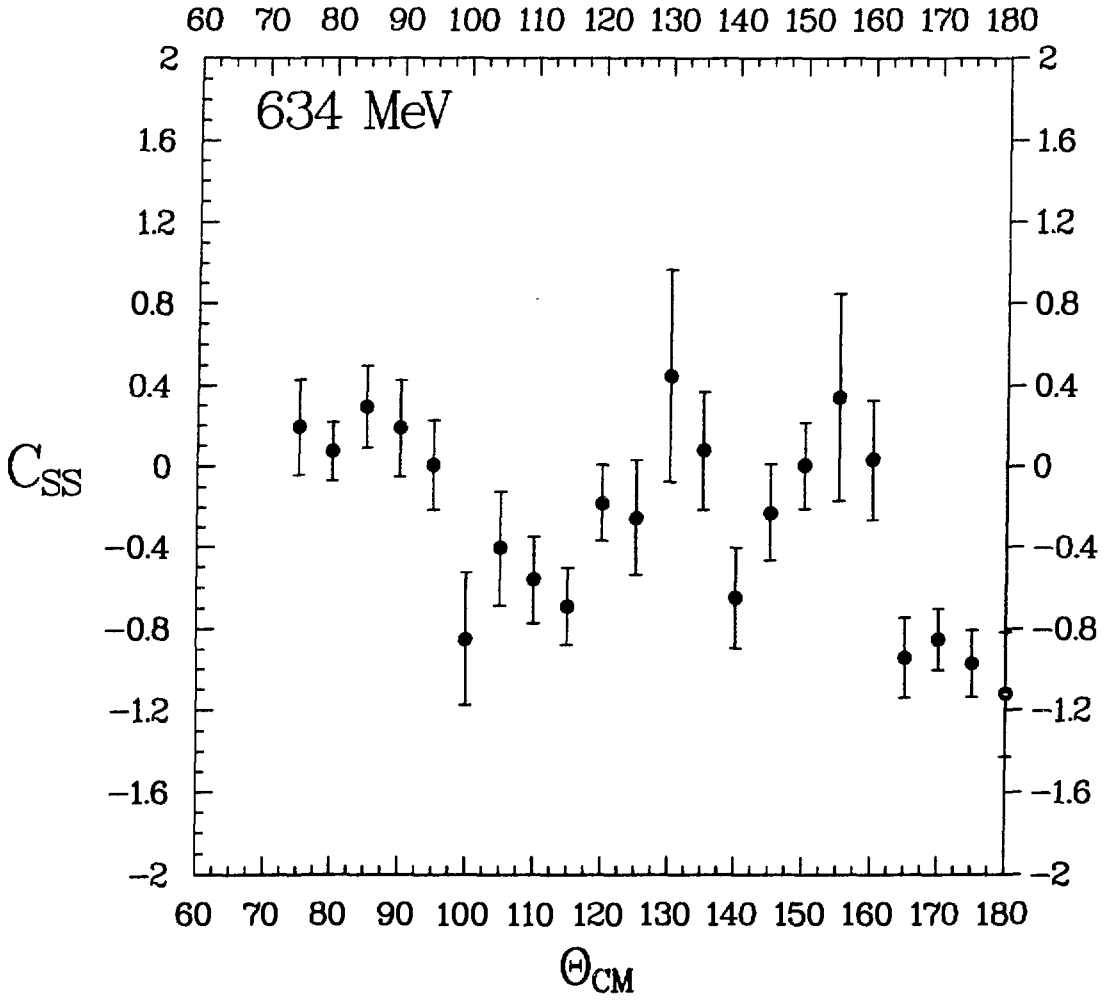

Figure 7.5: The C_{SS} data for an incident neutron beam energy of $634 MeV$.

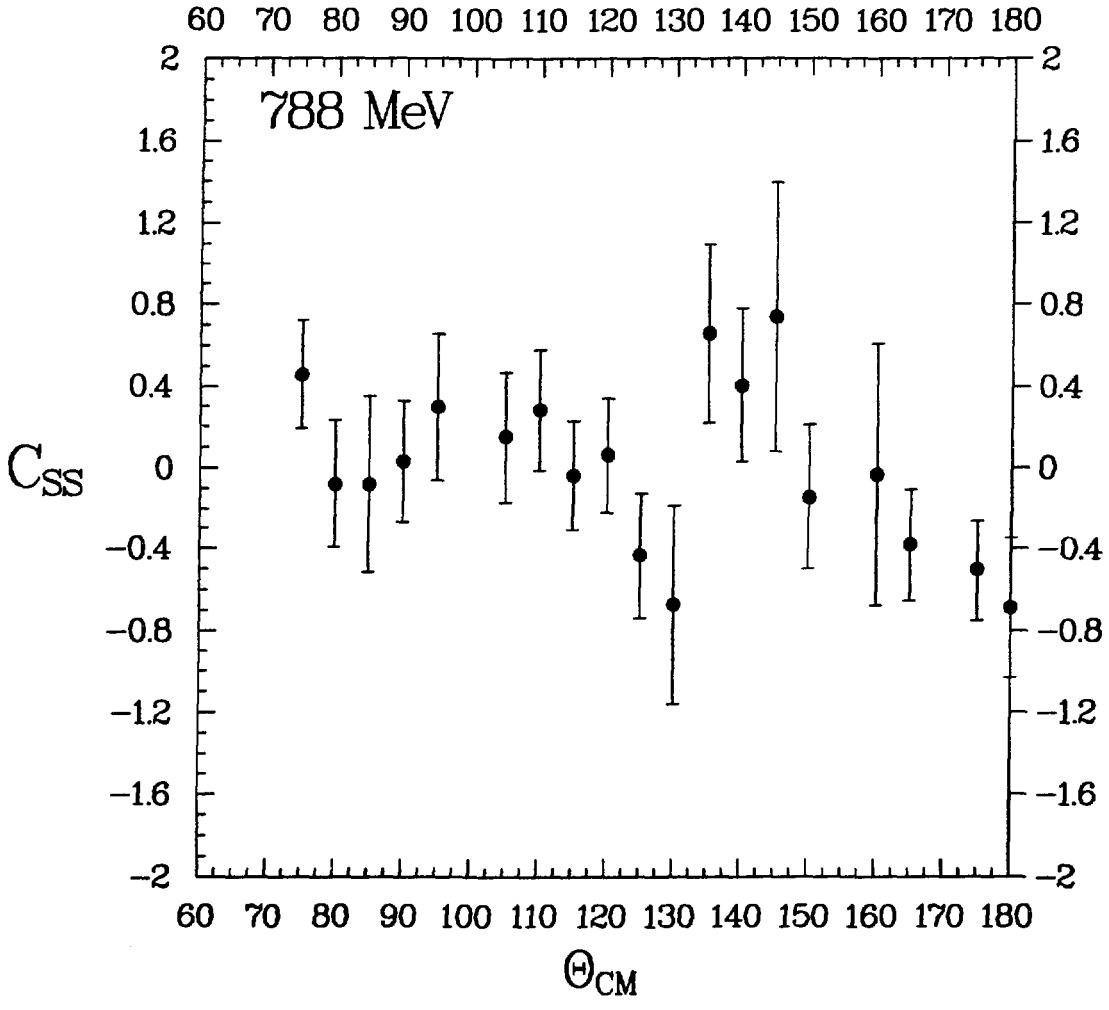

Figure 7.6: The C_{SS} data for an incident neutron beam energy of $788 MeV$.

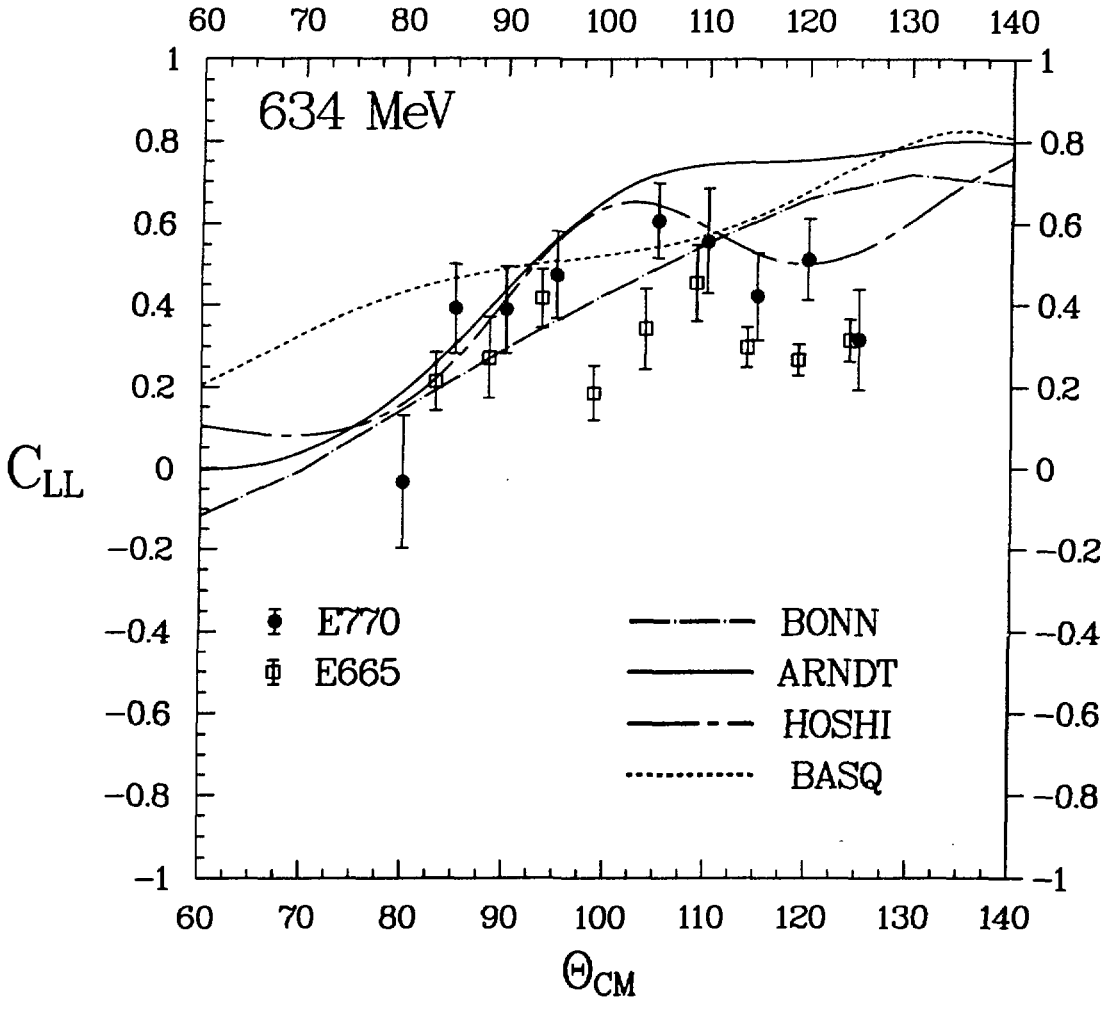

Figure 7.7: Comparison between C_{LL} as measured by LAMPF experiment E770 in 1985, and experiment E665 in 1983.

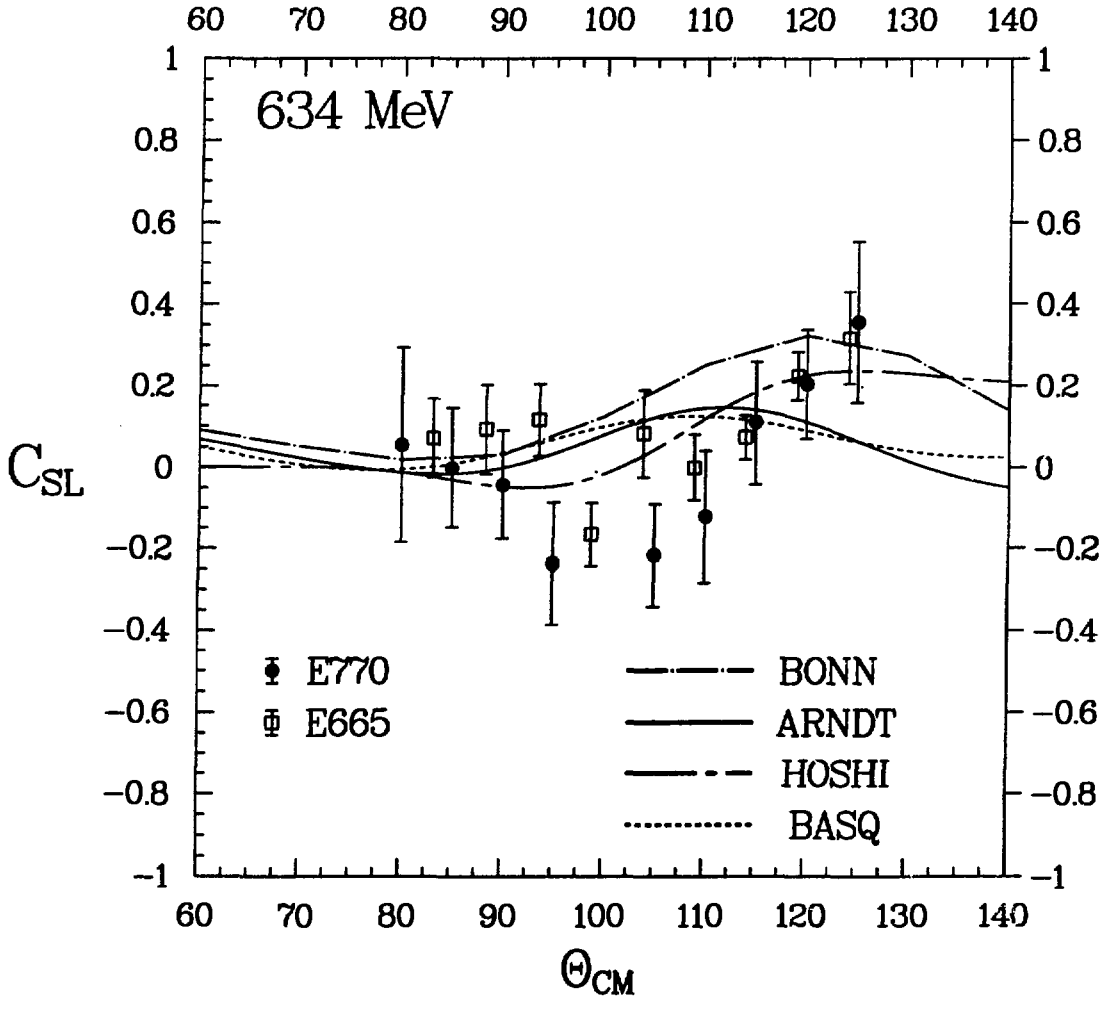

Figure 7.8: Comparison between C_{SL} as measured by LAMPF experiment E770 in 1985, and experiment E665 in 1983.

CHAPTER 8 SUMMARY AND CONCLUSIONS

The spin-spin correlation parameter C_{SS} for np elastic-scattering was measured for the incident neutron kinetic energies 484, 634, and $788 MeV$. Additionally, the parameters C_{LL} and C_{SL} were measured at $634 MeV$ as a cross-check with previously measured data [Ra-88]. The C_{LL} and C_{SL} data were found to agree to within one standard deviation with the earlier data.

The C_{SS} data presented in this dissertation are the first of this type ever measured. These results will most certainly affect the phase shifts and the isospin-0 amplitude determination. The extent to which the phase shifts will change remains to be determined by the various phase shift groups. It is, however, possible to make some qualitative comments about the various phase shift predictions.

It is apparent from Fig. 7.1 that all three of the phase shift predictions shown overpredict $C_{\sigma\sigma}$ by $\sim 10\%$ for $\theta_{cm} \geq 145^{o}$ at $484 MeV$. Many measurements of other spin observables near this energy, mainly from TRIUMF, exist for np elastic-scattering. The fact that the phase shift predictions do not agree well with our data may indicate that our results are incompatible with their results at some level. The $634 MeV$ $C_{\sigma\sigma}$ data

(Fig. 7.2) compare well with the most recent phase shift prediction, that of Arndt, et al. For $788MeV$, the $C_{\sigma\sigma}$ data (Fig. 7.3) tends to follow the trend predicted by Arndt, but deviates significantly between $130^o \leq \theta_{cm} \leq 150^o$. In fact, there clearly is significant peaking of $C_{\sigma\sigma}$ in this angular region as predicted by the 1978 phase shifts of Hoshizaki. This peaking is also noticable in the $788MeV$ pure C_{SS} as shown in Fig. 7.6. There is also significant energy variation in this angular region. Figure 8.1 shows this variation for the four angle bins centered at $\theta_{cm} = 135^o$, 140^o, 145^o, and 150^o, respectively.

In order to determine quantitatively how well the three phase shift predictions fit the data, the reduced chi-square for each prediction was calculated as follows:

$$\chi^2/\nu = \frac{1}{\nu}\sum \frac{(C_{\sigma\sigma,observed} - C_{\sigma\sigma,predicted})^2}{(\delta C_{\sigma\sigma,observed})^2} \tag{8.1}$$

where $\nu = N - 1$ is the number of degrees of freedom for the fit. Table 8.1 shows the χ^2/ν results. It is clear that at $484MeV$ none of the predictions fit the data well. For $634MeV$, Arndt and Basque do a somewhat better job than Hoshizaki. At $788MeV$, Basque has the best fit overall. All predictions, at all energies, however, agree with the data only at the 2-3 standard deviation level. Clearly, a better fit to the $C_{\sigma\sigma}$ data could be obtained.

In order to determine which isospin-0 partial waves will be the most sensitive to our data, the SAID program was run using the "GO8" option. This option allows experimenters to input their data into the program data base and have the change in

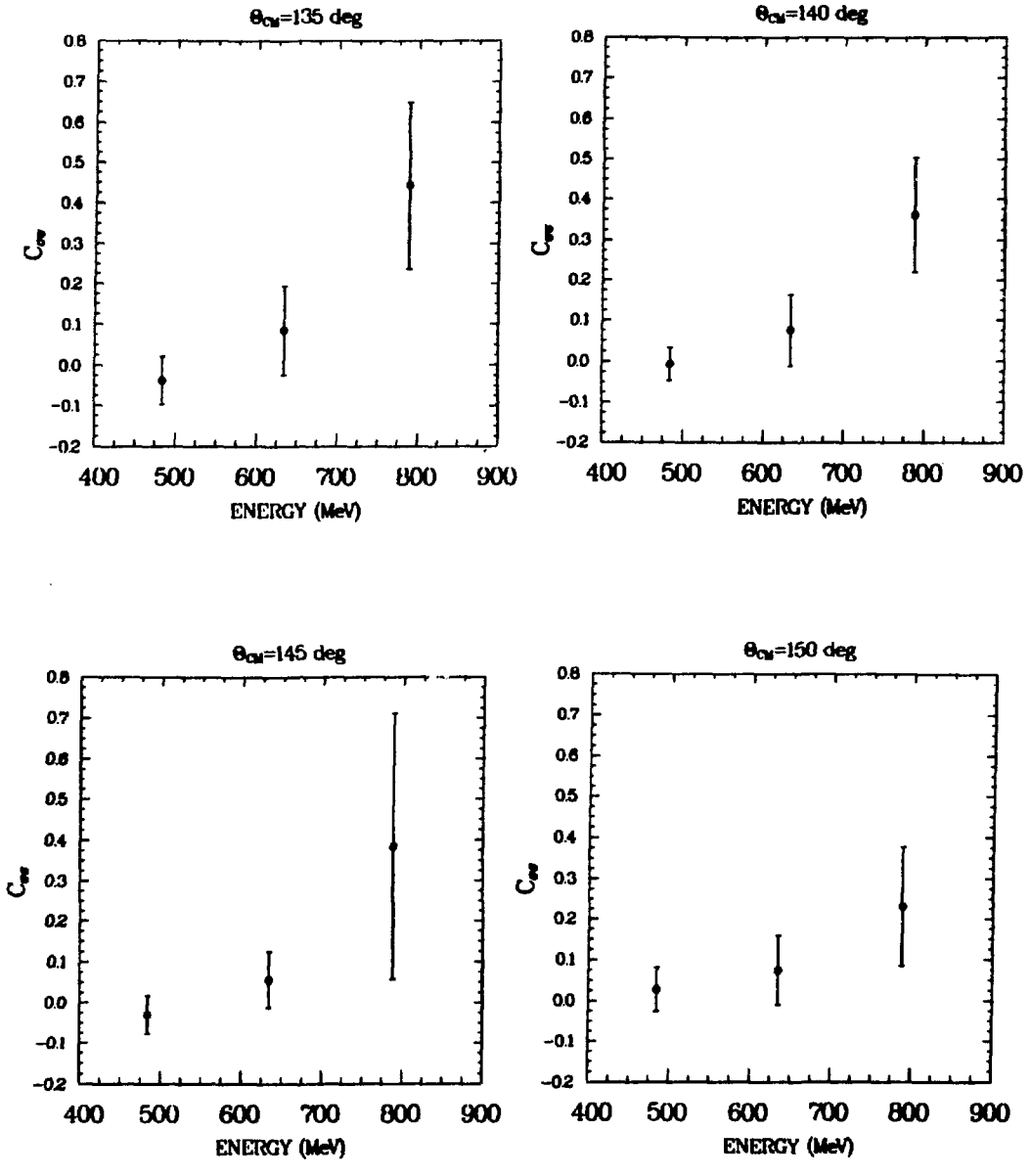

Figure 8.1: Energy variation of $C_{\sigma\sigma}$ for $135° \leq \theta_{cm} \leq 150°$.

Table 8.1: The χ^2/ν values calculated for each phase shift prediction to the $C_{\sigma\sigma}$ data.

Energy	Phase Shift Prediction	Degrees of Freedom	χ^2/ν	Probability
$484MeV$	Arndt	10	7.26	< 0.001
	Basque		7.95	< 0.001
	Hoshizaki		11.81	< 0.001
$634MeV$	Arndt	10	1.93	~ 0.035
	Basque		3.03	< 0.001
	Hoshizaki		8.76	< 0.001
$788MeV$	Arndt	9	2.51	~ 0.010
	Basque		2.33	~ 0.015
	Hoshizaki		4.03	< 0.001

the phase shifts calculated. Table 8.2 shows the results of this exercise for the three measurement energies. The single-energy solutions used were C500, C650, and C800. The most current global energy-independent solution was SM88.

It is clear from Table 8.2 that both spin-singlet and spin-triplet partial waves will be affected in the phase shift analysis by the C_{SS} results at all three measurement energies. Since C_{SS} is a complicated mixture of amplitudes which contain both spin-singlet and spin-triplet partial waves, it is difficult to determine precisely which amplitudes will be affected and to what extent.

For 484 and $634MeV$, the experimental uncertainties of the pure C_{SS} values extracted from the measured $C_{\sigma\sigma}$ are dominated primarily by the uncertainties of the other component spin-spin correlation parameters. In this respect, the measured values of $C_{\sigma\sigma}$ must in some way constrain the other spin-spin correlation parameters. How-

Table 8.2: The isospin-0 partial waves affected by the C_{SS} data.

Partial	Phase shift change (deg)		
Wave	$484MeV$	$634MeV$	$788MeV$
$^1S_0$	-0.01	0.01	0.0
$^1P_1$	-0.13	0.21	0.44
$^3S_1$	0.09	-0.16	-0.35
ϵ_1	-0.11	-0.08	0.20
$^3D_1$	-0.05	-0.17	-0.18
$^3D_2$	-0.06	0.01	-0.35
$^1F_3$	0.02	-0.03	0.03
$^3D_3$	-0.01	-0.07	-0.09
ϵ_3	0.04	-0.02	-0.04
$^3G_3$	0.03	0.03	-0.04
$^3G_4$	-0.08	-0.02	0.14
$^1H_5$	– –	-0.04	-0.09
$^3I_5$	-0.01	0.01	0.01

ever, it is presently unclear what effect this will have on the accuracy of the final $I = 0$ amplitude determination. The uncertainties of the $788MeV$, C_{SS} values are dominated by the rather large statistical uncertainties in $C_{\sigma\sigma}$. These data were taken over a much shorter period due to time constraints. Therefore, the uncertainties are dominated by poorer statistics, not by decreased experimental accuracy. The experimental uncertainties of the measured $C_{\sigma\sigma}$ for all three energies are smaller than for any other previously measured two-spin parameter for np elastic-scattering above $\sim 500MeV$.

Presently, the isospin-0 elastic-scattering amplitudes are undetermined. It has been estimated [Sp-84] that by including the data presented here, along with the LAMPF E665 data (C_{LL} and C_{SL}), and earlier P, C_{NN}, and $\frac{d\sigma}{d\Omega}$ data, that these amplitudes

could be determined to about the 40 – 50% level in the future in a model-independent fashion. Some amplitudes will without doubt be known better, and others worse, than expected. Our group expects to do a model-independent amplitude analysis. However, before it will be carried out, there is some additional smaller c.m. angle data which must be analyzed. By including these additional data in the amplitude analysis, it will be possible to determine the amplitudes over a wider angular range. Additionally, the raw data ($C_{\sigma\sigma}$) will be used in the analysis in order to take advantage of the smaller experimental uncertainties; which should better constrain the amplitudes.

References

[Ab-78] A. Abragam and M. Goldman, *Rep. Prog. Phys.*, vol. 41, 1978.

[Ar-68] R. A. Arndt, *Phys. Rev.* **165**, 1834 (1968).

[Ar-83] R. A. Arndt et al., *Phys. Rev. D***28**, 97 (1983).

[Ar-85] R. A. Arndt, SAID program (1985).

[Ar-87] R. A. Arndt, J. S. Hyslop, and L. D. Roper, *Phys. Rev. D***35**, 128 (1987).

[Au-72] P. Autones et al., *Nucl. Instrum.* **103**, 211 (1972).

[Au-77] I. P. Auer et al., *Phys. Lett.* **67***B*, 113 (1977).

[Au-81] I. P. Auer et al., *Phys. Rev. D***24**, 1771 (1981).

[Au-83] I. P. Auer et al., *Los Alamos National Laboratory Report* LA-UR-83-3612, 1983.

[Ba-82] R. Bhandari, *Lett. Nuovo Cim.*, vol. 37, no. 3, (1982).

[Bj-75] C. W. Bjork, thesis, *Los Alamos National Laboratory Report* LA-6192-T, 155 (1975).

[Bo-80] C. Bourrely, E. Leader and J. Soffer, *Phys. Repts.* **59** *no. 2*, 95 (1980).

[By-78] J. Bystricky, F. Lehar, and P. Winternitz *J. Physique* **39**, 7 (1978).

[By-87] J. Bystricky, C. Lechanoine-Leluc, and F. Lehar, *J. Physique* **48**, 199 (1987).

[Ch-85] J. S. Chalmers et al., *Phys. Lett.* **153***B*, 235 (1985).

[Co-80] G. R. Court, B. Craven, R. Gamet, and P. J. Hayman, *Nucl. Instrum.* **177**, 281 (1980).

[Da-61] O. I. Dahl et al., *Phys. Rev. Lett.* **6**, 142 (1961).

[De-67] H. Desportes, *Proceedings of the Second International Conference on Magnet Technology*, Edited by H. Hadley (Oxford 1967), p.603-610.

[De-75] T. DeGrand, R. L. Jaffe, K. Johnson, and J. Kiskis, *Phys. Rev. D***12**, 2060 (1975).

[Du-82] R. Dubois et al., *Nucl. Phys.* ***A377***, 554 (1982).

[Dy-82] O. B. van Dyck, *Los Alamos National Laboratory Report* LA-9160-SR, 1982.

[Ed-68] G. Eder, *Nuclear Forces - Introduction to Theoretical Nuclear Physics*, p. 11, 1968, The MIT Press, Cambridge.

[El-88] Ch. Elster et al., *Phys. Rev.* ***C37***, 1647 (1988).

[Fa-87] C. Fasano and T.-S. H. Lee, *Phys. Rev.* ***C36***, 1906 (1987).

[Fr-74] H. Frauenfelder and E. Henley, *Subatomic Physics*, p. 36, 1974, Prentice-Hall, Englewood Cliffs, N. J.

[Gi-71] G. Giacomelli, *Prog. in Nucl. Phys.* **12**, 214 (1971).

[Go-60] M. L. Goldberger, M. T. Grisaru, S. N. MacDowell, and D. Y. Wong, *Phys. Rev.* **120**, 2250 (1960).

[Gr-82] W. Grein and P. Kroll, *Nucl. Phys.* ***A377***, 505 (1982).

[Ha-74] F. Halzen and G. H. Thomas, *Phys. Rev.* ***D10***, 344 (1974).

[Ha-86] W. Haberichter and H. M. Spinka, *Proc. of the Workshop On Radiation Damage to Wire Chambers*, LBL-21170, 99 (April 1986).

[Ha-88] W. Haberichter et al., *Nucl. Instrum.* ***A270***, 361 (1988).

[He-83] E. M. Henley, L. S. Kisslinger, and G. A. Miller, *Phys. Rev.* ***C28***, 1277 (1983).

[Hi-88] D. Hill, private communication.

[Ho-68] N. Hoshizaki, *Suppl. of the Prog. of Theor. Phys.* **42**, 110 (1968).

[Ho-77] N. Hoshizaki, *Prog. Theor. Phys.* **58**, 716 (1977).

[Ho-78] N. Hoshizaki, *Prog. Theor. Phys.* **60**, 1796 (1978).

[Ho-79] E. W. Hoffman, *IEEE Trans. on Nucl. Sci.*, Ns-26, 3995 (1979).

[Ja-59] M. Jacob and G. C. Wick, *Ann. Phys. (N.Y.)* **7**, 404 (1959).

[Ja-75] J. D. Jackson, *Classical Electrodynamics*, p. 556, 1975, John Wiley and Sons, Inc.

[Ja-77] R. L. Jaffe, *Phys Rev. Lett.* **38**, 195 (1977) , and *Phys. Rev. Lett.* **38**, 617 (1977).

[Ka-77] T. Kamae et al., *Phys. Rev. Lett.* **38**, 421 (1977).

[Ka-84] M. Kamram, *Phys. Repts.* **108** *no. 5*, 275 (1984).

[Kl-81] W. M. Kloet and J. A. Tjon, *Phys. Lett.* ***106B***, 24 (1981).

[Kl-83a] W. M. Kloet and J. A. Tjon, *Nucl. Phys.* **A392**, 271 (1983).

[Kl-83b] W. M. Kloet and J. A. Tjon, *Phys. Rev.* **C27**, 430 (1983).

[La-51] W. E. Lamb, Jr. and R. C. Retherford, *Phys. Rev* **81**, 222 (1951).

[LA-85] *Introduction to Q*, LAMPF Document MP-1-3401-3 (1985).

[Le-67] F. Lehar and P. Winternitz, *Fortschr.* **15**, 495 (1967).

[Li-82] P. W. Lisowski et al., *Phys. Rev. Lett.* **49**, 255 (1985).

[Lo-85] M. P. Locher, M. E. Sainio and A. Svarc, *Swiss Institute for Nuclear Research Report* Pr-85-12 (1985).

[Mc-81a] M. W. McNaughton et al., *Phys. Rev.* **C23**, 1128 (1981).

[Mc-81b] M. W. McNaughton and E. P. Chamberlain, *Phys. Rev.* **C24**, 1778 (1981).

[Mo-82] C. L. Morris, *Nucl. Instrum.* **196**, 263 (1982).

[Mu-83] P. J. Mulders, *Phys. Rev. D28*, 443 (1983).

[Ni-77] K. Nield and R. Daly, *Argonne National Laboratory Report* ANL-HEP-PR-77-32, 1977.

[Oa-63] R. J. Oakes, *Phys. Rev.* **131**, 2239 (1963).

[Oe-54] R. Oehme, *Phys. Rev.* **98**, 147 (1954).

[Oh-69] G. G. Ohlsen et al., *Los Alamos Scientific Laboratory Report* LA-4112, 1969.

[Oh-70] G. G. Ohlsen, *Los Alamos Scientific Laboratory Report* LA-4451, 1970.

[Oh-73] G. G. Ohlsen and P. W. Keaton, *Nucl. Instrum.* **109**, 41 (1973).

[Or-58] J. Orear, *University of California Radiation Laoratory Report* UCRL-8417, 15 (1958).

[PDG-86] Particle Data Group, *Phys. Lett.* **170***B*, 59 (1986).

[Pu-57] L. D. Puzikov, R. M. Ryndin, and Ya. A. Smorodinski, *Sov. Phys. JETP* **5**, 489 (1957).

[Ra-88] M. W. Rawool, *Los Alamos National Laboratory Report* LA-11387-T, 124 (1988).

[Ri-81] P. J. Riley et al., *Phys Lett.* **103***B*, 313 (1981).

[Ro-85] L. Rosen, *Los Alamos National Laboratory Report* LA-UR-85-3437, 5 (1985).

[Sc-65] A. Scotti and D. Y. Wong, *Phys. Rev.* bf 138B, 145 (1965).

[Sh-74] S. Shlaer, *Los Alamos National Laboratory Report* LA-5511-MS, p.1.

[Sh-88] R. L. Shypit et al., *Phys. Rev. Lett.* **60**, 901 (1988).

[Sp-84] H. Spinka, *Phys. Rev. D***30**, 1461 (1984).

[Sp-85] H. Spinka, private communication.

[Sp-88a] D. W. L. Sprung and S. Klarsfeld, *Phys. Lett. B*, vol. 206, no. 2, 182 (1988).

[Sp-88b] H. Spinka, *Argonne National Laboratory Report* ANL-HEP-TR-88-14, 1988.

[St-57] H. P. Stapp, T. Y. Ypsilantis, and N. Metropolis, *Phys. Rev.* **105**, 302 (1957).

[Ue-82] T. Ueda, *Phys. Lett.* **119***B*, 281 (1982).

[Ve-82] B. J. Verwest, *Phys. Rev. C***25**, 482 (1982).

[Wi-61] W. S. C. Williams, *An Introduction to Elementary Particles*, 1961.

[Wo-52] L. Wolfenstein and J. Ashkin, *Phys. Rev.* **85** , 947 (1952).

[Yo-85] For a review and a list of references, see A. Yokasawa, *The Proceedings of the Sixth International Symposium on Polarization Phenomena in Nuclear Physics*, Osaka, Japan, August 26-30, 1985.

Appendix A Bound Nucleon Polarization

The following is the contents of an internal memorandum sent to each member of the E770 collaboration discussing the effective bound nucleon polarization of the background nuclei in the polarized target.

ARGONNE NATIONAL LABORATORY
9700 South Cass Avenue, Argonne, Illinois 60439

09 January 1985 Telephone 312/972-

To: E-770 Collaboration

From: D. Hill, H. Spinka DH HS

Subject: **Estimates of Effective Nucleon Polarization Arising from the Polarized Background Nuclei of the Polarized Target**

This note summarizes the current state of our thinking and knowledge on this subject. Please be aware that we have obtained the essential "physics" input, that is, the nuclear wave function estimates, from Dieter Kurath (ANL-Physics). We are writing this document in order to disseminate the information that we have, and to serve as a framework for (we hope) further discussion and refinements. Although our calculations have the appearance of completeness, in that we arrive at a "result", great uncertainty remains in what we have called the "selectivity" parameter. It would be desirable to reduce that uncertainty, or, at least, to quantify the degree of uncertainty.

Estimates of polarized "background" effects require at least four different types of information:

I) Nuclear Wave Functions

II) Nuclear Polarizations

III) Target Composition

IV) Selectivity of the scattering experiment ("Glauber" effects, kinematical bias, etc.)

We here concern ourselves with scattering experiments in which the momentum transfer is large, so that the background nuclei can be viewed as collections of quasi-free nucleons. In this case we must estimate the effective polarized nucleon content of the background nuclei. We will cast our estimate in the form

$$P_B(t_3) = [\Sigma_i n_i E_i(t_3) P_i S_i(t_3)]/\Sigma_i n_i N_i(t_3), \quad (1)$$

where $P_B(t_3)$ is the effective polarization for background nucleons of isospin projection t_3, n_i is the number density in the target of nuclei of type labeled "i", $E_i(t_3)$ is the (maximal) expectation value of the nucleon polarization operator for nuclei of type "i", P_i is the nuclear polarization, $S_i(t_3)$ is a "selectivity" parameter, and $N_i(t_3)$ is the number of relevant nucleons per nucleus, i.e., $N_i(p) = Z_i$ and $N_i(n) = A_i - Z_i$, where "p" and "n" indicate protons or neutrons, respectively.

I. Estimates of $E_i(t_3)$

Dr. Kurath has suggested two largely independent approaches to estimating $E(t_3) = \text{max.}\ [\langle S_{zt_3}\rangle/S]$:

A. The first approach uses transition amplitude estimates from Ref. 1, which rely on a pure 1p-shell model for nuclei with $4<A<16$, and which reflect information about excited nuclear states in addition to ground-state properties. In Table I we list the amplitudes taken from Ref. 1 and the results, including values for some nuclei that are of more general interest. Specifically, we have taken

$$\langle S_{zt_3}\rangle_{\text{max.}} = 1/2 \left(\frac{6J}{J+1}\right)^{1/2} \cdot A^{\text{gnd. st.}}_{1(01)t_3}, \quad (2)$$

where J is the total angular momentum of the ground-state nucleus and the spin-dependent amplitude is written in the notation of Ref. 1. For completeness, we note that the corresponding "orbital" contribution is estimated as

$$\langle L_{zt_3}\rangle_{\text{max.}} = \left(\frac{4J}{J+1}\right)^{1/2} \cdot A^{\text{gnd. st.}}_{1(10)t_3}, \quad (3)$$

and we include these values in Table I in order to make it clear that $\langle J_{zt_3} \rangle = \langle S_{zt_3} \rangle + \langle L_{zt_3} \rangle$, as a check on internal consistency. Dr. Kurath thinks that these estimates are generally trustworthy at around the 10% level, perhaps a little better for some nuclei and somewhat worse for others.

Incidentally, a striking datum of Table I is the nearly total dominance of p↑ in ^{7}Li↑. This would seem to indicate that ^{7}LiH would be an excellent polarized proton target material for certain experiments (e.g., inclusive), contrary to what some of us (D.H.!) have thought.

B. The second approach uses only the observed total angular momentum and magnetic moment μ of the ground state, plus some more-or-less plausible assumptions. The first assumption is that the magnetic moments of the bound nucleons are equal to their free values:

$$\mu = 2\mu_p \langle S_{zp} \rangle_{max.} + 2\mu_n \langle S_{zn} \rangle_{max.} + \langle L_{zp} \rangle_{max.} \qquad (4)$$

where $\mu_p = 2.793$, $\mu_n = -1.913$ nuclear magnetons. The second assumption is that i-spin is a good quantum number. For the even-A, T=0 nuclei, one then has

$$\langle L_{zn} \rangle = \langle L_{zp} \rangle,$$
$$\langle S_{zn} \rangle = \langle S_{zp} \rangle,$$

and for the total angular momentum,

$$\langle L_{zp} \rangle_{max.} + \langle S_{zp} \rangle_{max.} = J/2 \quad . \qquad (5)$$

Equations (4) and (5) have unique solutions,

$$\begin{aligned} \langle S_{zp} \rangle_{max.} &= (\mu - J/2)/[2(\mu_p + \mu_n)-1] \\ &= 1.32(\mu - J/2), \end{aligned} \tag{6}$$

$$\begin{aligned} \langle L_{zp} \rangle_{max.} &= [J(\mu_p + \mu_n)-\mu]/[2(\mu_p + \mu_n)-1] \\ &= 1.32(0.880J-\mu) . \end{aligned}$$

For the odd-A nuclei, the constraint on μ only reduces the total degrees of freedom to two. However, if one considers the observed moment, μ_m, of the "mirror" nuclei in the same spirit, the degrees of freedom can be further reduced by one:

$$\begin{aligned} \mu &= 2\mu_p\langle S_{zp} \rangle_{max.} + 2\mu_n\langle S_{zn} \rangle_{max.} + \langle L_{zp} \rangle_{max.} , \\ \mu_m &= 2\mu_p\langle S_{zn} \rangle_{max.} + 2\mu_n\langle S_{zp} \rangle_{max.} + \langle L_{zn} \rangle_{max.} , \\ J &= \langle S_{zp} \rangle_{max.} + \langle S_{zn} \rangle_{max.} + \langle L_{zp} \rangle_{max.} + \langle L_{zn} \rangle_{max.} , \end{aligned} \tag{7}$$

and the solution can be expressed as

$$\begin{aligned} \langle S_{zp} \rangle_{max.} + \langle S_{zn} \rangle_{max.} &= (\mu + \mu_m - J)/[2(\mu_p + \mu_n)-1] \\ &= 1.32 (\mu + \mu_m - J) . \end{aligned} \tag{8}$$

Unfortunately, one degree of freedom remains, but the result may still give us some guidance.

Table II lists the results of Eqs. (6) and (8). Under comparison, Tables I and II are seen to be in fair agreement, except for the nitrogen isotopes.

Although the above two approaches are not entirely independent in that they both assume constituent nucleons having "free" moments, perhaps it is not unreasonable to use the results as an indication of the possible uncertainties. We have done this in Table III, for the nuclei of specific interest for E-770. Essentially, these limits correspond to the mean of the Table I and Table II values $\pm \Delta$, where Δ is the difference between the results of Tables I and II. Obviously, in the case of ^{11}B, some further "guesstimating" has been done.

II. Estimate of P_i

Table IV lists the vector polarizations of the various nuclei that are to be expected in an "equal spin temperature" (EST) situation. EST is known to be valid in several of the older target materials, and has been (roughly) verified for the new "ethylamine" material in the case of ^{11}B. This assumption is apparently invalid for some other materials, notably radiolytically-doped NH_3.

III. Estimate of a_i

Table V lists the target composition for "ethylamine" target material. The number densitites are normalized to $n_H = 1$. The contributions of the metal and plastic parts of the target refrigerator are not included.

IV. Estimate of $S_i(t_i)$

The "selectivity" parameter is perhaps the greatest source of uncertainty in this calculation. Roughly speaking, it is a measure of the extent to which the effects of "valence" nucleons are amplified in the scattering experiment. As such, it must depend both upon the exact type of nucleus, and on the type

of scattering experiment, and may even vary over the dynamic range of a given experiment. It seems likely to us that $S > 1$ for most medium-energy experiments. For some high-energy experiments which see "anomalous" A-dependence effects, one could have $S < 1$. With a degree of confidence that only the deeply ignorant can muster, we shall decree that $S_i(t_3) = 2$, uniformly for E-770.

V. Results

For the "ethylamine" material, Eq. (1) then becomes

$$\begin{aligned} &\text{"upper limit":} \quad P_B(p) = 0.0035P(^{10}B) + 0.0118P(^{11}B) - 0.0164P(^{14}N), \\ &\text{"lower limit":} \quad P_B(p) = 0.0033P(^{10}B) + 0.0085P(^{11}B) - 0.0555P(^{14}N), \end{aligned} \tag{9}$$

where we have conservatively applied the upper and lower limits of Table III conspiratorially for all three nuclear species.

Table VI lists the results as a function of $P(^1H)$.

It is worth noting that the potential background polarisation could be significantly reduced by enriching to 100% ^{10}B. For that case Eqs. (9) become

$$\begin{aligned} &\text{"upper limit":} \quad P_B(p) = 0.0177P(^{10}B) - 0.0164P(^{14}N) \\ &\text{"lower limit":} \quad P_B(p) = 0.0165P(^{10}B) - 0.0555P(^{14}N) \end{aligned} \tag{10}$$

For example, for $P(^1H) = 70\%$, $P_B(p) = +0.0029, -0.0006$.

Please let us have your comments.

1. T.-S.H. Lee and D. Kurath, Phys. Rev. C21, 293 (1980).

Table I

Results for $\langle S_z \rangle$ Based on the Model of Reference 1

Nucleus	J	t_3	g.s. A 1(01)	g.s. A 1(10)	$\langle S_z \rangle$	$\langle L_z \rangle$	$\langle S_z \rangle + \langle L_z \rangle$
^{6}Li	1	p or n	0.507	0.043	0.439	0.061	0.500
^{7}Li	3/2	p	0.525	0.262	0.498	0.406	0.904
		n	0.005	0.381	0.005	0.590	0.595
^{10}B	3	p or n	0.387	0.629	0.410	1.089	1.499
^{11}B	3/2	p	0.329	0.590	0.312	0.914	1.226
		n	0.006	0.174	0.006	0.270	0.276
^{13}C	1/2	p	-0.003	0.115	-0.002	0.133	0.131
		n	-0.235	0.464	-0.166	0.536	0.370
^{14}N	1	p or n	-0.257	0.511	-0.223	0.723	0.500
^{15}N	1/2	p	-0.236	0.577	-0.167	0.666	0.499

TABLE II

Results for $\langle S_z \rangle$ Based on Observed Moments

Nucleus	μ	$\langle S_{zp} \rangle$	$\langle L_{zp} \rangle$	$\langle S_{zp} \rangle + \langle S_{zn} \rangle$
^{6}Li	0.822	0.424	0.076	---
^{7}Li	3.256	---	---	?
^{7}Be	?			
^{10}B	1.801	0.397	1.103	---
^{11}B	2.688	---	---	0.295
^{11}C	-0.964			
^{13}C	0.702	---	---	-0.158
^{13}N	(-)0.322			
^{14}N	0.404	-0.126	0.626	---
^{15}N	-0.283	---	---	-0.084
^{15}O	0.719			

TABLE III

"Limits" on $\langle S_{zp} \rangle$

Nucleus	$\langle S_{zp} \rangle$ "Lower Limit"	$\langle S_{zp} \rangle$ "Upper Limit"
^{10}B	+ 0.39	+ 0.42
^{11}B	+ 0.25	+ 0.35
^{14}N	- 0.27	- 0.08

Table IV

Nuclear Vector Polarization at Equal Spin Temperature

^{1}H	^{2}H	^{6}Li	^{7}Li	^{10}B	^{11}B	^{13}C	^{14}N	^{15}N
0.100	0.0206	0.0182	0.0649	0.0288	0.0536	0.0253	0.00967	-0.0120
0.200	0.0415	0.0390	0.130	0.0580	0.108	0.0509	0.0195	-0.0215
0.300	0.0633	0.0602	0.197	0.0884	0.164	0.0777	0.0298	-0.0320
0.400	0.0865	0.0825	0.266	0.121	0.222	0.106	0.0408	-0.0433
0.500	0.112	0.107	0.338	0.156	0.284	0.137	0.0528	-0.0559
0.600	0.141	0.135	0.416	0.195	0.351	0.173	0.0667	-0.0704
0.650	0.157	0.151	0.457	0.217	0.388	0.192	0.0745	-0.0786
0.700	0.176	0.168	0.500	0.242	0.427	0.215	0.0833	-0.0879
0.750	0.196	0.188	0.546	0.269	0.470	0.240	0.0934	-0.0984
0.800	0.221	0.212	0.596	0.301	0.518	0.269	0.105	-0.111
0.850	0.251	0.241	0.652	0.340	0.572	0.306	0.120	-0.127
0.900	0.292	0.280	0.716	0.390	0.638	0.354	0.141	-0.148
0.930	0.326	0.313	0.762	0.431	0.687	0.394	0.158	-0.167
0.960	0.376	0.362	0.818	0.490	0.750	0.454	0.185	-0.195
0.980	0.435	0.419	0.868	0.554	0.809	0.521	0.217	-0.229
0.990	0.490	0.473	0.903	0.609	0.854	0.582	0.249	-0.262
0.9950	0.540	0.523	0.928	0.657	0.887	0.637	0.280	-0.295
0.9980	0.600	0.582	0.951	0.710	0.919	0.701	0.320	-0.337
0.9990	0.641	0.623	0.963	0.744	0.936	0.742	0.349	-0.367
0.9995	0.678	0.660	0.972	0.773	0.950	0.779	0.377	-0.397
0.99990	0.752	0.735	0.986	0.826	0.971	0.847	0.441	-0.464
0.999990	0.829	0.815	0.994	0.877	0.986	0.911	0.522	-0.550

TABLE V

Target Composition of EA(.85)BA(.15), Immersed in LHe^4, Neglecting the Dopant. Packing fraction = 0.65.

Nucleus	Density (g/cm^3)	n/n_H
^1H	0.0887	1.000
^4He	0.049	0.139
^{10}B	0.00532	0.00604
^{11}B	0.0234	0.0242
^{12}C	0.247	0.214
^{14}N	0.181	0.147

TABLE VI

Background Proton Polarization vs. $P(^1H)$

$P(^1H)$	$P_B(p)$ "Lower Limit"	$P_B(p)$ "Upper Limit"
0.100	0.00001	0.0006
0.300	0.00002	0.0018
0.500	-0.00001	0.0030
0.700	-0.0002	0.0045
0.800	-0.0005	0.0055
0.900	-0.0011	0.0066
0.930	-0.0015	0.0070
0.960	-0.0023	0.0076
0.980	-0.0034	0.0080
0.990	-0.0046	0.0082
0.995	-0.0059	0.0082
0.9990	-0.0090	0.0080
0.99990	-0.014	0.0072
0.999990	-0.018	0.0062
1.	-0.044	-0.0011

Appendix B Least-Squares Fit With One-Point Constraint

The equations which are solved, by least-squares fitting, to determine each component of the magnetic field are discussed below. The equations are obtained by taking derivatives of the function C with respect to the coefficients and the constraint:

$$\frac{\partial C}{\partial a_m} = \sum_{i=1}^{5}(-x_i^m)\left[B_{ij} - \sum_{n=0}^{2} a_n x_i^n\right] - \lambda x_k^m = 0 \quad m = 0,1,2 \tag{B.1}$$

$$\frac{\partial C}{\partial \lambda} = F = B_{kj} - \sum_{n=0}^{2} a_n x_k^n = 0\,. \tag{B.2}$$

Rewriting the above expressions gives

$$\sum_{n=0}^{2} a_n \left[\sum_{i=1}^{5} x_i^{n+m}\right] - \lambda x_k^m = \sum_{i=1}^{5} B_{ij} x_i^m \quad (m - equations) \tag{B.3}$$

$$\sum_{n=0}^{2} a_n x_k^n = B_{kj}\,. \quad (1 - equation) \tag{B.4}$$

Therefore the system of equations to be solved is

$$\begin{pmatrix} \sum_i x_i^0 & \sum_i x_i & \sum_i x_i^2 & -x_k^0 & a_0 \\ \sum_i x_i & \sum_i x_i^2 & \sum_i x_i^3 & -x_k & a_1 \\ \sum_i x_i^2 & \sum_i x_i^3 & \sum_i x_i^4 & -x_k^2 & a_2 \\ x_k^0 & x_k & x_k^2 & 0 & \lambda \end{pmatrix} = \begin{pmatrix} \sum_i B_{ij} \\ \sum_i B_{ij} x_i \\ \sum_i B_{ij} x_i^2 \\ B_{kj} \end{pmatrix}$$

where $i = 1, 2, 3, 4, 5$. This system of equations is solved by a subroutine which was written at ANL and uses the Crout algorithm.

The error in the coefficients is given by the diagonal elements in the error matrix for the fit [Or-58]:

$$E = \begin{pmatrix} (\Delta a_0)^2 & & & \\ & (\Delta a_1)^2 & & \\ & & & \\ & & & (\Delta a_n)^2 \end{pmatrix}$$

The error matrix is simply the inverted weight matrix. The elements of the weight matrix are given by

$$W_{nm} = \frac{1}{2}\frac{\partial^2 C}{\partial a_n a_m} = \frac{1}{2}\sum_i x_i^{n+m} \tag{B.5}$$

Therefore, for $N = 2$:

$$W = \frac{1}{2}\begin{pmatrix} \sum_i x_i^0 & \sum_i x_i & \sum_i x_i^2 \\ \sum_i x_i & \sum_i x_i^2 & \sum_i x_i^3 \\ \sum_i x_i^2 & \sum_i x_i^3 & \sum_i x_i^4 \end{pmatrix}$$

This matrix is inverted to give the error matrix. It should be noted that W is just a submatrix of the solution matrix.

Appendix C The Monte-Carlo Program

On the following pages is a listing of the Monte-Carlo program used to check the magnetic field parameterization of our spectrometer. It was also used to correct the scattering angle of the recoil proton for the effects of the polarized target magnetic field. The main program is listed first, followed by the various subroutines.

```
      PROGRAM DICE

C
C MONTE CARLO PROGRAM TO GENERATE  np- ELASTIC SCATTERING EVENTS AND n,p GOES
C TO PI,D EVENTS FOR EXPERIMENTS E665/770.    B.GARNETT
C
      IMPLICIT NONE
      INTEGER RUNNO,EXPNO
      INTEGER NUM_PART,CASE,IPLANE
      INTEGER I,J,K,II,JJ,KK,IPER,ICNT
      INTEGER MAXEVT
      LOGICAL HIT,HERA,FIRST,GOOD_MOMENTUM
      CHARACTER REC*80,ANS*1,WHICHSEED*1
      REAL*8 NUT_MAS,PI,FRAC,TANG_SCM_Z
      PARAMETER (NUT_MAS=939.6D0)
      PARAMETER (TANG_SCM_Z=335.28D0)
      COMMON /COUNT/ICNT,IPER
      COMMON /POSZ/POS(23)
      REAL*8 POS
      COMMON /SCM/Z1,D1,D2
      REAL*8 L1,Z1,D1,D2,T
      COMMON /BLOCK2/ISTART,KKK
      INTEGER ISTART,KKK
      COMMON /BNOTXYZ/ BNOTX,BNOTY,BNOTZ,XNEAR,YNEAR,ZNEAR
      REAL*8 BNOTX,BNOTY,BNOTZ
      INTEGER XNEAR,YNEAR,ZNEAR
      COMMON /BEAM/EBEAM
      COMMON /OUTPT/BDAT,WTCOFFS,XYZNOT
      REAL*8 BDAT(3,7,4),WTCOFFS(3,7),XYZNOT(3)
      COMMON /RELA/GAMMA,VELOC,C,ENEUTRON
      REAL*8 GAMMA,VELOC,C,ENEUTRON
      COMMON /NON_P_1/ P_P,HERA_ANG,SCM_ANG,PHICOTH,KPERIM
      INTEGER*2 KPERIM  !FLAG CONTROLLING EVENT GENERATION
      REAL*8 P_P,HERA_ANG,SCM_ANG,PHICOTH(6)  ! PHICOTH(PHI MIN.,PHI MAX.,THETA MIN.,THETA MAX.)
      REAL*8 UDPHI,LDPHI                !PHICOTH(5)=UDPHI,PHICOTH(6)=LDPHI
      COMMON /NON_V_1/ P,P_TOT
      REAL*8 P(7),P_TOT                 ! P(X,Y,Z,Px,Py,Pz,t),P_TOT
      COMMON /SEED/ ISEED,IENERGY,V(98),IDUM
      INTEGER*4 ISEED,IENERGY,MAP,IDUM
      REAL*4 V
      COMMON /ANGLE/THETA,PHI,ALPHA
      REAL*8 ENERGY,EBEAM,ALPHA,THETA,PHI
      COMMON /GUN/GTHETA,GPHI
      REAL*8 GTHETA,GPHI
      REAL*8 PX,PY,PZ,PT
      COMMON /DEUT/DODEUT,INDEX
      INTEGER*2 INDEX
      LOGICAL DODEUT
        LOGICAL STAT,LIB$INIT_TIMER,LIB$SHOW_TIMER
      EQUIVALENCE (P(4),PX),(P(5),PY),(P(6),PZ)
      EQUIVALENCE(P(7),T)
      DATA ISEED/-28677519/
      DATA HERA_ANG/0.0/
      DATA C/29.979246D0/
      DATA L1/247.9/
      DATA PI/3.14159265358D0/
C*      STAT =LIB$INIT_TIMER()  !START CPU TIMER
C*      IF(.NOT. STAT) THEN
C*        CALL LIB$STOP(%VAL(STAT))
C*      END IF
      FIRST=.TRUE.
      HIT=.FALSE.
      DODEUT=.FALSE.
      HERA=.TRUE.
      IDUM=ISEED          !RANO NEEDS THIS TO INITIALIZE
      INDEX=1
      ISTART=0
      T=0.0D0
      OPEN(19,NAME='POSZ.DAT',STATUS='OLD')
      DO I=1,23
      READ(19,*)POS(I)
      ENDDO
      CLOSE(19)
      OPEN(20,NAME='PHICOTH.DAT',STATUS='OLD')
      DO I=1,6
```

```
      READ(20,*)PHICOTH(I)
      ENDDO
      READ(20,*)KPERIM
      CLOSE(20)
      WRITE(6,*)'CHOOSE SCM FIELD MAP (HIGH FIELD=1,LOW=2):'
      READ(5,*)MAP
* READ IN APPROPRIATE FIELD MAP
      CALL SCM_MAP_READ(MAP)
99    WRITE(6,2)
      READ(5,*)NUM_PART
      WRITE(6,4)
4     FORMAT(1X,'ENTER NUMBER OF GOOD EVENTS:'$)
      READ(5,*)MAXEVT
      WRITE(6,7)
      READ(5,1001) ANS
      IF((ANS.EQ.'Y').OR.(ANS.EQ.'y')) THEN
      DODEUT=.TRUE.
      WRITE(6,11)
      READ(5,1001)ANS
      IF((ANS.EQ.'N').OR.(ANS.EQ.'n')) INDEX=2
      ENDIF
      WRITE(6,1)
      READ(5,*)IENERGY
      WRITE(6,*)'ENTER THE SPECTROMETER ANGLE (DEG.):'
      READ(5,*)SCM_ANG
      WRITE(6,*)'ENTER EXPERIMENT NUMBER (665 OR 770):'
      READ(5,*)EXPNO
      WRITE(6,*)'ENTER RUN NUMBER (WILL DETERMINE WHICH
     * SURVEY CONSTANTS ARE USED) :'
      READ(5,*)RUNNO
      WRITE(6,*)'READING IN THE SURVEY CONSTANTS'
      CALL SURVEY(EXPNO,RUNNO)
      WRITE(6,*)'HERA ON (Y/N) ? :'
      READ(5,1001)ANS
      IF((ANS.EQ.'N').OR.(ANS.EQ.'n')) THEN
      HERA=.FALSE.
      GOTO 30
      ENDIF
      WRITE(6,*)'ENTER TARGET POLARIZATION ANGLE (DEG.-RELATIVE TO BEAM
     *):'
      READ(5,*)ALPHA
30    WRITE(6,3)
      READ(5,13)REC
      WRITE(6,*)'IS THIS THE FIRST RUN WITH THESE PARAMETERS (Y/N) ? :'
      READ(5,1001) WHICHSEED
        IF((WHICHSEED.EQ.'N').OR.(WHICHSEED.EQ.'n')) THEN
        OPEN(21,NAME='SEED.DAT',STATUS='OLD')
        READ(21,1200)ISEED
        IDUM=1            !TO REENTER RAND W/O REINITIALIZING NEED IDUM>0
        DO 1215 I=1,98
        READ(21,1210)V(I)
1215    CONTINUE
        CLOSE(21)
        ENDIF
1     FORMAT(1X,'ENTER ENERGY (1,2,OR 3) - 500MeV=1,650MeV=2
     *,800MeV=3 : ')
2     FORMAT(1X,'ENTER NUMBER OF TRACKS TO RUN:'$)
3     FORMAT(1X,'ENTER THE NAME OF THE FILE TO WRITE
     *THE DATA TO:(1 TO 80 CHARS)'$)
7     FORMAT(1X,'DO YOU WISH TO DO DEUTERON KINEMATICS (Y/N) ?')
11    FORMAT(1X,'DO YOU WANT FORWARD/CM ANGLES (Y/N) ?')
13    FORMAT(1A80)
      GOTO (100,200,300)IENERGY
100   ENERGY=493.0D0
      GOTO 400
200   ENERGY=643.0D0
      GOTO 400
300   ENERGY=793.0D0
C ANGLES ARE IN RAD
400   SCM_ANG=SCM_ANG*PI/180.0D0
      ALPHA=ALPHA*PI/180.D0
      EBEAM=ENERGY
      ENEUTRON=EBEAM
      ENERGY=(ENERGY+NUT_MAS)
      ENERGY=ENERGY*ENERGY
      P_P=DSQRT(ENERGY-(NUT_MAS*NUT_MAS))
```

```
C       OPEN(90,NAME=REC,STATUS='NEW',DISP='KEEP',RECORDSIZE=1300,
C      *BLOCKSIZE=8000,SHARED)
       OPEN(90,STATUS='NEW',DISP='KEEP',RECORDSIZE=1300,
      *BLOCKSIZE=8000,SHARED)
**** CREATE THE SEED FILE FOR THE RANDOM NUMBER GENERATOR
         OPEN(39,NAME='SEED.DAT',STATUS='NEW')
**** OPEN AN OUTPUT FILE TO WRITE S1 POSITIONS IN - FOR DIAGNOSTICS ****
       OPEN(61,NAME='S1XY.DAT',STATUS='NEW',DISP='KEEP',SHARED)
       WRITE(61,425)
425    FORMAT('DO IT')
       WRITE(61,451)
       WRITE(61,*)'-30.48,-13.97'
       WRITE(61,*)'-30.48,13.97'
       WRITE(61,*)'30.48,13.97'
       WRITE(61,*)'30.48,-13.97'
       WRITE(61,*)'-30.48,-13.97'
         IF(NUM_PART.LE.2000) THEN
         WRITE(61,450)NUM_PART
         ELSE
         I=2000
         WRITE(61,450)I
         ENDIF
C
C********OPEN FILE TO STORE X,Y IN S1 FOR GOOD EVENTS**********
C
       OPEN(62,NAME='GS1XY.DAT',STATUS='NEW',DISP='KEEP',SHARED)
       WRITE(62,425)
       WRITE(62,451)
       WRITE(62,*)'-30.48,-13.97'
       WRITE(62,*)'-30.48,13.97'
       WRITE(62,*)'30.48,13.97'
       WRITE(62,*)'30.48,-13.97'
       WRITE(62,*)'-30.48,-13.97'
         IF(MAXEVT.LE.2000) THEN
         WRITE(62,450)MAXEVT
         ELSE
         I=2000
         WRITE(62,450)I
         ENDIF
C
450    FORMAT('PLOT IT(',I5,',-1,8,0,')
451    FORMAT('PLOT IT(5,0,16,0')
****   OPEN AN OUTPUT FILE TO WRITE THETA AND PHI FOR THE GOOD EVENTS
       OPEN(69,NAME='PHITHETA.DAT',STATUS='NEW',DISP='KEEP',SHARED)
       WRITE(69,425)
       WRITE(69,450)NUM_PART
       IPEN=0
       DO 1000 I=1,NUM_PART
C*       STAT =LIB$SHOW_TIMER()
C*       WRITE(6,*)'TIME AT MAIN DO LOOP'
C*       IF(.NOT.STAT) THEN
C*         CALL LIB$STOP(%VAL(STAT))
C*       END IF
       IPLANE=2
       ICNT=I
       IF(HIT) CALL RES_PUT
       HIT=.FALSE.
       CALL INI_MANETR
       GOOD_MOMENTUM = .FALSE.
       DO WHILE (.NOT.GOOD_MOMENTUM)
         CALL INIT_P
         CALL TARGET(GOOD_MOMENTUM)
       END DO
       IF(HIT) GOTO 1000
C COMMENT CALL TO PUT_P OUT IF CALCULATING PROJECTIONS IN THERA2.SUB
       CALL PUT_P(.TRUE.,1)
C THE LENGTH,P(7) IS THE TIME THE PARTICLE SPENT IN THE TARGET
C IN C     [1] ==> PLANE NUMBER
C      [2] ==> LOGICAL: FLAG SET IF PARTICLE HIT SOMETHING
       IF (.NOT. HERA) THEN
       PT=DSQRT(PX*PX+PY*PY+PZ*PZ)
       CALL EXTR_PARMS(PT)
       GOTO 40
       ENDIF
       CALL P_TRACE(1,IPLANE,HIT,FIRST)
       IF(HIT) GOTO 1000
```

```
C TRANSLATE AND ROTATE X,Z,Px,Pz TO THE SCM COORD. SYSTEM.
 40     CALL HERASCM(P(1),P(3),.FALSE.)
        CALL HERASCM(P(4),P(6),.TRUE.)
        IF(P(6).LE.0.0D0) GOTO 1000
        IF((IPLANE.GE.3).AND.(IPLANE.LE.5)) GOTO 60
        IF((IPLANE.GE.6).AND.(IPLANE.LE.8)) GOTO 70
        IF(IPLANE.GE.9) GOTO 80
****
 50     CALL P_TRACE(2,IPLANE,HIT,FIRST)
        IF(HIT) GOTO 1000
        IPLANE=3
 60     CALL P_TRACE(3,IPLANE,HIT,FIRST)
        IF(HIT) GOTO 1000
        IPLANE=4
 70     CALL P_TRACE(4,IPLANE,HIT,FIRST)
        IF(HIT) GOTO 1000
        IPLANE=5
 80     CALL P_TRACE(5,IPLANE,HIT,FIRST)
        IF(HIT) GOTO 1000
        IPLANE=6
        CALL P_TRACE(6,IPLANE,HIT,FIRST)
        IF(HIT) GOTO 1000
        IPLANE=7
        CALL P_TRACE(7,IPLANE,HIT,FIRST)
        IF(HIT) GOTO 1000
        IPLANE=8
        CALL P_TRACE(8,IPLANE,HIT,FIRST)
        IF(HIT) GOTO 1000
        CALL PUT_P(.FALSE.,2)      ! A RECORD IS WRITTEN WHEN PUT_P IS CALLED WITH THE ARG=.FALSE.
        WRITE(69,990)@THETA,GPHI
990     FORMAT(F6.2,',',F6.2)
          IPER=IPER+1
          IF(IPER.EQ.MAXEVT) GOTO 1010
1000    CONTINUE
1010    CONTINUE
C*        STAT =LIB$SHOW_TIMER()
C*        WRITE(6,*)'TIME AT END OF MAIN DO LOOP'
C*        IF(.NOT.STAT) THEN
C*          CALL LIB$STOP(%VAL(STAT))
C*        END IF
        WRITE(6,*)'TOTAL NO. EVENTS,NO. GOOD EVENTS,% GOOD EVENTS:'
          FRAC=FLOAT(IPER)/FLOAT(ICNT)
          WRITE(6,*) ICNT,IPER,100.0*FRAC
1001    FORMAT(A1)
1100    CLOSE(90)
**** UNIT 61 IS THE SIXY POSITION FILE
        WRITE(61,*)'RETURN'
        WRITE(61,*)'END'
        CLOSE(61)
**** UNIT 62 IS THE GOOD SIXY POSITION FILE
        WRITE(62,*)'RETURN'
        WRITE(62,*)'END'
        CLOSE(62)
**** UNIT 69 IS THE GOOD THETA,PHI FILE
        CLOSE(69)
**** UNIT 39 IS THE SEED FILE
          WRITE(39,1200)ISEED
          DO 1220 J=1,98
          WRITE(39,1210)V(J)
1210      FORMAT(F11.8)
1220      CONTINUE
1200      FORMAT(O15)
          CLOSE(39)
        STOP ' NORMAL END'
        END

        SUBROUTINE WRITER(I)
* USED FOR DIAGNOSTICS TO PRINT POSITION AND MOMENTUM TO THE SCREEN.
        COMMON /NON_V_1/XP,P_TOT
        REAL*8 XP(7),P_TOT
        WRITE(6,*)'I= ',I
        WRITE(6,*)'X,Y,Z:
        WRITE(6,*)XP(1),XP(2),XP(3)
        WRITE(6,*)'PX,PY,PZ:'
        WRITE(6,*)XP(4),XP(5),XP(6)
        RETURN
```

```
      END

      SUBROUTINE INIT_P
* THIS SUBROUTINE GENERATES THE NEUTRON BEAM MOMENTUM.  IT IS CHOSEN AT RANDOM
* AND GENERATED AS A GAUSSIAN DISTRIBUTION WITH AN ENERGY DEPENDENT FWHM AS
* DETERMINED BY BJORK.  THE INTERACTION POINT IN THE TARGET IS ALSO GENERATED HERE.
      IMPLICIT NONE
      EXTERNAL GAUS_S,IN_TARG,GAUS_M,RANO
      REAL*4 RANO
      REAL*8 GAUS_S,GAUS_M
      LOGICAL IN_TARG
      PARAMETER NUT_MAS=939.6D0
      PARAMETER PI=3.14159265358D0
      PARAMETER WIDTH1=14.93D0
      PARAMETER WIDTH2=17.35D0
      PARAMETER WIDTH3=21.83D0
      PARAMETER CONST=2.354D0                                    ! FWHM=2.354*SIGMA
      PARAMETER TARG_RAD=1.85D0
      PARAMETER TARG_DIAG=6.22D0                                 ! DIAGONAL +.1 OF THE TARGET
      PARAMETER COLL_ANG=4.554D-6                                ! .5 OF COLLIMATOR SOLID ANGLE, BJORK THESIS, PP. 155
      COMMON /RELA/GAMMA,VELOC,C,ENEUTRON
      REAL*8 GAMMA,VELOC,C,ENEUTRON
      COMMON /MOM_P_1/ P_P,MERA_ANG,SCM_ANG,PHICOTH,KPERIM
      INTEGER*2 KPERIM
      REAL*8 P_P,MERA_ANG,SCM_ANG,PHICOTH(6)
      COMMON /MOM_V_1/ P,P_TOT
      REAL*8 P(7),P_TOT                                          ! P(X,Y,Z,Px,Py,Pz,L)
      REAL*8 POS_X,POS_Y,POS_Z,POS_R                             ! POSITION VALUES
      REAL*8 P_PHI,P_THA,T_ANG                                   ! MOMENTUM VALUES
      REAL*8 SIGMA
      COMMON /TGT_PT/POS_X,POS_Y,POS_Z
      COMMON /SEED/ ISEED,IENERGY,V(98),IDUM
      INTEGER*4 ISEED,IENERGY,IDUM
      REAL*4 V
      REAL*8 TEMP
      INTEGER*4 II
        INTEGER I
      LOGICAL IN

      GOTO (10,20,30)IENERGY
10    SIGMA=WIDTH1/CONST
      GOTO 40
20    SIGMA=WIDTH2/CONST
      GOTO 40
30    SIGMA=WIDTH3/CONST
*40    P_TOT=GAUS_S(SIGMA,P_P,1.267)                              !GAUSSIAN MOMENTUM DISTRIBUTION OUT TO FWHM
********USE MONOENERGETIC NEUTRONS
40    P_TOT=P_P
C
      TEMP=RANO(IDUM,ISEED,V)
      P_THA=DACOS(1.0-COLL_ANG*TEMP)
      P_phi=2.0D0*PI*RANO(IDUM,ISEED,V)
      ENEUTRON=DSQRT(P_TOT*P_TOT+NUT_MAS*NUT_MAS)
      P(4)=P_TOT*COS(P_PHI)*SIN(P_THA)
      P(5)=P_TOT*SIN(P_PHI)*SIN(P_THA)
      P(6)=P_TOT*COS(P_THA)
      POS_R=GAUS_M(TARG_RAD,TARG_RAD)
*100   T_ANG=2.0D0*PI*RAN(ISEED)
*      POS_X=POS_R*DCOS(T_ANG)
*      POS_Y=POS_R*DSIN(T_ANG)
*      POS_Z=TARG_DIAG*(.5-RAN(ISEED))
* INTERACTION PT. NOW AT TARGET CENTER
       POS_X=0.0D0
       POS_Y=0.0D0
       POS_Z=0.0D0
*      IN=IN_TARG(POS_X,POS_Y,POS_Z)
*      IF(.NOT.IN) GOTO 100
      P(1)=POS_X
      P(2)=POS_Y
      P(3)=POS_Z
      P(7)=0.0D0
      RETURN
      END
C
      SUBROUTINE TARGET(GOOD_MOMENTUM)
* THIS SUBROUTINE DETERMINES THE PROTON (OR DEUTERON) INITIAL MOMENTUM FROM THE
```

```
* GENERATED NEUTRON MOMENTUM AND np - KINEMATICS.
      EXTERNAL RANO
      INTEGER NFLAG
      REAL*8 PRO_MAS,NUT_MAS,PI
      REAL*8 DUT_MAS,PINOT_MAS
      REAL*8 GN
      REAL*4 RANO
      PARAMETER (PRO_MAS=938.256D0)
      PARAMETER (NUT_MAS=939.6D0)
      PARAMETER (DUT_MAS=1875.587D0)
      PARAMETER (PINOT_MAS=134.963D0)
      PARAMETER (PI=3.141592653589D0)
      PARAMETER (GN=8.0D0)
      COMMON /RELA/GAMMA,VELOC,C,ENEUTRON
      REAL*8 GAMMA,VELOC,C,ENEUTRON
      COMMON /MON_P_1/ P_P,HERA_ANG,SCM_ANG,PHICOTH,KPERIM
      INTEGER*2 KPERIM  !FLAG CONTROLLING EVENT GENERATION
      REAL*8 P_P,HERA_ANG,SCM_ANG,PHICOTH(6)   !PHICOTH(PHI MIN.,PHI MAX.,THETA MIN.,THETA MAX. - IN CM COORD.
        REAL*8 UDPHI,LDPHI
      COMMON /MON_V_1/ P,P_TOT
      COMMON /ANGLE/THETA,PHI,ALPHA
      COMMON /GUN/GTHETA,GPHI
      REAL*8 GTHETA,GPHI
      COMMON /BEAM/EBEAM
      REAL*8 EBEAM,SPECANG
      REAL*8 P(7),P_TOT                    ! P(X,Y,Z,Px,Py,Pz,L)
      REAL*8 P1(3),P2(3),COTH,PHI,THETA,SINPHI,COSPHI,ALPHA
      COMMON /SEED/ ISEED,IENERGY,V(98),IDUM
      INTEGER*4 ISEED,IDUM
      REAL*4 V
      COMMON /DEUT/DODEUT,INDEX
      INTEGER*2 INDEX,NSOLN
      LOGICAL DODEUT
      REAL*8 M3,M4,CMTHETA(2)
      REAL*8 XT,YT
      LOGICAL SIGN,GOOD_MOMENTUM

      SIGN=.FALSE.

      IF(DODEUT) THEN
      M3=DUT_MAS
      M4=PINOT_MAS
      ELSE
      M3=PRO_MAS
      M4=NUT_MAS
      ENDIF

      P1(1)=P(4)
      P1(2)=P(5)
      P1(3)=P(6)
      P2(1)=0.0D0
      P2(2)=0.0D0
      P2(3)=0.0D0
* HERE THE ANGLE THETA IS THE ANGLE WITH RESPECT TO THE Z-AXIS IN THE
* XZ-PLANE.  PHI IS THE ANGLE ABOVE(PHI>0) OR BELOW(PHI<0) THIS PLANE.
C
        UDPHI=PHICOTH(5)
        LDPHI=PHICOTH(6)
      IF (KPERIM.EQ.0) THEN
222   GTHETA=RANO(IDUM,ISEED,V)*(PHICOTH(4)-PHICOTH(3))+PHICOTH(3)
      GPHI=RANO(IDUM,ISEED,V)*(PHICOTH(2)-PHICOTH(1))+PHICOTH(1)
        IF(GPHI.GT.(PHICOTH(2)+UDPHI*(GTHETA-PHICOTH(3)))) THEN
          GOTO 222
        ELSE IF(GPHI.LT.(PHICOTH(1)+LDPHI*(PHICOTH(4)-GTHETA)))THEN
          GOTO 222
        END IF
      ELSE IF (KPERIM.LT.9) THEN
        GTHETA=PHICOTH(3)
        GPHI=PHICOTH(1)+(PHICOTH(2)-PHICOTH(1))*DFLOAT(KPERIM-1)/GN
        KPERIM=KPERIM+1
      ELSE IF (KPERIM.LT.17) THEN
        GTHETA=PHICOTH(4)
        GPHI=PHICOTH(1)+(PHICOTH(2)-PHICOTH(1))*DFLOAT(KPERIM-9)/GN
        KPERIM=KPERIM+1
      ELSE IF (KPERIM.LT.25) THEN
        GTHETA=PHICOTH(3)+(PHICOTH(4)-PHICOTH(3))*DFLOAT(KPERIM-17)/GN
```

```
          GPHI=PHICOTH(1)+LDPHI*(PHICOTH(4)-GTHETA)
          KPERIM=KPERIM+1
        ELSE IF (KPERIM.LT.33) THEN
          GTHETA=PHICOTH(3)+(PHICOTH(4)-PHICOTH(3))*DFLOAT(KPERIM-25)/GN
          GPHI=PHICOTH(2)+UDPHI*(GTHETA-PHICOTH(3))
          KPERIM=KPERIM+1
        ELSE IF (KPERIM.GT.32) THEN
          KPERIM=0          !GO BACK TO RANDOM ANGLE GENERATION
        END IF
C
* THETA AND PHI DETERMINED HERE ARE THE USUAL POLAR COORDINATES.
        PHI=GPHI*PI/180.0D0                    !CONVERT TO RADIANS FOR TUBORG
        THETA=GTHETA*PI/180.0D0
        XT= -DCOS(PHI)*DSIN(THETA)
        YT= DSIN(PHI)
* TRANSFORM TO POLAR COORDINATES
        IF((THETA.EQ.0.0D0).AND.(PHI.EQ.0.0D0)) GOTO 100
        IF((THETA.EQ.0.0D0).AND.(PHI.GT.0.0D0)) THEN
          THETA=DABS(PHI)
          PHI=PI/2.0D0
          GOTO 100
        ENDIF
        IF((THETA.EQ.0.0D0).AND.(PHI.LT.0.0D0)) THEN
          THETA=DABS(PHI)
          PHI=(3.0D0/2.0D0)*PI
          GOTO 100
        ENDIF
        IF((PHI.EQ.0.0D0).AND.(THETA.GT.0.0D0)) THEN
          PHI=PI
          GOTO 100
        ENDIF
        COTH=DCOS(PHI)*DCOS(THETA)
        THETA=DACOS(COTH)
        IF(THETA.EQ.0.0D0) THEN
          PHI=0.0D0
          GOTO 100
        ENDIF
        SINPHI=DSIN(PHI)/DSIN(THETA)
        PHI=DASIN(SINPHI)
* DETERMINE WHICH QUADRANT (XY-PLANE) THE PARTICLE WILL LIE IN
         IF ((XT.LT.0.0D0).AND.(YT.GT.0.0D0)) PHI=PI-PHI  !2nd QUADRANT
         IF ((XT.LT.0.0D0).AND.(YT.LT.0.0D0)) PHI=PI-PHI  !3rd QUADRANT
*****
100     CALL RECOIL_KIN(P1,THETA,PHI,EBEAM,GOOD_MOMENTUM)
*****
        P(4)=P1(1)
        P(5)=P1(2)
        P(6)=P1(3)
        RETURN
        END

        SUBROUTINE HERA_TRACE(X,Y,Z,X2,Y2,Z2,IPLANE,HIT)
* TRANSFORMS COORDINATES TO THE SCM105 FRAME AND CHECKS IF PARTICLE IS IN A
* DETECTOR PLANE.
        IMPLICIT REAL*8 (A-H,O-Z)
        LOGICAL HIT,FIRST,NEXT
        COMMON /SCM/CASE,L1,Z1,D1,D2
        INTEGER CASE,IPLANE
        COMMON /PRINT/XI,YI,ZI
        COMMON /ANGLE/THETA,PHI,ALPHA
        COMMON /MOM_V_1/P,P_TOT
        COMMON /POSZ/POS
        DIMENSION P(7),POS(23)
        EQUIVALENCE (P(7),T)
        FIRST=.TRUE.
        X0=X
        Y0=Y
        Z0=Z
        XP=X2
        YP=Y2
        ZP=Z2
        CALL X_ROT(X0,Y0,Z0,ALPHA,1.0D0)
        CALL X_ROT(XP,YP,ZP,ALPHA,1.0D0)
        CALL HERA_ROT(X0,Y0,Z0,ALPHA,-1.0D0)
        CALL HERA_ROT(XP,YP,ZP,ALPHA,-1.0D0)
        CALL HERASCM(X0,Z0,.FALSE.)
```

```
      CALL HERASCM(XP,ZP,.FALSE.)
100   IF(ZP.GT.POS(IPLANE)) THEN
      CALL INTERP(POS(IPLANE),X0,Y0,Z0,XP,YP,ZP,NEXT)
* INCREMENT TIME - OF - FLIGHT. TOF IS IN NANOSECONDS.
      IF (ZP.GT. POS(2)) THEN
      CALL TOF_INC(DT,X0,Y0,Z0,XP,YP,ZP)
      T=T+DT
      ENDIF
      CALL CHKXY(IPLANE,HIT,FIRST,2)
      IF(HIT) RETURN
      CALL PUT_P(.TRUE.,2)
      IF(NEXT) THEN
      IPLANE=IPLANE+1
      GOTO 100
      ENDIF
      IPLANE=IPLANE+1
      ENDIF
      RETURN
      END

      SUBROUTINE P_TRACE(I_PP,IP,HIT,FIRST)
* THIS SUBROUTINE DETERMINES THE POSITIONS OF THE PARTICLE IN THE 22 DETECTOR PLANES.
      IMPLICIT NONE
      EXTERNAL IN_TARG
      LOGICAL IN_TARG
      PARAMETER N_PLANE=23
      PARAMETER SCM_DIV=100.0D0
      PARAMETER DIV_STEP=10.0D0
      PARAMETER INT_STEP=100.0D0
      PARAMETER SCM_F_S=-124.0D0
      PARAMETER SCM_R_R=124.0D0
      PARAMETER F_S_TOL=1.0D0
      COMMON /MOM_V_1/ P_V,P_TOT
      COMMON /PRINT/XI,YI,ZI
      REAL*8 XI,YI,ZI
      COMMON /RELA/GAMMA,VELOC,C,ENEUTRON
      REAL*8 GAMMA,VELOC,C,ENEUTRON
      COMMON /ANGLE/THETA,PHI,ALPHA
      REAL*8 THETA,PHI,ALPHA
      COMMON /POSZ/POS
      REAL*8 P_V(7),DL,D_T,P_TOT,T,DT
      REAL*8 X,Y,Z,PX,PY,PZ
      REAL*8 X2,Y2,Z2,PX2,PY2,PZ2,R
      REAL*8 TOL(N_PLANE),POS(N_PLANE),I,J,K
      INTEGER I_PP,I_PLANE,IC,II,LIMIT,IP,INWHERE
      LOGICAL HIT,LFLAG,FIRST,LFOO2,NEXT
      EQUIVALENCE (P_V(1),X),(P_V(2),Y),(P_V(3),Z)
      EQUIVALENCE (P_V(4),PX),(P_V(5),PY),(P_V(6),PZ),(P_V(7),T)
      DATA TOL/23*.01/
      HIT=.FALSE.
      LFLAG=.TRUE.
      NEXT=.FALSE.
      I_PLANE=IP
      INWHERE=I_PP
      GOTO (10,20,30,40,50,60,70,80)INWHERE
       WRITE(6,*) 'I_WHERE TOO LARGE IN P_TRACE'
      STOP 102
C THIS IS THE TARGET IN HERA
10    CALL HERA_ROT(X,Y,Z,ALPHA,1.0D0)
      CALL HERA_ROT(PX,PY,PZ,ALPHA,1.0D0)
      CALL X_ROT(X,Y,Z,ALPHA,-1.0D0)
      CALL X_ROT(PX,PY,PZ,ALPHA,-1.0D0)
      CALL THERA2(I_PLANE,HIT)
      IF(HIT) RETURN
      CALL X_ROT(X,Y,Z,ALPHA,1.0D0)
      CALL X_ROT(PX,PY,PZ,ALPHA,1.0D0)
      CALL HERA_ROT(X,Y,Z,ALPHA,-1.0D0)
      CALL HERA_ROT(PX,PY,PZ,ALPHA,-1.0D0)
      IP=I_PLANE
      RETURN
C BECAUSE OF THE SET UP OF THIS SUBROUTINE, POS(1) IS NULL, THE VALUE IS NEVER USED
C INCREMENTING FROM THE TARGET TO THE SCINTILLATOR - S1:
20    FIRST=.TRUE.
      DL=0.5D0
      D_T=DL/(VELOC*GAMMA)
21    CALL MAGETR(P_TOT,X,Y,Z,PX,PY,PZ,D_T,X2,Y2,Z2,PX2,PY2,PZ2,HIT)
```

```
      IF(HIT) RETURN
      IF(Z2.GT.POS(I_PLANE)) THEN
      CALL INTERP(POS(I_PLANE),X,Y,Z,X2,Y2,Z2,NEXT)
 * CORRECT TOF FOR OVERSHOOTING FIRST PLANE
      CALL TOF_INC(DT,XI,YI,ZI,X2,Y2,Z2)
      T=T+DT
      GOTO 29
      ENDIF
      X=X2
      Y=Y2
      Z=Z2
      PX=PX2
      PY=PY2
      PZ=PZ2
      GOTO 21
29    CALL CHKXY(I_PLANE,HIT,FIRST,1)
      IF(HIT) RETURN
      CALL PUT_P(.TRUE.,2)
      RETURN
C THE NEXT IS A MULTI PLANE DETECTOR(P0), ==>3 PLANES.
C SO...
30    FIRST=.FALSE.
      DL=0.5D0
      D_T=DL/(VELOC*GAMMA)
31    CALL MANSTR(P_TOT,X,Y,Z,PX,PY,PZ,D_T,X2,Y2,Z2,PX2,PY2,PZ2,HIT)
       IF(Z2.GT.POS(2)) THEN
       CALL TOF_INC(DT,X,Y,Z,X2,Y2,Z2)
       T=T+DT
       ENDIF
      IF(HIT) RETURN
      IF(Z2.GT.POS(I_PLANE)) THEN
      CALL INTERP(POS(I_PLANE),X,Y,Z,X2,Y2,Z2,NEXT)
      GOTO 39
      ENDIF
      X=X2
      Y=Y2
      Z=Z2
      PX=PX2
      PY=PY2
      PY=PY2
      GOTO 31
39    CALL CHKXY(I_PLANE,HIT,FIRST,1)
      IF(HIT) RETURN
      CALL PUT_P(.TRUE.,2)
      I_PLANE=I_PLANE+1
      IF(I_PLANE.LE.5) GOTO 30
      RETURN
C DETECTOR P1:
40    I_PLANE=6
      DL=0.5D0
      D_T=DL/(VELOC*GAMMA)
41    CALL MANSTR(P_TOT,X,Y,Z,PX,PY,PZ,D_T,X2,Y2,Z2,PX2,PY2,PZ2,HIT)
       IF(Z2.GT.POS(2)) THEN
       CALL TOF_INC(DT,X,Y,Z,X2,Y2,Z2)
       T=T+DT
       ENDIF
      IF(HIT) RETURN
      IF(Z2.GT.POS(I_PLANE)) THEN
      CALL INTERP(POS(I_PLANE),X,Y,Z,X2,Y2,Z2,NEXT)
      GOTO 49
      ENDIF
      X=X2
      Y=Y2
      Z=Z2
      PX=PX2
      PY=PY2
      PZ=PZ2
      GOTO 41
49    CALL CHKXY(I_PLANE,HIT,FIRST,1)
      IF(HIT) RETURN
      CALL PUT_P(.TRUE.,2)
      I_PLANE=I_PLANE+1
      IF(I_PLANE.LE.8) GOTO 41
      RETURN
C DETECTOR PLANES P2R(X<0) FIRST, P2L(X>0) NEXT:
50    I_PLANE=9
```

```
      DL=0.5D0
      D_T=DL/(VELOC*GAMMA)
 51   CALL MANETR(P_TOT,X,Y,Z,PX,PY,PZ,D_T,X2,Y2,Z2,PX2,PY2,PZ2,HIT)
       IF(Z2.GT.POS(2)) THEN
       CALL TOF_INC(DT,X,Y,Z,X2,Y2,Z2)
       T=T+DT
       ENDIF
      IF(HIT) RETURN
      IF(Z2.GT.POS(I_PLANE)) THEN
      CALL INTERP(POS(I_PLANE),X,Y,Z,X2,Y2,Z2,NEXT)
      GOTO 58
      ENDIF
      X=X2
      Y=Y2
      Z=Z2
      PX=PX2
      PY=PY2
      PZ=PZ2
      GOTO 51
C DETERMINE IF IN P2R OR P2L
 58   IF (I_PLANE.NE.9) GOTO 59      !REMEMBER TO REPLACE 58 HERE
      CALL CHKXY(I_PLANE,HIT,FIRST,1)      !CHECK IF IN PLANE P2RX
      IF(.NOT.HIT) THEN
      CALL PUT_P(.TRUE.,2)
      I_PLANE=10
      LIMIT=12
      GOTO 51
      ENDIF
      HIT=.FALSE.
      I_PLANE=12
      LIMIT=15
      GOTO 51
 59   CALL CHKXY(I_PLANE,HIT,FIRST,1)
      IF(HIT) RETURN
      CALL PUT_P(.TRUE.,2)
      I_PLANE=I_PLANE+1
      IF(I_PLANE.LE.(LIMIT-1)) GOTO 51
      RETURN
C IN 60-69 TRACE TO P3 THROUGH THE SCM105 FIELD:
 60   I_PLANE=15
      DL=4.0D0
      D_T=DL/(VELOC*GAMMA)
 61   CALL MANETR(P_TOT,X,Y,Z,PX,PY,PZ,D_T,X2,Y2,Z2,PX2,PY2,PZ2,HIT)
       IF(Z2.GT.POS(2)) THEN
       CALL TOF_INC(DT,X,Y,Z,X2,Y2,Z2)
       T=T+DT
       ENDIF
      IF(HIT) RETURN
      IF(Z2.GT.POS(I_PLANE)) THEN
      CALL INTERP(POS(I_PLANE),X,Y,Z,X2,Y2,Z2,NEXT)
      GOTO 69
      ENDIF
      X=X2
      Y=Y2
      Z=Z2
      PX=PX2
      PY=PY2
      PZ=PZ2
      GOTO 61
 69   CALL CHKXY(I_PLANE,HIT,FIRST,1)
      IF(HIT) RETURN
      CALL PUT_P(.TRUE.,2)
      I_PLANE=I_PLANE+1
      IF(I_PLANE.LE.18) GOTO 61
      RETURN
C DETECTOR P4:
 70   I_PLANE=19
      DL=0.5D0
      D_T=DL/(VELOC*GAMMA)
 71   CALL MANETR(P_TOT,X,Y,Z,PX,PY,PZ,D_T,X2,Y2,Z2,PX2,PY2,PZ2,HIT)
       IF(Z2.GT.POS(2)) THEN
       CALL TOF_INC(DT,X,Y,Z,X2,Y2,Z2)
       T=T+DT
       ENDIF
      IF(HIT) RETURN
      IF(Z2.GT.POS(I_PLANE)) THEN
```

```
      CALL INTERP(POS(I_PLANE),X,Y,Z,X2,Y2,Z2,NEXT)
      GOTO 79
      ENDIF
      X=X2
      Y=Y2
      Z=Z2
      PX=PX2
      PY=PY2
      PZ=PZ2
      GOTO 71
 79   CALL CHKXY(I_PLANE,HIT,FIRST,1)
      IF(HIT) RETURN
      CALL PUT_P(.TRUE.,2)
      I_PLANE=I_PLANE+1
      IF(I_PLANE.LE.22) GOTO 71
      RETURN
C DETECTOR S2:
 80   I_PLANE=23
      DL=0.5D0
      D_T=DL/(VELOC*GAMMA)
 81   CALL MANETR(P_TOT,X,Y,Z,PX,PY,PZ,D_T,X2,Y2,Z2,PX2,PY2,PZ2,HIT)
      IF(Z2.GT.POS(2)) THEN
      CALL TOF_INC(DT,X,Y,Z,X2,Y2,Z2)
      T=T+DT
      ENDIF
      IF(HIT) RETURN
      IF(Z2.GT.POS(I_PLANE)) THEN
      CALL INTERP(POS(I_PLANE),X,Y,Z,X2,Y2,Z2,NEXT)
* CORRECT TOF FOR OVERSHOOTING THE LAST DETECTOR PLANE
      CALL TOF_INC(DT,XI,YI,ZI,X2,Y2,Z2)
      T=T-DT
      GOTO 89
      ENDIF
      X=X2
      Y=Y2
      Z=Z2
      PX=PX2
      PY=PY2
      PZ=PZ2
      GOTO 81
 89   CALL CHKXY(I_PLANE,HIT,FIRST,1)
      RETURN
      END
C
      SUBROUTINE HERA_ROT(X,Y,Z,ALPHA,SI)
* THIS SUBROUTINE ROTATES THE LABORATORY COORD. SYSTEM TO THE HERA MAGNET
* COORD. SYSTEM (POLARIZATION ALWAYS ALONG THE Z-AXIS).
      IMPLICIT NONE
      REAL*8 X,Y,Z,XX,YY,ZZ,ALPHA,SI
      REAL*8 CH,SH
* SI=+1.0D0 COUNTERCLOCKWISE ROT., SI=-1.0D0 CLOCKWISE ROT.
* ROTATE ABOUT Z-AXIS BY 90 DEGREES
      XX=Y*SI
      YY=-X*SI
      X=XX
      Y=YY
      RETURN
      ENTRY X_ROT(X,Y,Z,ALPHA,SI)
* ROTATE ABOUT X-AXIS BY ANGLE ALPHA
      CH=DCOS(ALPHA)
      SH=DSIN(ALPHA)
      YY=(CH*Y)+(SH*Z*SI)
      ZZ=(CH*Z)-(SH*Y*SI)
      Y=YY
      Z=ZZ
      RETURN
      END
C
      LOGICAL FUNCTION IN_TARG(X,Y,Z)
* CHECKS IF THE PARTICLE IS IN THE TARGET.
      IMPLICIT NONE
      REAL*8 H_TARG_LEN,TARG_RAD
      PARAMETER (H_TARG_LEN=5.0D0)
      PARAMETER (TARG_RAD=1.85D0)
      REAL*8 X,Y,Z,Z2,R
      R=DSQRT(X*X+Y*Y)
```

```
      Z2=DABS(Z)
      IF(Z2.GT.H_TARG_LEN/2.0D0) THEN
       IN_TARG=.FALSE.
       RETURN
      ENDIF
      IF(R.GT.TARG_RAD) THEN
       IN_TARG=.FALSE.
       RETURN
      ENDIF
      IN_TARG=.TRUE.
      RETURN
      END
C
      LOGICAL FUNCTION IN_HERA(X,Y,Z)
* CHECKS IF THE PARTICLE IS STILL IN THE TARGET WHILE IN THE HERA FIELD.
      IMPLICIT NONE
      REAL*8 H_TARG_LEN,TARG_RAD
      PARAMETER (H_TARG_LEN=5.0D0)
      PARAMETER (TARG_RAD=1.85D0)
      REAL*8 X,Y,Z,Z2,R
      REAL*8 XP,YP,ZP
      COMMON /ANGLE/THETA,PHI,ALPHA
      REAL*8 THETA,PHI,ALPHA
      XP=X
      YP=Y
      ZP=Z
      CALL X_ROT(XP,YP,ZP,ALPHA,1.0D0)
      CALL HERA_ROT(XP,YP,ZP,ALPHA,-1.0D0)
      R=DSQRT(XP*XP+YP*YP)
      Z2=DABS(ZP)
      IF(Z2.GT.H_TARG_LEN/2.0D0) THEN
       IN_HERA=.FALSE.
       RETURN
      ENDIF
      IF(R.GT.TARG_RAD) THEN
       IN_HERA=.FALSE.
       RETURN
      ENDIF
      IN_HERA=.TRUE.
      RETURN
      END
C
      DOUBLE PRECISION FUNCTION GAUS_S(SIG,MU,N_SD)
* GENERATES THE GAUSSIAN BEAM MOMENTUM DISTRIBUTION.
      IMPLICIT NONE
C SIG IS VARIANCE,MU IS CENTROID
C RETURNS A VALUE WITHIN N_SD OF STARDARD DEVIATIONS.
      PARAMETER SQ_2_PI=2.506628274620
      REAL*8 SIG,MU,XV,P,BP,S_P
      REAL*8 N_SD
      COMMON /SEED/ISEED,IENERGY,V(98),IDUM
      INTEGER*4 ISEED,IDUM,IENERGY
      REAL*4 V
      S_P=SQ_2_PI*SIG
1     BP=RAN(ISEED)/S_P
      XV=MU+(N_SD*SIG*(1.0-2.0*RAN(ISEED)))
      P=((XV-MU)/SIG)**2
      P=EXP(-.5*P)/S_P
      IF(P.LT.BP) GOTO 1
      GAUS_S=XV
      RETURN
      END
C
      DOUBLE PRECISION FUNCTION GAUS_M(SIG,RMAX)
* GENERATES A GAUSSIAN TARGET RADIUS - INTERACTION POINT IN THE TARGET.
      REAL*8 SIG,RMAX,SMIN,R
C SIG IS VARIANCE,MU IS CENTROID.
C VALUE RETURNED IS      X_MIN<GAUS_M<X_MAX (INCLUSIVE)
      COMMON /SEED/ISEED,IENERGY,V(98),IDUM
      INTEGER*4 ISEED,IDUM,IENERGY
      REAL*4 V
      SMIN=-(RMAX*RMAX)/(SIG*SIG)*2
      SMIN=EXP(SMIN)
   10 R=1.0D0-SMIN
      R=SMIN+(R*RAN(ISEED))
      R=DSQRT(-2.0D0*(SIG*SIG)*DLOG(R))
```

```
      IF (R.GT.RMAX) GOTO 10
      GAUS_M=R
      RETURN
      END
C
      SUBROUTINE EXTR_PARMS(P_TOT)
* CALCULATES SOME MISC. KINEMATICAL QUANTITIES.
      IMPLICIT NONE
      PARAMETER PRO_MAS=938.256D0
      PARAMETER DUT_MAS=1875.587D0
      COMMON /DEUT/DODEUT,INDEX
      LOGICAL DODEUT
      INTEGER*2 INDEX
      REAL*8 P_TOT
      COMMON /RELA/GAMMA,VELOC,C,EMEUTRON
      REAL*8 GAMMA,VELOC,C,EMEUTRON
      COMMON /MOM_P_1/ P_P,MERA_ANG,SCM_ANG,PHICOTH,KPERIM
      INTEGER*2 KPERIM  !FLAG CONTROLLING EVENT GENERATION
      REAL*8 P_P,MERA_ANG,SCM_ANG,PHICOTH(6)
      REAL*8 DPOO,DGOO
      DPOO=PRO_MAS/P_TOT
      IF(DODEUT) DPOO=DUT_MAS/P_TOT
      DPOO=1.0D0/(DPOO*DPOO +1.0D0)
      VELOC=DSQRT(DPOO)
      GAMMA=1.0D0/DSQRT(1.0D0-VELOC*VELOC)
      VELOC=VELOC*C
      RETURN
      END
C
      SUBROUTINE PUT_P(ARG,INTARG)
* WRITES THE PARTICLE POSITION AND MOMENTUM TO AN INTERNAL RECORD.  IF THE EVENT
* MAKES IT THROUGH THE ENTIRE SPECTROMETER, THE RECORD IS WRITTEN TO AN OUTPUT FILE.
      IMPLICIT NONE
        COMMON/S1SAVE/S1X,S1Y
      COMMON /PRINT/XI,YI,ZI
        REAL*8 S1X,S1Y
      REAL*8 XI,YI,ZI,IP(7)
      COMMON /MOM_V_1/ P,P_TOT
      REAL*8 P(7),Q(7),P_TOT                                  ! P(X,Y,Z,Px,Py,Pz,L)
      LOGICAL ARG,FIRST
      CHARACTER LREC*8000
      INTEGER IPTR,J,I,K
      INTEGER INTARG
      EQUIVALENCE (IP(1),XI),(IP(2),YI),(IP(3),ZI)
      DATA FIRST,IPTR/.TRUE.,1/
      IP(4)=0.0D0
      IP(5)=0.0D0
      IP(6)=0.0D0
      IP(7)=P(7)
C FILE 90 IS OPENED IN THE CALLING PROGRAM.
      IF(INTARG.EQ.2) THEN
      WRITE(LREC(IPTR:IPTR+55),1) IP                          ! WRITE TO INTERNAL RECORD
      ELSE
20    WRITE(LREC(IPTR:IPTR+55),1) P                           ! WRITE TO INTERNAL RECORD
      ENDIF
1     FORMAT(7A8)
      IF(.NOT.ARG) THEN                                       ! IF ARG THEN WRITE TO FILE
        DO 9 I=1,1120,56
        READ(LREC(I:I+55),1) Q
        WRITE(90,*) (Q(K),K=1,3)
        WRITE(90,*) (Q(K),K=4,6)
        WRITE(90,*) Q(7)
9       CONTINUE
        WRITE(90,*) '%'
C       WRITE(90,2) LREC(1:IPTR+55)                           ! AND RESET POINTERS
3       FORMAT(1X,7D10.4)
2       FORMAT(1344A1)
        IPTR=1
C
C********WRITE X,Y COORD OF S1 FOR GOOD EVENT
C
        WRITE(62,100)S1X,S1Y
100     FORMAT(F8.2,',',F8.2)
        RETURN
      ENDIF
      IPTR=IPTR+56                                            ! SET POINTER
```

```
      RETURN
      ENTRY RES_PUT
      IPTR=1
      RETURN
      END
C
      SUBROUTINE MANETR (P,X1,Y1,Z1,PX1,PY1,PZ1,D,X2,Y2,Z2,
     1PX2,PY2,PZ2,HIT)
C USES RUNGE-KUTTA AND PREDICTOR-CORRECTOR ROUTINES,
C
C PREDICTOR - CORRECTOR ROUTINE FOR NUMERICAL INTEGRATION
C OF A PARTICLE TRAJECTORY THROUGH A MAGNETIC FIELD.
C WRITTEN BY HAL SPINKA.
      IMPLICIT REAL*8  (A-H,O-Z)
      LOGICAL HIT
      COMMON /DEUT/DODEUT,INDEX
      INTEGER*2 INDEX
      LOGICAL DODEUT
      COMMON/ZNMINT/TAU,XN,YN,ZN,XNP,YNP,ZNP,CMASS
      COMMON/BLOCK2/ISTART,KK
      DIMENSION  X(9,8),XP(9,8),DIF(9),PRED(18),COR(9)
      IF(DODEUT) THEN
      CMASS = 1875.587D0
      ELSE
      CMASS = 938.256 D0
      ENDIF
      C = 29.979246 D0
C INITIALIZE FOR ISTART=0 OR KK=1,2,3
      XN = X1
      YN = Y1
      ZN = Z1
      XNP = PX1/CMASS
      YNP = PY1/CMASS
      ZNP = PZ1/CMASS
      IF (ISTART.NE.0)  GO TO 2
      X(1,4) = XN/C
      X(2,4) = YN/C
      X(3,4) = ZN/C
      X(4,4) = XNP
      X(5,4) = YNP
      X(6,4) = ZNP
      XP(1,4) = XNP
      XP(2,4) = YNP
      XP(3,4) = ZNP
      DO 1  L=1,9
      DIF(L) = 0.0
1     CONTINUE
      KK = 0
      ISTART = 1
      CALL XPPYPP(XN,YN,ZN,XNP,YNP,ZNP,XP(4,4),XP(5,4),XP(6,4),HIT)
      IF(HIT) RETURN
2     IF (KK.GE.3)  GO TO 3
      CALL RUNGE (D,P,HIT)
      IF(HIT) RETURN
      KK = KK + 1
      L = KK + 4
      CALL XPPYPP(XN,YN,ZN,XNP,YNP,ZNP,XP(4,L),XP(5,L),XP(6,L),HIT)
      IF(HIT) RETURN
      X(1,L) = XN/C
      X(2,L) = YN/C
      X(3,L) = ZN/C
      X(4,L) = XNP
      X(5,L) = YNP
      X(6,L) = ZNP
      XP(1,L) = XNP
      XP(2,L) = YNP
      XP(3,L) = ZNP
      GO TO 7
C NORMAL ENTRY INTO PREDICTOR - CORRECTOR ROUTINE
3     TAU = TAU + D
      DO 4  J=1,6
      X(J,1) = ((2.0 D0)*X(J,6) + X(J,5))/(3.0 D0)
      PRED(J) = X(J,1) + (D/(72.0 D0))*((191.0 D0)*XP(J,7) -
     1(107.0 D0)*XP(J,6) + (109.0 D0)*XP(J,5) -
     2(25.0 D0)*XP(J,4))
      PRED(J+9) = PRED(J) - (707.0 D0)*DIF(J)
```

```
 4      CONTINUE
        COR(1) = PRED(13)
        COR(2) = PRED(14)
        COR(3) = PRED(15)
        PRED(10) = C*PRED(10)
        PRED(11) = C*PRED(11)
        PRED(12) = C*PRED(12)
        CALL XPPYPP(PRED(10),PRED(11),PRED(12),PRED(13),PRED(14),
       1PRED(15),COR(4),COR(5),COR(6),HIT)
        IF(HIT) RETURN
        DO 5  J=1,6
        COR(J) = X(J,1) + (D/(72.0 D0))*((25.0 D0)*COR(J) +
       1(91.0 D0)*XP(J,7) + (43.0 D0)*XP(J,6) + (9.0 D0)*XP(J,5))
        DIF(J) = (PRED(J) - COR(J))/(750.0 D0)
        COR(J) = COR(J) + (43.0 D0)*DIF(J)
        X(J,8) = COR(J)
 5      CONTINUE
        XP(1,8) = COR(4)
        XP(2,8) = COR(5)
        XP(3,8) = COR(6)
        XN = COR(1)*C
        YN = COR(2)*C
        ZN = COR(3)*C
        XNP = COR(4)
        YNP = COR(5)
        ZNP = COR(6)
        CALL XPPYPP(XN,YN,ZN,XNP,YNP,ZNP,XP(4,8),XP(5,8),XP(6,8),HIT)
        IF(HIT) RETURN
        P = CMASS*DSQRT(XNP*XNP + YNP*YNP + ZNP*ZNP)
        DO 6  L=1,6
        DO 6  J=1,7
        X(L,J) = X(L,J+1)
        XP(L,J) = XP(L,J+1)
 6      CONTINUE
 7      X2 = XN
        Y2 = YN
        Z2 = ZN
        PX2 = XNP*CMASS
        PY2 = YNP*CMASS
        PZ2 = ZNP*CMASS
        RETURN
        ENTRY INI_MANETR
        ISTART=0
        RETURN
        END
C
        SUBROUTINE RUNGE (D,P,HIT)
C SUBROUTINE FOR RUNGE-KUTTA NUMERICAL INTEGRATION.
        IMPLICIT REAL*8 (A-H,O-Z)
        LOGICAL HIT
        COMMON/ENMINT/TAU,XN,YN,ZN,XNP,YNP,ZNP,CMASS
        HALF = 0.5
        SIXTH = (1.0 D0)/(6.0 D0)
        EIGHTH = 0.125
        C = 29.979246 D0
 20     CALL XPPYPP(XN,YN,ZN,XNP,YNP,ZNP,XK1,YK1,ZK1,HIT)
        IF(HIT) RETURN
CFIRST STEP   TAU1 = TAU + HALF*D
        YN1 = YN +(HALF*D*YNP + EIGHTH*D*D*YK1)*C
        XN1 = XN +(HALF*D*XNP + EIGHTH*D*D*XK1)*C
        ZN1 = ZN +(HALF*D*ZNP + EIGHTH*D*D*ZK1)*C
        XNP1 = XNP + HALF*D*XK1
        YNP1 = YNP + HALF*D*YK1
        ZNP1 = ZNP + HALF*D*ZK1
   40 CALL XPPYPP(XN1,YN1,ZN1,XNP1,YNP1,ZNP1,XK2,YK2,ZK2,HIT)
        IF(HIT) RETURN
C SECOND STEP   TAU2 = TAU + HALF*D
        XN2 = XN +(HALF*D*XNP + EIGHTH*D*D*XK1)*C
        YN2 = YN +(HALF*D*YNP + EIGHTH*D*D*YK1)*C
        ZN2 = ZN +(HALF*D*ZNP + EIGHTH*D*D*ZK1)*C
        XNP2 = XNP + HALF*D*XK2
        YNP2 = YNP + HALF*D*YK2
        ZNP2 = ZNP + HALF*D*ZK2
 60     CALL XPPYPP(XN2,YN2,ZN2,XNP2,YNP2,ZNP2,XK3,YK3,ZK3,HIT)
        IF(HIT) RETURN
C THIRD STEP   TAU3 = TAU + D
```

```
      XN3 = XN +(D*XNP + HALF*D*D*XK3)*C
      YN3 = YN +(D*YNP + HALF*D*D*YK3)*C
      ZN3 = ZN +(D*ZNP + HALF*D*D*ZK3)*C
      XNP3 = XNP + D*XK3
      YNP3 = YNP + D*YK3
      ZNP3 = ZNP + D*ZK3
 80   CALL XPPYPP(XN3,YN3,ZN3,XNP3,YNP3,ZNP3,XK4,YK4,ZK4,HIT)
      IF(HIT) RETURN
C FOURTH STEP
      TAU = TAU + D
      XN = XN +(D*XNP + SIXTH*D*D*(XK1+XK2+XK3))*C
      YN = YN +(D*YNP + SIXTH*D*D*(YK1+YK2+YK3))*C
      ZN = ZN +(D*ZNP + SIXTH*D*D*(ZK1+ZK2+ZK3))*C
      XNP = XNP + SIXTH*D*(XK1+XK2+XK3+XK3+XK3+XK4)
      YNP = YNP + SIXTH*D*(YK1+YK2+YK2+YK3+YK3+YK4)
      ZNP = ZNP + SIXTH*D*(ZK1+ZK2+ZK2+ZK3+ZK3+ZK4)
      P = CMASS*DSQRT(XNP*XNP + YNP*YNP + ZNP*ZNP)
      RETURN
      END
C
      SUBROUTINE XPPYPP (X,Y,Z,XP,YP,ZP,XPP,YPP,ZPP,HIT)
C SUBROUTINE TO EVALUATE DERIVATIVES OF P
      IMPLICIT REAL*8 (A-H,O-Z)
      COMMON /DEUT/DODEUT,INDEX
      INTEGER*2 INDEX
      REAL*8 BX,BY,BZ,X,Y,Z
      LOGICAL HIT,DODEUT
C*
      PARAMETER DUT_MAS=1875.587D0
      PARAMETER PRO_MAS=938.256D0
      PARAMETER CONST=9.57876D-6
      CONST1=CONST
C THIS PARAMETER IS E/M FOR PROTONS IN UNITS OF  1/(MSEC GAUSS)
      CALL SCN_MP3 (X,Y,Z,BX,BY,BZ,HIT)
      IF(HIT) RETURN
      IF(DODEUT) CONST1=CONST1*PRO_MAS/DUT_MAS
 10   XPP = CONST1*(YP*BZ - ZP*BY)
      YPP = CONST1*(ZP*BX - XP*BZ)
      ZPP = CONST1*(XP*BY - YP*BX)
 20   RETURN
      END


      SUBROUTINE TOF_INC(DT,X1,Y1,Z1,X2,Y2,Z2)
      IMPLICIT REAL*8 (A-H,O-Z)
      COMMON /RELA/GAMMA,VELOC,C,EMNEUTRON

      DX=X2-X1
      DY=Y2-Y1
      DZ=Z2-Z1
      DL=DSQRT(DX*DX+DY*DY+DZ*DZ)
      DT=DL/VELOC
      RETURN
      END

      DOUBLE PRECISION FUNCTION GAUS_S(SIG,MU,N_SD)
      IMPLICIT NONE
C SIG IS VARIANCE,MU IS CENTROID
C RETURNS A VALUE WITHIN N SD OF STANDARD DEVIATIONS.
      PARAMETER SQ_2_PI=2.506628274631D0
      REAL*8 SIG,MU,XV,P,BP,S_P
      COMMON /SEED/ISEED
      INTEGER*4 ISEED
      INTEGER N_SD
      S_P=SQ_2_PI*SIG
1     BP=RAN(ISEED)/S_P
      XV=MU+(N_SD*SIG*(1.0-2.0*RAN(ISEED)))
      P=((XV-MU)/SIG)**2
      P=EXP(-.5*P)/S_P
      IF(P.LT.BP) GOTO 1
      GAUS_S=XV
      RETURN
      END
```

```
      SUBROUTINE RECOIL_KIN(P1,THETA,PHI,EBEAM,GOOD_MOMENTUM)
C     CALCULATE RECOIL MOMENTUM COMPONENTS
      IMPLICIT REAL*8 (A-H,O-Z)
      REAL*8 NUT_MASS
      DIMENSION P1(3),PK3(2)
      COMMON /DEUT/DODEUT,INDEX
      LOGICAL DODEUT,GOOD_MOMENTUM
      INTEGER*2 INDEX,NSOLN
      PARAMETER (NUT_MASS=939.6D0)
      PARAMETER (PRO_MASS=938.26D0)
      PARAMETER (DUT_MASS=1878.59D0)
      PARAMETER (PI_MASS=134.96D0)

        IF(DODEUT) THEN
        AM3=DUT_MASS
        AM4=PI_MASS
        ELSE
        AM3=PRO_MASS
        AM4=NUT_MASS
        ENDIF

        CALL KIN(NUT_MASS,PRO_MASS,AM3,AM4,EBEAM,THETA,TH3CM,PK3,NSOLN)
        IF(NSOLN.NE.0) GOOD_MOMENTUM=.TRUE.      !NSOLN=0 IS BAD MOMENTUM
        IF(INDEX.EQ.1) THEN
        P3=PK3(1)
        ELSE
        P3=PK3(2)
        ENDIF
        P1(1)=P3*DSIN(THETA)*DCOS(PHI)
        P1(2)=P3*DSIN(THETA)*DSIN(PHI)
        P1(3)=P3*DCOS(THETA)

      RETURN
      END



      SUBROUTINE LABCM(THETA)
*
* THIS SUBROUTINE TRANSFORMS THE PROTON LAB SCATTERING ANGLE TO THE C.M. FRAME.  IT WILL ONLY
* WORK FOR SCATTERING ANGLES LESS THAN 90 DEGREES.       B. GARNETT.
*
      REAL*8 THETA,GAMMA,BETA,ECM,A,B,C
      REAL*8 PPCM,S,T1,T2,T3,COSTH
      COMMON/RELA/NGAMMA,VELOC,SPDLGHT,ENEUTRON
      REAL*8 NGAMMA,VELOC,SPDLGHT,ENEUTRON
      COMMON/MOM P_1/ P_N,HERA_ANG,SCM_ANG,PHICOTH,KPERIM
      INTEGER*2 KPERIM  !FLAG CONTROLLING EVENT GENERATION
      REAL*8 P_N,HERA_ANG,SCM_ANG,PHICOTH(6)
      PARAMETER (PRO_MAS=938.256D0)
      PARAMETER (NUT_MAS=939.6D0)

      BETA=P_N/(ENEUTRON+PRO_MAS)
      S=(NUT_MAS*NUT_MAS)+(PRO_MAS*PRO_MAS)+(2.0D0*ENEUTRON*PRO_MAS)
      PPCM=P_N*PRO_MAS/DSQRT(S)
      ECM=DSQRT(PPCM*PPCM+PRO_MAS*PRO_MAS)
      GAMMA=1.0D0/DSQRT(1.0D0-BETA*BETA)
      A=GAMMA*PPCM*TAN(THETA)
      B=GAMMA*BETA*ECM*TAN(THETA)
      C=PPCM
      T1=A*B
      T2=A*A+C*C
      T3=T2-(B*B)
      COSTH=(-T1+C*DSQRT(T3))/T2
      THETA=DACOS(COSTH)
      RETURN
      END
```

```
      SUBROUTINE CHKXY(PLANENO,HIT,FIRST,INTARG)
***
*     CHECKS WHETHER X OR Y OF THE PROTON IS WITHIN
*     THE DETECTOR PLANE. REQUIRES DATA FILES CHMBRXY.DAT
*     AND OFFSETS.DAT .  B. GARNETT
***
      INTEGER PLANENO,INTARG
      LOGICAL HIT,FIRST
      REAL*8 CHMBRXY(88)
      COMMON/NON_V_1/PV,PTOT
      REAL*8 PV(7),PTOT
      COMMON /PRINT/XI,YI,ZI
      REAL*8 XI,YI,ZI

      HIT=.FALSE.
      IF(FIRST) THEN
      CALL XYREAD(CHMBRXY)
      FIRST=.FALSE.
      ENDIF

      IYMAX=(PLANENO-1)*4
      IYMIN=IYMAX-1
      IXMAX=IYMIN-1
      IXMIN=IXMAX-1

      YMAX=CHMBRXY(IYMAX)
      YMIN=CHMBRXY(IYMIN)
      XMAX=CHMBRXY(IXMAX)
      XMIN=CHMBRXY(IXMIN)

      IF(INTARG.EQ.2) THEN
        IF ((XI.LT.XMIN) .OR. (XI.GT.XMAX)) THEN
        HIT=.TRUE.
        RETURN
        ENDIF
        IF ((YI.LT.YMIN) .OR. (YI.GT.YMAX)) THEN
        HIT=.TRUE.
        RETURN
        ENDIF
      ELSE
        IF ((PV(1).LT.XMIN) .OR. (PV(1).GT.XMAX)) THEN
        HIT=.TRUE.
        RETURN
        ENDIF
        IF ((PV(2).LT.YMIN) .OR. (PV(2).GT.YMAX)) THEN
        HIT=.TRUE.
        RETURN
        ENDIF
      ENDIF
      RETURN
      END

      SUBROUTINE XYREAD(CHMBRXY)
      REAL*8 CHMBRXY(88),XOFF,YOFF
      OPEN(60,NAME='CHMBRXY.DAT',STATUS='OLD')
      OPEN(64,NAME='OFFSETS.DAT',STATUS='OLD')
      J=4
      DO 10 I=1,22
      READ(60,*)CHMBRXY(J-3),CHMBRXY(J-2),CHMBRXY(J-1),CHMBRXY(J)
      READ(64,*)XOFF,YOFF
      CHMBRXY(J-3)=CHMBRXY(J-3)+XOFF
      CHMBRXY(J-2)=CHMBRXY(J-2)+XOFF
      CHMBRXY(J-1)=CHMBRXY(J-1)+YOFF
      CHMBRXY(J)=CHMBRXY(J)+YOFF
      J=J+4
   10 CONTINUE
      CLOSE(60)
      CLOSE(64)
      RETURN
      END
```

```
      SUBROUTINE CROUT(A,N,B,M,DETERM,NMAX)
C
C     A=COEFF. MATRIX,N=NO. OF COLUMNS IN A,B=SOLN. MATRIX,
C     M=NO. COLUMNS IN B,DETERM=OUTPUT FROM CROUT,NMAX=NO. OF
C     ROWS IN A AND B.
C
C     SOLUTION OF LINEAR EQUATIONS BY THE CROUT METHOD
C
      REAL*8 A,B,DETERM,DOTP,V,AMAX,TEMP
      DIMENSION A(4,4),B(4,1)
      COMMON /F454/ V(100)
C
      DETERM=1.
C
      DO 1000 K=1,N
      KP1=K+1
      KM1=K-1
C
      TEMP=0.
      DO 20 I=K,N
      DO 2 L=1,K
    2 V(L)=A(I,L)
      A(I,K)=A(I,K)-DOTP(V,A(1,K),KM1)
      IF (ABS(A(I,K)).LT.TEMP) GO TO 20
    3 TEMP=ABS(A(I,K))
      IMAX=I
   20 CONTINUE
      AMAX=A(IMAX,K)
      DETERM=AMAX*DETERM
C
      IF (DETERM.EQ.0.) RETURN
C
      IF (IMAX.EQ.K) GO TO 600
      DETERM=-DETERM
      DO 50 J=1,N
      TEMP=A(K,J)
      A(K,J)=A(IMAX,J)
      A(IMAX,J)=TEMP
   50 CONTINUE
      IF (M.LE.0) GO TO 600
      DO 400 J=1,M
      TEMP=B(K,J)
      B(K,J)=B(IMAX,J)
      B(IMAX,J)=TEMP
  400 CONTINUE
C
  600 DO 666 L=1,K
  666 V(L)=A(K,L)
C
      IF (K.EQ.N) GO TO 850
      DO 700 I=KP1,N
  700 A(I,K)=A(I,K)/AMAX
C
      DO 800 J=KP1,N
  800 A(K,J)=A(K,J)-DOTP(V,A(1,J),KM1)
C
  850 IF (M.LE.0) GO TO 1000
      DO 900 J=1,M
  900 B(K,J)=B(K,J)-DOTP(V,B(1,J),KM1)
C
 1000 CONTINUE
C
      IF (M.LE.0) GO TO 8000
      DO 8000 I=1,N
      K=N+1-I
      DO 6666 L=K,N
 6666 V(L)=A(K,L)
      DO 7000 J=1,M
 7000 B(K,J)=(B(K,J)-DOTP(V(K+1),B(K+1,J),I-1))/A(K,K)
 8000 CONTINUE
      RETURN
      END
C
C
      FUNCTION DOTP(A,B,N)
      REAL*8 A,B,DOTP
      DIMENSION A(1),B(1)
      DOTP=0.
      IF (N.EQ.0) RETURN
      DO 100 I=1,N
  100 DOTP=DOTP+A(I)*B(I)
```

```
      SUBROUTINE HERASCM(X,Z,DO_P)
***
*     THIS SUBROUTINE TRANSFORMS THE X AND Z POSITIONS OF A
*     PARTICLE FROM THE HERA COORDINATE SYSTEM (ORIGIN AT THE
*     CENTER OF THE TARGET) TO THE SCM SYSTEM (ORIGIN AT THE
*     CENTER OF THE SCM105). A TRANSLATION IS FIRST PERFORMED,
*     FOLLOWED BY A ROTATION.  B. GARNETT
***
      IMPLICIT NONE
      LOGICAL DO_P
      COMMON /SCM/Z1,D1,D2
      REAL*8 Z1,D1,D2
      COMMON /MON_P_1/P_P,HERA_ANG,SCM_ANG,PHICOTH,KPERIM
      INTEGER*2 KPERIM   !FLAG CONTROLLING EVENT GENERATION
      REAL*8 P_P,HERA_ANG,SCM_ANG,PHICOTH(6)
      REAL*8 X,Z,Z0,XTEMP,ZTEMP,X_DISPL,Z_DISPL
      REAL*8 COSANG,SINANG,ANG_ROT,TANANG
      REAL*8 D12,COS1,SIN1,ANGLE
      REAL*8 XPRIME,ZPRIME
      PARAMETER PI=3.14159265358D0
      PARAMETER L1=247.9D0

      ANGLE=SCM_ANG
      COS1=DCOS(ANGLE)
      SIN1=DSIN(ANGLE)
      D12=D1+D2
      TANANG=(D2-D1)/L1
      ANG_ROT=DATAN(TANANG)
      SINANG=DSIN(ANG_ROT)
      COSANG=DCOS(ANG_ROT)
      X_DISPL=0.5D0*D12*COSANG
      Z_DISPL=Z1+(0.5D0*L1)

* ROTATE COORDINATE SYSTEM BY THE SCM ANGLE ( FROM Z-AXIS ALONG BEAM
* THROUGH THE SPECTROMETER ANGLE - Z' THROUGH CENTER OF THE SCM105)
      XTEMP=X
      X=(X*COS1)+(Z*SIN1)
      Z=(-XTEMP*SIN1)+(Z*COS1)

***   TRANSLATION TO THE PRIMED FRAME. SKIP THIS PART IF ROTATING MOMENTUM.   ***
      IF(DO_P) THEN
      XPRIME=X
      ZPRIME=Z
      GOTO 100
      ENDIF
      XPRIME=X-X_DISPL
      ZPRIME=Z-Z_DISPL

***   ROTATION TO THE DOUBLE PRIMED FRAME   ***
100   X=(XPRIME*COSANG)+(-ZPRIME*SINANG)        !CAREFUL WITH SIGNS
      Z=(XPRIME*SINANG)+(ZPRIME*COSANG)         !CAREFUL WITH SIGNS

999   RETURN
      END
```

```
      SUBROUTINE SCM_MAP_READ(IFS)
      PARAMETER VECD=3
      PARAMETER XDIM=41
      PARAMETER YDIM=15
      PARAMETER ZDIM=121
      INTEGER*2 MAGMAP(VECD,XDIM,YDIM,ZDIM)
      INTEGER*4 IFS
      REAL*8 XF,YF,ZF
      COMMON/FOLDAT/MAGMAP,XF,YF,ZF
        IF(IFS.EQ.2) GOTO 2000
        IF(IFS.NE.1) STOP 'INVALID FIELD SELECTED IN SCM_MAP_READ'
        WRITE(6,1)
1       FORMAT(' READING IN THE HIGH FIELD SCM105 MAP')
        OPEN(50,NAME='SCM_Y.HFL',STATUS='OLD',READONLY)
        READ(50,*) YF
       READ(50,982)(((MAGMAP(2,I,J,K),I=1,41),J=1,15),K=1,121)
        CLOSE(50)
        OPEN(50,NAME='SCM_X.HFL',STATUS='OLD',READONLY)
        READ(50,*) XF
       READ(50,982)(((MAGMAP(1,I,J,K),I=1,41),J=1,15),K=1,121)
        CLOSE(50)
        OPEN(50,NAME='SCM_Z.HFL',STATUS='OLD',READONLY)
        READ(50,*) ZF
       READ(50,982)(((MAGMAP(3,I,J,K),I=1,41),J=1,15),K=1,121)
        CLOSE(50)
        RETURN
2000    WRITE(6,2)
2       FORMAT(' READING IN THE LOW FIELD SCM105 FIELD')
        OPEN(50,NAME='SCM_Y.LFL',STATUS='OLD',READONLY)
        READ(50,*) YF
       READ(50,982)(((MAGMAP(2,I,J,K),I=1,41),J=1,15),K=1,121)
        CLOSE(50)
        OPEN(50,NAME='SCM_X.LFL',STATUS='OLD',READONLY)
        READ(50,*) XF
       READ(50,982)(((MAGMAP(1,I,J,K),I=1,41),J=1,15),K=1,121)
        CLOSE(50)
        OPEN(50,NAME='SCM_Z.LFL',STATUS='OLD',READONLY)
        READ(50,*) ZF
       READ(50,982)(((MAGMAP(3,I,J,K),I=1,41),J=1,15),K=1,121)
        CLOSE(50)
      RETURN
  982 FORMAT(41A2)
      END
```

```
      SUBROUTINE LOSE_IT
* THIS SUBROUTINE USES THE BETHE-BLOCH EQN. TO DETERMINE ENERGY
* LOSS IN THE TARGET.
      IMPLICIT REAL*8 (A-H,O-Z)
      COMMON /DEUT/DODEUT,INDEX
      LOGICAL DODEUT
      COMMON /TGT_PT/POS_X,POS_Y,POS_Z
      COMMON /NON_V_1/PMOM(7),PTOT
      PARAMETER PRO_MASS=938.256D-3                !PROTON MASS - GEV
      PARAMETER DUT_MASS=1875.587D-3               !DEUTERON MASS - GEV
      PARAMETER N=6.0225D23                        !AVAGADRO'S NUMBER
      PARAMETER ZC=6.0D0                           !AT. NO. CARBON
      PARAMETER A=12.01D0                          !AT. WT. CARBON
      PARAMETER C_DENSITY=2.265D0                  !DENSITY OF CARBON
      PARAMETER C1=2.8178D-13                      !BOHR RADIUS
      PARAMETER ELEC_MASS=0.511D-3                  !ELECTRON MASS - GEV
      PARAMETER ION_POTL=8.6018D-8                 !IONIZATION POT'L FOR CARBON - GEV
      PARAMETER PI=3.14159265D0
      EQUIVALENCE (PMOM(1),X),(PMOM(2),Y),(PMOM(3),Z)
      EQUIVALENCE (PMOM(4),PX),(PMOM(5),PY),(PMOM(6),PZ)
* DO SOME KINEMATICS
      PD_MASS=PRO_MASS
      IF(DODEUT) PD_MASS=DUT_MASS
      SQ_PD_MASS=PD_MASS*PD_MASS
      PTOT_SQ=PX*PX+PY*PY+PZ*PZ
      BETA=1.0D0+(SQ_PD_MASS)/PTOT_SQ
      BETA=DSQRT(1.0D0/BETA)
      PTOTAL=DSQRT(PTOT_SQ)
* DETERMINE THE ANGLES FOR THE SCATTERING DIRECTION
      THETA=DACOS(PZ/PTOTAL)
      IF(PX.EQ.0.0D0) THEN
      PHI=0.0D0
      ELSE
      PHI=DATAN(PY/PX)
      ENDIF
* DETERMINE DE/DX USING THE BETHE-BLOCH EQN.
      DX=X-POS_X
      DY=Y-POS_Y
      DZ=Z-POS_Z
      DL=DSQRT(DX*DX+DY*DY+DZ*DZ)
      EKIN=DSQRT(PTOT_SQ+SQ_PD_MASS)-PD_MASS
      DEDX=-4.0D0*PI*ZC*(N*C_DENSITY/A)
       BETA_SQ=BETA*BETA
      TEMP1=2.0D0*ELEC_MASS*BETA_SQ
      TEMP2=ION_POTL*(1.0D0-BETA_SQ)
      TEMP=DLOG(TEMP1/TEMP2)-BETA_SQ
      DEDX=DEDX*(C1*C1)*ELEC_MASS
      DEDX=DEDX*TEMP/BETA_SQ
* CALCULATE ENERGY LOSS DE=(DE/DX)(DX) AND NEW TOTAL MOMENTUM
        DE=DEDX*DL*1000.
        WRITE(37,*)DE
      EKIN=EKIN+(DEDX*DL)
      EKIN_SQ=EKIN*EKIN
      PTOTAL=DSQRT(EKIN_SQ+2.0D0*EKIN*PD_MASS)
* DETERMINE NEW MOMENTUM COMPONENTS
      PX=PTOTAL*DSIN(THETA)*DCOS(PHI)
      PY=PTOTAL*DSIN(THETA)*DSIN(PHI)
      PZ=PTOTAL*DCOS(THETA)
      RETURN
      END
```

```
      SUBROUTINE SURVEY(EXPNO,RUNNO)
* THIS SUBROUTINE  PUTS THE APPROPRIATE SURVEY CONSTANTS INTO THE
* COMMON BLOCK - SCM, AS DETERMINED BY THE EXPERIMENT NUMBER AND
* RUN NUMBER.  THE SURVEY CONSTANTS ARE USED BY THE SUBROUTINE
* HERA_SCM TO CORRECTLY TRANSLATE AND ROTATE TO THE SCM105 COORDINATE
* SYSTEM.       B. GARNETT
      INTEGER EXPNO,RUNNO
      COMMON /SCM/Z1,D1,D2
      REAL*8 Z1,D1,D2

      IF(EXPNO.EQ.665) GOTO 500

      IF((RUNNO.GE.28).AND.(RUNNO.LE.791)) THEN
      Z1=208.0D0
      D1=0.254D0
      D2=-0.762D0
      RETURN
      ENDIF

      IF((RUNNO.GE.792).AND.(RUNNO.LE.1239)) THEN
      Z1=250.7D0
      D1=-0.1D0
      D2=0.15D0
      RETURN
      ENDIF

      IF((RUNNO.GE.1240).AND.(RUNNO.LE.1336)) THEN
      Z1=251.25D0
      D1=-0.34D0
      D2=-0.17D0
      RETURN
      ENDIF

      IF((RUNNO.GE.1337).AND.(RUNNO.LE.1408)) THEN
      Z1=234.1D0
      D1=0.64D0
      D2=-0.32D0
      RETURN
      ENDIF

      IF((RUNNO.GE.1409).AND.(RUNNO.LE.1471)) THEN
      Z1=217.5D0
      D1=-0.32D0
      D2=-0.48D0
      RETURN
      ENDIF

      IF((RUNNO.GE.1472).AND.(RUNNO.LE.1550)) THEN
      Z1=229.2D0
      D1=0.0D0
      D2=-0.254D0
      RETURN
      ENDIF

      IF((RUNNO.GE.1551).AND.(RUNNO.LE.1637)) THEN
      Z1=209.4D0
      D1=0.7D0
      D2=0.7D0
      RETURN
      ENDIF

      IF((RUNNO.GE.1638).AND.(RUNNO.LE.1690)) THEN
      Z1=220.0D0
      D1=0.40D0
      D2=0.625D0
      RETURN
      ENDIF

      IF((RUNNO.GE.1691).AND.(RUNNO.LE.1773)) THEN
      Z1=225.0D0
      D1=0.0D0
      D2=-0.15D0
      RETURN
      ENDIF
```

```
500     IF((RUNNO.GE.30).AND.(RUNNO.LE.318)) THEN
        Z1=212.6D0
        D1=0.2D0
        D2=0.4D0
        RETURN
        ENDIF
        IF((RUNNO.GE.319).AND.(RUNNO.LE.561)) THEN
        Z1=218.2D0
        D1=3.8D0
        D2=1.3D0
        RETURN
        ENDIF
        IF((RUNNO.GE.562).AND.(RUNNO.LE.676)) THEN
        Z1=213.6D0
        D1=-1.0D0
        D2=-0.2D0
        RETURN
        ENDIF
        IF((RUNNO.GE.677).AND.(RUNNO.LE.830)) THEN
        Z1=214.5D0
        D1=-0.64D0
        D2=0.0D0
        RETURN
        ENDIF
        IF((RUNNO.GE.831).AND.(RUNNO.LE.948)) THEN
        Z1=208.5D0
        D1=0.4D0
        D2=-0.3D0
        RETURN
        ENDIF
        IF((RUNNO.GE.949).AND.(RUNNO.LE.963)) THEN
        Z1=210.3D0
        D1=-1.27D0
        D2=-0.64D0
        RETURN
        ENDIF

        END
```

```
      SUBROUTINE ROTATE(X,Z)
***
*     THIS SUBROUTINE TRANSFORMS THE X AND Z POSITIONS OF A
*     PARTICLE FROM THE HERA COORDINATE SYSTEM (ORIGIN AT THE
*     CENTER OF THE TARGET) TO THE SCM SYSTEM (ORIGIN AT THE
*     CENTER OF THE SCM105). A TRANSLATION IS FIRST PERFORMED,
*     FOLLOWED BY A ROTATION.  B. GARNETT
***
      INTEGER CASE
      REAL*8 XTEMP,X,Z,XPRIM1,ZPRIM1,SIN1,COS1,COSTH,SINTH
      REAL*8 A,Z0,Z1,Z2,L1,D1,D2,ZTEMP,TEMP1,TEMP2
      COMMON /MON_P_1/P_P,HERA_ANG,SCM_ANG,PHICOTH,KPERIM
      INTEGER*2 KPERIM  !FLAG CONTROLLING EVENT GENERATION
      REAL*8 P_P,HERA_ANG,SCM_ANG,ANGLE,PHICOTH(6)
      REAL*8 ATHETA,CTHETA,DTHETA,COS2,COS3,COS4,SIN2,SIN3,SIN4
      PARAMETER PI=3.14159265358D0

      TEMP1=DABS(D2)-DABS(D1)
      TEMP2=DABS(D2)+DABS(D1)
      ANGLE=SCM_ANG
      COS1=DCOS(ANGLE)
      ZTEMP=L1/(2.0*COS1)
      ATHETA=DATAN(TEMP2/L1)
      CTHETA=DATAN(TEMP1/L1)
      DTHETA=DATAN(-TEMP1/L1)
      COS2=DCOS(ATHETA)
      COS3=DCOS(CTHETA)
      COS4=DCOS(DTHETA)
      SIN1=DSIN(ANGLE)
      SIN2=DSIN(ATHETA)
      SIN3=DSIN(CTHETA)
      SIN4=DSIN(DTHETA)

****
*     WRITE(6,*)'IM IN HERA SCM:'
*     DUMMY=SCM_ANG*180.0D0/PI
*     WRITE(6,*)'SCM_ANG= ',DUMMY
*     WRITE(6,*)'X,Z: ',X,Z
*     WRITE(6,*)'COS1,SIN1: ',COS1,SIN1
****
* ROTATE COORDINATE SYSTEM BY THE SCM ANGLE ( FROM Z-AXIS ALONG BEAM THROUGH THE SCATTERING ANGLE - Z' THROUGH
* CENTER OF THE SCM105)
      XTEMP=X
      X=(X*COS1)+(Z*SIN1)
      Z=(-XTEMP*SIN1)+(Z*COS1)
****
*     WRITE(6,*)'STILL IN HERASCM'
*     WRITE(6,*)'XPRIME: ',X
*     WRITE(6,*)'ZPRIME: ',Z
      GOTO 999
****
*     GOTO(10,20,30,40,50,60,70,80)CASE
* CASE A:
   10 A=0.5*TEMP1*COS2
      Z2=ZTEMP+DABS(0.5*TEMP1*SIN2)
      COSTH=COS2
      SINTH=SIN2
      GOTO 100
* CASE B:
   20 A=-0.5*TEMP1*COS2
      Z2=ZTEMP+DABS(-0.5*TEMP1*SIN2)
      COSTH=COS2
      SINTH=SIN2
      GOTO 100
* CASE C:
   30 A=0.5*TEMP2*COS3
      Z2=ZTEMP+DABS(0.5*TEMP2*SIN3)
      COSTH=COS3
      SINTH=SIN3
      GOTO 100
* CASE D:
   40 A=0.5*TEMP2*COS4
      Z2=ZTEMP-DABS(0.5*TEMP2*SIN4)
      COSTH=COS4
      SINTH=SIN4
```

```
      GOTO 100
* CASE E:
   50 A=-0.5*TEMP2*COS3
      Z2=ZTEMP+DABS(-0.5*TEMP2*SIN3)
      COSTH=COS3
      SINTH=SIN3
      GOTO 100
* CASE F:
   60 A=-0.5*TEMP2*COS4
      Z2=ZTEMP-DABS(-0.5*TEMP2*SIN4)
      COSTH=COS4
      SINTH=SIN4
      GOTO 100
* CASE G:
   70 A=-0.5*(-TEMP1)*COS2
      Z2=ZTEMP-DABS(0.5*TEMP1*SIN2)
      COSTH=COS2
      SINTH=SIN2
      GOTO 100
* CASE H:
   80 A=0.5*(-TEMP1)*COS2
      Z2=ZTEMP-DABS(-0.5*TEMP1*SIN2)
      COSTH=COS2
      SINTH=SIN2

***   TRANSLATION TO THE PRIMED FRAME   ***
  100 Z0=DABS(Z1)+DABS(Z2)
      XPRIM1=X-A
      ZPRIM1=Z-Z0
      GOTO(300,200,300,300,200,200,300,200)CASE

***   ROTATION TO THE DOUBLE PRIMED FRAME   ***
* POSITIVE ROT.
  200 X=(XPRIM1*COSTH)-(ZPRIM1*SINTH)
      Z=(XPRIM1*SINTH)+(ZPRIM1*COSTH)
      RETURN
* NEGATIVE ROT.
  300 X=(XPRIM1*COSTH)+(ZPRIM1*SINTH)
      Z=(-XPRIM1*SINTH)+(ZPRIM1*COSTH)
999   RETURN
      END
```

```
      SUBROUTINE THERA2(I_PLANE,HIT)
* THIS SUBROUTINE TRACES THE PARTICLE THROUGH THE HERA FIELD.  AS SOON
* AS THE PARTICLE EXITS THE TARGET, LOSE_IT IS CALLED TO DETERMINE THE ENERGY LOSS.
* SUBROUTINE HERA_TRACE IS CALLED TO CHECK IF THE PARTICLE IS IN A DETECTOR PLANE.
      IMPLICIT REAL*8 (A-H,O-Z)
      COMMON/HXYZ/HX,HY,HZ,HO
      COMMON /NON_V_1/PMOM(7),PTOT
      INTEGER I_PLANE
      LOGICAL LFOO,FIRST,HIT,PROJ
      PARAMETER HOO=25.0D0
      PARAMETER DL=2.0D0
      EQUIVALENCE (PMOM(1),X1),(PMOM(2),Y1),(PMOM(3),Z1)
      EQUIVALENCE (PMOM(4),PX1),(PMOM(5),PY1),(PMOM(6),PZ1)
      EQUIVALENCE (PMOM(7),T)
      FIRST=.TRUE.
      PROJ=.TRUE.
      T=0.0D0
      OPEN(4,NAME='HERA.DAT',STATUS='OLD')
      CALL FIELD
      PXSQ=PX1*PX1
      PYSQ=PY1*PY1
      PZSQ=PZ1*PZ1
      PT=DSQRT(PXSQ+PYSQ+PZSQ)
      HO=HOO*10.D0
      NSTEP=0
      I_PLANE=2
      P=PT/1000.D0
      PX1=PX1/1000.D0
      PY1=PY1/1000.D0
      PZ1=PZ1/1000.D0
   10 NSTEP=NSTEP+1
      CALL TRAJ(P,X1,Y1,Z1,PX1,PY1,PZ1,DL,X2,Y2,Z2,PX2,PY2,PZ2)
*      IF(PROJ) THEN
*       CALL PROJECT_IT(X1,Y1,Z1,X2,Y2,Z2)
*       PROJ=.FALSE.
*      ENDIF
      LFOO=IN_HERA(X2,Y2,Z2)
      IF((.NOT.LFOO).AND.(FIRST)) THEN                    !IF OUT OF TARGET, THEN CALCULATE ENERGY LOSS
      CALL LOSE_IT
      CALL EXTR_PARMS(PT)
      FIRST=.FALSE.
      ENDIF
      CALL HERA_TRACE(X1,Y1,Z1,X2,Y2,Z2,I_PLANE,HIT)
      IF(HIT) THEN
      CLOSE(4)
      RETURN
      ENDIF
      X1=X2
      Y1=Y2
      Z1=Z2
      PX1=PX2
      PY1=PY2
      PZ1=PZ2
      R=SQRT(X2*X2+Y2*Y2+Z2*Z2)
      IF(R.LE.180.0D0) GO TO 10
9000  FORMAT(I8,3F8.2,5X,3F10.4,3F10.1)
1234  FORMAT(/,3X,'NSTEP',5X,'X',7X,'Y',7X,'Z',13X,'PX',9X,'PY',
     18X,'PZ',9X,'HX',8X,'HY',8X,'HZ')
      PX1=PX1*1000.D0
      PY1=PY1*1000.D0
      PZ1=PZ1*1000.D0
      CLOSE(4)
      RETURN
      END

      SUBROUTINE TRAJ (P,X1,Y1,Z1,PX1,PY1,PZ1,DL,X2,Y2,Z2,PX2,PY2,PZ2)
      IMPLICIT DOUBLE PRECISION (A-H,O-Z)
      COMMON/MAP/RIM1(20),RIM2(20),ZIM1(20),ZIM2(20),M1B(20),M2B(20),
     1JJA(20),KFA(20),RI(100),ZI(120),HZI(100,30),HRI(100,30),MM
      COMMON/HXYZ/HX,HY,HZ,HO
      DATA MM/4/
C
C**     CALCULATION OF A STEP OF DIMENSION DL(IN CM),H IN GAUSS
C**     X1,...PX1,... POSITION AND MOMENTUM AT START
C**     X2,...PX2,... POSITION AND MOMENTUM AT END  (CM AND GEV/C)
```

```
C**     OZ IS THE AXIS OF THE MAGNET AND OX VERTICAL (Y=Z.X)
C
      T=DL/P
      IF((PX1.EQ.0.0D0).AND.(PY1.EQ.0.0D0)) THEN
       X2=X1
       Y2=Y1
       Z2=Z1+PZ1*T/2.0D0
       PX2=PX1
       PY2=PY1
       PZ2=PZ1
       RETURN
      ENDIF
      XB=X1+PX1*T/2.D0
      YB=Y1+PY1*T/2.D0
      ZB=Z1+PZ1*T/2.D0
      RB=SQRT(XB**2+YB**2)
      ZBA=ABS (ZB)
      DO 31 JA=1,MM
      R12=(RB-RIM1(JA))*(RB-RIM2(JA))
      IF(R12)32,32,31
 32   Q12=(ZBA-ZIM1(JA))*(ZBA-ZIM2(JA))
      IF(Q12)33,33,31
 31   CONTINUE
      GO TO 4
 33   JI=JJA(JA)
      M11=JI+M1B(JA)-2
      KI=KFA(JA)
      KF1=KI+M2B(JA)-2
      DO 6 J1=JI,M11
      R12=(RB-RI(J1))*(RB-RI(J1+1))
      IF(R12)3,3,6
 6    CONTINUE
      GO TO 4
 3    DO   1K=KI,KF1
      Q12=(ZBA-ZI(K))*(ZBA-ZI(K+1))
      IF(Q12)2,2,1
 1    CONTINUE
 4    HT=0.D0
      GO TO 261
 2    K1=K-KI+1
 9    RE=HRI(J1,K1)
      RF=HRI(J1+1,K1)
      RG=HRI(J1,K1+1)
      RH=HRI(J1+1,K1+1)
      QE=HZI(J1,K1)
      QF=HZI(J1+1,K1)
      QG=HZI(J1,K1+1)
      QH=HZI(J1+1,K1+1)
      RQ=RI(J1)
      RQM=RI(J1+1)
      ZP=ZI(K)
      ZPL=ZI(K+1)
      EMU=(ZBA-ZP)/(ZPL-ZP)
      ELA=(RB-RQ)/(RQM-RQ)
      HZ=((QG*EMU+QE*(1.D0-EMU))*(1.D0-ELA)+(QH*EMU+QF*(1.D0-EMU))*
     2 ELA)*HO
      HR=((RG*EMU+RE*(1.D0-EMU))*(1.D0-ELA)+(RH*EMU+RF*(1.D0-EMU))*
     2 ELA)*HO
      IF(ZB.LT.0.) HR=-HR
      HX=0.D0
      HY=HX
      IF(RB.LT.1E-10) GO TO 120
      HX=HR*XB/RB
      HY=HR*YB/RB
120   HT=SQRT(HZ**2+HR**2)
      IF(HT)261,261,260
261   X2=X1+PX1*T
      Y2=Y1+PY1*T
      Z2=Z1+PZ1*T
      PX2=PX1
      PY2=PY1
      PZ2=PZ1
      GO TO 500
 260  PHT=(PX1*HX+PY1*HY+PZ1*HZ)/HT
      PPT=SQRT(P**2-PHT**2)
      RPH=PHT/HT
```

```
      PPX1=PX1-RPH*HX
      PPY1=PY1-RPH*HY
      PPZ1=PZ1-RPH*HZ
      FX1=PPY1*HZ-PPZ1*HY
      FY1=PPZ1*HX-PPX1*HZ
      FZ1=PPX1*HY-PPY1*HX
      FT=SQRT(FX1**2+FY1**2+FZ1**2)
      RA=PPT/(300.D0*HT)*1.E09
      TET=PPT/RA*T
      Z=PHT*T
      STET=SIN (TET)
      CTET=COS (TET)
      X=RA*(1.-CTET)
      PX=PPT*STET
      Y=RA*STET
      PZ=PHT
      PY=PPT*CTET
      AFX=FX1/FT
      AFY=FY1/FT
      AFZ=FZ1/FT
      APX=PPX1/PPT
      APY=PPY1/PPT
      APZ=PPZ1/PPT
      AHX=HX/HT
      AHY=HY/HT
      AHZ=HZ/HT
      X2=X1+AFX*X+APX*Y+AHX*Z
      Y2=Y1+AFY*X+APY*Y+AHY*Z
      Z2=Z1+AFZ*X+APZ*Y+AHZ*Z
      PX2=AFX*PX+APX*PY+AHX*PZ
      PY2=AFY*PX+APY*PY+AHY*PZ
      PZ2=AFZ*PX+APZ*PY+AHZ*PZ
  500 CONTINUE
      RETURN
C
C**    READING OF THE FIELD MAP AS A PERCENTAGE OF THE CENTRAL FIELD
C**    H0=CENTRAL FIELD (DIVIDED BY 100)
      ENTRY FIELD
      READ(4,103)(RIM1(J),RIM2(J),ZIM1(J),ZIM2(J),M1B(J),M2B(J),J=1,MM)
   11 JF=0
      KF=0
      DO 800 JA=1,4
      JI=JF+1
      JF=JF+M1B(JA)
      JJA(JA)=JI
      M2=M2B(JA)
      KI=KF+1
      KF=KF+M2B(JA)
      KFA(JA)=KI
      READ(4,101)(RI(J),J=JI,JF)
      READ(4,101)(ZI(J),J=KI,KF)
      READ(4,101)((HZI(J,K),K=1,M2),J=JI,JF)
      READ(4,101)((HRI(J,K),K=1,M2),J=JI,JF)
  800 CONTINUE
      RETURN
  101 FORMAT(5X15F5.2)
  103 FORMAT(2(5X4F6.1,2I3),1X)
      END
```

```
      SUBROUTINE DETCOF(BVEC,XYZ,IN,IP,JB,NEXT)
*
*     THIS SUBROUTINE DOES A LEAST-SQUARES FIT TO A POLYNOMIAL
*     OF ORDER-IP WITH A ONE POINT CONSTRAINT.  THIS SUBROUTINE
*     REQUIRES SUBROUTINE PACKAGE CROUT.SUB .  B.GARNETT
*
*     BVEC= B-FIELD VALUES TO BE FIT (BX,BY,OR BZ'S)
*     XYZ= 3xIN ARRAY OF X,Y,Z VALUES TO FIT
*     IN= NUMBER OF POINTS TO FIT
*     IP= ORDER OF POLYNOMIAL TO FIT
*     JB= B-FIELD COMPONENT IDENTIFIER BX=1,BY=2,BZ=3
*
      REAL*8 SUM(8),BSUM(4)
      REAL*8 XYZ(3,5),COFMAT(4,4)
      REAL*8 WTMAT(3,3),BVEC(3,5),DZERO(3)
      REAL*8 BDAT(3,7,4),WTCOFFS(3,7),AZERO(3)
      LOGICAL NEXT
      COMMON /OUTPT/ BDAT,WTCOFFS,XYZNOT,XNEAR,YNEAR,ZNEAR
      REAL*8 XYZNOT(3)
      INTEGER XNEAR,YNEAR,ZNEAR

      KSUB=3
      DO 40 I=1,3
      AZERO(I)=0.0D0
      DZERO(I)=0.0D0
   40 CONTINUE
      DO 1000 K=1,3                          !X=1,Y=2,Z=3
      J1=IP+3
      J2=IP+1
      J3=IP+2
        DO 50 I=1,J1
   50   SUM(I)=0.0D0
        DO 75 I=1,J3
   75   BSUM(I)=0.0D0
        DO 80 I=1,3
        DO 80 J=1,3
        WTMAT(I,J)=0.D0
   80   CONTINUE
        DO 90 I=1,4
        DO 90 J=1,4
        COFMAT(I,J)=0.D0
   90   CONTINUE
*
*     DO SUMATIONS AND STORE IN ARRAY- SUM
*
        SUM(1)=1.0*DFLOAT(J1)
        DO 100 J=2,J1
          DO 100 I=1,IN
  100     SUM(J)=SUM(J)+XYZ(K,I)**(DFLOAT(J-1))
        SUM(6)=1.0
        DO 200 J=2,3
  200   SUM(J+J1)=XYZ(K,KSUB)**(DFLOAT(J-1))
*
*     READ SUMS INTO COEFFICIENT AND WEIGHT MATRICES
*
        DO 300 J=0,IP
          DO 300 I=1,J2
          COFMAT(J+1,I)=SUM(I+J)
          WTMAT(J+1,I)=SUM(I+J)
  300     CONTINUE
        DO 400 L=1,J2
        COFMAT(J3,L)=SUM(L+J1)
        COFMAT(L,J3)=SUM(L+J1)
  400   CONTINUE                               !ROW AND COLN. FOR CONSTRAINT
        COFMAT(J3,J3)=0.0D0
*
*     B-FIELD SUMS AND READ INTO ARRAY- BSUM
*
        DO 450 I=1,5
  450   BSUM(1)=BSUM(1)+BVEC(K,I)
        DO 500 J=2,J2
          DO 500 I=1,IN
  500     BSUM(J)=BSUM(J)+BVEC(K,I)*(XYZ(K,I)**(DFLOAT(J-1)))
          BSUM(J3)=BVEC(K,KSUB)
*
```

```
      CALL CROUT(COFMAT,4,BSUM,1,POO,4)      !DETERMINE COEFF'S
      CALL MATINV(WTMAT,3,3,DET)             !INVERT WEIGHT MATRIX
      AZERO(K)=BSUM(1)
      DZERO(K)=WTMAT(1,1)
      IF (K.EQ.1) IOFF=1
      IF (K.EQ.2) IOFF=J2
      IF (K.EQ.3) IOFF=2*IP+1

      IF (NEXT) THEN
      L=3
      M=4
      ELSE
      L=1
      M=2
      ENDIF

        DO 600 I=1,2
        BDAT(JB,I+IOFF,L)=BSUM(I+1)
        BDAT(JB,I+IOFF,M)=(WTMAT(I+1,I+1))**.5
  600   CONTINUE

        BDAT(JB,1,L)=AZERO(1)
        BDAT(JB,1,M)=(DZERO(1))**.5

 1000 CONTINUE
      RETURN
      END


      SUBROUTINE MATINV(ARRAY,N,NORDER,DET)
*
*     MATRIX INVERSION SUBROUTINE FROM BEVINGTON P.302
*     B.GARNETT
*
*     ARRAY= INPUT MATRIX WHICH IS REPLACED BY ITS INVERSE
*     NORDER,N= DEGREE OF MATRIX (ORDER OF DETERMINANT)
*     DET= DETERMINANT OF INPUT MATRIX
*
      INTEGER N,NORDER
      REAL*8 ARRAY(N,N),AMAX,SAVE,DET
      INTEGER IK(10),JK(10)
   10 DET=1.
   11 DO 100 K=1,NORDER
      AMAX=0.
   21   DO 30 I=K,NORDER
          DO 30 J=K,NORDER
   23     IF (ABS(AMAX)-ABS(ARRAY(I,J))) 24,24,30
   24     AMAX=ARRAY(I,J)
          IK(K)=I
          JK(K)=J
   30   CONTINUE
   31 IF (AMAX) 41,32,41
   32 DET=0.
      GO TO 140
   41 I=IK(K)
      IF (I-K) 21,51,43
   43   DO 50 J=1,NORDER
        SAVE=ARRAY(K,J)
        ARRAY(K,J)=ARRAY(I,J)
   50   ARRAY(I,J)=-SAVE
   51 J=JK(K)
      IF (J-K) 21,61,53
   53   DO 60 I=1,NORDER
        SAVE=ARRAY(I,K)
        ARRAY(I,K)=ARRAY(I,J)
   60   ARRAY(I,J)=-SAVE
   61   DO 70 I=1,NORDER
        IF (I-K) 63,70,63
   63   ARRAY(I,K)=-ARRAY(I,K)/AMAX
   70   CONTINUE
   71   DO 80 I=1,NORDER
          DO 80 J=1,NORDER
          IF (I-K) 74,80,74
   74     IF (J-K) 75,80,75
   75     ARRAY(I,J)=ARRAY(I,J)+ARRAY(I,K)*ARRAY(K,J)
   80   CONTINUE
```

```
 81    DO 90 J=1,NORDER
       IF (J-K) 83,90,83
 83    ARRAY(K,J)=ARRAY(K,J)/AMAX
 90    CONTINUE
     ARRAY(K,K)=1./AMAX
100  DET=DET*AMAX
101  DO 130 L=1,NORDER
     K=NORDER-L+1
     J=IK(K)
     IF (J-K) 111,111,105
105   DO 110 I=1,NORDER
      SAVE=ARRAY(I,K)
      ARRAY(I,K)=-ARRAY(I,J)
110   ARRAY(I,J)=SAVE
111  I=JK(K)
     IF (I-K) 130,130,113
113   DO 120 J=1,NORDER
      SAVE=ARRAY(K,J)
      ARRAY(K,J)=-ARRAY(I,J)
120   ARRAY(I,J)=SAVE
130  CONTINUE
140  RETURN
     END
```

```
      SUBROUTINE SCM_HF3(X,Y,Z,BX,BY,BZ,HIT)
*
*     THIS SUBROUTINE CALCULATES BX,BY,BZ FOR AN ARBITRARY X,Y,Z VALUE
*     WITHIN THE FIELD MAP. THIS SUBROUTINE REQUIRES SUBROUTINE PACKAGE
*     DETCOF.SUB .  B.GARNETT
*
      PARAMETER VECD=3
      PARAMETER XDIM=41
      PARAMETER YDIM=15
      PARAMETER ZDIM=121
      PARAMETER SCMXDIM=101.6
      PARAMETER SCMYDIM=33.02
      PARAMETER SCMZDIM=153.63
      PARAMETER XSCM=106.68
      PARAMETER YSCM=41.91
      PARAMETER ZSCM=63.183
      REAL*8 XBXYZ,YBXYZ,BZXYZ
      REAL*8 X,Y,Z
      REAL*8 XF,YF,ZF,TEMP
      REAL*8 XNEW,YNEW,ZNEW,BXYZ,BNOT(3)
      REAL*8 XMR,YMR,ZMR,DX,DY,DZ,XYZNOT(3)
      REAL*8 XP,YP,ZP,BX,BY,BZ,NEWXYZ(3,5)
      REAL*8 BDAT(3,7,4),BVEC(3,5),XYZ(3,5),WTCOFFS(3,7)
      INTEGER*2 MAGMAP(VECD,XDIM,YDIM,ZDIM)
      INTEGER XMIN,YMIN,ZMIN,XNEAR,YNEAR,ZNEAR
      LOGICAL NEXT,HIT
      COMMON/POLDAT/MAGMAP,XF,YF,ZF
      COMMON /BNOTXYZ/ BNOTX,BNOTY,BNOTZ,XEAR,YEAR,ZEAR
      INTEGER XEAR,YEAR,ZEAR
      REAL*8 BNOTX,BNOTY,BNOTZ
      COMMON /OUTPT/BDAT,WTCOFFS,XYZNOT,XNEAR,YNEAR,ZNEAR
      COMMON /DEBUG/IBUG
      INTEGER IBUG
      XP=X
      YP=Y
      ZP=Z
*
*     POINT NOT IN FIELD MAP, DROP OUT
*
      IF ((XP.LT.-SCMXDIM).OR.(XP.GT.SCMXDIM)) GO TO 999
      IF ((YP.LT.-SCMYDIM).OR.(YP.GT.SCMYDIM)) GO TO 999
      IF ((ZP.LT.-SCMZDIM).OR.(ZP.GT.SCMZDIM)) GO TO 999
*
*     IF IN MAP, TRANSFORM X,Y,Z IN CM. TO X,Y,Z IN MAP COORDINATES
*
      TEMP=(DFLOAT(XDIM)-1.)/2.
      XP=(-XP/SCMXDIM)*TEMP+(TEMP+1.)

      TEMP=(DFLOAT(YDIM)-1.)/2.
      IF(Y.EQ.0.0D0) YP=TEMP+1.0D0
      IF(Y.LT.0.0D0) YP=(-YP/(SCMYDIM-2.54))*TEMP+(TEMP)
      IF(Y.GT.0.0D0) YP=(-YP/(SCMYDIM-2.54))*TEMP+(TEMP+1.)
      TEMP=2.54-SCMYDIM
      IF ((Y.GE.-SCMYDIM).AND.(Y.LT.TEMP)) THEN
       YP=(YP-TEMP)/2.54+2.
      ENDIF
      IF ((Y.GT.-TEMP).AND.(Y.LE.SCMYDIM)) THEN
       YP=(YP+TEMP)/2.54+(DFLOAT(YDIM)-1.)
      ENDIF

      TEMP=(DFLOAT(ZDIM)-1.)/2.
      ZP=(-ZP/SCMZDIM)*TEMP+(TEMP+1.)
*
       XMIN=INT(XP)
       YMIN=INT(YP)
       ZMIN=INT(ZP)
       XMR=DFLOAT(XMIN)
       YMR=DFLOAT(YMIN)
       ZMR=DFLOAT(ZMIN)
       XNEAR=NINT(XP)
       YNEAR=NINT(YP)
       ZNEAR=NINT(ZP)
       XEAR=XNEAR
       YEAR=YNEAR
       ZEAR=ZNEAR
```

```
      DX=XP-DFLOAT(XNEAR)
      DY=YP-DFLOAT(YNEAR)
      DZ=ZP-DFLOAT(ZNEAR)

      IF (XNEAR.EQ.XMIN) THEN
      XYZNOT(1)=3.
      ELSE
      XYZNOT(1)=4.
      ENDIF

      IF (YNEAR.EQ.YMIN) THEN
      XYZNOT(2)=3.
      ELSE
      XYZNOT(2)=4.
      ENDIF

      IF (ZNEAR.EQ.ZMIN) THEN
      XYZNOT(3)=3.
      ELSE
      XYZNOT(3)=4.
      ENDIF

*
*     READ IN XYZ ARRAY FOR FIRST SET OF POINTS TO FIT, READ FIELD
*     VALUES AT THESE POINTS INTO BVEC, AND DETERMINE COEFFICIENTS.
*
      CALL RAYRED(XMIN,YMIN,ZMIN,XYZ)
*
*     RENORMALIZE THE XYZ VALUES TO RANGE FROM 1 TO 5.
*
      IF (YMIN.EQ.1) THEN
      CALL RAYRED2(NEWXYZ)
      ELSE
      CALL RAYRED(3,3,3,NEWXYZ)
      ENDIF
*
      NEXT=.FALSE.
      DO 100 I=1,3                    !BX=1,BY=2,BZ=3
      CALL B_READ(XYZ,I,BVEC,1)
      CALL DETCOF(BVEC,NEWXYZ,5,2,I,NEXT)
  100 CONTINUE
*
*     SECOND SET OF POINTS
*
      CALL RAYRED(4,4,4,NEWXYZ)       !RENORMALIZE SECOND SET
      NEXT=.TRUE.
      DO 200 I=1,3                    !BX=1,BY=2,BZ=3
      CALL B_READ(XYZ,I,BVEC,2)
      CALL DETCOF(BVEC,NEWXYZ,5,2,I,NEXT)
  200 CONTINUE
*
*     CALCULATE WEIGHTED AVERAGES OF THE COEFFICIENTS
*
      CALL WT_AVE(XP,YP,ZP,XMIN,YMIN,ZMIN)
*
*     CALCULATE BX,BY,BZ FOR THE ARBITRARY POINT (X,Y,Z)
*
      DO 500 L=1,3
  500 BNOT(L)=DFLOAT(MAGMAP(L,XNEAR,YNEAR,ZNEAR))
      CALL BCALC(1,DX,DY,DZ,BXYZ)
        XBXYZ=BXYZ*XF*1.0D-4
      BX=BXYZ+BNOT(1)
        BX=BX*XF*1.0D-4
        BNOTX=BNOT(1)*XF*1.0D-4
      CALL BCALC(2,DX,DY,DZ,BXYZ)
        YBXYZ=BXYZ*YF*1.00D-4
      BY=BXYZ+BNOT(2)
        BY=BY*YF*1.0D-4
        BNOTY=BNOT(2)*YF*1.0D-4
      CALL BCALC(3,DX,DY,DZ,BXYZ)
        ZBXYZ=BXYZ*ZF*1.0D-4
      BZ=BXYZ+BNOT(3)
        BZ=BZ*ZF*1.0D-4
        BNOTZ=BNOT(3)*ZF*1.0D-4
 1000 RETURN
  999 IF ((ZP.GE. -SCMZDIM).AND.(ZP.LE.ZSCM)) THEN
```

```
      IF (ABS(XP).GE.XSCM) HIT=.TRUE.
      IF (ABS(YP).GE.YSCM) HIT=.TRUE.
     ENDIF
     BX=0.0D0
     BY=0.0D0
     BZ=0.0D0
     RETURN
     END

     SUBROUTINE BCALC(INDX,XX,YY,ZZ,BXYZ)
     REAL*8 XX,YY,ZZ,BXYZ,XXYYZZ(3)
     REAL*8 BDAT(3,7,4),WTCOFFS(3,7),XYZNOT(3)
     REAL*8 DBXYZ(3),DBXYZ2(3),XYZMR(3)
     REAL*8 X,Y,Z,DXM,DYM,DZM
     COMMON /OUTPT/BDAT,WTCOFFS,XYZNOT,XNEAR,YNEAR,ZNEAR
     INTEGER XNEAR,YNEAR,ZNEAR
     COMMON /DEBUG/IBUG
     INTEGER IBUG

     XXYYZZ(1)=XX
     XXYYZZ(2)=YY
     XXYYZZ(3)=ZZ

     J=0
     DO 10 I=2,6,2
     J=J+1
     DBXYZ(J)=WTCOFFS(INDX,I)+2.*WTCOFFS(INDX,I+1)*XYZNOT(J)
10   CONTINUE

     K=0
     DO 20 I=3,7,2
     K=K+1
     DBXYZ2(K)=WTCOFFS(INDX,I)
20   CONTINUE

     BXYZ=0.D0
     DO 30 I=1,3
     BXYZ=BXYZ+DBXYZ(I)*XXYYZZ(I)+DBXYZ2(I)*(XXYYZZ(I)**2.)
30   CONTINUE

     RETURN
     END

     SUBROUTINE WT_AVE(XX,YY,ZZ,XIN,YIN,ZIN)
     REAL*8 XX,YY,ZZ,A,B,C,D,TEMP1,TEMP2
     REAL*8 BDAT(3,7,4),DLOW(3),DHI(3),WTCOFFS(3,7)
     INTEGER XIN,YIN,ZIN,I,J,K
     COMMON /OUTPT/BDAT,WTCOFFS,XYZNOT,XNEAR,YNEAR,ZNEAR
     REAL*8 XYZNOT(3)
     INTEGER XNEAR,YNEAR,ZNEAR
     COMMON /DEBUG/IBUG
     INTEGER IBUG

     DLOW(1)=XX-DFLOAT(XIN)
     DLOW(2)=YY-DFLOAT(YIN)
     DLOW(3)=ZZ-DFLOAT(ZIN)
     DHI(1)=1.-DLOW(1)
     DHI(2)=1.-DLOW(2)
     DHI(3)=1.-DLOW(3)
     DO 5 I=1,3
     DO 5 J=1,7
5    WTCOFFS(I,J)=0.

     DO 10 I=1,3
     DO 10 J=1,7
     K=-999
      IF (J.LE.3) K=1
      IF ((J.EQ.4).OR.(J.EQ.5)) K=2
      IF (J.GT.5) K=3

      IF ((BDAT(I,J,2).EQ.0.).OR.(BDAT(I,J,4).EQ.0.)) THEN
      WTCOFFS(I,J)=BDAT(I,J,1)*DLOW(K)+BDAT(I,J,3)*DHI(K)
      GO TO 10
      ENDIF

      A=BDAT(I,J,1)/BDAT(I,J,2)**2.
```

```
        B=BDAT(I,J,3)/BDAT(I,J,4)**2.
        C=1./BDAT(I,J,2)**2.
        D=1./BDAT(I,J,4)**2.
        TEMP1=A*DLOW(K)+B*DHI(K)
        TEMP2=C*DLOW(K)+D*DHI(K)
        WTCOFFS(I,J)=TEMP1/TEMP2
   10 CONTINUE
      RETURN
      END

      SUBROUTINE SCM_MAP_READ(IFS)
      PARAMETER VECD=3
      PARAMETER XDIM=41
      PARAMETER YDIM=15
      PARAMETER ZDIM=121
      INTEGER*2 MAGMAP(VECD,XDIM,YDIM,ZDIM)
      INTEGER*4 IFS
      REAL*8 XF,YF,ZF
      COMMON/POLDAT/MAGMAP,XF,YF,ZF
        IF(IFS.EQ.2) GOTO 2000
        IF(IFS.NE.1) STOP 'INVALID FIELD SELECTED IN SCM_MAP_READ'
        WRITE(6,1)
1       FORMAT(' READING IN THE HIGH FIELD SCM105 MAP')
        OPEN(50,NAME='SCM_Y.HFL',STATUS='OLD',READONLY)
        READ(50,*) YF
       READ(50,982)(((MAGMAP(2,I,J,K),I=1,41),J=1,15),K=1,121)
        CLOSE(50)
        OPEN(50,NAME='SCM_X.HFL',STATUS='OLD',READONLY)
        READ(50,*) XF
       READ(50,982)(((MAGMAP(1,I,J,K),I=1,41),J=1,15),K=1,121)
        CLOSE(50)
        OPEN(50,NAME='SCM_Z.HFL',STATUS='OLD',READONLY)
        READ(50,*) ZF
       READ(50,982)(((MAGMAP(3,I,J,K),I=1,41),J=1,15),K=1,121)
        CLOSE(50)
        RETURN
2000    WRITE(6,2)
2       FORMAT(' READING IN THE LOW FIELD SCM105 FIELD')
        OPEN(50,NAME='SCM_Y.LFL',STATUS='OLD',READONLY)
        READ(50,*) YF
       READ(50,982)(((MAGMAP(2,I,J,K),I=1,41),J=1,15),K=1,121)
        CLOSE(50)
        OPEN(50,NAME='SCM_X.LFL',STATUS='OLD',READONLY)
        READ(50,*) XF
       READ(50,982)(((MAGMAP(1,I,J,K),I=1,41),J=1,15),K=1,121)
        CLOSE(50)
        OPEN(50,NAME='SCM_Z.LFL',STATUS='OLD',READONLY)
        READ(50,*) ZF
       READ(50,982)(((MAGMAP(3,I,J,K),I=1,41),J=1,15),K=1,121)
        CLOSE(50)
      RETURN
  982 FORMAT(41A2)
      END

      SUBROUTINE RAYRED(IX,IY,IZ,XYZ)
      REAL*8 XYZ(3,5)
      DO 10 J=1,5
       XYZ(1,J)=DFLOAT(IX-3+J)
       XYZ(2,J)=DFLOAT(IY-3+J)
       XYZ(3,J)=DFLOAT(IZ-3+J)
   10 CONTINUE
      RETURN
      ENTRY RAYRED2(XYZ)
      XYZ(2,1)=1.5D0
      DO 20 K=2,5
      XYZ(2,K)=DFLOAT(K)
   20 CONTINUE
      DO 30 L=1,5
      XYZ(1,L)=DFLOAT(L)
      XYZ(3,L)=DFLOAT(L)
   30 CONTINUE
      RETURN
      END

      SUBROUTINE B_DETERM(TEMP,I,VEC)
      PARAMETER VECD=3
```

```
      PARAMETER XDIM=41
      PARAMETER YDIM=15
      PARAMETER ZDIM=121
      INTEGER*2 MAGMAP(VECD,XDIM,YDIM,ZDIM)
      REAL*8 VEC(5),TEMP(3,5)
      REAL*8 XF,YF,ZF
      COMMON/POLDAT/MAGMAP,XF,YF,ZF
      DO 10 II=1,5
      J=NINT(TEMP(1,II))
      K=NINT(TEMP(2,II))
      L=NINT(TEMP(3,II))
      IF ((J.LT.1).OR.(J.GT.XDIM)) THEN
      VEC(II)=0.1D0
      ELSE
      IF ((K.LT.1).OR.(K.GT.YDIM)) THEN
      VEC(II)=0.1D0
      ELSE
      IF ((L.LT.1).OR.(L.GT.ZDIM)) THEN
      VEC(II)=0.1D0
      ELSE
      VEC(II)=DFLOAT(MAGMAP(I,J,K,L))
      ENDIF
      ENDIF
      ENDIF
   10 CONTINUE
      RETURN
      END

      SUBROUTINE B_READ(BXYZ,III,BVEC,K)
      REAL*8 BXYZ(3,5),BVEC(3,5),TEMP(3,5),BDAT(3,7,4)
      REAL*8 VEC(5),NEARX,NEARY,NEARZ,XYZNOT(3)
      REAL*8 WTCOFFS(3,7)
      INTEGER XNEAR,YNEAR,ZNEAR
      COMMON /OUTPT/BDAT,WTCOFFS,XYZNOT,XNEAR,YNEAR,ZNEAR

      NEARX=DFLOAT(XNEAR)
      NEARY=DFLOAT(YNEAR)
      NEARZ=DFLOAT(ZNEAR)
*
*     B AS A FCN. OF X
*
      DO 10 I=1,5
      TEMP(1,I)=BXYZ(1,I)
      TEMP(2,I)=NEARY
      TEMP(3,I)=NEARZ
   10 CONTINUE
      CALL SECOND(K,1,BXYZ,TEMP)
      CALL B_DETERM(TEMP,III,VEC)
      DO 15 J=1,5
   15 BVEC(1,J)=VEC(J)

*
*     B AS A FCN. OF Y
*
      DO 20 I=1,5
      TEMP(1,I)=NEARX
      TEMP(2,I)=BXYZ(2,I)
      TEMP(3,I)=NEARZ
   20 CONTINUE
      CALL SECOND(K,2,BXYZ,TEMP)
      CALL B_DETERM(TEMP,III,VEC)
      DO 25 J=1,5
   25 BVEC(2,J)=VEC(J)

*
*     B AS A FCN. OF Z
*
      DO 30 I=1,5
      TEMP(1,I)=NEARX
      TEMP(2,I)=NEARY
      TEMP(3,I)=BXYZ(3,I)
   30 CONTINUE
      CALL SECOND(K,3,BXYZ,TEMP)
      CALL B_DETERM(TEMP,III,VEC)
      DO 35 J=1,5
   35 BVEC(3,J)=VEC(J)
```

```
      RETURN
      END

      SUBROUTINE SECOND(K,INDEX,XYZ,TEMP)
      REAL*8 TEMP(3,5),XYZ(3,5)

      IF (K.NE.2) GO TO 999
      DO 10 I=1,5
   10 TEMP(INDEX,I)=XYZ(INDEX,I)+1.
  999 RETURN
      END
```

```
      SUBROUTINE XYREAD(CHMBRXY)
      REAL*8 CHMBRXY(88),XOFF,YOFF
      OPEN(60,NAME='CHMBRXY.DAT',STATUS='OLD')
      OPEN(64,NAME='OFFSETS.DAT',STATUS='OLD')
      J=4
      DO 10 I=1,22
      READ(60,*)CHMBRXY(J-3),CHMBRXY(J-2),CHMBRXY(J-1),CHMBRXY(J)
      READ(64,*)XOFF,YOFF
      CHMBRXY(J-3)=CHMBRXY(J-3)+XOFF
      CHMBRXY(J-2)=CHMBRXY(J-2)+XOFF
      CHMBRXY(J-1)=CHMBRXY(J-1)+YOFF
      CHMBRXY(J)=CHMBRXY(J)+YOFF
      J=J+4
   10 CONTINUE
      CLOSE(60)
      CLOSE(64)
      RETURN
      END
```

Appendix D Spin Precession

Using a magnetic field, it is possible to precess the spin of a particle. Below is a brief discussion of this phenomenon and how it was applied to this experiment.

In the laboratory frame, the spin precession is given by [Ja-75]:

$$\frac{d\vec{\sigma}}{dt} = \frac{e}{mc}\vec{\sigma} \times \left[\left(\frac{g}{2} - 1 + \frac{1}{\gamma}\right)\vec{B} - \left(\frac{g}{2} - 1\right)\frac{\gamma}{\gamma+1}\left(\vec{\beta}\cdot\vec{B}\right)\vec{\beta}\right] \qquad \text{(D.1)}$$

where g is the gyromagnetic ratio. One can define an orthogonal coordinate system $\left(\hat{L}, \hat{S}, \hat{N}\right)$ with $\hat{L}$ along the direction of motion and $\hat{S}$ in the horizontal plane a follows:

$$\hat{L} = \frac{\vec{\beta}}{\beta} \qquad \text{(D.2)}$$

$$\hat{S} = \hat{y} \times \hat{L} \qquad \text{(D.3)}$$

$$\hat{N} = \hat{L} \times \hat{S} \qquad \text{(D.4)}$$

where $\hat{y}$ is a unit vector in the vertical direction.

Using $\beta = \frac{v}{c} = \frac{1}{c}\frac{dl}{dt}$, then $dt = \frac{1}{\beta c}dl$ in the laboratory frame. With this result equation D.1 can be written in component form with respect to the above defined

coordinate system as follows:

$$\frac{d\sigma_L}{dl} = \frac{e}{\beta mc^2}\left(\frac{g}{2}-1+\frac{1}{\gamma}\right)(\sigma_S B_N - B_S\sigma_N) + \left(\frac{g}{2}-1\right)\frac{\gamma}{\gamma+1}\left(\vec{\beta}\cdot\vec{B}\right)(\sigma_N\beta) \quad \text{(D.5)}$$

$$\frac{d\sigma_S}{dl} = \frac{e}{\beta mc^2}\left(\frac{g}{2}-1+\frac{1}{\gamma}\right)(\sigma_N B_L - B_N\sigma_L) \quad \text{(D.6)}$$

$$\frac{d\sigma_N}{dl} = \frac{e}{\beta mc^2}\left(\frac{g}{2}-1+\frac{1}{\gamma}\right)(\sigma_L B_S - B_L\sigma_S) + \left(\frac{g}{2}-1\right)\frac{\gamma}{\gamma+1}\left(\vec{\beta}\cdot\vec{B}\right)(\sigma_S\beta) \quad \text{(D.7)}$$

It should be apparent from the equations above that if the spin is oriented along the field, there is no precession. During our experiment there was no component of N-type spin, only a linear combination of S and L-type before the spin precession magnets, LORRAINE and CASTOR. The field orientations of these two magnets were always in the $\pm\hat{N}$ direction, therefore giving $\vec{\beta}\cdot\vec{B}=0$. Using $\frac{e}{mc^2}=\frac{4\pi}{hc}\mu$, where μ is the particle magnetic moment, Eqns. D.5-D.7 reduce to the following two equations:

$$\frac{d\sigma_L}{dl} = \frac{4\pi}{\beta hc^2}\mu\left(\frac{g}{2}-1+\frac{1}{\gamma}\right)(\sigma_S B_N) \quad \text{(D.8)}$$

$$\frac{d\sigma_S}{dl} = \frac{4\pi}{\beta mc^2}\mu\left(\frac{g}{2}-1+\frac{1}{\gamma}\right)(-\sigma_L B_N) \quad \text{(D.9)}$$

Therefore, a particle with pure $\hat{S}$-type spin could be precessed to $\hat{L}$-type and vice versa.

Appendix E Spinology for $C_{\sigma\sigma}$

In order to extract pure C_{SS} values from the measured values of $C_{\sigma\sigma}$, it was necessary to do various spinology. The spin of the neutron beam at JPAN is given by

$$\vec{P}_B = (-\hat{x}\sin\theta_B + \hat{z}\cos\theta_B)P_B$$

where θ_B is the angle of a beam particle's spin with respect to its direction of motion along the beam axis. The polarized target magnet was rotated in order to detect the recoil protons. The expression for the target spin direction in terms of the rotation angle is given by

$$\vec{P}_T = (-\hat{x}\sin\theta_T + \hat{z}\cos\theta_T)P_T$$

where $\theta_T = 37.5°$. The neutron beam spin was precessed by the HERA field, so that at the target center,

$$\begin{aligned}\frac{d\sigma}{d\tau} &\sim -\vec{\sigma}\times\vec{B} \\ &\sim -\vec{P}_B\times\vec{P}_T \\ &\sim -\hat{y}\sin(\theta_B-\theta_T)\ .\end{aligned}$$

The negative sign reflects the fact that the gyromagnetic ratio of the neutron is less than zero. The net rotation will be by an angle θ_P.

In order to find the modified beam spin direction at the target center, one must first rotate coordinates such that the new z-direction is along $\vec{P}_T$ and $\hat{y}$ is unchanged. It is then necessary to rotate $\vec{P}_B$ by θ_P, and then finally convert back to the laboratory coordinate system. Therefore, using the following rotation transformation

$$\begin{aligned} \hat{x} &= \hat{x'}\cos\theta_T - \hat{z'}\sin\theta_T \\ \hat{y} &= \hat{y'} \\ \hat{z} &= \hat{x'}\sin\theta_T - \hat{z'}\cos\theta_T \end{aligned}$$

it is possible to express the beam spin direction in terms of the rotated coordinate system:

$$\begin{aligned} \frac{\vec{P}_B}{P_B} &= \hat{x'}(-\cos\theta_T\sin\theta_B + \cos\theta_B\sin\theta_T) \\ &+ \hat{z'}(\sin\theta_B\sin\theta_T + \cos\theta_B\cos\theta_T) \ . \end{aligned}$$

The precession by θ_P will leave the $\hat{z'}$ component unchanged, but will mix $\hat{x'}$ and $\hat{y'}$. Therefore, the beam spin direction as given in the precessed coordinate system is

$$\begin{aligned} \frac{\vec{P'}_B}{P_B} &= \hat{x'}\cos\theta_P(-\cos\theta_T\sin\theta_B + \cos\theta_B\sin\theta_T) \\ &+ \hat{y'}\sin\theta_P(-\cos\theta_T\sin\theta_B + \cos\theta_B\sin\theta_T) \\ &+ \hat{z'}(\sin\theta_B\sin\theta_T + \cos\theta_B\cos\theta_T) \ . \end{aligned}$$

By using the following inverse coordinate transformation,

$$\begin{aligned} \hat{x'} &= \hat{x}\cos\theta_T + \hat{z'}\sin\theta_T \\ \hat{y'} &= \hat{y} \\ \hat{z'} &= -\hat{x}\sin\theta_T + \hat{z}\cos\theta_T \end{aligned}$$

it is possible to express the precessed spin direction in terms of the laboratory coordinates. This transformed spin direction is given by

$$\begin{aligned} \frac{\vec{P'}_B}{P_B} &= \hat{x}[-\cos\theta_P\cos\theta_T\sin(\theta_B-\theta_T) - \sin\theta_T\cos(\theta_B-\theta_T)] \\ &- \hat{y}\sin\theta_P\sin(\theta_B-\theta_T) \\ &+ \hat{z}[-\cos\theta_P\sin\theta_T\sin(\theta_B-\theta_T) + \cos\theta_T\cos(\theta_B-\theta_T)] \ . \end{aligned}$$

The magnetic field of HERA causes an effective rotation of the scattering plane by causing the outgoing proton to spiral out of the target. This means that protons with laboratory angles less than θ_T will be bent down and hence, the particles will originate above the horizontal plane of the polarized target center. The rotation angle is proportional to $\vec{P} \times \vec{B}$. If one calls the rotation angle θ_R, then $\vec{P}_B$ and $\vec{P}_T$ can be rotated into this new coordinate system by the transformation:

$$\begin{aligned} \hat{x} &= \hat{x''}\cos\theta_R + \hat{y''}\sin\theta_R \\ \hat{y} &= -\hat{x''}\sin\theta_R + \hat{y''}\cos\theta_R \\ \hat{z} &= \hat{z''} \ . \end{aligned}$$

Therefore, by inserting the above expressions for the coordinates into the expressions for $\vec{P}_T$ and $\vec{P}_T$, given earlier, the net results are

$$\begin{aligned}
\vec{P}_T &= P_T\{-\sin\theta_T(\hat{x}''\cos\theta_R + \hat{y}''\sin\theta_R) + \hat{z}''\cos\theta_T\} \\
\vec{P}'_B &= P_B\{-(\hat{x}''\cos\theta_R + \hat{y}''\sin\theta_R)[\cos\theta_P\cos\theta_T\sin(\theta_B \\
&- \theta_T) + \sin\theta_T\cos(\theta_B - \theta_T)] \\
&- (-\hat{x}''\sin\theta_R + \hat{y}''\cos\theta_R)\sin\theta_P\sin(\theta_B - \theta_T) \\
&+ \hat{z}''[-\cos\theta_P\sin\theta_T\sin\theta(\theta_B - \theta_T + \cos\theta_T\cos(\theta_B - \theta_T)]\}
\end{aligned}$$

The measured spin parameter is then given by

$$C_{\sigma\sigma} = aC_{SS} + bC_{NN} + dC_{LL} + eC_{SL}$$

where

$$\begin{aligned}
a &= -\sin\theta_T\cos\theta_R[-\cos\theta_R\cos\theta_p\cos\theta_T\sin(\theta_B - \theta_T) \\
&- \cos\theta_R\sin\theta_T\cos(\theta_B - \theta_T) + \sin\theta_R\sin\theta_p\sin(\theta_B - \theta_T)] \\
b &= -\sin\theta_T\sin\theta_R[-\sin\theta_R\cos\theta_p\cos\theta_T\sin(\theta_B - \theta_T) \\
&- \sin\theta_R\sin\theta_T\cos(\theta_B - \theta_T) - \cos\theta_R\sin\theta_p\sin(\theta_B - \theta_T)] \\
d &= \cos\theta_T[-\cos\theta_p\sin\theta_T\sin(\theta_B - \theta_T) + \cos\theta_T\cos(\theta_B - \theta_T)] \\
e &= -\sin\theta_T\cos\theta_R[-\cos\theta_p\sin\theta_T\sin(\theta_B - \theta_T) + \cos\theta_T\cos(\theta_B - \theta_T)]
\end{aligned}$$

$$+ \quad \cos\theta_T[-\cos\theta_R\cos\theta_p\cos\theta_T\sin(\theta_B-\theta_T)-\cos\theta_R\sin\theta_T\cos(\theta_B-\theta_T)$$

$$+ \quad \sin\theta_R\sin\theta_p\sin(\theta_B-\theta_T)] \ .$$

A computer program was written to calculate the neutron spin precession angle and the rotation angle of the scattering plane in the HERA magnetic field.

☆U.S. GOVERNMENT PRINTING OFFICE: 1988-673-034/00102